Galactic Archaeology with Asteroseismology: From Oscillations to the Evolution of the Milky Way

by

Ben Matthew Rendle

A thesis submitted to the

University of Birmingham

for the degree of

DOCTOR OF PHILOSOPHY

Sun, Stars and Exoplanets

School of Physics and Astronomy

University of Birmingham

Birmingham, B15 2TT

April 2019

Abstract

Determining precise ages is one of the most limiting factors in accurately characterising the formation history of the Milky Way. Current uncertainties of order $> 40\%$ render age estimates meaningless for stars older than 10 Gyr. It is anticipated that the major Galactic structures formed within the first few Gyr of the Milky Ways history, hence a higher temporal resolution is necessary to study this epoch.

In this thesis, we present a series of results aimed at progressing the accuracy to which ages can be determined through asteroseismology. We introduce a new stellar parameter determination code, which can use oscillation mode frequencies as inputs. We show the code performs to expectation from the literature and that including the oscillation modes improves the accuracy and precision of the parameter determinations compared to existing methods.

Ensemble asteroseismic grid modelling is applied to the K2 Campaign 3 and 6 fields. We find evidence for a bimodal age distribution for populations extending vertically within the Galactic disc, indicating multiple star formation epochs. Improvements in age resolution are still required to confirm any quiescence between distribution peaks. Increasing observational baselines and using individual mode frequencies may hold the key to achieving the temporal resolution required.

Acknowledgements

Writing this thesis was never truly to be an individual effort, and there are many people to thank for getting me to this point. First and foremost, I'd like to thank my supervisor, Andrea Miglio, for the support he gave me to develop into the researcher I am today. His input and help both scientifically and personally have been greatly appreciated throughout my studies. I'd also like to thank Bill Chaplin for his assistance as my secondary supervisor, Guy Davies for being a font of statistical knowledge and Gaël Buldgen for his assistance in guiding me out of an analytical mire and seeing the light at the end of a project. Special thanks also go to Cristina Chiappini for her relentless belief in my work and continual expert input, and to Clare Worley and Paula Jofre for words of wisdom and support in my forays into the world of observational astronomy. A final academic thanks go to all the PhD students in the HiROS group at UoB throughout my stay for keeping me sane (apart from Friday afternoons), being a continual sounding board of reason and a source of eloquent and tasteful memes.

I'd like to thank my Mum and Dad for their continual belief in me to pursue my interests and for their desire to see me be happy. It's given me the freedom to express myself and make it through the tough moments. I wouldn't have achieved this without them. Thanks also go to my brother, John, for always being interested in what I do, no matter how complex or random the ideas I tell him are. In addition, a large thank you must go to my girlfriend, Elle. We met at the start and she's been ever present throughout. She's seen the highs and lows, but still believed in me and

continues to make me smile after a long day, helping me switch off and provide the perfect balance to my life. Jack, Joe and Morgan, you know the impact on my life you've had and thanks go to all my other friends who have helped and assisted me in any way. You know who you are.

A final thanks goes out to UoB Korfball and Birmingham Panthers KC. My time with both clubs has provided the perfect amount of silliness and shenanigans, along with incredible friendships and highlights. A special thanks goes to Alex Quy in particular. The mischief, drama and DMCs wouldn't have been the same without you.

I would also like to extend my thanks to my examiners Yveline Lebreton and Sean McGee for making the viva a pleasure and their valuable feedback to complete this thesis.

Contents

List of Figures

List of Tables

Introduction and Overview of the Thesis

Chapter 1

Introduction and Plan

To understand how anything works, one must first understand the principle components of what is being studied. This approach can be applied to anything from the inner mechanics of how a watch ticks, to understanding how atoms and molecules interact with each other. By knowing the most fundamental properties of the constituents of a given object, in most cases one theoretically has all the tools required to comprehend the bigger picture they are constituents of. Despite this, the emerging picture can remain unclear. The building blocks may not be perfect, and their interpretation often varies depending upon the approach taken to bring the fundamental components together. Finding a cohesion between approaches and a definitive set of well characterised fundamental properties are continual challenges faced by the scientific community, and lay at the heart of one of the major questions in near-field cosmology - how did the Milky Way form and evolve?

Prior to considering the challenges behind dissecting the Milky Way's history and current state, we need to understand why it is important to study it in the wider context. Why should we focus on what's surrounding us when we have a wealth of information spanning multiple epochs and stages of formation for distant galaxies? What can our own Galaxy teach us that others cannot? The study of galaxies is one of the cornerstones of modern astrophysics. Not only can one trace the movement of baryonic matter in the Universe since primordial times, but also

the interactions between, and movements of, the dark matter halos in which they are expected to have formed. Galaxy evolution can be used as a probe of the widely accepted ΛCDM (e.g. White & Rees 1978) cosmological model, confirming the importance of hierarchical accretion and other predictions through cosmic time. Hence, a detailed knowledge of galaxy evolution can have widespread implications for other aspects of astrophysics too.

Though highly important, the evolution of galaxies in general remains a problem without a definitive answer. Though technologies and methods have advanced significantly since the 1970's, the statement by Weinberg (1977) still rings remarkably true today:

"...the theory of the formation of galaxies is one of the great outstanding problems in astrophysics, a problem that today seems far from solution...".

Today, we are capable of harvesting great quantities of data about galaxies both near and far, yet understanding the finer nuances and complexities of their formation is still something that evades us. With the increasing data quality and volume, the picture is steadily becoming clearer, yet the community is still limited to assembling theories surrounding formation mechanisms from snapshots of similar looking galaxies at different cosmological redshifts. Information on global kinematics and chemical composition are obtainable, giving clues as to the effects of merger events and episodes of star formation, yet a consistent and categorical meaning of these features is still being discerned. Detailed studies of the constituent populations within galaxies has the potential to resolve important mechanisms and processes, but this is often not possible and is not likely achievable in the near future. The Milky Way may offer a solution to this, though.

The rapidly developing field of near-field cosmology (commonly referred to as Galactic Archaeology, GA) seeks to use the fossil record of the Milky Way to begin to answer some of the fundamental questions surrounding galaxy formation and evolution. Studying the Milky Way provides the unique opportunity to characterise multiple, diverse stellar populations with high resolution spectroscopic and astrometric techniques to achieve levels of detail unobtainable in the studies of other galaxies. Knowing the detailed chemo-dynamics of the Galaxy provides an excellent basis for defining populations and predicting their nominal dispersion and evolution, but it is the measurements of temporal information for these populations that makes studies of the Milky Way so unique and valuable. The ability to derive accurate ages for individual stars affords the opportunity to develop a detailed map of the processes affecting the Milky Way during different epochs. Ageing stellar populations and coupling this with chemo-dynamical information enables one to not only determine when a certain population formed, but also the likely conditions at the time of formation. The ability to discern information such as this makes the Milky Way an important test bed for clarifying aspects of galaxy formation and evolution. Yet, there are still many questions to be answered before extra-galactic studies could start to be benefitted by the inferences of GA.

Even though it has been studied in detail since the 1960's (see Eggen et al. 1962), a complete theory regarding the development and nature of the Milky Way remains elusive. From the origins of globular clusters to the number of large scale components from which it is composed, there are many contentious issues regarding the Milky Way. Each debate is worthy of a thesis in its own right, given the complexities and number of approaches that can be taken to comprehensively analyse each problem. Hence, one focus of this thesis is on a particular aspect - the nature of the *vertical structure of the Milky Way*. The Milky Way is thought to be a structurally typical disc galaxy, consisting of a bulge, prominent disc and halo. Though there are varying theories surrounding the structure of the bulge and halo, it is the composition of the

disc-like component that of interest here. Since the seminal work of Gilmore & Reid (1983) using stellar population densities to demonstrate two geometrically defined discs within the Galaxy, researchers have strived to comprehensively characterise them. The observation of multiple discs is not unique to the Milky Way, with many disc galaxies showing similar structures (e.g. NGC 1288, NGC 2336; see Efremov 2011 for further examples). Therefore, understanding the composition, ages and dynamics of these populations will provide an excellent basis from which inferences about other galaxies can be made.

Though powerful in potential, there is little agreement to be found when defining the thin and thick discs. In recent years, the understanding of these components as purely geometrical entities has evolved. In-depth studies of their chemistry and kinematics has led to caution over how one should define them, as the characteristics and positioning of the components has the potential to vary dependent upon the definition used. This is not entirely problematic. The conflict in ideas has highlighted the true complexity of galaxy evolution and encouraged a diversity of ideas to explain phenomena not only occurring within the Milky Way, but in other galaxies too. Despite this, there is an overwhelming ambition to produce a well constrained definition of our Galaxy's structure. More precise stellar properties are required if this is to be achieved.

To fully disentangle the populations of the discs, high precision stellar parameters are required for the stars within them. Photometric colours and magnitudes are available for billions of stars (see e.g. Skrutskie et al. 2006; Saito et al. 2012; Ivezić et al. 2012), but only a fraction of these have precision measurements of their chemistry and kinematics (Bland-Hawthorn & Gerhard, 2016). In the Gaia-era, this number is ever growing with continually improving kinematic measurements for hundreds of thousands of stars being matched with an increasing number of all-sky spectroscopic surveys such as Gaia-ESO (Gilmore et al., 2012), RAVE (Kunder et al., 2017), APOGEE (Eisenstein et al., 2011a; Majewski et al., 2017), LAMOST

(Deng et al., 2012; Zhao et al., 2012), GALAH (Buder et al., 2018; Dalton et al., 2014), SEGUE-2 (Eisenstein et al., 2011b; Yanny et al., 2009), DESI (DESI Collaboration et al., 2016), MOONS (Cirasuolo et al., 2014), WEAVE (Dalton et al., 2014) and 4MOST (de Jong et al., 2014). This will not fully solve the problem though. The majority of the work in this thesis is dedicated to breaking this impasse through precise age determinations. Precise ages will provide a greater temporal resolution of the disc populations. This allows one to assess when each population developed and whether its characteristics differ greatly enough from another epoch to be considered a distinct population/component. Age uncertainties of less than 20% are currently difficult to achieve (uncertainties are often much greater than this), but this order of precision is necessary otherwise very little can be inferred from a broad spread of ages.

One technique capable of providing the precision in age required is asteroseismology. Simplistically, asteroseismology is the study of oscillations in stars. Asteroseismology of solar-like oscillators in particular is useful to make precise inferences of stellar parameters (Christensen-Dalsgaard, 1986; Gough, 2001). As the pulsations propagate through the stellar interior, information regarding its internal e.g. density stratification, hence the evolutionary state of the star, can be recovered. This means tighter constraints can be placed on parameters such as the mass and density. Improved constraints such as these lead to improvements in the precision of age determinations. For this reason, solar-like oscillators (especially giants) are fantastic probes of the MW. At present, asteroseismology has been applicable to only a small number of fields observed by the CoRoT (Baglin et al., 2006), *Kepler* (Borucki et al., 2010a) and K2 (Howell et al., 2014) missions, limiting its reach and effectiveness to characterise Galactic populations. The on-going TESS (Ricker et al., 2015) and future PLATO (Rauer et al., 2014) missions will revolutionise this though, taking the power and potential of asteroseismology to all regions of the Galaxy.

Though an excellent tool for making precise parameter determinations, astero-

seismic techniques can still be improved for greater precision. The discussion within this thesis will be based off of asteroseismic studies of red giant stars. In particular for red giants, the age of the star scales with mass (see Davies & Miglio 2016). Within asteroseismology, there are multiple approaches that can be taken to calculate the mass, each of which varies in precision and accuracy. The traditional approach is to use global asteroseismic parameters (see chapter 4 for details) within scaling relations (e.g. Kjeldsen & Bedding 1995). The relations provide uncertainties in mass of order $\sim 10\%$, corresponding to age uncertainties of $\sim 30\%$ or more. An alternative method is to use the individual modes of oscillation for parameter determinations. Using individual modes can reduce the mass uncertainties by at least a factor of 3, implying age uncertainties of order $\sim 10 - 20\%$ are feasible. A caveat is that the results are heavily dependent on the quality of the stellar models used for the parameter determination. Provided that any modelling systematics/biases are correctly accounted for, this remains a highly effective method of producing high precision results.

The primary objective of this thesis is to explore the possible impact of asteroseismology in the context of Galactic studies and precise age determinations. I will examine the questions surrounding the vertical structure of the Milky Way within the scope of the *Kepler* and K2 space missions. Stellar populations directly above and below the Galactic plane will be characterised to search for tracers of the suspected multiple disc components. The precision to which asteroseismic measurements can be made will also be explored. The inferences possible when only global asteroseismic relations can be used are shown with K2 studies. A high precision study using the code Asteroseismic Inference on a Massive Scale (AIMS; Reese 2016b; Lund & Reese 2018; Rendle et al. 2019) will also be performed to demonstrate the high temporal resolution potentially available to astronomers when individual mode frequencies are available.

The remainder of this section is divided into two parts. Chapters 2 and 3 provide

an introduction to the Milky Way, its key characteristics and a discussion of possible formation mechanisms. I also include an overview of the current challenges in population and stellar modelling, along with key tracers for stellar population studies in the Galaxy. In chapter 4, I then introduce the field of asteroseismology, providing an overview of the field and how it has helped revolutionise stellar parameter determinations.

Chapter 2

Milky Way and Galactic Archaeology

Understanding and classifying the fundamental properties and formation mechanisms of galaxies is a cornerstone of characterising the evolutionary processes of large scale, extra-galactic structures. Observations at different redshifts have provided valuable insight into the features and mechanisms involved in the evolutionary stages of galaxies. Despite this, it remains difficult to ascertain the finer nuances of galaxy evolution without knowing further information about the stellar populations within the galaxy in question. At the distance scales of galaxies, resolving and characterising these populations is often challenging and for the majority of cases not possible. Fortunately, we find ourselves in a privileged position to do just this.

Since the Greeks named it *'Kiklios Galaxios'*, humanity has tried to understand the Milky Way (MW). William Hershel first mapped the MW in 1785, but not until recently have we begun to fully grasp the intricacies of it. Galactic archaeology (GA) is the field through which current progress is being made. It is a rapidly expanding field, using stars as fossil remnants within the MW to understand its formation history. The objective of the field is to understand the mechanics and structure of the galaxy through the study of the collective properties of stellar populations (typically the chemistry and kinematics). The global and individual properties of such populations contain key information imprinted from prior epochs of evolution within the MW. Accessing and correctly interpreting this information is key when

wanting to understand galactic evolution.

Large scale spectroscopic surveys have dominated GA so far, with collaborations such as Gaia-ESO, RAVE, APOGEE, LAMOST and GALAH running dedicated programs to assist galactic archaeology studies. Mining these data catalogues and identifying over-densities in high dimensional space (e.g. chemistry and age) allows one to study a posteriori the position of stars in the phase space (e.g. see Hogg et al. 2016; Ting et al. 2018; Frankel et al. 2018), uncovering the efficiency of secular processes as well as chemical evolution timescales. Increasing knowledge of individual chemical abundances for stellar populations facilitates more and more detailed studies within this field, with processes such as chrono-chemical tagging becoming more prominent.

Astrometric information is often used to complement spectroscopic findings, providing positions and proper motions for the stars. Combining this with the radial velocities obtainable with spectroscopy, one can begin to compute 3D velocity vectors. This allows a detailed mapping of a star's kinematics. Understanding the motion of a star theoretically allows one to trace its movements back to its origins (one must be cautious of the limitations imposed here by unknown interactions and perturbations in the assumed gravitational field). One could therefore cluster stars born from the same region to give unique insight into the conditions in which these stars formed. With chemical abundances now known for large quantities of stars in the galaxy, combining techniques such as chemical tagging (e.g. De Silva et al. 2009; Pompéia et al. 2011; Hawkins et al. 2015) with kinematic information will allow trace element abundances to be more accurately tracked to their point of origin. In particular, the addition of *Gaia* DR2 (Gaia Collaboration et al., 2018a) parallaxes and dynamical information is vastly improving this field with the wealth of information available.

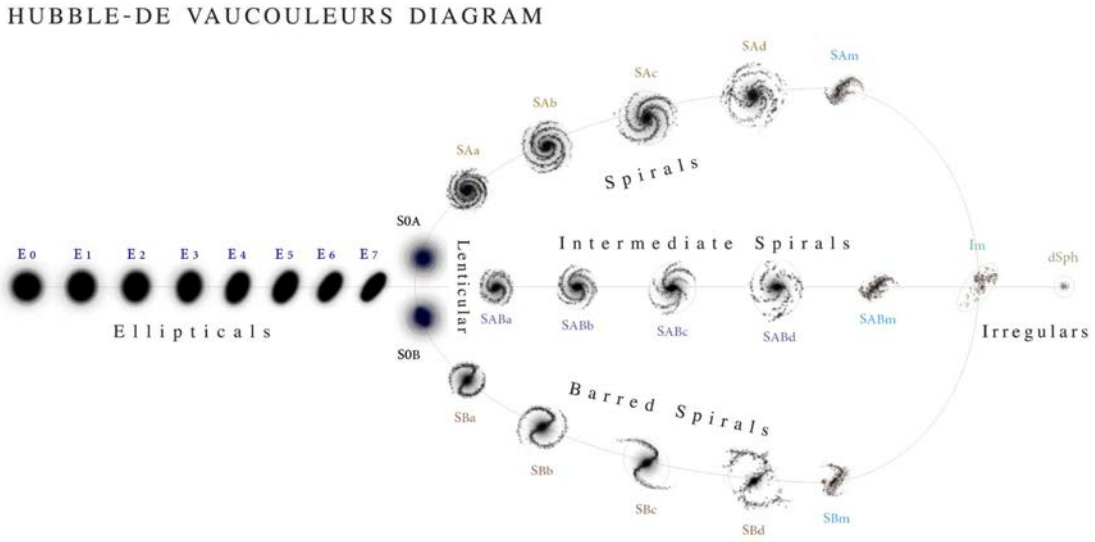

Figure 2.1: The Hubble-de Vaucouleurs Diagram, depicting the different galaxy morphologies and sub-categories observed to date. *Credit: Antonio Ciccolella.*

2.1 General Model of Galaxy Formation

Prior to assessing our current state of knowledge, and gaps therein, of the MW, it is prudent to contextualise the Galaxy within our understanding of galaxy evolution in general. The current, widely accepted cosmological model is the cold dark matter model (ΛCDM; White & Rees 1978). This model predicts the imprinting of density perturbations on the primordial Universe during an epoch of rapid inflation (Guth 1981; see Linde 2018 for a recent review). Increases in local gravitational forces due to the perturbations caused these fluctuations to collapse. Initially, only dark matter was able to flow into these gravitational wells as it was decoupled from radiation and baryonic matter. As the gravitational potential of these wells increased with the infall of dark matter, when baryonic material began to cool after decoupling from radiation, it was also attracted to and started to collapse into the over-densities. The subsequent collapse of baryonic material deep within the gravitational wells led to the formation of the first stars and importantly, the seeds of galaxy formation.

The collapsing of baryonic matter into the early gravitational wells led to the for-

mation of filamentary structures and proto-galaxies. Further hierarchical accretion of matter to larger wells generated merger events between proto-galaxies, influencing the array of galaxy morphologies we observe today (e.g. Peebles 1971; Press & Schechter 1974). The Hubble-de Vaucouleurs diagram, Fig. 2.1 (Hubble, 1936; de Vaucouleurs, 1959a; Sandage, 1961), represents the broad classification of galaxy types, distinguishing four main categories: elliptical, irregular, lenticular and spiral. The Milky Way is considered a barred spiral galaxy (SBc), but within sub-categories there can be a large amount of variation, with MW analogues showing structural differences (e.g. bulge and disc sizes). Hence, to understand galaxy formation is to understand the consequences of merger events and accretion episodes at different cosmic times. This ultimately leads to a greater understanding of the cosmology responsible for the events that shaped the galaxies we observe today.

The resolution to which we are able to study the MW compared to other galaxies means it is an excellent test bed for galaxy evolution theories. Even if few other galaxies exhibit similar structures to the MW, understanding the general processes and permutations of its evolution will assist in providing valuable constraints on the formation of other galactic types.

2.2 The Milky Way as a Galaxy

Our understanding of the Milky Way has traditionally come from comparisons to properties of external galaxies. The components and features of external galaxies have been measured for a long time (e.g. see de Vaucouleurs 1959b) and has allowed the community to define the generic morphology of the Galaxy. It is commonly known that the MW comprises of a bulge component with a boxy-peanut shaped bar, an extended stellar disc containing spiral arms, and a diffuse halo. Each of these attributes are typical of other observed disc-like galaxies. The extent and nature of the components vary in size and brightness from galaxy to galaxy, but the core features are consistent. Evidence of substructure within galactic components is also

regularly observed in galactic studies. Halo structures are often too diffuse to discern, but the stratification of galactic discs has been observed, with varying degrees of domination between the so-called thin and thick components. Edge on observations of disc galaxies have provided this insight, whereas top-down view points illustrate the spiral structure we predict through observations of stellar densities in the MW.

Presently, the definition of each galactic component, particularly for the MW, is still debated. Here, I will give a brief overview of the nature of the Galactic bulge, halo and spiral structure, as well as the outstanding problems facing astronomers today. Questions surrounding the nature of the Galactic disc are discussed in Section 2.2.1. What follows is primarily to provide context. For a more comprehensive review, I refer the reader to Bland-Hawthorn & Gerhard (2016) and references therein.

The Galactic Bulge: The Galactic bulge sits at the centre of the Galaxy. It contains the supermassive black hole (SMBH), Sagittarius A*, and the central bar component of the MW. The bulge is traditionally thought to be one of the first components to be created when a galaxy forms and to provide the material which collapses to form the central SMBH. It is a gas rich environment in which we expect star formation to be continuing throughout the Galaxy's evolution. At the heart of a galaxy, the bulge interacts with all of the galactic components, but this does not mean its properties, formation and interactions are well understood or defined.

For example, the bar is thought to influence the rotation rate of the spiral arms and stars in the MW, but the exact mechanism by which this occurs is yet to be fully constrained (Dehnen, 2000; Wegg et al., 2015). Additionally, the shape of the bar - a boxy peanut (e.g. Dwek et al. 1995; Athanassoula 2005) - is not common place among other galaxies observed, making it more difficult to discern how this may have grown and what further implications this type of structure may have for the rest of the Galaxy. Another question is the origin of the Milky Way bulge. The component is not as prominent as in other MW analogues, suggesting that it was not formed as a distinct accretion event. A possible theory behind its structure could

be that it grew out of the Galactic disc through secular or dynamical processes (e.g. Combes & Sanders 1981; Raha et al. 1991; Guedes et al. 2013), but the processes behind this requires further development.

The Galactic Halo: The halo of the Milky Way is the most diffuse component of the Galaxy. Typically comprised of old stars, it contains satellite galaxies, globular clusters and stellar streams which are relics of past merger events. Though the general picture is accepted, with increasing data there is further debate surrounding its structure. A stratified halo model is now being developed, out of which differing stellar population trends are being predicted. The discovery of *Gaia*-Enceladus (Helmi et al., 2018), the remnants of a galaxy merger with the MW $\sim$ 10 Gyr ago, with *Gaia* DR2 has leant weight to this debate, supporting theories that the inner halo should be dominated by mergers with massive progenitors (Helmi et al., 2003; Cooper et al., 2010). Associated with this is the interaction of the so-called inner halo with the disc and bulge - where does one component end and the other begin (e.g. Morrison et al. 1990; Helmi et al. 2018)? Is it a definitive boundary or an organic transition from one to the other? Clear definitions of each are still being sought after, but further work on characterising the inner halo will assist here.

A further problem surrounding the halo is again associated with its formation. Was it a single accretion event that created the halo we see today, or has it built up over time (Morrison et al., 2009; Haywood et al., 2018)? Developing a comprehensive understanding of halo populations will shed light on this. In particular, improvements in temporal resolution will help to disentangle any multiple populations and the hierarchy in which events occurred during its creation.

Spiral Structure: The MW is thought to have between 2-4 spiral arms (e.g. Georgelin & Georgelin 1976; Bash 1981; Drimmel & Spergel 2001; Urquhart et al. 2014). These are not strictly connected to the Galactic bar, but there is expected to be a gravitational interaction between the components which is responsible for the rotation rates of the arms. Spiral arms have been shown to be typically bluer than

the rest of the host galaxy (with exception of the bulge in some cases), indicating that they are predominant hubs of star formation (younger stars are typically hotter than old stars, emitting shorter wavelengths; e.g. Ragan et al. 2018). But what are the spiral arms made of and how do they propagate? A popular theory is that the spiral arms are a propagating density wave (e.g. Lin & Shu 1964), creating over-densities of cool gas beyond the Jeans mass, promoting star formation (e.g. Taylor 1993). The origins and sustenance of such a wave though remains unclear, as does the interactions of stars with the wave once they've been created (e.g. Toomre 1981; Sellwood & Carlberg 1984; Dobbs & Pringle 2010; Hunt et al. 2018).

It is clear there is still a lot to learn about the MW in both its past and present states. For each component there appears to be multiple problems that require solving before a comprehensive image of galaxy formation can be developed. The disc of the MW is no different in this respect.

2.2.1 Stratification of the Milky Way Disc

Of all the MW components, the structure of the disc is one of the topics most fervently debated in recent times. Considering our position within the Galaxy, observations of disc stars are simple and can be performed in great numbers. One must bare in mind that many of the conclusions drawn about the disc come from knowledge at the Solar radius ($\sim$ 8 kpc from the Galactic centre) and the local neighbourhood. Dust extinction in the Galactic plane towards the bulge largely inhibits observations of the wider Galaxy. Infrared is able to penetrate further into the MW, revealing greater structure within the disc itself and revealing more information about the arms, but it is mainly a lack of reliable distances for stars beyond the solar neighbourhood that has limited our current understanding of the disc.

From side-on observations of nearby galaxies, for 40 years we have known is it

possible to have stratification within disc galaxies (Burstein, 1979; Tsikoudi, 1979). So-called thin and thick disc components, have been observed. These components are normally geometrically defined. The thick disc was observed to be more diffuse and extended compared to the thin disc, even enveloping the narrower component. Thick discs have also been found to be redder in external galaxies, with little evidence of any colour gradients, hinting that they consist of a uniform, old stellar population (Dalcanton & Bernstein, 2002; Rejkuba et al., 2009) compared to the thin disc which shows more varied properties. It is, however, more difficult to discern the chrono-chemical structure of such galaxies, with degeneracies between age and metallicity from broadband photometry (e.g. Schiavon 2007; Conroy & van Dokkum 2012a,b; Pinna et al. 2019).

The work of Gilmore & Reid (1983) first confirmed the presence of multiple disc components within the MW. Using vertical stellar number densities, they were able to fit a two-component exponential to the distribution and show that two different scale heights were required to reproduce the observed trends. This led to the belief of two, distinct populations being present in the MW disc. The thin disc stars were defined as belonging to a population with a short scale height ($\sim$ 300 pc), whereas thick disc stars were defined as having a much more extended scale height ($\sim$ 1 kpc). Since this discovery, researchers have looked to enhance the classification of these two components primarily through measurements of their chemistry and dynamics. This has resulted in multiple definitions of what characteristics a star belonging to the thin or the thick disc should have.

Martig et al. (2016b) present a succinct overview of the different disc structure descriptors. Here, I develop this to include the basic details of the disc definitions according to which regime is used.

Geometric: Based on the decomposition of vertical stellar density profiles (e.g. Yoshii 1982; Gilmore & Reid 1983; Yoachim & Dalcanton 2006; Jurić et al. 2008), or defined by a fixed transition height above the disc midplane (e.g. Yoachim &

Dalcanton 2008; Rejkuba et al. 2009; Cheng et al. 2012a). Typically, exponents are fitted to density profiles to determine whether a single or multilple component fit is required. The number of components required for the fit indicates the number of populations, with characteristic scale heights for each exponent used. Measurements by Jurić et al. (2008) required two components with scale heights of $\sim$ 300 pc for the thin disc and $\sim$ 900 pc for the thick disc. Scale heights have been shown to vary consistently when looking in bins of constant age or [Fe/H] (e.g. Bovy et al. 2012a,b, 2016b; Mackereth et al. 2017a), suggesting a gradual transition between discs rather than a clear distinction. One therefore must be clear to define the population sample when discussing the geometric properties of the Galactic disc.

Chemical: The thin and thick discs can be separated chemically through a dichotomy in [α/Fe] at a fixed [Fe/H]. The observed bimodality has been extensively studied at a broad range of Galactic radii and vertical distances (e.g. Fuhrmann 1998; Bensby et al. 2003, 2005; Bensby 2014; Navarro et al. 2011; Anders et al. 2014; Nidever et al. 2014; Hayden et al. 2015). Nidever et al. (2014) and Hayden et al. (2015) specifically focus on red giant stars in order to probe deeper regions of the Galaxy. The overall agreement is that the high-[α/Fe] ([α/Fe] $\gtrsim$ 0.1) sequence is dominated by older stars, at greater $|Z|$ - thick disc; the low-[α/Fe] ([α/Fe] $\gtrsim$ 0.1) sequence is dominated by younger stars, closer to the Galactic mid-plane - thin disc. Section 2.3 contains further information regarding how this may have come to be.

Dynamical: The use of velocity dispersions and stellar motions to distinguish components (e.g. Morrison et al. 1990; Majewski 1992; Soubiran et al. 2003; Haywood et al. 2013). Each galactic component is expected to have a different kinematic signature, with the thick disc expected to be kinematically hotter than the thin disc as the orbits of the stars are more elliptical and vary in and out of the plane. This separation can be depicted using a Toomre Diagram (see Fig. 2.2).

These definitions above are rarely used in isolation. When describing the thin and thick disc, often all 3 descriptors are used. One is required to be careful though,

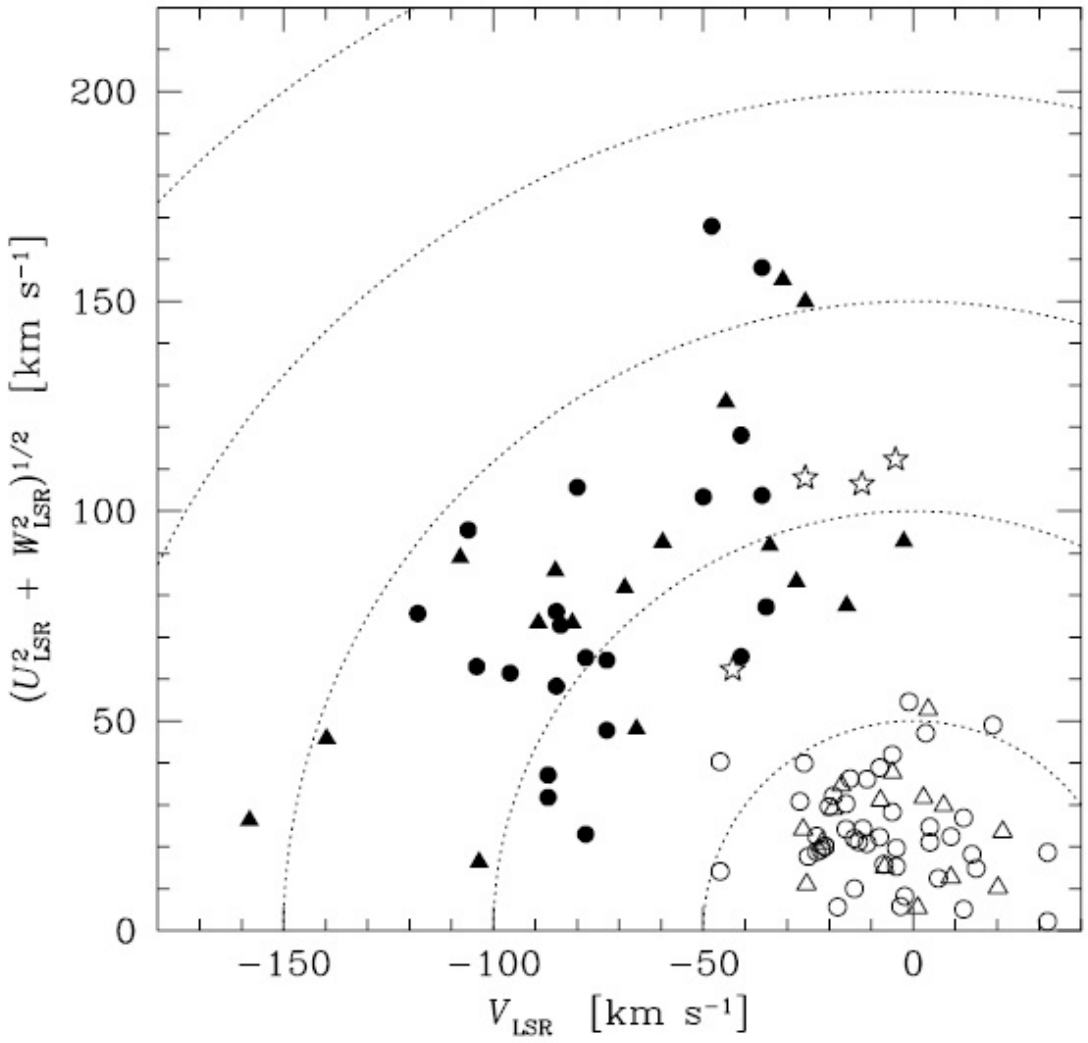

Figure 2.2: A Toomre diagram showing the kinematic distribution of the thin and thick disc, marked by open and filled symbols, respectively. The figure was originally presented in Bensby et al. (2005). Stars with SOFIN or UVES observations are marked by triangles and those from Bensby et al. (2003) are marked by circles. Transition objects are marked by open stars.

as combining the definitions does not always provide further clarity. For example, a chemically defined thin disc star may have kinematic properties associated with the thick disc and vice versa. This degeneracy has led to caution in the manner by which one defines the discs and care should be taken to appropriately describe the population analysed. For example, it has been shown that the chemical and geometric definitions are inconsistent beyond a Galactic radius of $\sim$ 10 kpc (e.g. Minchev et al. 2015). The [α/Fe] enhanced population is predominantly found to be in the inner disc, with scale length of only a few kilo-parsecs (e.g. Bensby et al. 2011; Cheng et al. 2012b; Bovy et al. 2012b; Nidever et al. 2014; Hayden et al. 2015). This implies that an [α/Fe] enhanced population will not strongly dominate beyond 1 kpc above the mid-plane at Galactic radii greater than $\sim$ 10 kpc. It is instead expected that the geometric thick disc is comprised of multiple components which flare up out of the mid-plane at large Galactic radii, changing its chemical properties but maintaining the expected geometry (Minchev et al., 2015). This is possible to infer through the use of mono-age populations. The inclusion of age information is able to break the degeneracy as all components can then be linked to a common time frame. The age must therefore be more accurate and precise than present determinations if this is to be performed effectively and provide further clarity.

2.2.2 Creating Two Components from One

Comprehensively classifying the Galactic disc is a stepping stone to solving the problem of how this component may have formed. Knowing its properties in the present allows for constraints to be put on its past and improve predictions surrounding its evolution. With increasing numbers of observations to compare predictions to, simplistic models such as the 'closed box model' fail to stand up to observations. These models assume no additional material is accreted to the Galaxy and a single chemical enrichment model (e.g. Schmidt 1959, 1963). Though a solution that can predict the general properties of the MW, models such as this have important

limitations compared to observations. One of the most prominent limitations is the G-dwarf problem. The problem is an overestimation of the number of metal poor G-dwarf stars distributed within the Galactic disc compared to observations within the solar vicinity (see Tinsley 1980). An additional problem is the assumed chemical homogeneity of globular clusters formed in this model. Variations in chemical composition between globular clusters have however been found, further discrediting the validity of closed box models for MW evolution.

The failure to reproduce the anticipated metallicity distribution of stars and globular clusters motivated the inclusion of more detailed processes in evolution models. The consideration of accretion events, stellar migration and gas flows have since become important factors in evolutionary models to ensure that the underlying population properties can be correctly predicted. Two particular types of evolutionary model have become popular through their ability to replicate well the chemical trends not only in the solar vicinity, but throughout the extended disc too: the 'two-infall model' (Chiappini et al., 1997, 2001); the 'radial migration' model (Schönrich & Binney, 2009a,b).

The two-infall model as proposed by Chiappini et al. (1997, 2001) predicts two distinct epochs of star formation. An initial phase of rapid, intense star formation leads to an enrichment in [α/Fe] of the interstellar medium (ISM) due to Type-II supernovae. A quiescence in star formation is then enforced, during which enrichment from Type-Ia supernovae begins to dominate and the [α/Fe] of the ISM decreases. A secondary period of extended gas infall then reignites star formation, but at much slower rate than before (more detail is given in section 2.3). The two episodes of star formation produce an old, α-enhanced population and a younger, reduced [α/Fe] population consistent with expectations of the thick and thin discs. Though largely successful, the model is sensitive to the pause in star formation and can struggle to produce a chemical bimodality over an extended range of [Fe/H] (Andrews et al., 2017).

The Schönrich & Binney (2009a,b) radial migration model implements a more continuous star formation history (SFH) than the two-infall model. This model assumes a continuous flow of gas to the Galaxy, and hence a continual SFH. The gas is allowed to vary smoothly and the Galaxy evolution is treated in bins extending radially out from the centre. Gas is allowed to pass between adjacent bins. This is important in order to account for stars that appear to be chemically inconsistent with the local population. The model is reliant upon this mixing in order to reproduce the expected chemical bimodality. It assumes 'inside-out' formation, where α-enhanced stars are expected to have formed rapidly towards the Galactic centre, whereas low-α stars form at later times away from the bulge and inner Galaxy. The bimodality is therefore reliant upon the inward and outward migrations of these two populations. A weakness of this model is that simulations predict that the bimodality is not as distinct as one would expect from observations (Andrews et al., 2017).

Both models discussed succeed in demonstrating that external influences are important to understanding the evolution of the MW. Whilst replicating current trends within the MW better than the closed box model, each model again limits itself to singular processes to control the evolution of the Galaxy. Considering secular processes, such as heating of the initial disc by massive mergers and satellite interactions (e.g. Villalobos & Helmi 2008; Kazantzidis et al. 2009), or direct accretion of pre-enriched stars assists with the replication of vertical spatial structures (e.g. Abadi et al. 2003b), but requires further development in order to reproduce expected chemical enrichment trends. The development of N-body and 'zoom-in' simulations, adapted from cosmology, are beginning to bring these components together (e.g. Martig et al. 2009, 2012; Minchev et al. 2013; Brook et al. 2012) and have had reasonable success in producing MW analogues. As ever, continual refinement is required in order to fully comprehend the unique blend of each scenario that is required in order to unequivocally reproduce current observations of the MW.

2.3 Elemental Synthesis and Stellar Evolution

As discussed in Section 2.2.1, the Galactic disc appears to show a chemical bimodality in [α/Fe] for a given [Fe/H] at the solar radius (Hayden et al. 2015 show how this varies across the Galactic disc). This gives the appearance of two distinct structures within the disc, but how could this be possible? The initial chemistry of a star is determined by the composition of the ISM when the gas cloud collapses. How much this cloud has been polluted by enriched materials (mass loss via winds, supernovae - SN) will then affect the proportion of α-elements (O, Ne, Mg, Ca, Si, Ti; Weiss et al. 2006) and heavy metals (e.g. Fe) the star will composed of. The levels of enrichment of each set of elements is primarily dictated by the rate of type-II and type-Ia SN. Type-II SN are the result of massive stars collapsing after the build up of Fe in their core, resulting in an explosion that releases a large amount of α-elements into the ISM. Type-Ia SN are predominantly thought to be the consequence of a white dwarf star within in binary system accreting fresh hydrogen from its companion (see Wang & Han 2012; Toonen 2017; Toonen et al. 2018 and references therein for a review). Once the layer is dense enough, hydrogen fusion will ignite and cause the white dwarf to go supernova. This process contributes large amounts of Fe and other heavy elements to the ISM. Studying the historic rates of these two SN types provides clues as to the chemical evolution of the MW.

Fig. 2.3 depicts the SN enrichment of the Galaxy as a function of stellar age, according to Spitoni et al. (2019). In the early Galaxy, type-II SN were dominant. Unlike type-Ia, type-II SN do not require the formation of a binary system containing a white dwarf. This leads to a delay time in the number of type-Ia SN increasing. Due to this delay, the early Galaxy was enriched with α-elements. Some Fe was also produced, but is not a dominant contributor to the chemical composition of the ISM at this time. This is shown by the high-[α/Fe] (> 0.2) at low [Fe/H] (< -0.6) on Fig. 2.3. As the feedback from type-Ia SN begins to increase, the α-element

abundances begin to dilute. This process leads to the decreasing slope towards higher [Fe/H]. All of this occurs on a rapid timescale within the first few Gyr of the Galaxy's formation, hence why observing high-[α/Fe] values is associated with older stars and an older Galactic component.

The two processes outlined explain the slope observed between 12.7 and 9.4 Gyr on Fig. 2.3, but not the significant population of the low-α (< 0.05) sequence. If one considers the two-infall model as the mechanism for the creation of the thick and thin disc, then a second accretion of pristine material to the disc is required. Increasing the content of primordial elements (e.g. H, He, Li...) will act to dilute the Fe content of the disc. This reduces the [Fe/H] content, but maintains a constant [α/Fe] leading to the tail parallel to the x-axis (9.4 to 8.7 Gyr; Fig. 2.3). The infall of material will also increase the star formation rate again. The formation of massive stars will then increase the type-II SN rate comparative to the rate of type-Ia SN. This produces a secondary α-enrichment of the ISM (7.7 Gyr). The increase in type-Ia SN feedback is more rapid this time though, as it starts again from a higher initial rate. This leads to a rapid turning over of the trend and the high density of points within the low-α sequence.

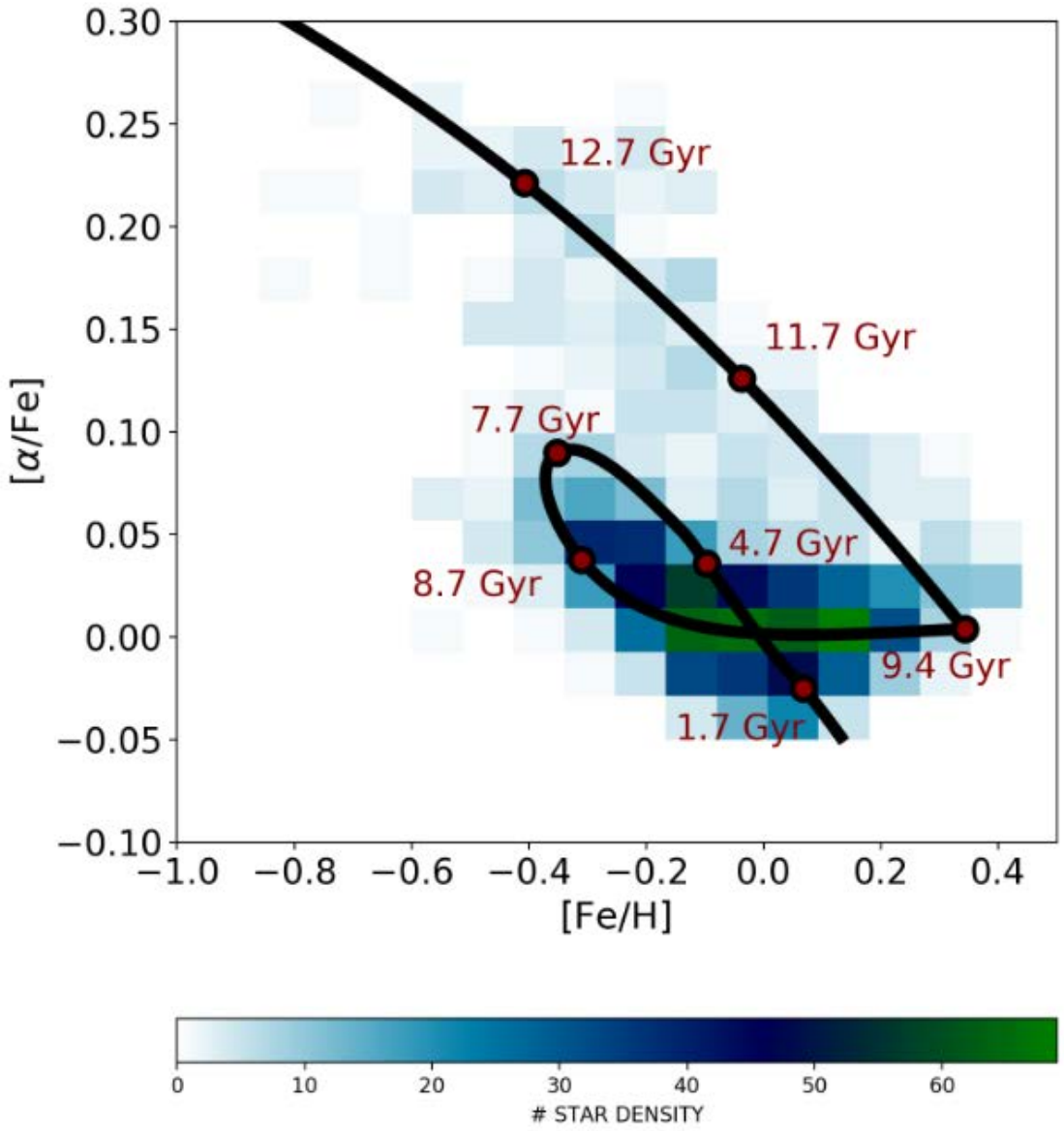

Figure 2.3: Spitoni et al. (2019) figure 2: The [α/Fe] vs. [Fe/H] distribution of stars from Silva Aguirre et al. (2018). Bins coloured to show the density of stars at a given abundance ratio. The chemical evolution model of Spitoni et al. (2019) is fitted (black line), with red circles indicating the age of stars at specific points.

Chapter 3

Stars as Galactic Chronometers

A key aspect of understanding how a galaxy forms and evolves is being able to ascertain when specific events occurred and populations formed. The chemistry and dynamics of stars provide a snapshot of the properties of the Galaxy as it is now, but one needs to reconstruct the temporal sequence to understand the evolution of these properties. To do this, one can use stars as Galactic fossils as they lock into their photosphere the information about the chemistry (for elements unaffected by internal mixing), and to some extent their motions (need to account for interactions with spiral arms, radial migration, heating etc.) from when they were formed. Clustering together stars of similar age, chemistry and kinematics, or 'tagging' them, allows one to assemble a history of formation events. The nature of the formation events can then allow conclusions to be drawn regarding how the MW has evolved. Precise ageing of Galactic components provides a tool to clarify the disc definitions and formation processes offered by geometric, kinematic and chemical definitions.

To decipher the individual features of the MW (e.g. typical ages of the discs), an age resolution of order 10-20% is highly desired. This translates to an uncertainty of $\pm$1.2 Gyr at 8 Gyr and $\pm$1.8 Gyr at 12 Gyr (assuming 15% uncertainty). This level of resolution and beyond will lend significant confidence to any inferred trends and mechanisms relating to events and triggers that may have influenced the properties of specific populations. This is particularly true for stars beyond 10 Gyr, which

are expected to contain a fossil record of rapid evolution of the MW. The temporal resolution is typically poor though, making the need for accurate determinations highly important. Figure 3.1 shows the impact of uncertainties to the features of a population age distribution. Using a magnitude limited synthetic population of red giant stars from TRILEGAL (a TRIdimensional modeL of thE GALaxy, Girardi et al. 2012), the original, 'pristine', age distribution is shown in blue. A prominent old population spike at $\sim$ 11 Gyr and a young distribution peaking at $\sim$ 6 Gyr can be seen. Uncertainties of 10% (orange) and 40% (green) were then applied and the distributions overlaid. The wash out of the original distribution is notable for both uncertainties. At the 10% level, the features are less pronounced but the two populations are recognisable. At 40%, the two populations are indistinguishable. There is no clear young or old prominence and little can be discerned from the distribution. This highlights the importance of obtaining high precision stellar ages for Galactic studies.

Stellar age determinations can be made simply through numerous methods. Soderblom (2010) provides a comprehensive review of the methodologies currently practiced and available. The author defines 5 categories of age determinations, each with different precision levels and feasibility. From perceived high to low quality (Soderblom, 2013), the categories are as follows:

i) Fundamental: The fundamental age is one computed where the internal physics and parameters of the star are well known and precisely defined. There is only 1 star for which we know the fundamental age - the Sun ($4567 \pm 1 \pm 5$ Myr, Soderblom 2013). This is not surprising as it has been observed to a level of detail that is beyond our current capacity for any other star. The radioactive dating of solar system materials strongly constrains the age. The limitations of the information obtainable from other stars compared to the Sun for constraining their internal processes and lack of materials from their local environment mean fundamental ages are unlikely to be possible in the short term.

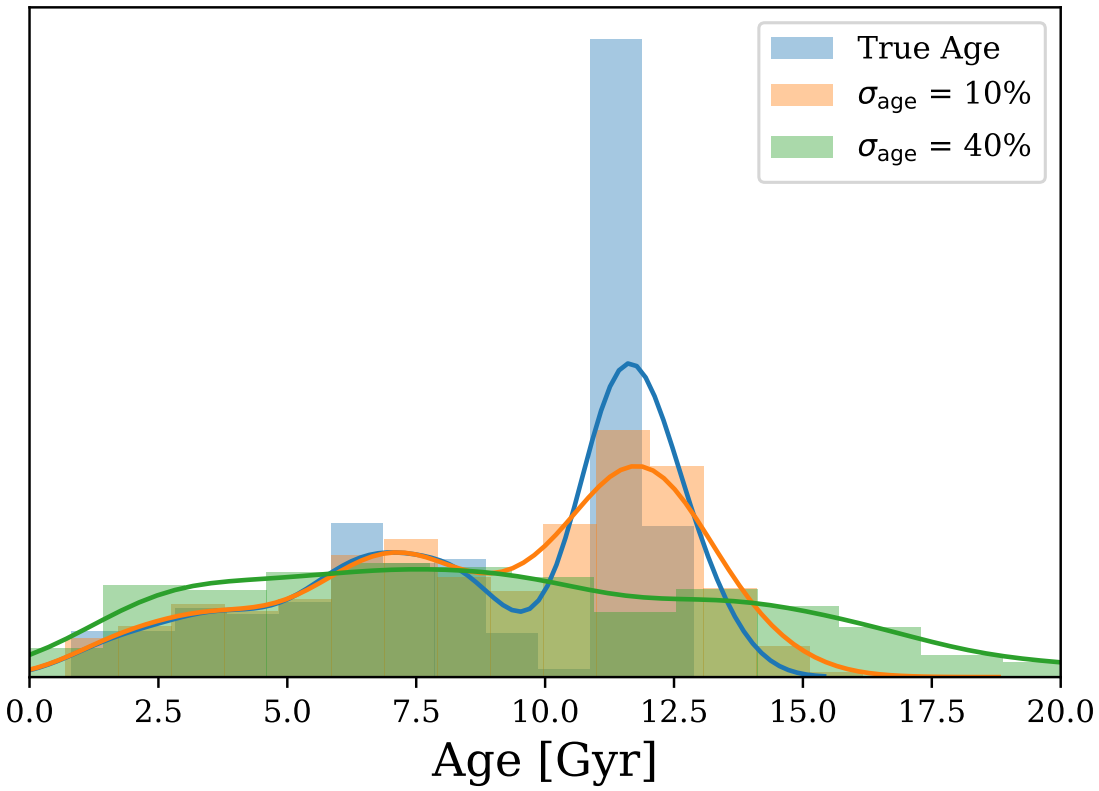

Figure 3.1: The age distribution for a synthetic MW population (TRILEGAL) is shown (blue). This population is perturbed by age uncertainties of 10% (orange) and 40% (green) to demonstrate the necessity for high precision age determinations. It is clear that even at 10% some structural details of the population are blurred, with all structure lost when the uncertainty is 40%.

ii) Semi-fundamental: Semi-fundamental ages can be derived for stars for which we have well-understood physics, but require some informed assumptions to be made due to the limitations of observations. Nucleocosmochronometry is an example of one such technique. It is a particularly good method for ageing old stars as the technique uses the long half-lives of U and Th isotopes. The method has been limited to only a handful of stars as it is difficult to accurately implement (Soderblom, 2010). Assumptions of the initial U and Th abundances are required (r-process elements can be used to guide predictions) which can lead to variations in age by up to a factor of 2 (Soderblom, 2013). Also, very high resolution spectra are necessary to detect the U and Th lines as the signatures are very weak. Nucleocosmochronometry has the potential to be a very powerful age determination tool, but is currently limited to boutique studies and is not appropriate for large scale Galactic population studies.

iii) Model-dependent: Methods utilising inferences of ages from Solar calibrated stellar models. Stellar modelling is the basis of much of the parameter determinations for stars in modern astrophysics. The precision to which a parameter determination can be made relies heavily on the input physics to generate the models and the quality of the stellar input parameters obtained. The technique can be robust and easily applied to ensembles of stars. Limitations to this include the understanding and accommodating of systematics in the models. Techniques including isochrone placement, fitting to the Main Sequence Turn Off (MSTO) in clusters and asteroseismology are considered model dependent techniques.

iv) Empirical: Techniques using observables, such as activity or rotation, for which the physical mechanism is not well constrained, but that are known to change with age. Relations are usually calibrated using model-dependent inferences for stars in open clusters. This calibration method is limited by the lack of open clusters older than ~ 2 Gyr, reducing the validity of the relations for older ages.

v) Statistical: The use of inferences from broad parameter trends with age to date a star. This can include inferences from trends such as the age-metallicity and

age-velocity relations across the Galaxy. These relations are simple to apply, but are subject to scatter within the sample populations and are thus more suited to defining population ages than for individual stars. With increasing use of Bayesian inference and machine learning techniques, the statistical determinations are beginning to become more reliable. High quality, large scale training sets with parameters determined from other methods (usually model-dependent) are being used to infer statistical relations based off of other methodologies. The combination of these statistical techniques and model-dependent methods is emerging as the future direction for enmasse stellar age determinations.

For successful Galactic studies, of order 1000s of stars are required to ensure the Galaxy is well sampled and strong inferences can be made. An age determination technique that is easily applicable to large datasets, but not overtly time consuming is therefore required. Though empirical and statistical methods both have their merits, model-dependent techniques will be used here. The achievable level of precision and the capability of ensemble analysis is what makes these techniques attractive for Galactic studies. Isochrone fitting is typically the preferred ageing tool for stellar populations, but Jørgensen & Lindegren (2005) show using synthetic populations that isochrones are unevenly spaced, leading to biased results and typical uncertainties of $\sim 50\%$ (blue distributions, Fig. 3.2). This is significantly far from the resolution desired, thus the technique was not used here.

An alternative model-dependent approach is to use asteroseismology. Age dating with asteroseismology is similar to that of isochrone fitting, but the constraints on the physical parameters are significantly improved. Instead of only using traditional parameters such as $T_{\rm eff}$, luminosity and photospheric chemical composition, asteroseismology tightly constrains the mass and radius. Consequently, uncertainties typically of order 25-35% can be expected for MS and red giant stars alike (see Chaplin & Miglio 2013) when using global parameters and modelling (green distributions, Fig. 3.2). If the individual mode frequencies can be measured, it is possible

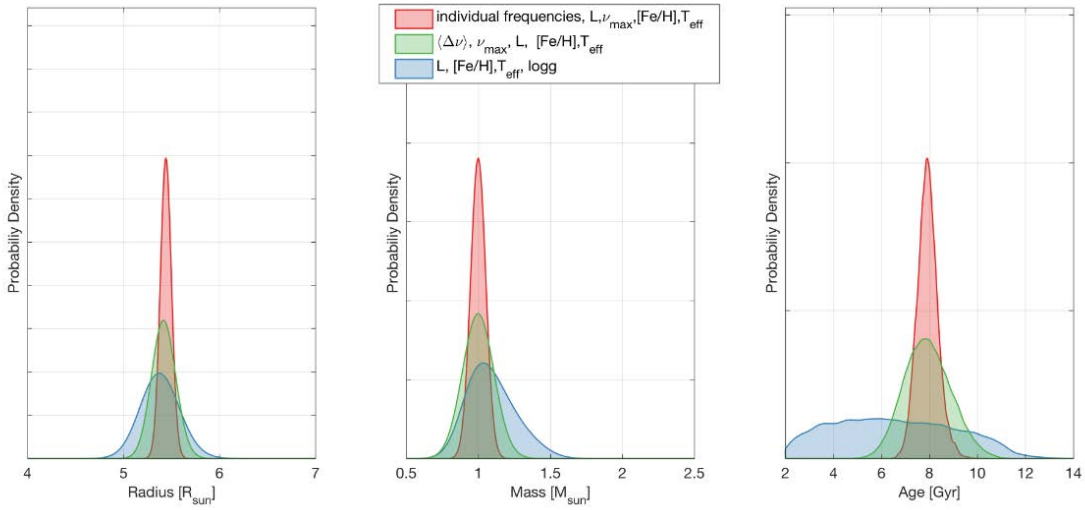

Figure 3.2: Figure 7 of Miglio et al. (2017): The posterior probability densities of radius (left), mass (centre) and age (right) for a bright ($m_V = 9$) RGB star ($\nu_{max} \sim 110\mu$Hz). Different combinations of astrometric, spectroscopic and asteroseismic constraints have been used to obtain the distributions.

to reduce $\sigma_{\rm Age}$ below the desired 20% (red distributions, Fig. 3.2). Analysis with global asteroseismic parameters is more widely available at present, but with continual revisions of and improvements in stellar modeling techniques, the precision achievable will continue to improve and constrain age determinations further.

3.1 Evolutionary Tracers

Discerning accurate ages requires excellent data and accurate models. Understanding the Milky Way at distances beyond the Solar Neighbourhood ($\sim$ 500 parsecs) requires candidates from which exquisite data can be extracted. Once obtained, these candidates would then prove to be excellent tracers of Galactic structure and provide precise properties to characterise the Galaxy's evolution. Red giant stars are an example of excellent candidates to fulfill such a role.

For a given distance, a red giant star would appear brighter compared to a main sequence (MS) star because of its greater intrinsic luminosity. One is therefore able to detect a greater number of photons and achieve a better signal-to-noise ratio for the red giant. This means one can acquire better spectra and astrometry for

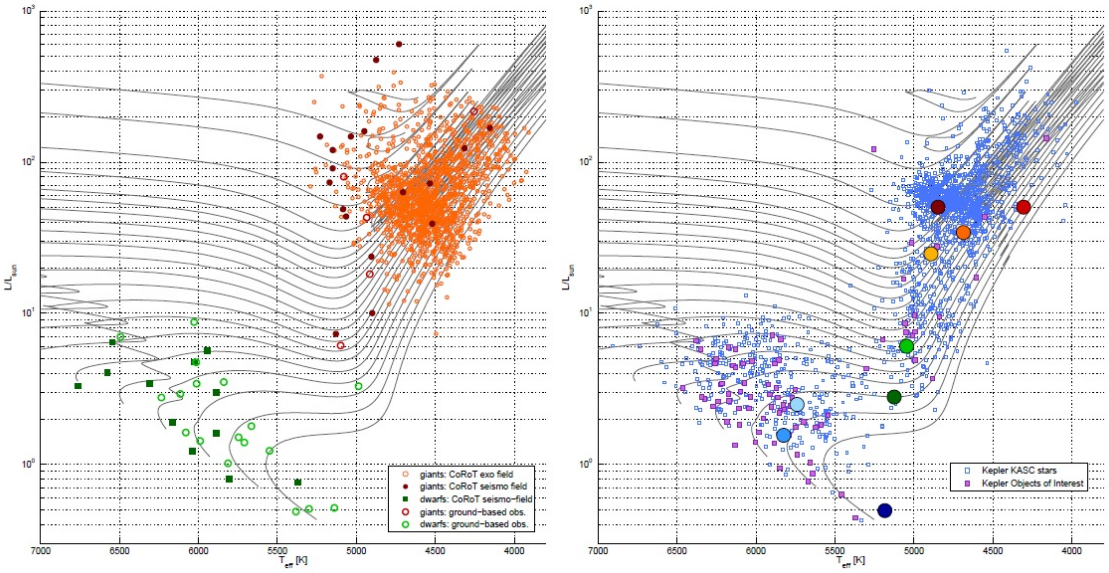

Figure 3.3: Hertzsprung-Russell diagram from Chaplin & Miglio (2013) showing the location of stars with detected oscillations from CoRoT and ground-based telescopes (left) and by *Kepler* (right). The grey lines indicate evolutionary tracks of the same metallicity, incrementing from 0.7-2.7 $M_\odot$ in 0.1 $M_\odot$ steps.

giants than MS stars over greater distances. Obtaining detailed information about these stars over distances of order kilo-parsecs makes red giants excellent probes of Galactic structure. In addition, the desired precise asteroseismic measurements are easier to observe at such distances for giants due to the greater oscillation amplitudes of the modes. The oscillation frequencies of the giants are also better suited to the long cadence observation modes of the *Kepler* and K2 missions, naturally producing a larger sample of detections for giant stars. It must be noted that low-mass red giants ($M \lesssim 2.5 M_\odot$) exhibiting Solar-like oscillations are the focus here.

Moreover, the surface chemistry of red giants can be considered a reflection of the ISM composition at birth as elements such as Fe, O and Mg are largely unaffected by internal mixing processes and diffusion. By time a star reaches the red giant phase of its evolution, its deep convective envelope ensures that the star's near-surface chemical composition is representative of the envelope's composition (the envelope extends typically to a fractional radius of a few percent from the centre of the star on the RGB). This region is less affected by internal mixing processes such as diffusion,

which is a strong chemical transport mechanism in MS stars. On the other hand, when the convective envelope reaches regions deep in the stellar interiors, elements that had been processed by nuclear reactions may be brought to the surface in a process known as dredge up. Changes in the surface abundance of giants due to dredge up are becoming increasingly well constrained, allowing for these processes to be accounted for in the analysis and sensible predictions made. One topic of particular interest regarding the chemical properties of red giants is the effect of the dredge ups on the [C/N] ratio. The dredge up process allows fresh material from the core to be brought up into the convective envelope, hence to the photosphere, of a star. This process is known to affect the [C/N] ratio, and astronomers are investigating its applicability as a mass and age indicator (e.g. see Masseron & Gilmore 2015; Salaris et al. 2015; Martig et al. 2016a; Ness et al. 2016). In addition, there are still open issues related to the roles of e.g. rotation and thermohaline mixing (see Lagarde et al. 2019) in accurately determining the [C/N] ratio.

The short timescale that a star spends on the RGB is also a highly desirable quality in red giants. Figure 3.4 shows the vastly different amount of time a star will spend in each evolutionary state for a 0.8 $M_{\odot}$ and a 1 $M_{\odot}$. The RGB lifetime is significantly shorter than the duration of time spent on the MS in both cases (timescales vary as a function of mass and metallicity). With a lifespan of order of $\sim 10\%$ compared to that spent on the MS in this instance, low mass red giant stars can effectively be aged by the amount of time they have spent on the MS.

The amount of time a star spends on the MS is dictated by its mass due to the strong correlation between mass and luminosity. The timescale for the MS relies upon the amount of energy that is possible to release through Hydrogen burning, E_H, and how fast this is radiated away (L). One can approximate that the same fractional mass of Hydrogen is burnt in all stars, implying that $E_H \sim M_H \sim M$. Considering the value of L changes little over the course of the MS, one can apply the empirical relation between M and L determined at the zero-age MS: $L \propto M^{\nu}$.

The progenitor mass (M) of the MS star thus proves to be an excellent proxy for age for red giant stars. The relation

$$\tau_{\rm MS} \propto \frac{M}{L(M)} \propto M_{\rm ini}^{-(\nu-1)}, \tag{3.1}$$

($L(M)$, luminosity as a function of mass; $\nu = 3 - 5$, Kippenhahn et al. 2012) provides a simple scaling between the progenitor mass and time spent on the MS ($\tau_{\rm MS}$). Hence, it is important to be able to constrain the mass of the star in order to obtain an accurate age. It is possible to detect solar-like oscillations in red giants of mass $\sim 0.8 - 3.0 {\rm M}_{\odot}$. This corresponds to an age range of $\sim 0.1 - 14$ Gyr. The breadth of ages, representative chemical composition of formation conditions and the ability to observe to great distances makes red giants excellent candidates for exploring the evolution of the Milky Way.

3.1.1 The Importance of being Certain

The determination of stellar parameters often relies heavily on the use of stellar models. No exception is made in this thesis. Stellar evolution models are by no means perfect. There are still processes within stars (e.g. modelling of convective boundary mixing, e.g. 'overshooting') that prove challenging to model either through a lack of clear theory behind the process, or conflicting implementation methods causing variance between codes. A trade off is often accepted by modellers, focusing on which prescription of input physics would be most suitable for the populations to be modelled. Understanding the limitations or biases present within stellar models will allow for representative model uncertainties for parameters to give confidence in the results.

Noels et al. (2016) present a discussion of present uncertainties in stellar modelling. One of the key messages they present is that the 'best model' selected from a grid will not always be the same. Different input physics and treatments of evolutionary mechanisms will influence the likelihood predictions for certain parameter

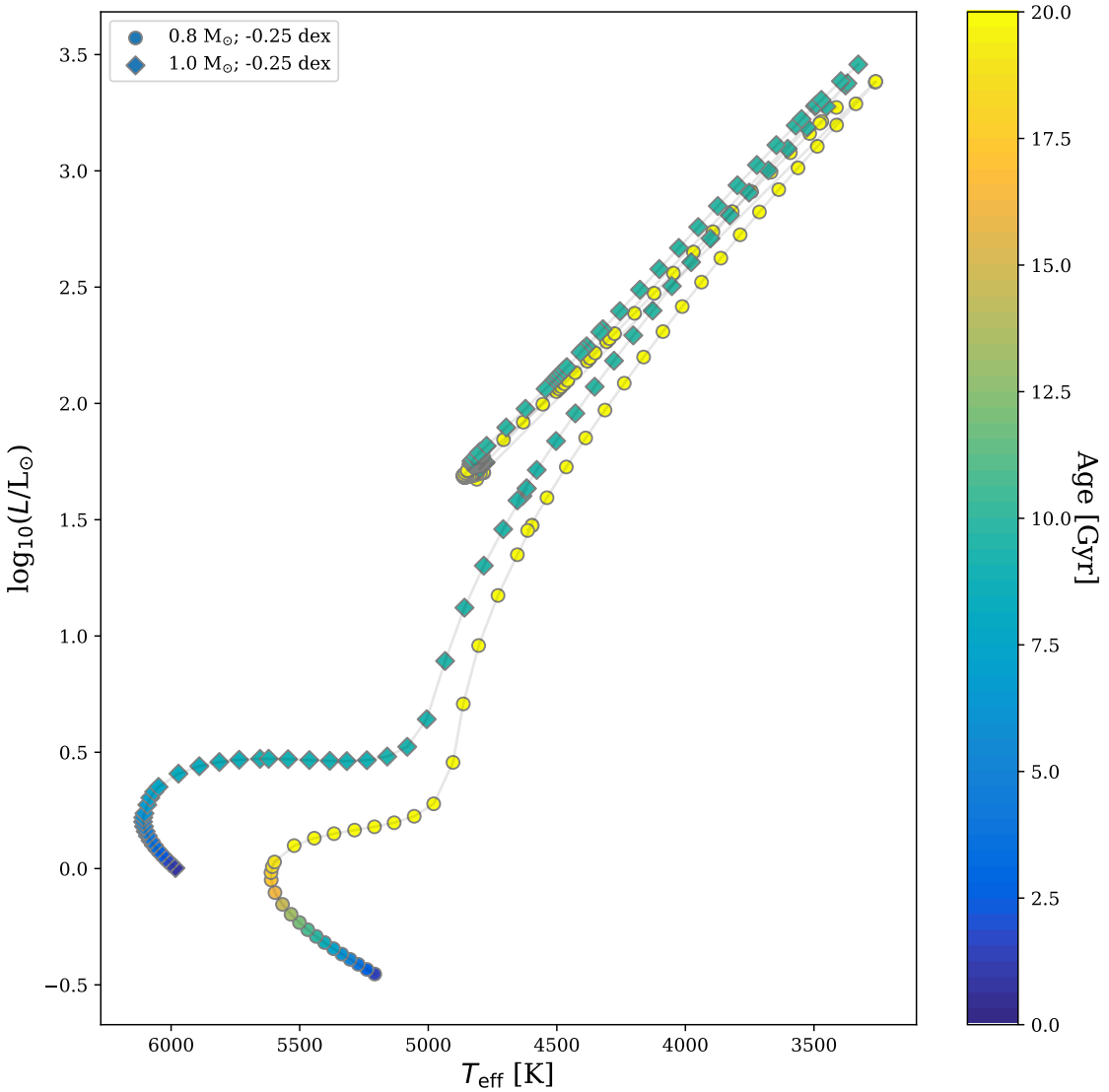

Figure 3.4: HRD for a 0.8 $M_\odot$ (circles) and 1 $M_\odot$ (diamonds) evolutionary tracks ([Fe/H]: -0.25 dex). The colour bar indicates the age of each model. The grey line traces the shape of the evolutionary track. The leftmost tracks above 1.5 $\log(L/L_\odot)$ are core-Helium burning stars.

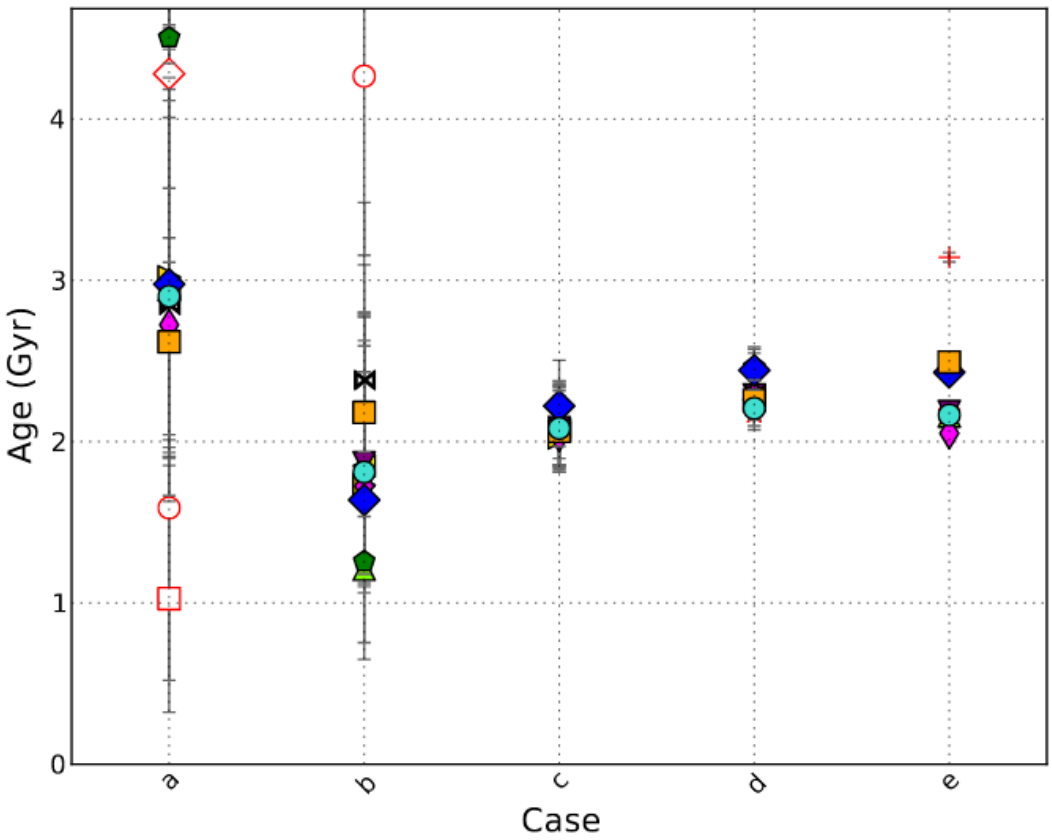

Figure 3.5: Stellar age uncertainties for different combinations of photometric, spectroscopic and asteroseismic constraints. Constraints are added cumulatively from left to right (a: $T_{\rm eff}, L$, [Fe/H]; b: a $+ \langle \Delta\nu \rangle$; c: b $+ \langle d_{02} \rangle$; d: a $+ r_{02}(n), rr_{01/10}(n)$; e: a $+ \nu_{n,l}$. Each symbol represents a different input physics for the models. Cyan circles show the best model. Figure taken from Lebreton & Goupil (2014).

combinations. Hence, one must be wary of the inherent biases of the modelling code and input physics used to fully understand the returned results (see Noels & Bragaglia 2015; Salaris 2016). The uncertainties associated with the best fit models are representative of the internal uncertainties of the grid itself, which is a reflection of the uncertainties of the input physics used. Silva Aguirre et al. (2017) show an excellent example of this for the Sun. Six independent modelling pipelines were used to analyse solar data, and each returned a slightly different set of parameters and uncertainties resultant from different input physics in the models used.

Lebreton & Goupil (2014) illustrate the effect of improving/increasing the number of constraints used when fitting stellar models (see Fig. 3.5). They assess the

uncertainties on age determinations, with dramatic improvements seen when increasing numbers of asteroseismic constraints are added to the initial photometric and spectroscopic constraints applied. Uncertainties of order 25-45% have been reported for MS stars (Prada Moroni et al., 2016; Reese et al., 2016), which can be reduced to $\sim$ 15% if individual mode frequencies from asteroseismology are used (Silva Aguirre et al., 2015). This improves for stars in the red giant phase of evolution. Figure 3.6, taken from Miglio et al. (2012), demonstrates the age spread one can expect from a synthetic population (in this case modelling the CoRoT LRC01 field). It is evident that the modelled age spread for MS stars is significantly greater than that expected for red giants for a given mass and metallicity. This is indicative that mass can be used as a constraint to provide precise ages for giant stars from stellar models.

Though additional parameter constraints can be found through modelling, one must remain vigilant about the treatment of additional physical effects. Processes such as diffusion, rotation and mass loss are particularly important for red-giant stars. Many of the modelling uncertainties for MS stars are reduced for red giants either through greater chemical mixing from the deepening of convection zones or internal structural changes during the rapid transition across the sub-giant branch. It is known that atomic diffusion can reduce red giant age determinations by $\sim$ 5% when using grid modelling (Prada Moroni et al., 2016; Salaris, 2016) and that the rotation profiles of giants differ by 2 orders of magnitude between models and asteroseismic determinations (e.g. Eggenberger et al. 2012; Marques et al. 2013). Understanding and constraining these effects is important if results from stellar modelling are to be trusted and greater accuracy and precision obtained for stellar and Galactic studies.

Noels et al. (2016) also present a set of 'benchmark' uncertainties to which stellar parameters can be derived from models. Mass and radius uncertainties are expected to be of order 8-12% and 4-6% respectively. We can currently determine ages consistently to order 40%, with the potential to get down to 15% with sufficient

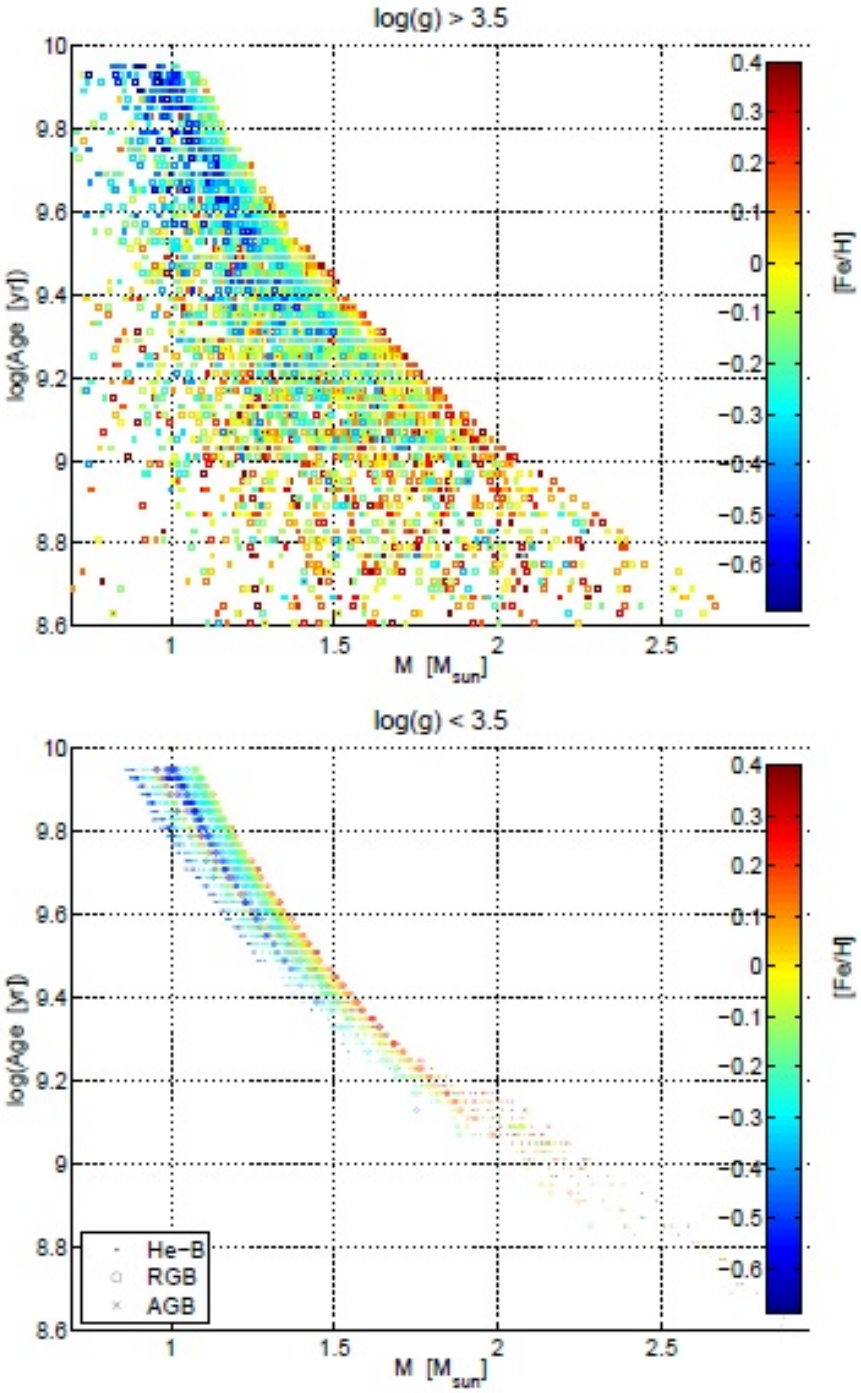

Figure 3.6: Age-mass-metallicity relation for a synthetic thin disc population, representative of CoRoT field LRc01. MS and red giant stars are shown in the upper and lower panels respectively. The different evolutionary states of the red giants are denoted by different symbols: dots - core Helium-burning; crosses - Asymptotic-Giant-Branch; open circles - RGB. Figure taken from Miglio et al. (2012).

information available. In addition to this, they propose a set of required uncertainty determinations for parameters such as mass, radius, $T_{\rm eff}$, [Fe/H] and age. The uncertainties are the predictions as to what level is required in order to be able to carry out successful Galactic studies. Table 3.1 is replication of Table 2 from Noels et al. (2016). The notable desired uncertainty is that on age. A 20-30% uncertainty is achievable, but one must be careful as a 30% uncertainty may appear excellent for a young star, but still offers significant uncertainty for older populations.

Table 3.1: Table 2 of Noels et al. (2016), detailing the desired accuracies for Galactic studies. In some cases, the necessary level is given, with the ultimate goal to be achieve presented in brackets.

Property	Uncertainty
R	$1-2\%$
M	$3-5\%$
$T_{\rm eff}$	$\lesssim 100$ K
$\log g$	$0.1-0.2$ dex (goal < 0.1 dex)
L	Reddening limited, even with excellent parallaxes
[Fe/H]	< 0.1 dex
[α/Fe]	$\lesssim 0.1$ dex
'good age'	$20-30\%$ (goal $< 15\%$)
$\rm V_{lineofsight}$	0.5 km s^{-1}
$\rm V_{Galactocentric}$	$10-20$ km s^{-1}

Chapter 4

Asteroseismology

The final 4 paragraphs of this chapter are taken almost verbatim from the introduction of the work of Rendle et al. (2019), of which I am first author.

The majority of inferences one is able to make about a star are based on the properties of their photospheres. The photons detected in any observation of a star are only able to tell us about the surface properties of star, from which inferences about its global parameters can be made. This is a good start, but to truly understand the fundamental mechanisms and processes of stellar evolution, one requires information about the stellar interior. Processes important to stellar modelling, such as diffusion and mixing, are predominantly internal processes and therefore opaque to standard observations. Finding alternative methods to probe the stellar interior is a necessity in order to provide constraints for accurate stellar evolution models. Fortunately, there is a class of stars for which this is possible: *variable stars*.

Variable stars are objects for which a time-dependent change in brightness can be observed. These changes occur on time scales significantly shorter than any evolutionary changes, providing greater insight into the current properties of the star or the system it inhabits. There are two types of variable star - intrinsic and extrinsic. Extrinsic variables show amplitude changes driven by external factors (e.g. binary systems), allowing one to understand stellar systems and their components

in greater detail. Intrinsic variables physically change their output as a consequence of internal processes. Supernovae are one such example, with internal mechanisms responsible for the collapse and explosion that drives the extraordinary increase in magnitude. Another class of intrinsic variables, as shall be discussed here, are pulsating variables.

The first type of pulsating star was discovered in 1596 by David Fabricius (Mira variable). A further 16 types (and possibly more) of stellar pulsators have been discovered (see Handler 2013; Table 4.1). Each type of pulsator has a different driving mechanism which characterises the magnitude and period of the oscillation. Mechanisms proposed for driving the oscillations include the ϵ-mechanism (variation in nuclear reaction rate; Rosseland & Randers 1938), $\kappa - \gamma$ mechanism (opacity driven oscillations; Baker & Kippenhahn 1962), convective blocking (expansion driven by blocking and releasing of energy at the base of the convective zone; e.g. Brickhill 1991) and solar-like oscillations. The mechanism type is greatly influenced by the physical properties of the star, which can be seen by the spread of the pulsator types across the Hertzsprung-Russell Diagram (HRD; Fig. 4.1).

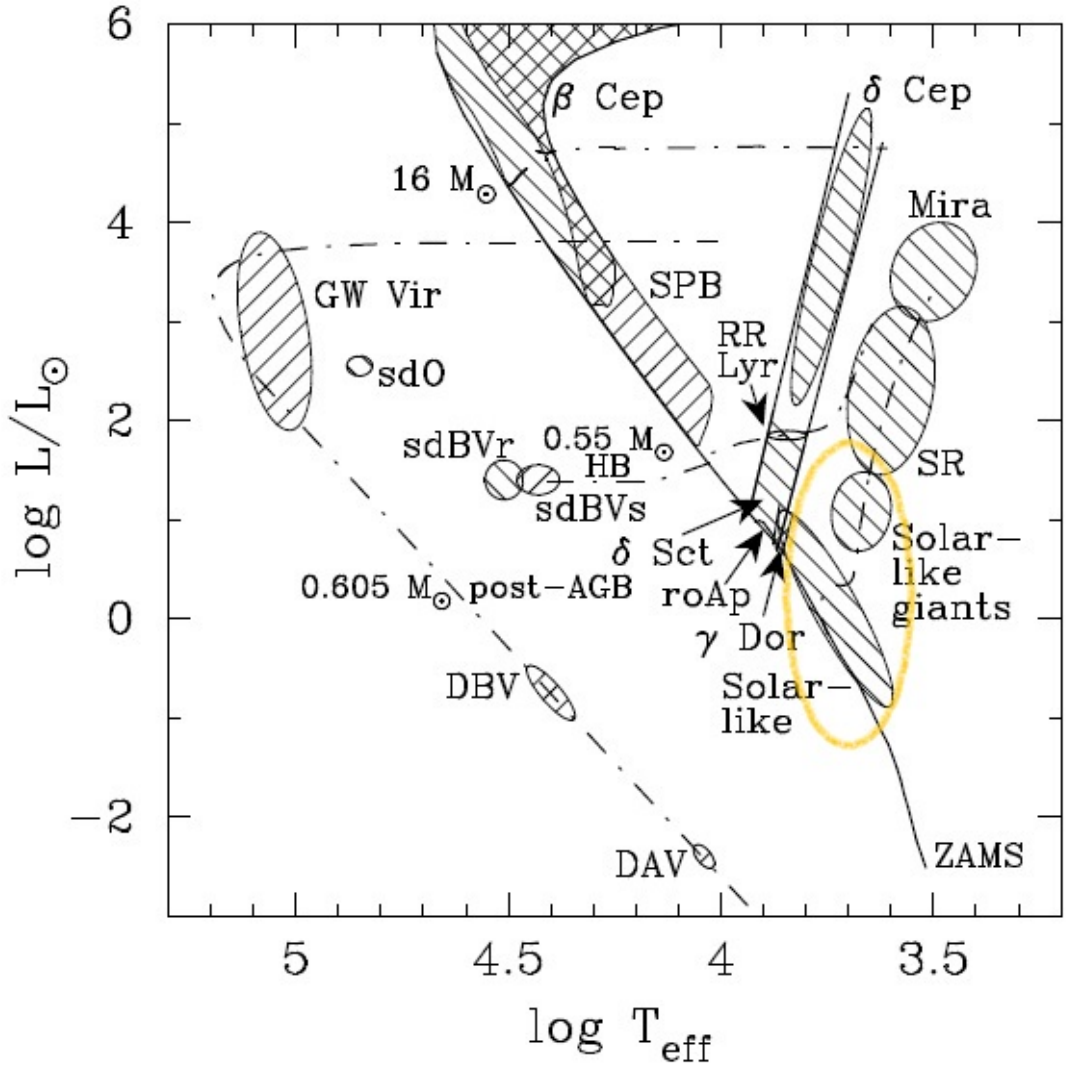

Figure 4.1: Hertzsprung-Russell diagram adapted from Handler (2009). The locations of confirmed oscillator classes are shown. The orange circle shows the location of the solar-like oscillators, both MS and red giant stars. Lines from top left to bottom right indicate p-mode dominated pulsators. Lines from bottom left to top right show g-mode dominated pulsators. Cross-hatched regions indicate potential hybrid pulsators.

Table 4.1: Table 1 of Handler (2013), showing classes of pulsating stars. The approximate period of the oscillation and discovery dates for each class are shown. Abbreviations relate to labels on Fig. 4.1.

Name	Approx. Period	Discovery
Mira variables	100 - 1000 d	Fabricius (1596)
Semiregular (SR)	20 - 2000 d	Herschel (1782)
δ Cephei	1 - 100 d	1784, Pigott, Goodricke (1786)
RR Lyrae	0.3 - 3 d	Fleming (1899)
δ Scuti	0.3 - 6 h	Campbell & Wright (1900)
β Cephei	2 - 7 h	Frost (1902)
ZZ Ceti (DAV)	2 - 20 min	Landolt (1968)
GW Virginis (DOV)	5 - 25 min	McGraw et al. (1979)
Rapidly oscillating Ap (roAp)	5 - 25 min	Kurtz (1982)
V777 Herculis (DBV)	5 - 20 min	Winget et al. (1982)
Slowly Pulsating B (SPB) stars	0.5 - 3 d	Waelkens & Rufener (1985)
Solar-like oscillators	3 - 15 min	Leighton (1962)
V361 Hydrae (sdBVr)	2 - 10 min	Kilkenny et al. (1997)
γ Doradus	0.3 - 1.5 d	Kaye et al. (1999)
Solar-like giant oscillators	1 - 18 hr	Frandsen et al. (2002)
V1093 Herculis (sdBVs)	1 - 2 hr	Green et al. (2003)
Pulsating subdwarf O (sdOV)	1 - 2 min	Woudt et al. (2006)

The study of all variable pulsators is broadly known as asteroseismology. As already alluded to in this thesis, low-mass red giant stars will be the primary focus of analysis. The circle on Fig. 4.1 indicates this region on the HRD. The low-mass regime is dominated by one class of pulsator in particular - solar-like oscillators. Subsequently, this thesis will only discuss this class of oscillator and uses of the term asteroseismology will refer specifically to solar-like oscillators.

Solar-like oscillations are stochastically driven oscillations originating in the tur-

bulent near-surface convective layers of a cool star. As discussed in Christensen-Dalsgaard (2002), these oscillations were tentatively first detected within the convective envelope of the Sun by Plaskett (1916), with their solar origins confirmed by Hart (1954, 1956). Leighton et al. (1962) used Doppler shift data to make the first definitive detections of the oscillations, with major theoretical advances in the understanding of these oscillations coming 10 years later. Theories independently developed by Ulrich (1970) and Leibacher & Stein (1971) both concluded that the waves generated in this region were acoustic in nature. Amongst other surveys and networks (e.g. IRIS DePontieu et al. 2014, Global Oscillations Network Group - GONG, ESA/NASA SOHO) Continual observations with the Birmingham Solar-Oscillations Network (BiSON) since 1976 have confirmed this theory and allowed for a comprehensive study of the Sun. The field of helioseismology was subsequently developed from resultant solar studies, with the application of this technique to other stars known as asteroseismology (comprehensive review given in Aerts et al. 2010).

Due to the nature of solar-like oscillations being similar to those found in the Sun, the excitation of these oscillations is found in stars with similar near-surface regions whereby the excitation mechanism for the oscillations is situated in the near-surface layers. Solar-like oscillators have a convective envelope which drives the excitation mechanism of these oscillations. This criterion restricts greatly the types of stars that are able to generate solar-like oscillations to those capable of supporting outer convective envelopes (see Kraft 1967 and van Saders & Pinsonneault 2013 for convective envelope critical conditions), but it is possible to observe these oscillations in evolved stars, not just those belonging to the main sequence. The breadth of evolutionary states that the oscillations are detectable in makes them a valuable probe of properties across a wide proportion of the Hertzsprung-Russell Diagram (HRD).

Near-surface convection acts to both drive and damp solar-like oscillations, resulting in small amplitude pulsations (few ppm in intensity; giants tens of ppm -

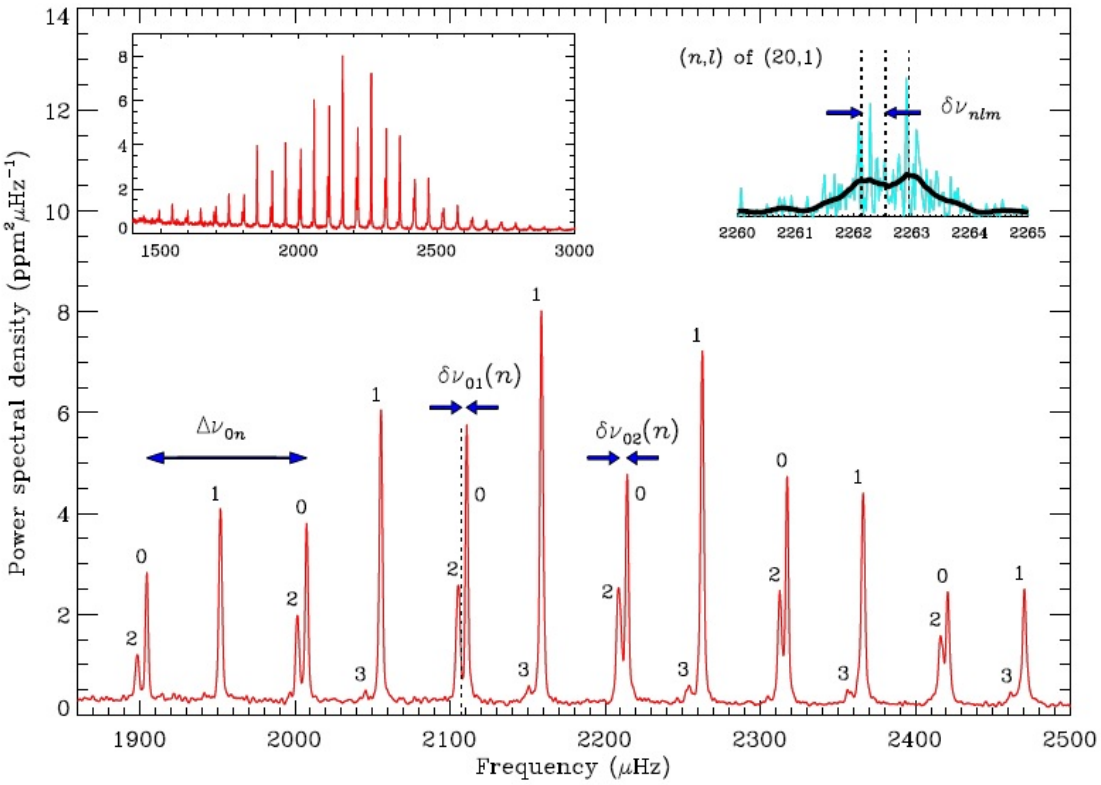

Figure 4.2: Figure 1 of Chaplin & Miglio (2013): oscillation spectrum of KIC 12069424 (16 Cyg A). Main plot: smoothed frequency-power spectrum, annotated to show the small ($\delta\nu$) and large ($\Delta\nu$) frequency separations. Spherical degree of modes are shown. Inset, top left: frequency-power spectrum over a broader frequency range, showing the Gaussian-like modulation (in frequency) of the observed mode powers. Inset, top right: rotational splitting of the non-radial $l = 1, n = 20$ mode.

see Fig. 4.4) compared to those of classic pulsators (up to 1000 times larger signal - can be more for Cepheids; Kjeldsen & Bedding 1997). These pulsations may not be detectable at such great distances as those of the Cepheids and RR-Lyrae, but they do reveal significant information about the stellar interior which cannot be discerned from a classical pulsator. Given the assumed spherical symmetry of the stellar structure, the generated standing waves are best described by a set of spherical harmonics, with angular degree l and radial order n and can be categorised by the restoring force required to maintain their stability (e.g. see Basu & Chaplin 2017).

Solar-like oscillation modes fall into two main categories: p-mode or g-mode. The modal denomination is determined by the restoring force that maintains the modes stability. p-modes, or pressure-modes, are subjected to a restoring force dominated by the pressure gradient. Modes existing solely within the radiative interior of a star are controlled by a combination of gravitational and buoyancy forces and are known as gravity- (g-) modes. For solar-type main sequence stars, typically only p-modes are observed, but in more evolved stars it is possible to detect modes with features typical of both p- and g-modes, known as mixed modes (Mosser et al., 2011, 2012b, 2014).

Mixed modes occur when core contraction as a star evolves raises the frequencies of the g-modes and outer envelope expansion reduces the p-mode frequencies. As the two types of oscillation come closer together in frequency, modes of the same degree, l, begin to interact and couple. Such interactions affect the mode characteristics, shifting the frequencies of the modes and allowing them to take on both g- and p-mode properties. Hence, the mixed modes contain information regarding the deep stellar interior as well as the acoustic cavity. Mixed modes are therefore useful probes of conditions within stars, and have been used to distinguish between RGB and red clump stars (e.g. Bedding et al. 2011; Mosser et al. 2011). Multiple g-modes are able to couple to a single p-mode because as a star evolves, the density of g-modes

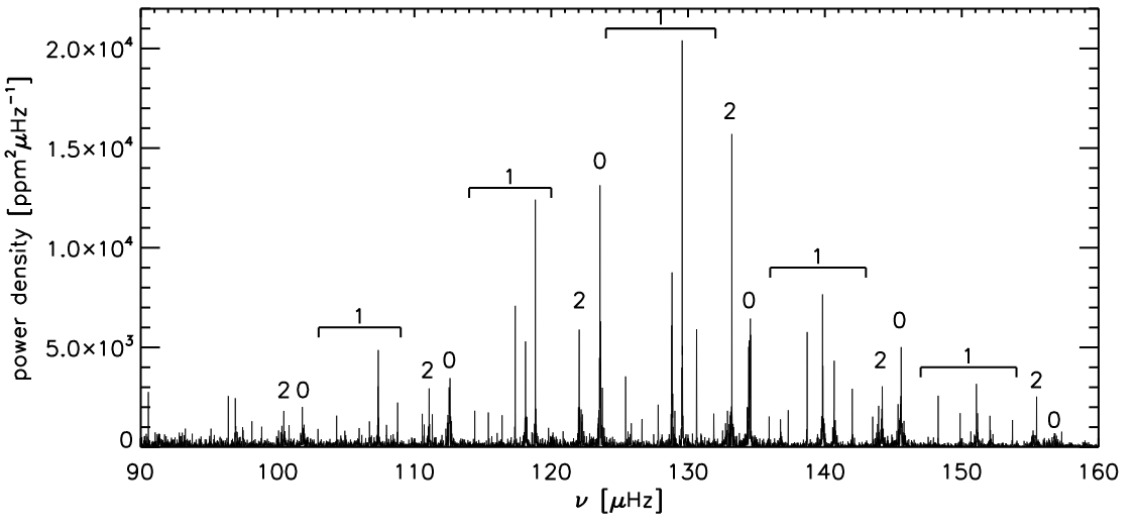

Figure 4.3: Figure 5 of Hekker & Mazumdar (2014): Power density of the red giant star, KIC9145955. The spherical degrees, l, of the modes are denoted. The dipole ($l = 1$) modes are mixed, with multiple peaks inplace of a single peak as expected with a pure p-mode. The approximate range of the mixed modes are indicated.

increases. Fig. 4.3 demonstrates how mixed modes may manifest themselves in an observed power spectrum.

In order for the modes to propagate within the stellar interior, a cavity is required to provide the necessary boundary conditions to allow for resonance. The upper bound of this cavity is governed by the acoustic cut off frequency ($\nu_{\rm ac}$) of the photosphere,

$$\nu_{\rm ac} = \frac{c}{4\pi \mathrm{H_p}}, \text{where,} \tag{4.1}$$

$$\mathrm{H_p} = \frac{\mathcal{R}\mathrm{T}}{\mu \mathrm{g}}, \tag{4.2}$$

where c is the adiabatic sound speed, $\mathrm{H_p}$ is the pressure scale height for an isothermal atmosphere (Brown et al., 1991; Kjeldsen & Bedding, 1995), $\mathcal{R}$ is the gas constant, T is the local temperature of the medium, g the local acceleration due to gravity and μ is the mean molecular weight. The pressure scale height determination (equation 4.2) is based on the assumptions of both an isothermal medium, effectively

fixing the values of T, μ and g.

Above the value of $\nu_{\rm ac}$, sound waves are no longer reflected and become travelling instead of standing waves. The critical criteria for this transition is given by $\nu_{\rm ac} > \nu$. This condition is normally met within the stellar photosphere and defines the upper bound to the stellar acoustic cavity.

The lower bound of the cavity for each oscillatory mode is dictated by the conditions of total internal reflection for the particular mode. As the acoustic wave propagates into the stellar interior, the sound speed increases causing the wave to be refracted away from the vertical until it reaches a depth at which its wave vector is perpendicular to its original orientation. At this point, total internal reflection occurs and the wave propagates towards the surface until it reaches the upper boundary of the cavity once more. The internal reflection point is dependant upon the angular degree of the mode, with lower value l modes able to penetrate further into the stellar interior ($l = 0$ mode passes directly through the centre of the star). The variation in depths achievable by the propagation of the angular degrees allows the deep stellar interior to be examined and inferences of their structure made.

Figure 4.2 shows a typical power spectrum for a main sequence star. The main modes of oscillation are shown as an envelope which can be described by a Gaussian function, the width of which has been shown to scale as a function of $\nu_{\rm max}$ (Stello et al., 2007; Mosser et al., 2010, 2012a). From information within this envelope, it is possible to determine the global acoustic parameters of a star: $\nu_{\rm max}$ and $\Delta\nu$.

$\nu_{\rm max}$ is the frequency of maximum power and can be predicted from additional stellar properties from the scaling relation between the mass (M), radius (R) and effective temperature ($T_{\rm eff}$) of the star,

$$\frac{\nu_{\rm max}}{\nu_{\rm max\odot}} = \left(\frac{\rm M}{\rm M_\odot}\right)\left(\frac{\rm R}{\rm R_\odot}\right)^{-2}\left(\frac{T_{\rm eff}}{T_{\rm eff,\odot}}\right)^{-0.5} \tag{4.3}$$

the value of which doesn't necessarily map onto a frequency of one of the modes as it corresponds to the maximum of the Gaussian function used to describe the

power excess. The solar values in equation 4.3 are used to calibrate the relation, with $T_{\mathrm{eff}\odot} = 5777$ K and $\nu_{\mathrm{max}\odot} = 3090\mu$Hz (Huber et al., 2011).

ν_{max} has been proven to be proportional to ν_{ac} (Brown et al., 1991; Belkacem et al., 2011, 2013) and, by association, related to the surface gravity of the star. Equation 4.1 therefore is also proportional to ν_{max},

$$\nu_{\mathrm{max}} \propto \nu_{\mathrm{ac}} \propto \frac{c}{\mathrm{H_p}} \tag{4.4}$$

With $\mathrm{c} \propto \sqrt{\mathrm{T}}$ and $\mathrm{H_p} \propto \frac{\mathrm{T}}{\mathrm{g}}$, the resultant equation linking ν_{max} to the stellar surface gravity is as follows,

$$\frac{\nu_{\mathrm{max}}}{\nu_{\mathrm{max}\odot}} = \frac{\mathrm{g}}{\mathrm{g}_\odot} \left(\frac{T_{\mathrm{eff}}}{T_{\mathrm{eff},\odot}} \right)^{-0.5} \tag{4.5}$$

The relation shown in equation 4.3 can also be used to predict whether, for a given cadence of the photometric observations, oscillations can be detected. As a star evolves from a MS star, through the sub-giant branch and becomes a red giant, the value of ν_{max} decreases from 10^3 to 10^1 micro Hertz. These changes in ν_{max} can help one to predict the evolutionary state of the star observed. This becomes more complicated beyond the He-flash though, as it is possible to have two evolutionary states for the same ν_{max}. Figure 4.4 demonstrates the movement of the oscillation envelope with position on the HR diagram, whereby the position of ν_{max} shifts to the left (decreasing) as the star becomes more evolved. Using this information allows more realistic target selection for asteroseismic analysis to occur. It can be used to understand the prospective yields of different evolutionary states for a given cadence of observations. Stars with a ν_{max} below the Nyquist frequency (ν_{Ny}) will preferentially be observed as the signal received from these stars will not be subject to aliasing or severe attenuation due to the finite integration time (Chaplin et al., 2014). One can therefore tailor observation modes by setting a ν_{Ny} limit beyond that of the target stars ν_{max} values.

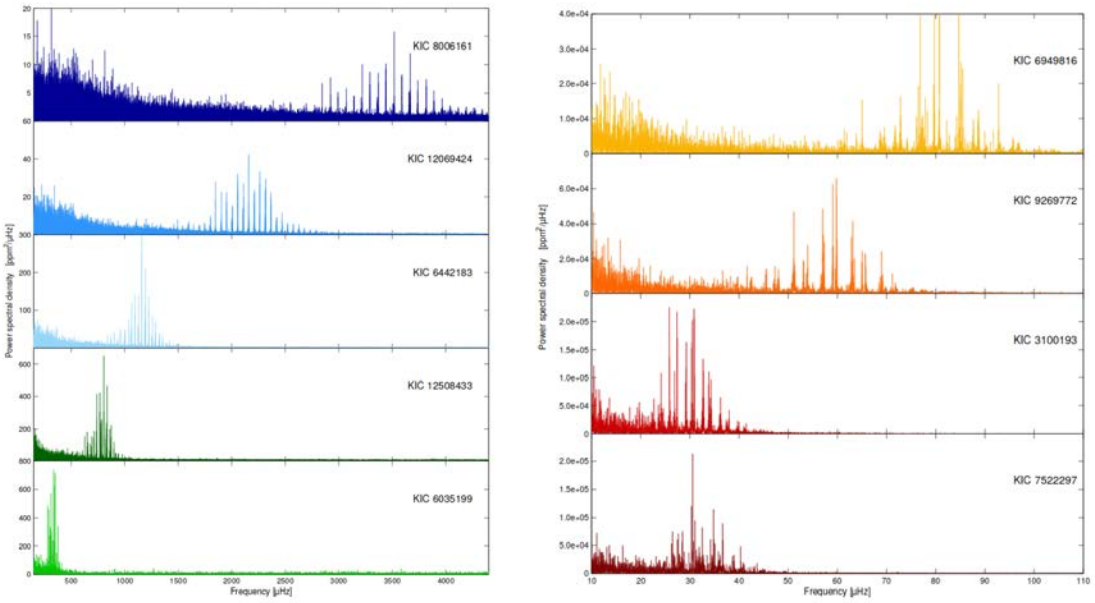

Figure 4.4: The power spectra of 9 stars observed by *Kepler*, adapted from Fig. 3 and Fig. 4 of Chaplin & Miglio (2013). The colours of the spectra relate to the coloured circles shown on Fig. 3.3. The left hand column shows the spectra for stars starting from the beginning of the MS (top) to the end of the sub-giant branch (bottom). The right hand column shows the power spectra for red giant stars from the base of the RGB (top), to the red clump (bottom). Each star has a mass of approx. 1 $M_{\odot}$.

The second global asteroseismic parameter, $\Delta\nu$, is the large frequency separation and is defined as the difference in frequency between acoustic modes of the same angular degree and consecutive radial order. On a mode by mode basis, it can be calculated directly from the oscillation frequencies using the relation,

$$\Delta\nu = \nu_{n+1} - \nu_n. \tag{4.6}$$

Alternatively, when modelling the large frequency separation (not applicable to observations), the approximation given by equation 4.7 relating it to the internal sound speed of the star, c, is,

$$\Delta\nu = \left[2\int_0^R \frac{dr}{c}\right]^{-1} \propto \sqrt{\frac{\overline{\rho}}{\rho_{\odot}}}. \tag{4.7}$$

In general though, it is the *average* large frequency separation, $\langle\Delta\nu\rangle$, that is usually determined. $\langle\Delta\nu\rangle$ is normally found to be a good approximation of the $\Delta\nu$

calculated from Eq. 4.7. It has also been shown to be a good approximation of the square root of the mean stellar density (Ulrich, 1986).

$\langle\Delta\nu\rangle$ can be calculated in multiple ways, from the application of weightings dependent upon a mode's proximity to $\nu_{\rm max}$, or applying an autocorrelation function to the power spectrum of the power spectrum and looking for patterns in frequency (e.g. Mosser & Appourchaux 2009b; Mathur et al. 2010a; Verner & Roxburgh 2011). For a given stellar model, the average value of the large separation is preferred to the $\Delta\nu$ calculated from numerically calculated frequencies. The frequencies carry information concerning the stellar interior, e.g. abrupt structural changes due to near-surface ionization zones and the base of the convective envelope (Chaplin & Miglio, 2013). The changes due to interior effects can be observed using an échelle diagram - diagram showing the individual mode frequencies modulated by $\langle\Delta\nu\rangle$. If Eq. 4.7 held true, given the correct frequency modulation one would expect to see straight, vertical ridges in frequency as the overtones would be perfectly separated by $\Delta\nu$. This is not the case though, with the shifts in frequency due to interactions between the oscillations and the stellar interior. Hence, the average large separation is typically adopted to account for such discrepancies.

As for p-modes, the asymptotic approximation can be used to express regularities in the g-mode spectra. Instead of a regular separation in frequency, g-modes are nearly equally spaced in period, giving rise to the period spacing ($\Delta\Pi$) which is an analogue of $\Delta\nu$. The period spacing is given by,

$$\Delta\Pi_l = \frac{\Delta\Pi_0}{L}, \tag{4.8}$$

where

$$\Delta\Pi_0 = 2\pi^2 \left(\int_{r1}^{r2} N \frac{dr}{r} \right)^{-1}, \tag{4.9}$$

$L = l + 1/2$ and N is the Brunt-Väisälä (buoyancy) frequency. The integral range

is between the base and top of the radiative zone. The Brunt-Väisälä frequency can be determined by,

$$N^2 = g\left(\frac{1}{\Gamma_1 P}\frac{\mathrm{dP}}{\mathrm{dr}} - \frac{1}{\rho}\frac{\mathrm{d}\rho}{\mathrm{dr}}\right), \tag{4.10}$$

where Γ_1 is the first adiabatic exponent, P the pressure and ρ the density of the medium. It is evident that N, and therefore $\Delta\Pi$, are sensitive to the density, therefore the composition of the radiative zone will influence the period spacing observed. The use of $\Delta\Pi$ is limited in the scope of this thesis, therefore for a more in depth study of the parameter, I refer the reader to Chaplin & Miglio (2013) and references therein.

As is shown in equations 4.3 and 4.7, both ν_{max} and $\Delta\nu$ can be derived using two fundamental stellar parameters: mass and radius ($\rho \propto M/R^3$). Rearranging these two equations allows one to solve for both the mass and radius from the global seismic parameters and T_{eff} with the following relations,

$$\frac{M}{\mathrm{M}_\odot} = \left(\frac{\nu_{\mathrm{max}}}{\nu_{\mathrm{max}\odot}}\right)^3 \left(\frac{\Delta\nu}{\Delta\nu_\odot}\right)^{-4} \left(\frac{T_{\mathrm{eff}}}{T_{\mathrm{eff},\odot}}\right)^{1.5} \tag{4.11}$$

$$\frac{R}{R_\odot} = \left(\frac{\nu_{\mathrm{max}}}{\nu_{\mathrm{max}\odot}}\right) \left(\frac{\Delta\nu}{\Delta\nu_\odot}\right)^{-2} \left(\frac{T_{\mathrm{eff}}}{T_{\mathrm{eff},\odot}}\right)^{0.5} \tag{4.12}$$

These relations provide a good initial asteroseismic parameter estimation and can be applied to stars from on the main sequence through to the red giant branch, with precisions beyond those achievable by spectroscopy or photometry alone. Typical uncertainties from scaling relations for mass and radius are of order 10-15% and 5% respectively (e.g. Gaulme et al. 2016; Brogaard et al. 2018; Buldgen et al. 2018a. Improvements in mass and radius estimations have led to consequent improvements in the accuracy to which other stellar parameters can be measured - in particular age. The use of scaling relations have their limitations though, particularly in the context of their use for red giants. Comparisons with measurements of open cluster

eclipsing binaries have shown the scaling relations to overestimate the mass and radii of red giant stars. This is a factor of 5% in radius and up to 15% in mass. Some divergence is expected in the giant regime considering the scaling relations are calibrated the Sun and the solar values of $\Delta\nu$ and $\nu_{\rm max}$ - a main sequence star. Consequently, revisions to equations 4.3 and 4.7 have been considered.

The asymptotic $\Delta\nu - \sqrt{\rho}$ relation has been studied extensively (e.g. White et al. 2011; Miglio et al. 2013a; Mosser et al. 2013; Guggenberger et al. 2016; Sharma et al. 2016; Rodrigues et al. 2017). It was found that the relation $\Delta\nu \propto \sqrt{\rho}$ only holds to order a few percent. A dependence on $T_{\rm eff}$ and [Fe/H] was determined for the relation, with an additional mass dependence at low log(g). It is seemingly straightforward to correct for this in stellar models. Where individual frequencies are available for models, it is possible to directly calculate $\Delta\nu$ for each model. Alternatively, one could implement a temperature and metallicity correction to determine an appropriate reference value of $\Delta\nu$ instead of the solar value (e.g. Sharma et al. 2016). Corrections using the adiabatic index (Γ_1) can also be used (Yıldız et al., 2016).

The $\nu_{\rm max}$ relation has been studied in less detail, with Belkacem et al. (2011) so far having made the most concerted effort to understand the origins of the relation and its applicability to red giant stars. Coelho et al. (2015) examined the temperature dependency of the relation for dwarf and sub-giants stars and found it to hold to within $\sim 1.5\%$. Yıldız et al. (2016) attempted to use Γ_1 as a calibration factor, but saw no improvement in mass and radii determinations. Viani et al. (2017) took this one step further and incorporated a Γ_1 and a mean molecular weight term into Eq. 4.3. The new calibration reduced the deviations in mass and radius from the scaling relations to observations, but the previously quoted uncertainties were maintained on the mass and radius. Comparisons to detailed modelling of stars (Stello et al., 2009; Silva Aguirre et al., 2015) and independently measured masses and radii (e.g. Bedding & Kjeldsen 2003; Bruntt et al. 2010; Miglio et al. 2012; Bedding 2014) have

also been performed in an attempt to calibrate the relation.

Despite their uncertainties and caveats, the scaling relations provide a good basis from which analysis of stellar parameters can be determined. Yet, the asteroseismic analysis can still be improved upon. Grid modelling is a robust and accurate technique commonly used to determine stellar parameters, utilising a series of user controlled inputs and an underlying grid of predetermined models to compute best fit, probabilistic solutions. As discussed in section 3.1.1, this method is highly dependent upon the input physics involved in the creation of the grid and spectroscopically or photometrically derived input parameters. Being able to combine both the robustness of grid modelling and high precision of asteroseismology would therefore be of great benefit to improving stellar parameter determinations.

Fundamentally, grid modelling is often still based on the use of the scaling relations and only act to account for the temperature and metallicity dependencies that the relations do not. More robust estimations can be made with stellar modelling when, for example, the average large frequency separations from model predicted radial mode frequencies and the use of gravity mode period spacings are considered in the parameter determinations (see Rodrigues et al. 2017; Serenelli et al. 2017). Though an improvement, these still do not exploit all of the information the individual modes contain, e.g., presence of acoustic glitches (Vorontsov, 1988; Gough, 1990; Miglio et al., 2010; Pérez Hernández et al., 2016; Verma et al., 2017) and long term internal structure changes from curvature of the large frequency separation (Hekker & Christensen-Dalsgaard, 2017; Mosser et al., 2012a).

Multiple asteroseismic modelling techniques have been developed with the objective to fully exploit seismic information (Guenther & Brown 2004, Miglio & Montalbán 2005, Bazot et al. 2008, Metcalfe et al. 2009, Gruberbauer et al. 2012), PARAM (da Silva et al., 2006; Rodrigues et al., 2014, 2017); see the KAGES (Silva Aguirre et al., 2015; Davies et al., 2016) and LEGACY (Lund et al., 2017; Silva Aguirre et al., 2017) projects for further pipelines.

The use of individual mode frequencies as constraints to the analysis, increases significantly both the precision and accuracy of the inferred masses, radii and age for both main sequence (e.g. Lebreton & Goupil 2014 for a recent review, Reese et al. 2016 for tests using artificial data, or results based on *Kepler*'s best data sets by Silva Aguirre et al. 2017) and red giant stars (Huber et al., 2013; Lillo-Box et al., 2014; Pérez Hernández et al., 2016; Li et al., 2018). Improving the use of seismic information will lead to more precise global stellar properties and allow for testing aspects of the micro- and macro-physics which are currently poorly constrained.

Exploiting the potential of individual mode frequencies hinges on the ability to be able to detect them. High quality data, with low background noise levels are required to be able to do this. Miglio et al. (2017) demonstrate the impact of observation time on the ability to extract individual mode frequencies. It is demonstrated that individual radial mode frequencies were possible to extract when observations lasted longer than 30 days, but suffered greater uncertainty due to entanglements with the more complex dipole and quadrupole mode patterns and lower resolution (see Fig. 4.5). Observations beyond 150 days were found to be sufficient to overcome this problem and achieve precise ($\sigma_\nu \sim 0.04 - 0.09$ μHz) mode determinations. Obtaining 150+ day observations has the potential to reduce age uncertainties $\sim 20\%$, approximately half of what can be achieved with 30 days worth of data. Stars with such extended baselines are limited to the CoRoT and nominal *Kepler* missions, with shorter observations of 80 days with K2 and 30 days with TESS. It is hoped that the future PLATO mission will involve multiple step and stare phases, whereby data can be collected over long enough periods to increase the range of observed stars with individual mode frequencies in a significant fraction of the Galaxy.

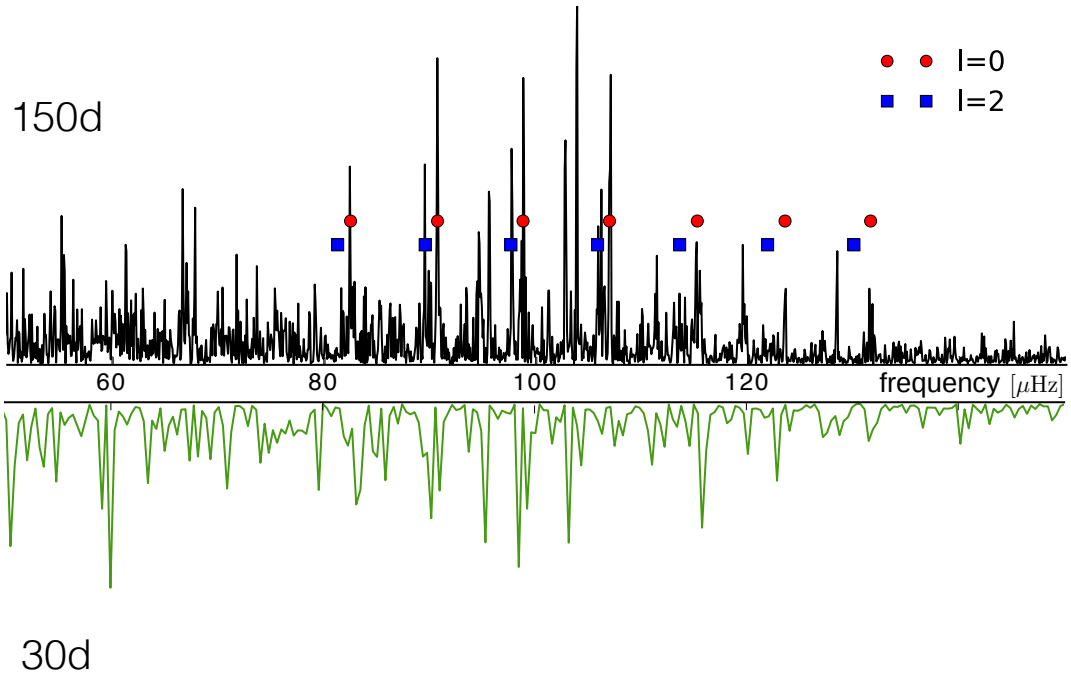

Figure 4.5: Figure 6 of Miglio et al. (2017). The power spectral density as a function of frequency for a bright ($V = 9$) giant observed by *Kepler*. The power spectrum has been adjusted to reflect a 150 day (top) and a 30 day (bottom) time series. The radial (l=0) and quadrupolar mode (l=2) individual mode frequencies are denoted in the upper panel by red circles and blue squares, respectively. Lower frequency resolution for the 30 day time series inhibits the ability to clearly identify individual modes, leading to a reduced precision and accuracy of the mode properties.

Determining Precise and Accurate Stellar Parameters with Asteroseismology

Chapter 5

Asteroseismic Inference on a Massive Scale

Almost the entirety of the text in this chapter is taken verbatim from Rendle et al. (2019), of which I was first author of the corresponding journal article. In terms of individual work performed, I completed the majority of the work, with the exception of the production of the stellar models and initial development of the AIMS *code (see Reese 2016a). The description of the interpolation process was developed with Daniel Reese.*

5.1 Introduction

At present, asteroseismic supporting space missions in operation and ground-based networks (TESS, Ricker et al. 2015; SONG, Andersen et al. 2014; Grundahl et al. 2017) or retired missions (CoRoT, Baglin et al. 2006; CoRot Team 2016; *Kepler*, Borucki et al. 2010a; K2, Howell et al. 2014) have generated high quality data for large ensembles of stars. Further missions are also in preparation (PLATO, Rauer et al. 2014). In order to model these stars, we need pipelines that can efficiently compare observations and models. They must be stable, robust and fast to deal with the current volume of data and the subsequent increases expected in the future.

We present here the stellar modelling pipeline, AIMS (Asteroseismic Inference on a Massive Scale, Reese 2016a; Lund & Reese 2018). AIMS is a pipeline designed to process the measured individual acoustic oscillation frequencies of stars coupled with

classical, spectroscopic or interferometric constraints to provide a powerful diagnostic tool for the determination of stellar properties. Much like Bazot et al. (2008), Gruberbauer et al. (2012), and BASTA (Silva Aguirre et al., 2015), AIMS uses a Bayesian approach. Bazot et al. (2008) implements an on-the fly model calculation with an MCMC algorithm to produce a representative sample of model parameters. This leads to a higher accuracy but at a significant computational cost, whereas the remaining codes use pre-computed grids (faster calculation time). Gruberbauer et al. (2012) and BASTA then evaluate probability distribution functions by scanning the grid. Like Bazot et al. (2008), AIMS also uses an MCMC algorithm, but what is unique is that it is combined with model interpolation. This provides a compromise between accuracy and efficiency.

This paper details the capabilities and potential of AIMS and its applicability within the scientific community. The paper is set out as follows: Section 5.2 describes the functionality of the code and section 5.3 describes the input grids containing the models used in the analysis. Sections 5.4 and 5.5 discuss the results of the various interpolation tests on the grids and the performance of the program in analysing artificial and real data. Finally, a comparison of the performance of AIMS using different combinations of asteroseismic and classical constraints is given in section 5.6. The results of these tests are discussed with a summary of the work in section 5.7.

5.2 AIMS

AIMS uses Bayesian statistics and a Markov-Chain-Monte-Carlo (MCMC) algorithm (`emcee`, Foreman-Mackey et al. 2013) to select models representative of the input data by interpolating in a pre-defined grid. The combination of these techniques allows for an efficient, comprehensive search of the parameter space defined by the grid parameters. User-defined priors and the likelihood function resulting from the input constraints shape the exploration of the parameter space. AIMS initialises the

grid search in the region of a set of models with the highest posterior probability. This increases the efficiency of the parameter space exploration, which in turn helps the MCMC algorithm converge faster.

The program itself has three modes of functionality: binary grid generation; interpolation testing; and stellar parameter characterisation. The performance and capabilities of interpolation mechanism and stellar parameter determination are tested here. Information on the other functions can be found in the supporting documentation[1].

To determine stellar parameters in a Bayesian manner, an affine invariant ensemble Markov chain Monte Carlo (MCMC) sampler (Goodman & Weare, 2010) is implemented via the `Python` package `emcee` developed by Foreman-Mackey et al. (2013). For a given data file, the user can employ so-called walkers that are initiated in a tightball configuration (optional), uniformly distributing the walkers within a sphere centred on an initial estimation of the most probable grid model. If tightball is not selected, the walkers are initiated through the sampling of model parameter priors. The step number for the walkers can be user defined. Parallel tempering is available with the option to define the number of temperatures, and the MCMC chains can be thinned.

To determine the properties of targets falling between grid points defined by the evolutionary tracks, AIMS uses a two step interpolation procedure of the model parameters:

1. Linear interpolation in the chosen evolutionary parameter along a track.

2. Interpolation between tracks.

This method allows for greater control over the evolutionary parameter (prevention of exceeding the boundaries of evolutionary tracks) and attempts to achieve

[1] AIMS Overview:
`http://bison.ph.bham.ac.uk/spaceinn/aims/version1.3/`

Table 5.1: The values of $X_{\rm init}$, $Z_{\rm init}$ and [Fe/H] attributed to the CLÉS grid of models.

$X_{\rm init}$	$Z_{\rm init}$	[Fe/H]
0.691	0.0300	0.25
0.716	0.0175	0.00
0.731	0.0100	-0.25
0.740	0.0057	-0.50
0.745	0.0032	-0.75

greater accuracy as consecutive models on an evolutionary sequence are not expected to change significantly. AIMS includes an accuracy test of the interpolation procedure and an additional program is joined to AIMS to visualise these results as a function of the global grid parameters.

The linear interpolation along a track can be modified to use various evolutionary parameters. However, only a parameter varying monotonically as a star evolves should be used to prevent any spurious results or unexpected errors within the interpolation. Examples of such variables include the Helium core mass in red giant branch (RGB) stars or the central hydrogen content for main sequence stars (MS).

5.3 The Grid - CLÉS with LOSC

The analysis performed by AIMS is based upon the exploration of a predefined grid of models. In this work, the grid is parameterised by mass (0.75-2.25 $M_\odot$, in 0.02 $M_\odot$ increments), initial metallicity ($Z_{\rm init}$) and initial hydrogen content ($X_{\rm init}$). The range of $X_{\rm init}$ and $Z_{\rm init}$ values ([Fe/H] values also included for completeness) used can be found in Table 5.1. Fig. 5.1 is a Hertzsprung-Russell diagram (HRD) showing the evolutionary tracks calculated for this grid for a given chemical composition. A gap between the MS and sub-giant branch can be observed due to the selection criteria used to split the nominal grid into specific MS and red giant sub grids, which is described in detail later.

The grid contains the evolutionary tracks of theoretical stellar models and their frequencies. Here, we considered $\sim$ 38000 models, but larger grids of up to $\sim$ 1.5

million models have been used in the past. The models were computed using the CLES (Code Liégeois d'Évolution Stellaire, Scuflaire et al. 2008a) stellar evolution code and the frequencies were generated using the LOSC (Liège Oscillation Code, Scuflaire et al. 2008b) pulsation code. We use the nuclear reaction rates of Adelberger et al. (2011), opacities of Iglesias & Rogers (1996) and the FreeEOS equation of state (Irwin, 2012). Microscopic diffusion was not included in the grid.

Convection takes place over a large range of length and time scales, as well as a variety of pressures, densities and temperatures. As such, the treatment of convection in stellar interiors is extremely complicated and requires the introduction of various approximations. The typical formalism of convection used in stellar evolution calculations is the mixing length theory (MLT). MLT is a simple, local, time-independent model, with the most commonly used implementation being from Bhm-Vitense (1958). The basic idea of the MLT is to approximate convective motions by blobs of gas that move vertically in the gravitational field between regions of higher and lower temperature. The MLT assumes a radial distance over which bubbles rise before dissolving in their surroundings: the so-called mixing length, Λ, which is proportional to the local pressure scale height H_P,

$\Lambda = \alpha_{MLT} H_P$.

The mixing-length parameter, α_{MLT}, is a parameter to be empirically calibrated. This typically calculated by reproducing the solar effective temperature at the solar age with a solar model. The mixing-length parameter was kept to a solar calibrated value of 1.67 and a convective overshoot of 0.05 times the local pressure scale height was used, assuming instantaneous chemical mixing and the radiative temperature gradient in the overshooting region. The border of the convective zones was calculated following the guidelines of Gabriel et al. (2014) to avoid spurious solutions for the evolution of convective cores.

Though the Asplund et al. (2009) (A09) abundances are more up to date and therefore likely more accurate than the Grevesse & Noels (1993) (GN93) values, the

GN93 abundances are used here due to their ability to more accurately model the Sun given and return characteristics closer to those expected from helioseismology. The A09 abundances are determined using 3D atmosphere modelling, compared to the 1D determinations used by GN93. The more sophisticated modelling of A09 predicts lower carbon and oxygen solar abundances than GN93, lowering the overall metallicity of the Sun. At present, the production of an accurate solar model with these abundances is difficult to achieve. Hence, despite the abundances likely being less accurate, as a convenience to ensure a good solar model the GN93 metallicities are used. One should of course vary the use of A09 vs GN93 to explore systematic uncertainties.

A simple enrichment law is utilised to determine the Helium content (Y) of an evolutionary track of a given Z within the grid. The change in Y with respect to Z is given by:

$$\mathrm{DY/DZ} = (1 - \mathrm{Y}_{0,\odot} - \mathrm{Y_p})/\mathrm{Z}_{\odot}, \tag{5.1}$$

where $\mathrm{Y_p}$ is the primordial Helium abundance, and $\mathrm{Y}_{0,\odot}$ is the initial Y of a solar calibrated model. It is evident that the gradient is calibrated to the solar metallicity, which is a simple assumption and dependent on the $\mathrm{Y}_{0,\odot}$ obtained in the solar calibration.

In this work, we used two sub-grids: one for MS and another for RGB stars. We based our criteria on the changes in chemical composition (variations of central hydrogen for the MS, helium core mass for the RGB), effective temperature and ν_{max} values. While AIMS is very versatile in the grids it can use, it should be noted that the tracks must contain a sufficient number of models to ensure an accurate interpolation. On the MS, we included modes with angular degree (ℓ) values of 0, 1 and 2 whereas the RGB grid only used radial modes ($\ell = 0$). This difference stems from intrinsic limitations of AIMS in processing non-radial modes of RGB stars which are highly non-linear. Both grids included radial orders of the frequencies in

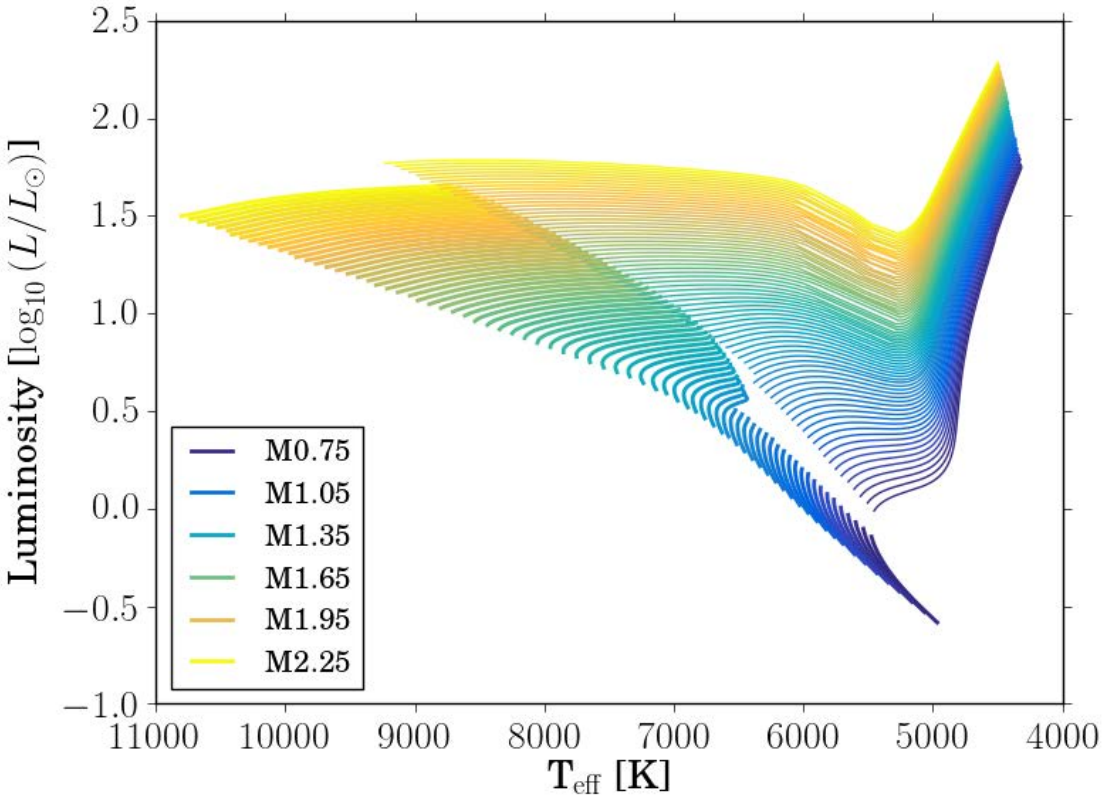

Figure 5.1: Hertzsprung Russell Diagram displaying the evolutionary tracks found within the CLÉS grid ($X_{\rm init} = 0.731$, $Z_{\rm init} = 0.0100$). The gap between the end of the MS and beginning of the sub-giant branch is due to the Helium core mass fraction selection criterion for the MS and RGB grids.

the range $n = 0 - 30$. It should be noted that the grids were built to test the functionality of the code that we will describe in sections 5.4 and 5.5.

5.4 Interpolation Testing

The objective of AIMS is to carry out precise asteroseismic analyses. Hence, it is paramount to ensure an accurate interpolation of the determined stellar properties to ensure the reliability of the modelling results. Here, we briefly present the interpolation procedure used in AIMS and the tests that can be made to certify accurate and reliable results.

5.4.1 Interpolation Procedure

AIMS uses a two step interpolation process to explore the regions between models, namely:

1. interpolation between evolutionary tracks

2. interpolation along an evolutionary track

Interpolation between the tracks relies on a multi-dimensional Delaunay tessellation (see Field 1991 and references therein) of the grid parameters excluding age. The tessellation and subsequent interpolation are carried out by python's `scipy.spatial.Delaunay` module which is based on the `Qhull`[2] package (Barber et al., 1996). Using a tessellation approach offers two advantages: the grid does not need to be structured, and fewer tracks (namely $n_{dim} + 1$ as opposed to $2^{n_{dim}}$, where $n_{dim} \geq 2$ is the number of dimensions excluding age) are used when interpolating at a given point, accelerating the calculations. During the tessellation, the parameter space is divided into simplices (i.e. triangles in the 2D case, tetrahedra in the 3D case, etc.). For a given point in this space, AIMS searches for the simplex containing it and carries out a linear combination of its vertices (or nodes). The interpolation coefficients correspond to barycentric coordinates provided by

[2] `http://www.qhull.org/`

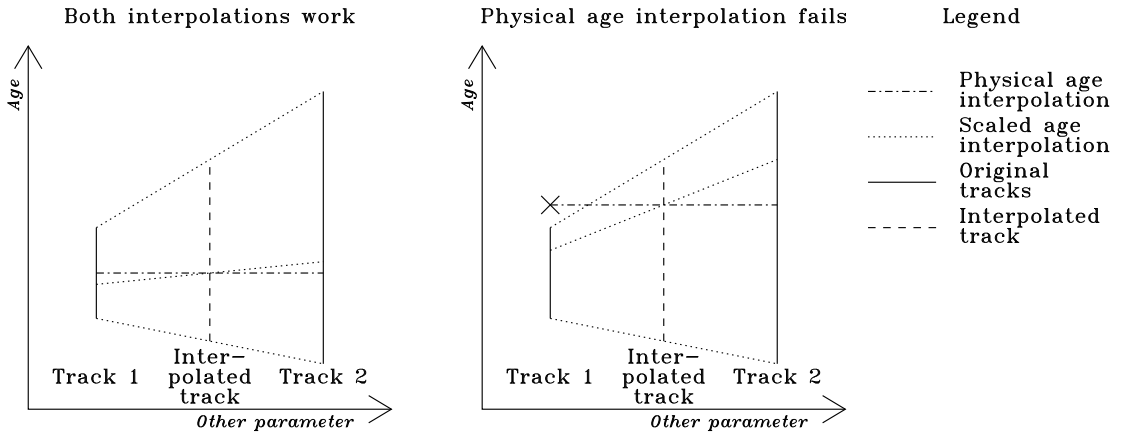

Figure 5.2: Comparison of physical and scaled age interpolation. In the right panel, only scaled age interpolation works.

`scipy.spatial.Delaunay`. These coefficients are simply the ratios between the volumes of the reduced simplices where one of the vertices has been replaced by the point where the interpolation is carried out and the volume of the original simplex.

Interpolation along the tracks consists of a linear interpolation in age between the two closest models. Points outside the tracks are rejected, i.e. AIMS does not perform extrapolation. AIMS can either interpolate according to the physical age, or according to an age parameter which has been scaled to go from 0 to 1 along the track (e.g. helium core mass in red giants). This latter option is more robust as it is less likely to lead to extrapolation (and hence model rejection) when the two interpolation steps are combined. Indeed, the point where the interpolation is being carried out only needs to be within the age span of the interpolated track rather than having to lie within the age span of all tracks involved in the interpolation, as illustrated in Fig. 5.2.

The determined coefficients are then used to interpolate the models by linearly combining the global parameters M, X_0 (the initial hydrogen content), Z_0 (the original metallicity), $T_{\rm eff}$, and ρ (the mean density). The radius and luminosity are then determined self-consistently from these interpolated parameters using the

relations:

$$R = \left(\frac{3M}{4\pi\rho}\right)^{1/3}, \qquad L = 4\pi\sigma R^2 T_{\rm eff}^4. \tag{5.2}$$

We note that the Boltzmann constant is interpolated as a precaution. The Boltzmann constant is not expected to change, but different grids may use different values. One would hope that the same value would be used within an entire grid of models, but instead of assuming this, we run an additional test.

The mean density is interpolated linearly rather than the radius in order to be consistent with the results from `InterpolateModel`.[3] Non-dimensional frequencies, $\omega/\sqrt{GM/R^3}$, with the same n and ℓ identification are interpolated linearly rather than their dimensional counterparts, as they vary much more slowly as a function of stellar parameters, as illustrated in Fig. 5.3. They are subsequently multiplied by $\sqrt{GM/R^3}$, using the interpolated values of M and R, in order to remain consistent with the interpolated global parameters. The interested reader is referred to the AIMS documentation for additional information.

5.4.2 Interpolation Results

In this section, we present the tests included in AIMS to check the suitability of the interpolation procedure to fit observational data. We compare the interpolation errors to the typical uncertainties of observed targets found in the literature. On the MS, we used 16-Cyg A, which yields a median frequency uncertainty on the $l = 0$ modes of 0.08 μHz (-1.097 in $\log_{10}$) and a smallest uncertainty of 0.04 μHz (-1.398 in $\log_{10}$). On the RGB, we use KIC4448777, which has a median frequency uncertainty on the $l = 0$ modes of 0.018 μHz (-1.745 in $\log_{10}$) and a smallest uncertainty of 0.014 μHz (-1.854 in $\log_{10}$).

[3] `https://bison.ph.bham.ac.uk/spaceinn/interpolatemodel/`, a program which interpolates the acoustic structure of models using outputs from AIMS.

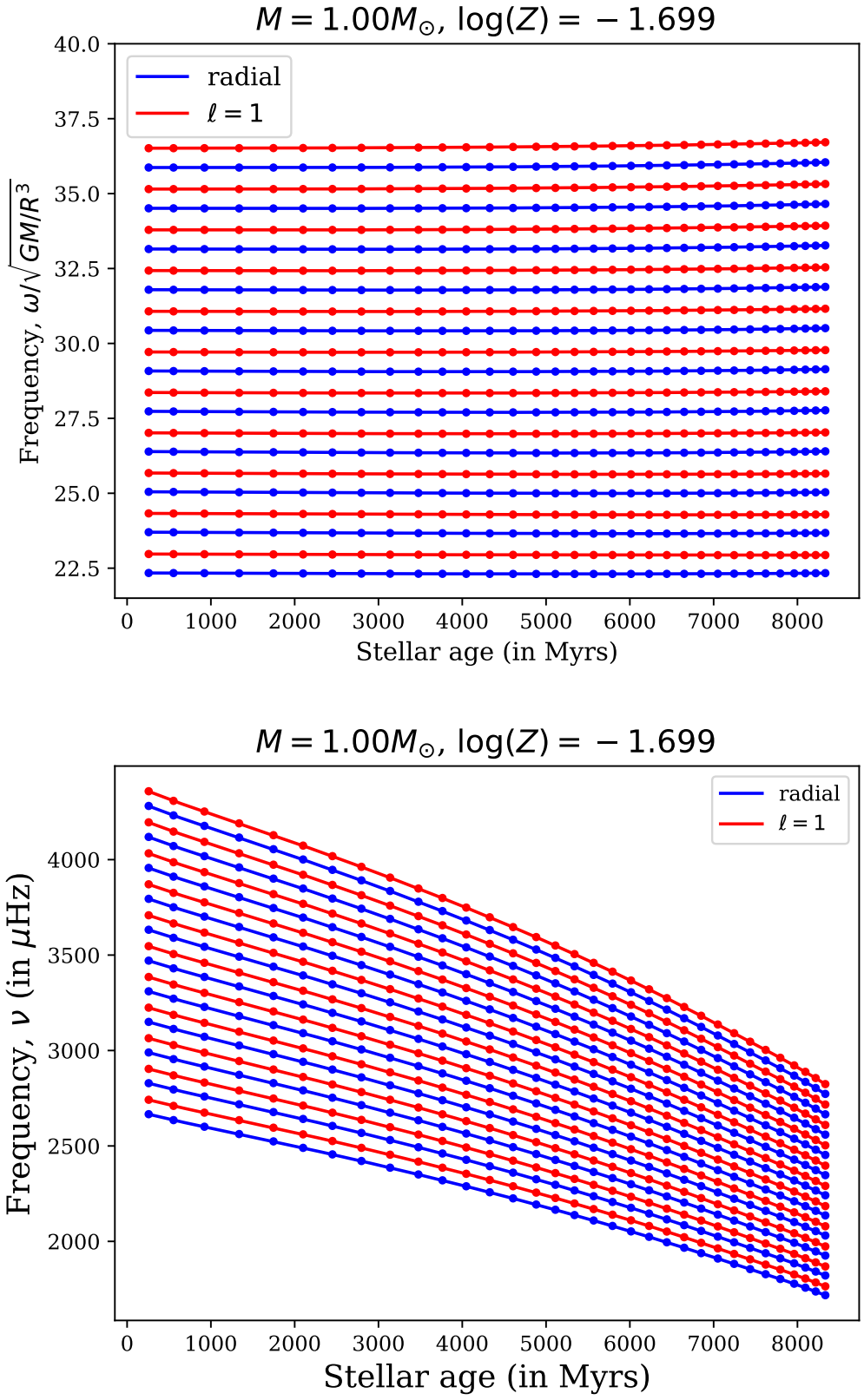

Figure 5.3: Frequencies as a function of stellar age along an evolutionary track. The upper panel corresponds to non-dimensional frequencies and the lower panel to their dimensional counterparts. The symbols correspond to frequencies from the non-interpolated models whereas the continuous lines represent the interpolated frequencies.

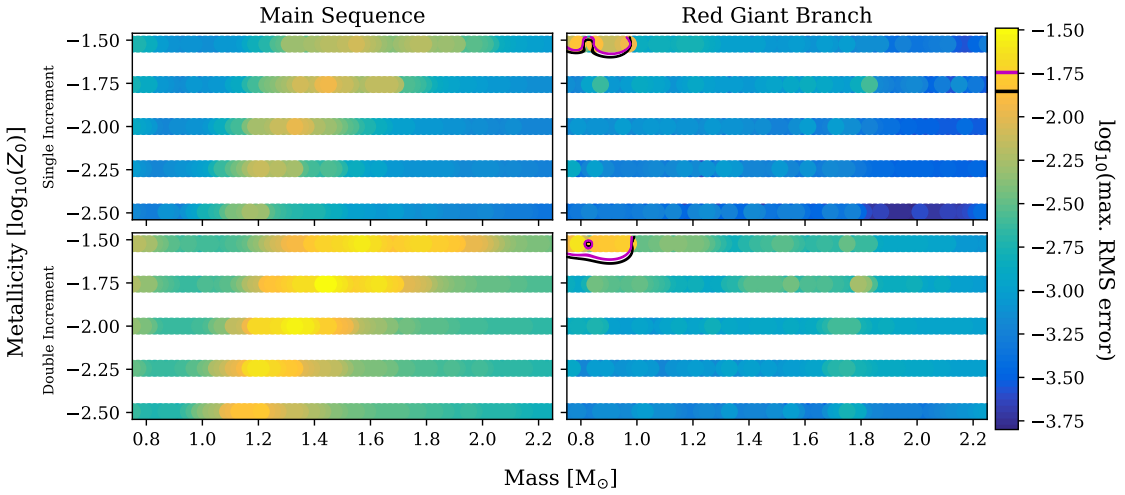

Figure 5.4: Average frequency interpolation errors over the range $\nu_{\max} \pm 0.2\nu_{\max}$ along evolutionary tracks for radial modes from the MS grid (left panels) and the RGB grid (right panels). The upper panels use increments of 1 along the tracks whereas the lower panel corresponds to increments of 2. The magenta and black contours correspond to the average and smallest error bars of KIC4448777. The average and lowest uncertainties for 16-Cyg A are not shown as they are greater than the uncertainty range shown

5.4.3 Interpolation along evolutionary tracks

The evaluation of the interpolation errors along an evolutionary track is made by testing how well both frequencies and global parameters of each model can be recovered from adjacent models at 1 and 2 increments away. Figure 5.4 shows the RMS average interpolation errors on the frequencies over the range $\nu_{\max} \pm 0.2\nu_{\max}$ for the MS and RGB grids detailed in Section 5.3. Overall the errors are smaller than the smallest frequency uncertainty of 16-Cyg A over the tested frequency range for both single and double increments. The behaviour of the interpolation error is in line with the expectations for a simple linear interpolation, as it increases by a factor of ~ 4. Increased errors are seen between 1.2 and 1.8 $M_\odot$ and are linked to the onset of a convective core during the evolution. The results are, however, satisfactory as they are well below the observational error bars.

On the RGB, the interpolation errors remain below the smallest and average uncertainties for KIC4448777 apart from a small region at low masses and high metallicities, which represents 2 to 3 % of the models, as highlighted in the right

panels of Fig. 5.4 by the black and magenta contours respectively. Again, using double increments in the interpolation leads to an increase in line with numerical expectations. While the RGB results may seem worse than for the MS, one must bear in mind the comparatively smaller error thresholds on the RGB. The RGB interpolation errors remain actually smaller than the MS, as shown in Fig. 5.4 and can of course be reduced by refining the grid.

5.4.4 Cross Track Interpolation

As a result of the multi-dimensional character of the parameter space and the use of Delaunay tessellation, the approach used to test cross-track interpolation in AIMS is quite different. The grid is partitioned in two sub grids: one to form the simplices for the interpolation and one containing the tracks to be recovered via interpolation. The partition is made randomly to avoid biasing the test towards one of the directions. This, however, means that the models are not always adjacent to the interpolated ones, reducing the representativity with respect to what is done in practice.

Panel (A) of Fig. 5.5 displays the recovered sub-grid from the MS interpolation. The RMS average interpolation errors are consistent with the MS and RGB values for along track interpolation, but extend to higher values in some regions. These predominantly follow the increased error pattern in Fig. 5.4. Higher uncertainties are expected though, as a greater range of parameter space than normally used is interpolated across. The maximum interpolation errors are the order of the average frequency uncertainty of 16-Cyg A. The errors are acceptable as the values are consistent with average observation uncertainties for interpolations over greater ranges than will be executed during real parameter determination.

Selecting a model from the recovered sub-grid, one can see how well the interpolation has reconstructed the original track. Panel (B) of Fig. 5.5 shows the recovered 1.47 $M_{\odot}$, $X_{\rm init} = 0.740$, $Z_{\rm init} = 0.0057$ track and panel (C) an echelle diagram for

the original and interpolated frequencies for a single model. The interpolated temperatures, luminosities and frequencies vary fractionally about the original values, illustrating further the accuracy of the interpolation method.

Figure 5.6 shows an example of the RGB grid. The variation in the residuals is minimal, confirming the proper behaviour of the interpolation. In additional tests, some instances show variations from the expected values along sections of the track. These features are largest when interpolating between grid points separated widely in mass (> 0.05 M$_\odot$) or metallicity, consistent with the regions of increased uncertainty in Fig. 5.5 outside of the convective onset region.

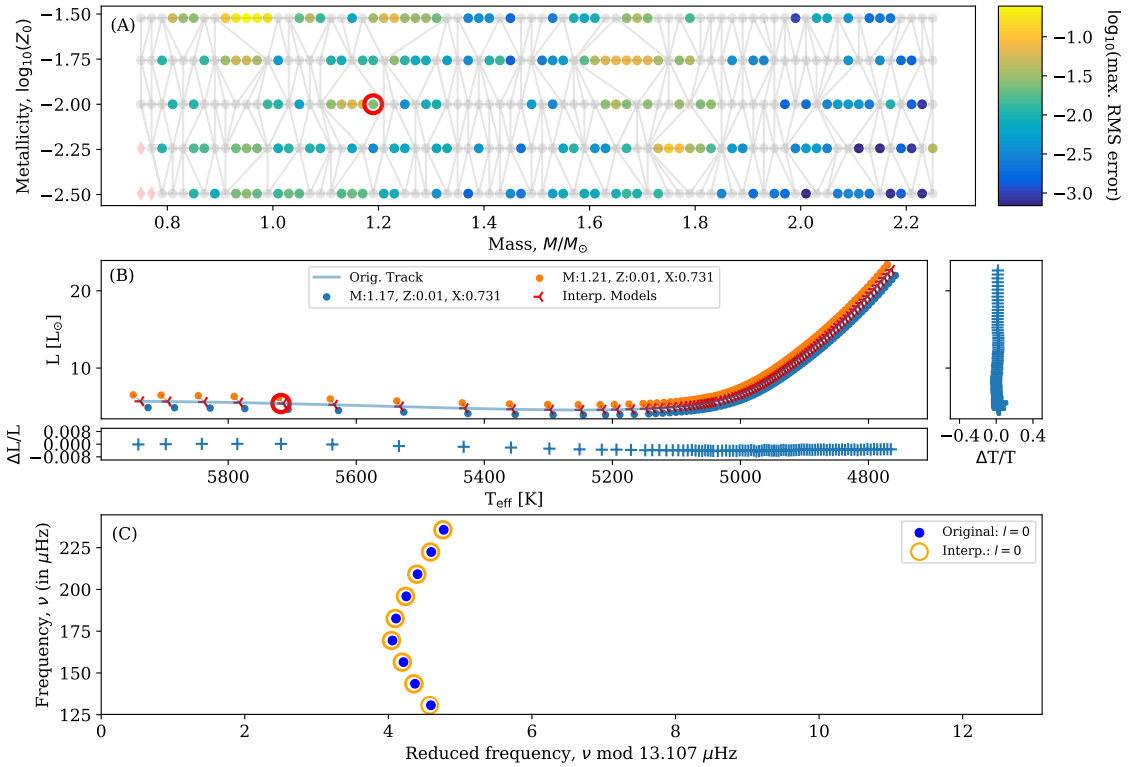

Figure 5.6: Results as for Fig. 5.5. A 1.19 M$_\odot$, $X_{\rm init} = 0.731$, $Z_{\rm init} = 0.0100$ track is tested here, but with a model from the RGB grid. A maximum interpolated frequency error of -2.088 is returned for this track and the mass of the Helium core is used as the interpolation parameter. The values of ΔT/T have been increased by a factor of 100 for ease of plotting. The frequencies in (C) have been increased by 5μHz to centre the frequency pattern.

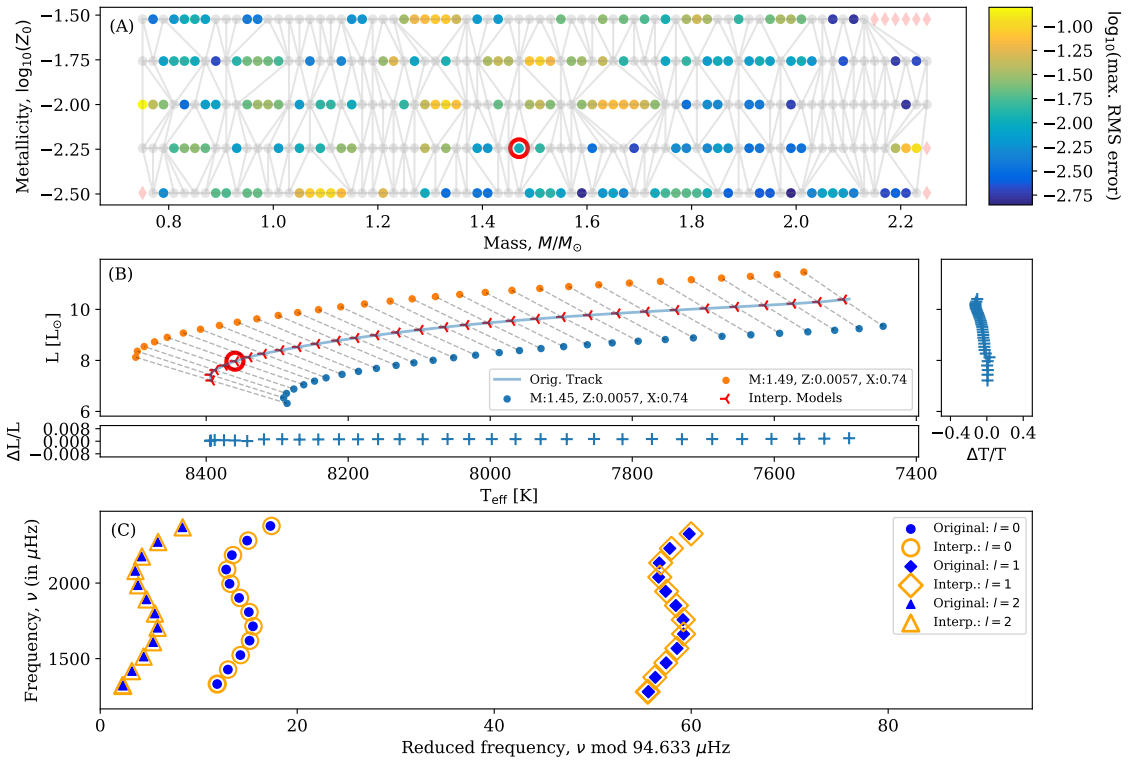

Figure 5.5: An example of results achieved recovering a 1.47 $M_\odot$, $X_{\rm init} = 0.740$, $Z_{\rm init} = 0.0057$ track during interpolation testing: (A) - Colour map of the maximum interpolated frequency uncertainty along each track. Points represent the positions re-interpolated tracks; the red circle shows the position of the track used in part (B). This track has a maximum $\log_{10}$ uncertainty on the interpolated frequencies of -1.990. The red circle highlights the location of the track. Grey points and lines show the triangulation simplices for the interpolation. Red diamonds denote tracks not interpolated due to no triangulation being possible. (B) - Hertzsprung-Russell Diagram showing the original track (blue line), interpolated track (red markers) and the models the track was interpolated from. Models used for interpolation are connected to the respective interpolated models by grey dashed lines and are shifted by 0.5 $L_\odot$ for additional clarity. The fractional difference residuals in luminosity and $T_{\rm eff}$ between the original and interpolated models are shown. The $T_{\rm eff}$ residuals have been inflated by a factor of 100. The red circle marks the model used in (C). (C) - An echelle diagram showing the original (blue, closed) and interpolated (orange, open) frequencies for the highlighted model in (B). Full frequency range is shown with diagram modulated by the original model $\Delta\nu$ value. All frequencies have been shifted by 5μHz in the x-direction for clarity.

5.4.5 Other Parameters

These tests can also be performed for parameters such as mass, radius, luminosity, effective temperature and surface metallicity ratios. Examples of the interpolation plots for radius and luminosity for the artificial main sequence star analysed are shown in Fig. 5.7. Again, these tests validated the quality of the grid at both the single and double increment level.

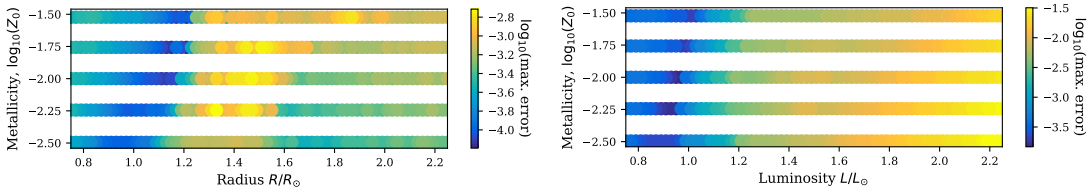

Figure 5.7: *Left*: Magnitude of the radius errors for the MS grid. *Right*: Magnitude of the luminosity errors for the MS grid. Interpolation from grid points a single increment from the original solution. The black circles show the grid node points. Uncertainties in Solar units.

5.5 Observational Outputs and Constraints

In this section, we present the robustness and accuracy of AIMS in reproducing accurately and precisely stellar parameters. The results presented here illustrate the absolute precision AIMS could achieve for the specific grid used in this study. It should be noted that the performance will depend on the grid and the free parameters included.

5.5.1 Artificial Data

At first, tests were performed using models from the underlying CLÉS grids. An observation file for a single, randomly selected model containing the artificial frequencies, $T_{\rm eff}$, $\nu_{\rm max}$, luminosity (L) and [Fe/H] values for the track was generated. This track was then removed from the grid. The input file was perturbed 100 times to simulate noise in the data signal. This artificial target was fitted using 100 AIMS runs and the average values from these consecutive fits and their uncertainties were

used to determine the degree of success of the procedure.

The asteroseismic constraints selected for use in the analysis were the individual mode frequencies. There are multiple options that can be selected for the seismic constraints, with each having a slightly different effect on the output parameters. Other constraints such as the average $\Delta\nu$ and various frequency separation ratios ($r_{0,1}$, $r_{0,2}$, $r_{1,0}$) could have been used. Using individual mode frequencies gives the smallest uncertainties on the derived parameters, but the final parameter values remain consistent throughout.

One should be cautious though as individual frequencies are not individually unique constraints and can lead to an underestimation of uncertainties. They are also significantly affected by surface effects (this is true of other parameters, e.g. mass, but the changes are more obvious in such cases), at a level such that the precision of the fit is determined by the uncertainties in the surface correction rather than the frequencies (see Buldgen et al. 2018a for examples).

5.5.1.1 Main Sequence

A 1.27 $M_{\odot}$, $Z_{\rm init} = 0.01$ and $X_{\rm init} = 0.731$ MS model with 21 mode frequencies (7 of each of $l = 0, 1, 2$) was selected (see Fig. 5.8). We used the uncertainty distribution of 16-CygA (Davies et al., 2015) for our artificial target. The magnitude of the uncertainties are of the same order as those used in the "Sun-as-a-star" tests in section 5.5.2. Uncertainties in [Fe/H] and $T_{\rm eff}$ were of order 0.1 dex and 80 K respectively. The uncertainty on the luminosity was selected to be of order 3% based on Gaia (Gaia Collaboration et al., 2018a) parallaxes, with a large proportion of the uncertainty due to the applied bolometric corrections (Torres, 2010a; Casagrande & VandenBerg, 2014b, 2018c). No surface effects were used for both the artificial target and the seismic modelling. For the step-up used in this work (400 walkers, 2000 burn-in, 500 steps, 10 temperatures, 4 cores), convergence was achieved in typically $<$ 25 minutes per star.

The values and uncertainties of the unperturbed model, the 100 realisations

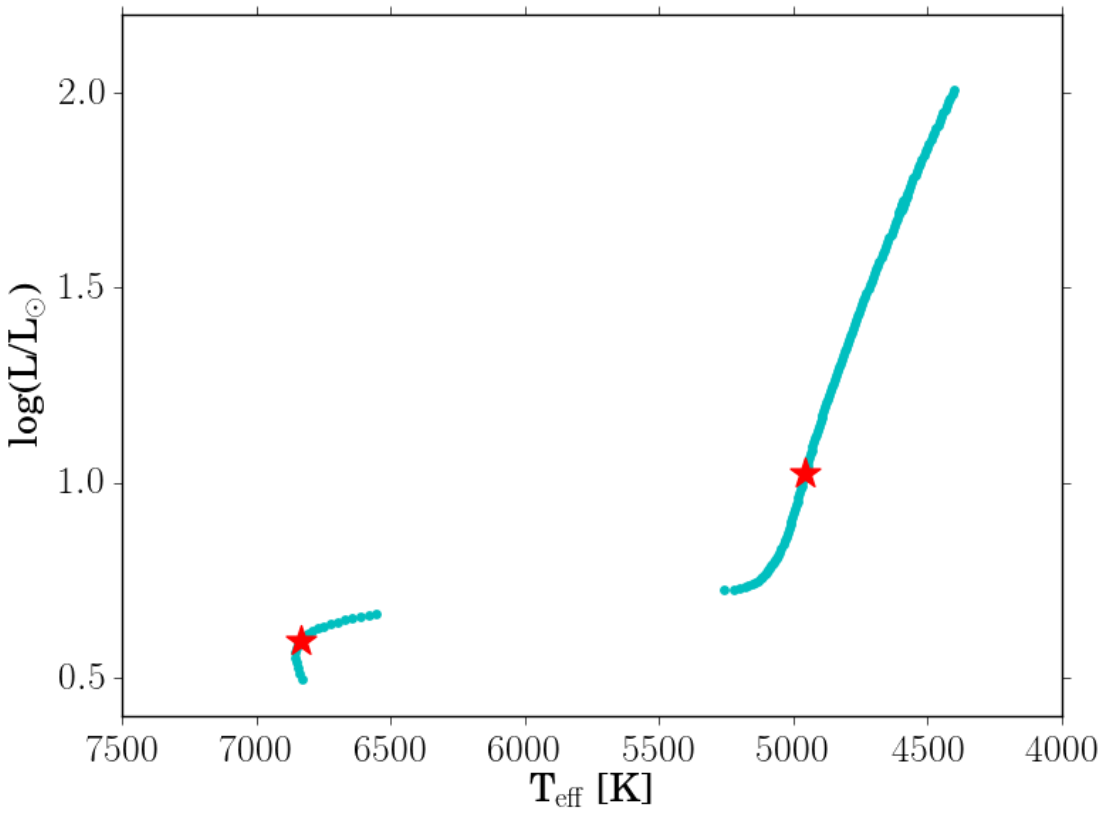

Figure 5.8: HR diagram showing the evolution of the 1.27 $M_{\odot}$, $Z_{\rm init}$ = 0.0100, $X_{\rm init}$ = 0.731 track. The red stars indicate the positions of the models selected for the artificial data analysis on the MS and RGB. Models prior to the zero-age-main-sequence (ZAMS) have been removed for clarity and final grid selection criteria have been applied.

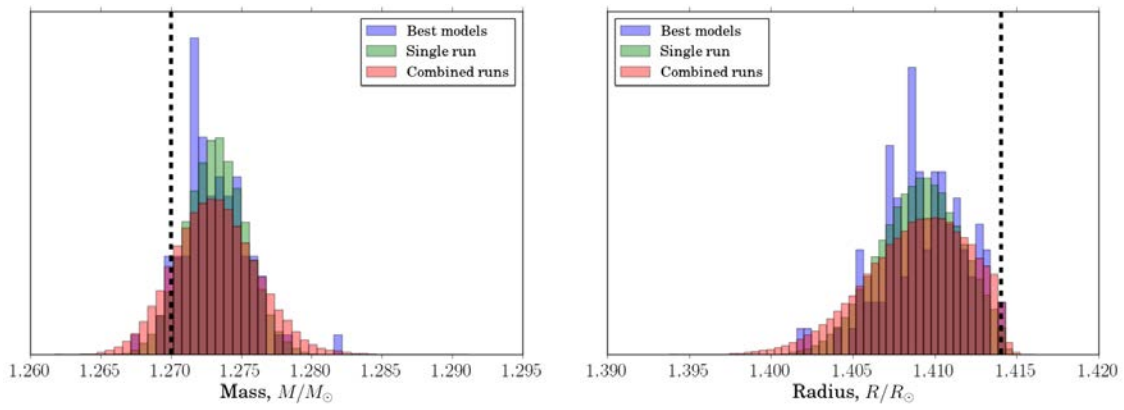

Figure 5.9: The mass (left) and radius (right) PDF distributions for MS the single model (green), 100 realisations (red) and best models from the MCMC runs (blue). The model mass and radii are 1.27 $M_{\odot}$ and 1.414 $R_{\odot}$, indicated by the vertical black, dotted line.

(combined runs) and the best models determined by the MCMC process for each of the perturbed runs were compared to the real values of the model. Examples of the PDF distributions for the mass and radius for each of the 3 trials are shown in Fig. 5.9.

The evidence from Fig. 5.9 indicates that the three different statistics agree reasonably well about a common value. The peaks of the distributions are not centred precisely about the expected values (black vertical lines) though. The weightings applied to each model to be combined greatly influences the final results. In this instance, models with a mass of 1.29 $M_\odot$ of the same $X_{\rm init}$ as the input model were preferentially selected compared to 1.25 $M_\odot$ models with the same $X_{\rm init}$ and 1.27 $M_\odot$ models of different $X_{\rm init}$ values. All models and weightings used during the analysis process are exported from the program and can be accessed to understand further which models and combinations are preferred for different stars. This can be used to understand and improve the construction of future grids.

The widths of the distributions are related to the uncertainties determined from each run. The uncertainties related to the single run are representative of the formal uncertainties output by AIMS, those of the best MCMC models are expected to be similar to results of the single (unperturbed) run. The test shows that both sets of uncertainties are very similar. Finally, the combined runs have uncertainties equal to the approximate summation of those of the previous two sets in quadrature, as the concatenation of the runs represents both the formal and random uncertainties.

The magnitude of the uncertainties also depends on the underlying grid. An incomplete grid, with insufficient models and/or frequencies will lead to systematic errors in the model selection. Indeed, AIMS rejects models which do not match the entire observed spectrum. The final output parameters are based upon the selection procedure. Hence, anything affecting the accuracy of the selection will affect the final results. As the performance relies upon the input criteria being accepted by a large number of models, an incomplete grid will increase the number of rejections,

reducing the accuracy of AIMS. A simple solution (performed here) is to reduce the number of input frequencies in the data file (e.g. limit range of ν to $\nu_{\rm max} \pm 0.5\ \nu_{\rm max}$), increasing the probability for models to match the input criteria.

To further examine the quality of the results, the number of standard deviations (N_σ) the output parameter ($x_{\rm calc}$) lay from the true value ($x_{\rm true}$) was determined using

$$N_\sigma = \frac{x_{\rm calc} - x_{\rm true}}{\sigma}. \tag{5.3}$$

These tests are shown in Fig. 5.10. It is clear that the best MCMC models outperform both combined and single models. The higher performance of the combined run stems from the increased abundance of data, providing a better convergence on the real value than a single run. As the results always lay within 1.5σ of the result, we can conclude that the fits were successful.

5.5.1.2 Red Giants

Using the same track and set of classical constraint parameters for consistency, a model from the RGB grid was selected and subjected to the same tests as the MS model. Frequency uncertainties were constructed as for the MS observational file. Uncertainties on the classical constraints were again consistent with the literature. The period spacing, $\Delta\Pi$, was included as a grid parameter ($\sigma_{\Delta\Pi} = 1\%$, Vrard et al. 2016) and consequently as one of the outputs in the results.

As before, PDFs of the mass and radius, in addition to an N_σ plot for all parameters, have been included. Figure 5.11 shows a tight relationship between each of the three model runs, sharing common peak values. The widths of the distributions of the RGB PDFs are broader than their MS counterparts. This is reflected in the increased uncertainties of the output values. Using fewer frequencies compared to the MS runs (9 RGB, 21 MS) and only $l = 0$ modes may contribute to this factor, but it is inherent from broader studies that larger RGB compared to MS uncertain-

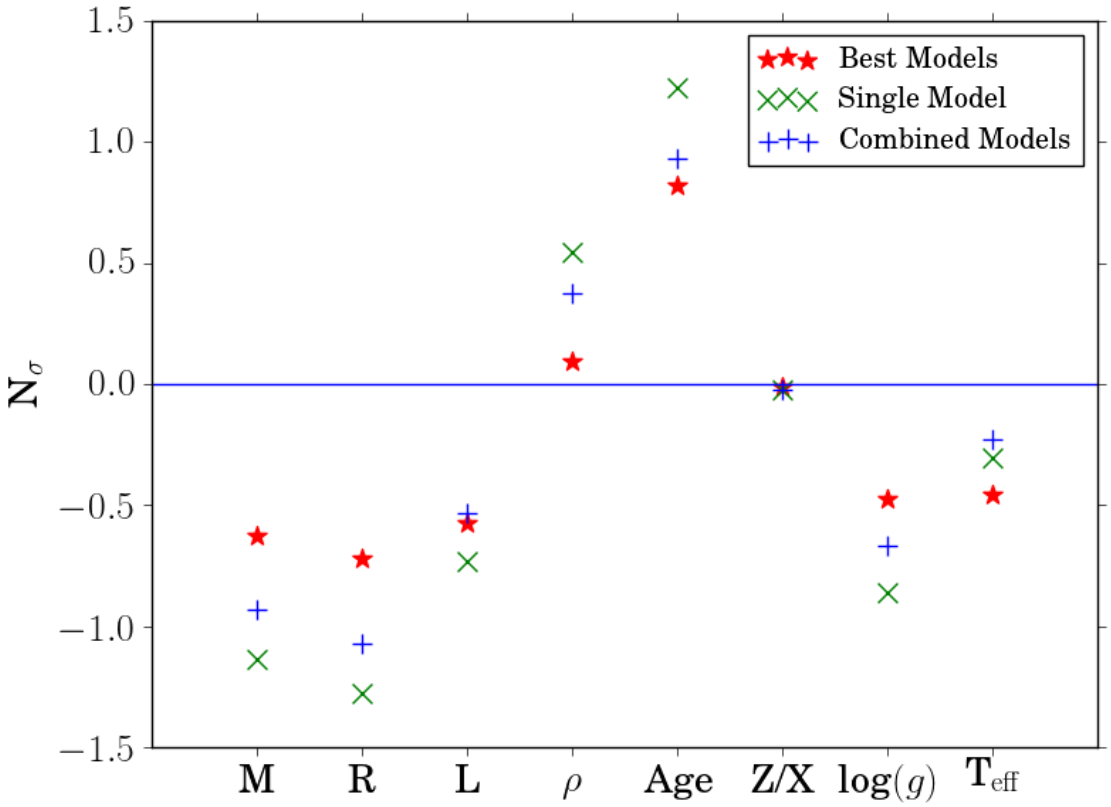

Figure 5.10: N_σ steps from the true value of each calculated parameter for the unperturbed (green), combined (blue) and best MCMC (red) models for the MS tests.

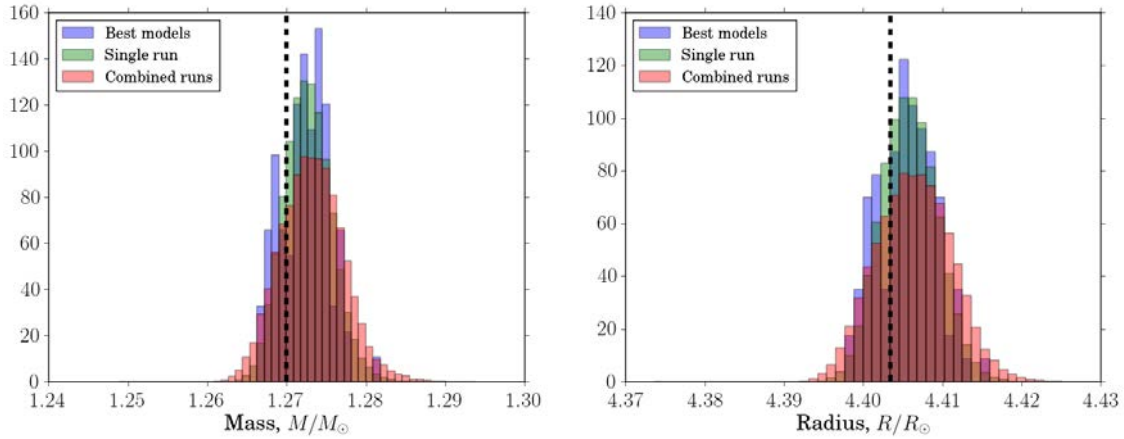

Figure 5.11: The mass (left) and radius (right) PDF distributions for RGB the single model (green), 100 realisations (red) and best models from the MCMC runs (blue). The model mass and radii are 1.27 $M_\odot$ and 4.403 $R_\odot$, indicated by the vertical black, dotted line.

ties are to be expected. A larger number of models are also rejected when searching the RGB grid, indicating fewer models are likely to be selected around the desired solution.

The trend in Fig. 5.12 closely resembles that observed in Fig. 5.10, but little should be read into this. Repeating the trials on multiple MS and RGB models from tracks in different regions of the grid resulted in different N_σ parameter distributions with each track. Each set of parameters returned is subject to different over/under estimations from models resulting from their grid location and the boundary conditions imposed on them. This variation in model determined variables and their associated likelihoods means consistency between N_σ patterns should not be expected from model to model. The focus should therefore be on the distribution of N_σ values which are all satisfactorily $< 1.5\sigma$ in each case.

5.5.2 The Sun

Besides artificial data, we used AIMS to reproduce solar data from the BiSON network of telescopes (Broomhall et al., 2009; Davies et al., 2014a; Hale et al., 2016), using the $l = 0, 1, 2$ and $n = 18 - 23$ modes. The frequency uncertainties were increased by a factor of $\sqrt{21/4}$ (Libbrecht, 1992; Toutain & Appourchaux, 1994;

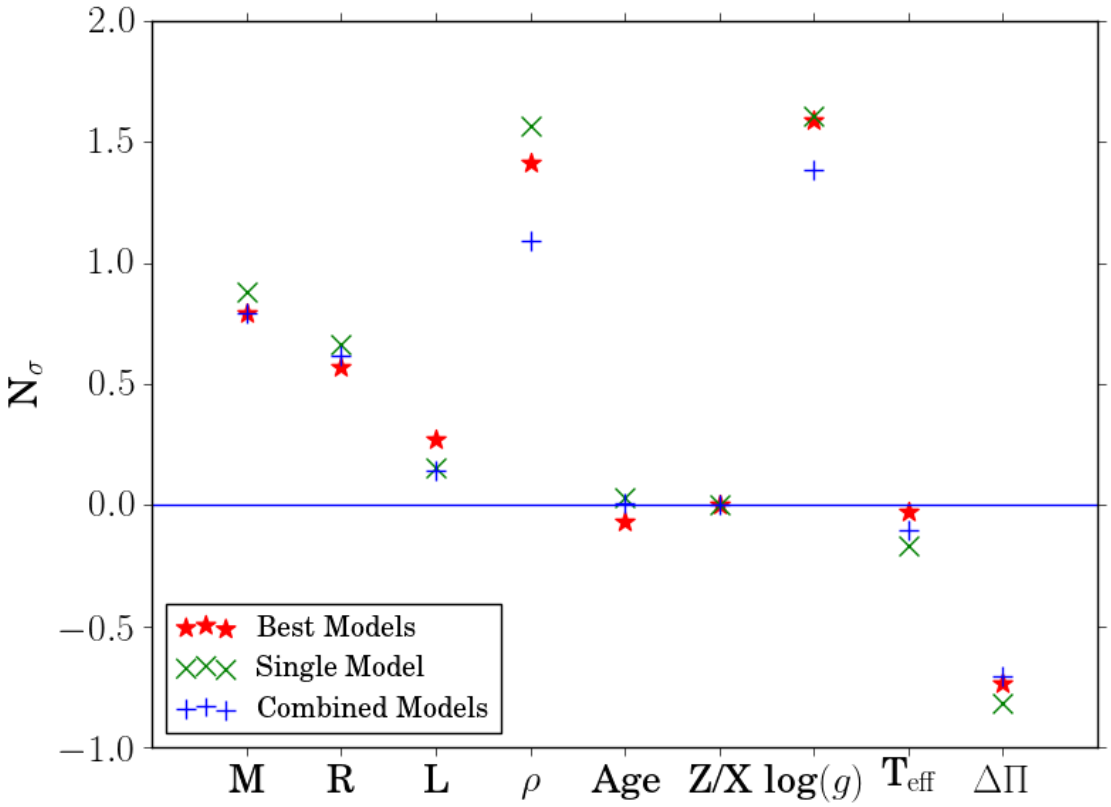

Figure 5.12: N_σ steps from the true value of each calculated parameter for the unperturbed (green), combined (blue) and best MCMC (red) models for the RGB tests.

Ballot et al., 2008) to perform a Sun-as-a-star analysis. The studies of Libbrecht (1992); Toutain & Appourchaux (1994); Ballot et al. (2008) showed the uncertainty in p-mode determination to be proportional to the inverse of the square root of observation time, T:

$$\sigma_{\mathrm{BiSON}} \propto 1/\sqrt{\mathrm{T}_{\mathrm{BiSON}}}\sigma_{\mathrm{Kep.}} \propto 1/\sqrt{\mathrm{T}_{\mathrm{Kep.}}} \tag{5.4}$$

Taking the ratio of the p-mode uncertainties, one can determine the scale factor between survey uncertainties,

$$\sigma_{\mathrm{Kep.}}/\sigma_{\mathrm{BiSON}} \propto \sqrt{\mathrm{T}_{\mathrm{BiSON}}/\mathrm{T}_{\mathrm{Kep.}}} \tag{5.5}$$

The BiSON and Kepler observation times are 21 and 4 years respectively, hence all frequency uncertainties were scaled by $\sqrt{21/4}$. We recall that a solar-calibrated value of the mixing length was used in the grid.

When working with real data, it is necessary to account for surface effects, which are not present in tests performed with artificial data. We used the two-term Ball and Gizon surface correction (Ball & Gizon, 2014), although other corrections are also included in AIMS: Ball and Gizon single-term (Ball & Gizon, 2014); Kjeldsen (Kjeldsen et al., 2008); Sonoi (single-term, scaling, two-term - Sonoi et al. 2015).

The fits were performed using two grids: the nominal CLÉS MS grid and an identical grid, but with microscopic diffusion included in the modelling (re-calibrated mixing length: 1.81). From Table 5.2, we can see that models without diffusion can reproduce quite well both the solar mass and radii, although not at the 1σ level, but that they present inaccuracies in age of about $\sim$1Gyr. This is in agreement with helioseismic results which reject solar models without microscopic diffusion (Christensen-Dalsgaard et al., 1993). However, models with microscopic diffusion show excellent agreement with solar values (Thoul et al., 1994). Fig. 5.13 confirms this, displaying N_σ results for multiple parameters of the Sun for grids with (blue

Table 5.2: Comparison of Solar parameters using grids with and without microscopic diffusion. Mass and radius are given in Solar units, density in g cm^{-3} and age in Myrs. Literature density and age are from Reese et al. (2012) and Bahcall et al. (1995).

Parameter	With Diff.	Without Diff.	Literature
Mass	0.997 ± 0.005	0.994 ± 0.003	1.0
Radius	0.999 ± 0.002	0.996 ± 0.001	1.0
$\langle\rho\rangle$	1.412 ± 0.001	1.4183 ± 0.0005	1.4104 ± 0.0012
Age	4578 ± 31	5264 ± 31	4570 ± 20

stars) and without (red crosses) microscopic diffusion.

Figure 5.14 shows the difference between the observed frequencies ($\nu_{\rm obs}$) and the theoretical (surface corrected - s.c., $\nu_{\rm theo\,s.c.}$) frequencies returned by AIMS for the grids with (left) and without (right) diffusion respectively. All available Solar frequencies are shown. Residuals are shown to illustrate the quality of the interpolation process, hence the robustness of the parameter determinations. A periodic trend is seen in both cases, with a much higher emphasis for the non-diffusive grid. This trend is the result of the large mismatch of helium abundance between the theoretical model and the Sun. Larger disparities are also observed above 3700 μHz as a consequence of the surface effects. This clearly illustrates the difficulties and weaknesses of using individual frequencies as direct constraints as the surface effects could bias the modelling results. Using constraints such as frequency ratios for MS stars can help mitigate such effects.

Looking at the reduced χ^2 values of the frequencies, it seems sensible to favour the values of the Solar parameters determined using the grid including diffusion:

$$\chi^2 = \sum_{\rm i} \frac{\left(\nu_{\rm theo\,s.c.,i} - \nu_{\rm obs,i}\right)^2}{\sigma_{\rm i}^2} \tag{5.6}$$

$$\chi^2_{\rm red} = \frac{\chi^2}{d.o.f.} \tag{5.7}$$

where $d.o.f.$ (degrees of freedom) is the number of input parameters minus the

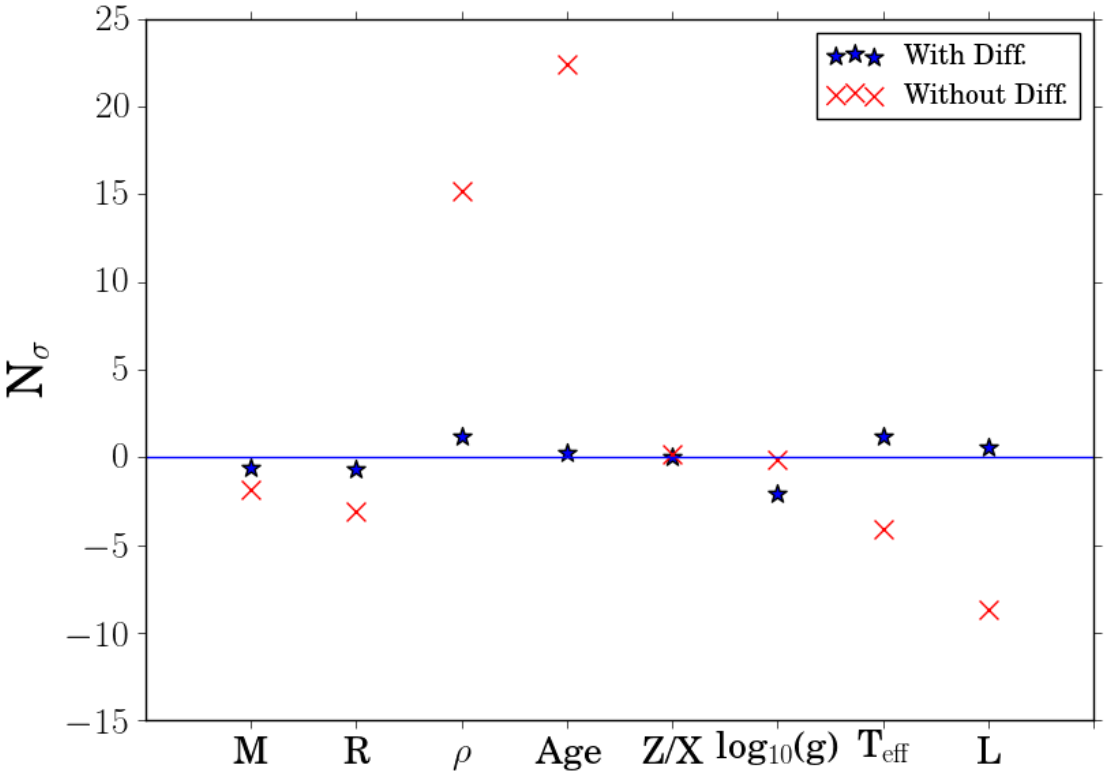

Figure 5.13: N_σ steps from the true value of the mass, radius, density, age (taken to be 4.57 ± 0.02 Gyr, Bahcall et al. 1995), Z/X ratio, $\log_{10}(g)$, $T_{\rm eff}$ and luminosity for the Sun for the grids with (blue stars) and without (red crosses) diffusion.

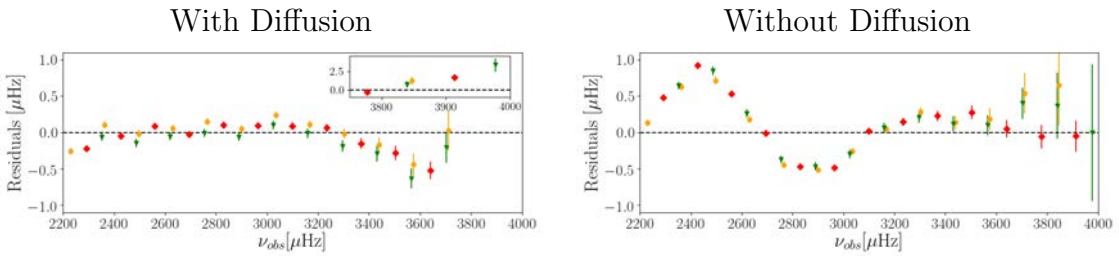

Figure 5.14: Frequency residuals ($\nu_{\rm obs} - \nu_{\rm theo}$) comparison between the observed and theoretical frequencies output by AIMS for the grid with (left) and without (right) microscopic diffusion. The $l = 0$ (orange), 1 (red) and 2 (green) modes are shown. The residuals subplot for the results with diffusion shows the residuals for frequencies $> 3750\mu$Hz. These residuals are much larger and therefore shown in a separate subplot to allow the underlying trend in the residuals to be observed.

Table 5.3: Solar parameters and uncertainties determined by AIMS using the frequency separation ratios $r_{0,1}$, $r_{0,2}$ and $r_{1,0}$ as asteroseismic constraints. Mass and radius are given in Solar units, density in g cm^{-3} and age in Myr. The diffusive grid was used.

Parameter	$r_{0,1}$	$r_{1,0}$	$r_{2,0}$
Mass	1.01 ± 0.02	1.00 ± 0.02	0.99 ± 0.03
Radius	1.01 ± 0.03	1.00 ± 0.03	0.99 ± 0.03
$\langle\rho\rangle$	1.40 ± 0.10	1.42 ± 0.10	1.44 ± 0.10
Age	4614 ± 258	4549 ± 204	4603 ± 139

number of free parameters, and σ the compound uncertainty on the frequencies. Indeed, $\chi^2_{\text{red,diff}} = 11.4$ whereas $\chi^2_{\text{red,non-diff}} = 52.5$. Testing the hypothesis that the model values are true, p values of 0.88 ($\chi^2_{\text{red,diff}}$) and 0.07 ($\chi^2_{\text{red,non-diff}}$) were returned. The order of magnitude difference between the reduced χ^2 values clearly indicates that the grid including diffusion is superior for the Solar analysis. As mass, radius and age are all within 1σ of the Solar values for this grid, we can conclude that the processes within AIMS perform well enough to produce the results to a high degree of accuracy. All of the uncertainties are lower than one would expect to find in the literature (see Silva Aguirre et al. 2017 for recent Solar values from multiple grids and codes) as they are of the same order of magnitude as in tests using artificial data.

To determine whether the small uncertainties resulted from the model or the use of individual mode frequencies, the Solar data was also tested using the $r_{0,1}$, $r_{0,2}$ and $r_{1,0}$ frequency separation ratios (Roxburgh & Vorontsov 2003; grid including microscopic diffusion used). An improvement in the returned parameters can be expected, as the ratios focus more on the stellar interior (Roxburgh & Vorontsov, 2003; Otí Floranes et al., 2005). Additionally, their reduced sensitivity to surface effects should also lead to an improvement. This is confirmed by the results in Table 5.3. The frequency ratios give values consistent with the ν_{ind} results and the expected Solar values, but with larger uncertainties. When using solely the frequency ratios[4], one filters out additional information (e.g. on the mean density of the star) and thus

[4]AIMS allows the use of other constraints along frequency ratios, such as the large frequency separation, while self consistently keeping track of the correlations between seismic indicators.

naturally the uncertainties are increased. While this leads to larger uncertainties on the stellar parameters, this degree of precision can also be seen as more robust with respect to systematic effects which can be underestimated when directly fitting the individual frequencies.

5.6 Impact of using different combinations of seismic and non-seismic constraints

In addition to testing the main functionalities of AIMS, the effect of the inclusion of certain combinations of constraints within the input observation file were explored. For all tests presented so far, the classical constraints used have been $\nu_{\rm max}$, $T_{\rm eff}$, L and [Fe/H]. In addition to these constraints, equal weighting has been given to the asteroseismic (input frequencies, ν_i) and classical constraints.

5.6.1 Main Sequence Fits

Four tests were performed on a single main sequence model (the same model used in Sect. 5.5.1.1) from within the grid, with the effect on the PDF distributions and uncertainties of the mass, radius and age of the artificial star recorded. The constraint variations were as follows:

i $T_{\rm eff}, L(\sigma_{Gaia})$, [Fe/H], no acoustic oscillation frequencies

ii $T_{\rm eff}$, [Fe/H], acoustic oscillation frequencies, no L

iii $T_{\rm eff}, L(\sigma_{Gaia})$, [Fe/H], $r_{0,2}$

iv $T_{\rm eff}, L(\sigma_{Gaia})$, [Fe/H], acoustic oscillation frequencies

Figure 5.15 displays the PDFs for mass, radius and age determinations. The inclusion or exclusion of luminosity from the constraints appears to have a minimal impact on the precision between cases (ii) and (iv). The increase in precision on each parameter may not be as significant as the inclusion of asteroseismology (narrowing

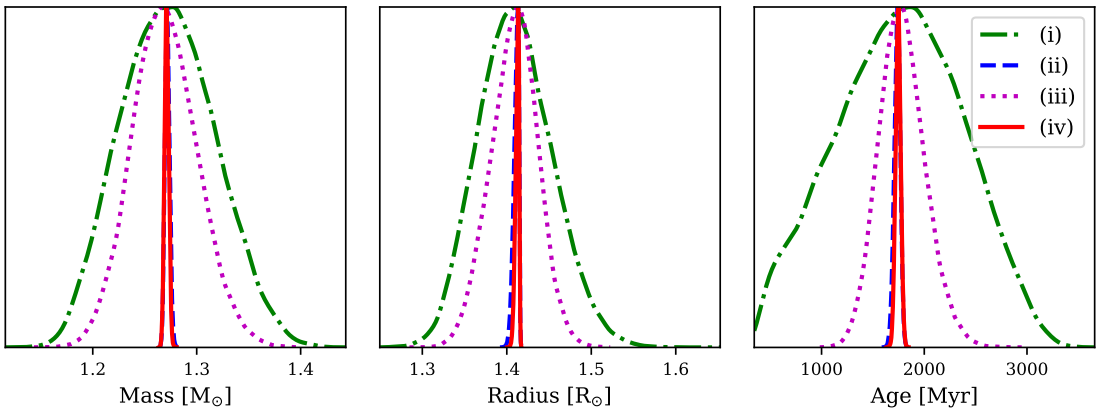

Figure 5.15: Comparison of input classical and seismic constraints for mass (left), radius (centre) and age (right) determination. The normalised distributions represent the different classical constraint criteria: (i) - green, dot-dashed; (ii) - blue, dashed; (iii) magenta, dotted; (iv) - red, solid.

of distributions observed in both cases), but an improvement is still observed when luminosity is included. Should other parameters (e.g. initial He abundance) be free to vary, an independent constraint on luminosity is important to lift any existing degeneracies present when using only seismology.

Table 5.4 shows the uncertainties for each set of constraints. Test (i) returns uncertainties of order of the typical literature values for age, mass and radii respectively, but tests (ii) and (iv) return values at least an order of magnitude smaller. The addition of more free parameters to the grid and the intrinsic differences they would cause between models would increase these uncertainties to be closer to those expected. However, the trend between constraint sets is clear. The decision to include or exclude the acoustic oscillation frequencies has a significant impact on all parameters, reducing the percentage errors by an order of magnitude.

Though reduced compared to case (i), case (iii) uncertainties are of the same order of magnitude despite the inclusion of asteroseismology and are in line with the best literature values. This illustrates the difference in precision achievable with the inclusion of global asteroseismic parameters compared to the use of individual mode frequencies when the same classical constraints are available. The potential

Table 5.4: Percentage uncertainties for the determined values of mass, radius and age for the MS model used in the observational tests, subject to the tested combinations of classical and asteroseismic constraints.

Constraint	Age (%)	Mass (%)	Radius (%)
(i)	34.64	3.69	3.12
(ii)	1.69	0.18	0.22
(iii)	12.65	2.48	1.98
(iv)	1.41	0.16	0.18

improvement in precision to be gained underlines the importance of the development of analysis codes, such as AIMS, capable of using individual acoustic oscillation frequencies for the furthering of asteroseismic studies.

5.6.2 Red Giant Fits

The process was repeated for an RGB model from the grid to illustrate that, despite less convincing interpolation results than on the MS, it also performs well in this regime. Consequently, a more comprehensive approach was taken. We compare the results of AIMS for red giant stars to an extensively used, pre-existing stellar parameter determination code to prove the capability of AIMS as an analysis tool. We chose the PARAM software (da Silva et al., 2006; Rodrigues et al., 2014, 2017), which is quite similar to AIMS in its philosophy, with the only significant difference being that AIMS uses asteroseismic data as an input. We run AIMS without using the input mode frequencies to make a more informed comparison between the capabilities of both codes.

A recent work by Rodrigues et al. (2017) (hereafter R17) investigates the effects of various combinations of constraints on the accuracy of stellar parameter determinations for a series of artificial red giant and red clump stars using PARAM. We repeated these tests using the same sets of classical and global seismic constraints in AIMS and our own RGB model. 10 different combinations of constraints were used:

(i) $\Delta\nu$

(ii) $\Delta\nu, \nu_{\rm max}$

(iii) $\Delta\nu, \Delta\Pi$

(iv) $\Delta\nu, \nu_{\rm max}, \Delta\Pi$

(v) $\Delta\nu, \Delta\Pi, L$

(vi) $\Delta\nu, \nu_{\rm max}, \Delta\Pi, L$

(vii) $\nu_{\rm max}, L$

(viii) $\log_{10}(g), L$

(ix) $\Delta\nu, \log_{10}(g)$

(x) $\Delta\nu, L$

From the above list, it is clear that asteroseismic parameters are still to be used as initial constraints with the large frequency separation ($\Delta\nu, \sigma_{\Delta\nu} = 0.05\mu$Hz), frequency of maximum power ($\nu_{\rm max}, \sigma_{\nu_{\rm max}} = 2\%$) and period spacing ($\Delta\Pi, \sigma_{\Delta\Pi} = 1\%$) featuring heavily. These parameters are all global seismic properties and are not necessarily reliant upon determination of individual frequencies. Hence, they can be input as classical constraints. In addition to the listed constraints, the effective temperature ($\sigma_{T_{\rm eff}} = 80$ K) and metallicity ($\sigma_{\rm [Fe/H]} = 0.1$ dex) were included for each case as in R17. The uncertainties used on L and $\log_{10}$(g) were 3% and 0.1 dex respectively. It should be noted that case (iii) of R17 was ignored here, with a value of $\Delta\nu$ calculated from the frequencies used throughout.

Figure 5.16 displays the results of these tests as the distributions of the determined values normalised to the true parameter values. In addition to the above sets of constraints, the model was tested using the standard constraints used throughout this work and with a direct fit of the individual mode frequencies. This is labelled 'ν_i'.

To further analyse the distributions, Table 3 from R17 has been recreated. Table 5.5 contains the relative uncertainties for the mass and age of the tested model for each combination of constraints. The majority of the results follow typically Gaussian distributions, but cases (i), (viii) and (ix) show asymmetry in their mass distributions. The sampling of the mass in these cases has reached the lower end of the grid, introducing a sampling bias as a build up of low mass samples occurs. This causes the asymmetry observed, which propagates to other parameters.

A direct comparison between the two sets of results is not appropriate due to the different models used, but a comparison of the overall trends is meaningful. The

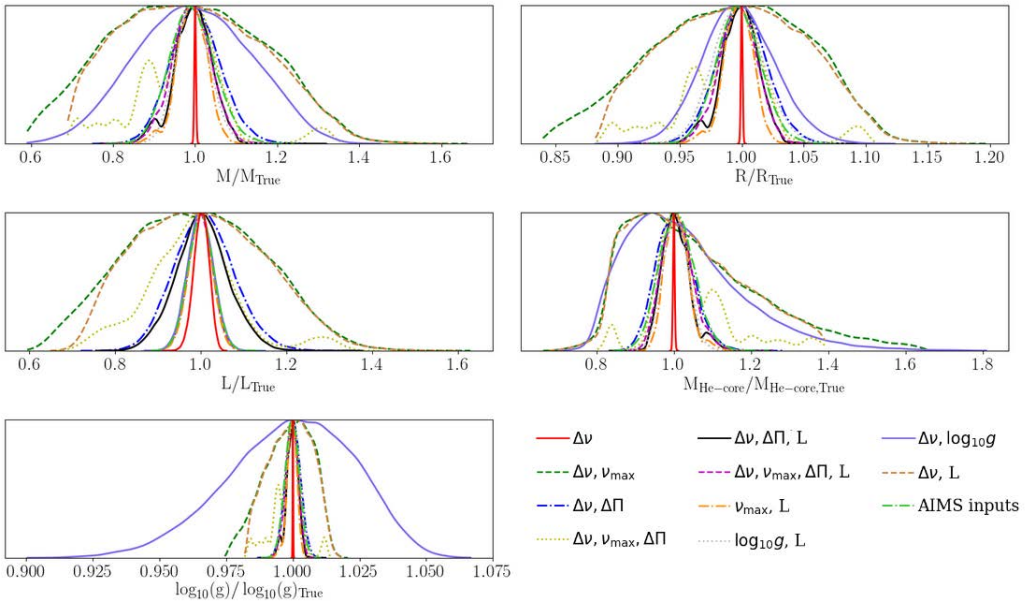

Figure 5.16: Comparison of the posterior probability distributions for multiple combinations of constraints used as inputs to AIMS without the use of the individual mode frequencies. The distribution marked 'AIMS inputs' shows the result obtained if the individual mode frequencies are used.

obtained values vary, but in general the distributions follow those of R17. This is reassuring and confirms that AIMS reacts to certain combinations of constraints in an expected manner.

Considering previous statements regarding AIMS uncertainties, the fractional uncertainties shown in Table 5.5 are comparable to those of PARAM. Removing the use of individual mode frequencies causes the inflation of the uncertainties due to the smaller number of constraints. Consistency between codes here is important to show that when global asteroseismic parameters are used as constraints, AIMS performs as well as a pre-established and trusted software. Some variation of the fractional uncertainties compared to R17 is present but likely stems from the differences in model parameters and grid properties, as well as modelling codes used in these tests.

Using all of the available information from the mode frequencies improved the fractional uncertainties with values of 0.002 and 0.029 in mass and age respectively. This test case also produces the best PDFs in Fig. 5.16, showing the potential of

Table 5.5: Fractional uncertainties for each combination of input constraints for AIMS run as PARAM. The RGB results from table 3 of R17 are displayed for direct comparison.

Constraints	σ_M/M		$\sigma_{\rm Age}$/Age	
	AIMS	R17	AIMS	R17
ν_i	0.002	-	0.029	-
$\Delta\nu$	0.184	0.173	0.735	0.734
$\Delta\nu, \nu_{\rm max}$	0.061	0.078	0.230	0.284
$\Delta\nu, \Delta\Pi$	0.119	0.109	0.475	0.336
$\Delta\nu, \nu_{\rm max}, \Delta\Pi$	0.047	0.054	0.190	0.192
$\Delta\nu, \Delta\Pi, L$	0.048	0.043	0.131	0.122
$\Delta\nu, \nu_{\rm max}, \Delta\Pi$, L	0.037	0.034	0.110	0.097
$\nu_{\rm max}, L$	0.041	0.039	0.108	0.107
$\log_{10}(g), L$	0.138	0.124	0.544	0.427
$\Delta\nu, \log_{10}(g)$	0.166	0.173	0.590	0.727
$\Delta\nu, L$	0.055	0.052	0.146	0.143

using constraints determined from individual frequencies.

5.6.3 Further Testing

In order to demonstrate the difference in performance between using all the available modes and only the global asteroseismic parameters on an MS star, the model used in section 5.5.1.1 was re-run using the same constraints and configuration as test (ii). Though it was not possible to perform such a comparison with PARAM results, the consistency of the AIMS results without the use of individual frequencies with PARAM allows meaningful comparisons.

Figure 5.17 shows the result comparison of two separate runs for mass and radius as before, as well as the relations for the luminosity, surface gravity and evolutionary parameter - age. An offset between the peaks of the distributions is present for various parameters, caused by the known helium-mass degeneracy (see Baudin et al. 2012 and references therein). As tighter constraints are placed on the luminosity of the star when asteroseismology is used, these degeneracies become lifted, allowing for tighter distributions around the expected solutions.

Table 5.6 shows the statistical trends observed in the related figures, giving the percentage uncertainty on each of the relevant parameters for the cases where the

Table 5.6: Percentage uncertainty of calculated variables with and without the use of individual frequencies as a constraint for an MS artificial model. 'With ν' indicates that the individual frequencies were used in the analysis. $\langle\Delta\nu\rangle$ indicates the runs without the use of the individual frequencies, but inclusion of the average large frequency separation as a constraint. The $l = 0, 1, 2$ modes were used.

Model	σ_{Mass}	σ_{Radius}	σ_{Lum}	σ_{g}	σ_{Age}
MS (with ν)	0.14%	0.06%	0.48%	0.01%	1.18%
MS ($\langle\Delta\nu\rangle$)	2.96%	1.12%	2.71%	0.10%	15.48%

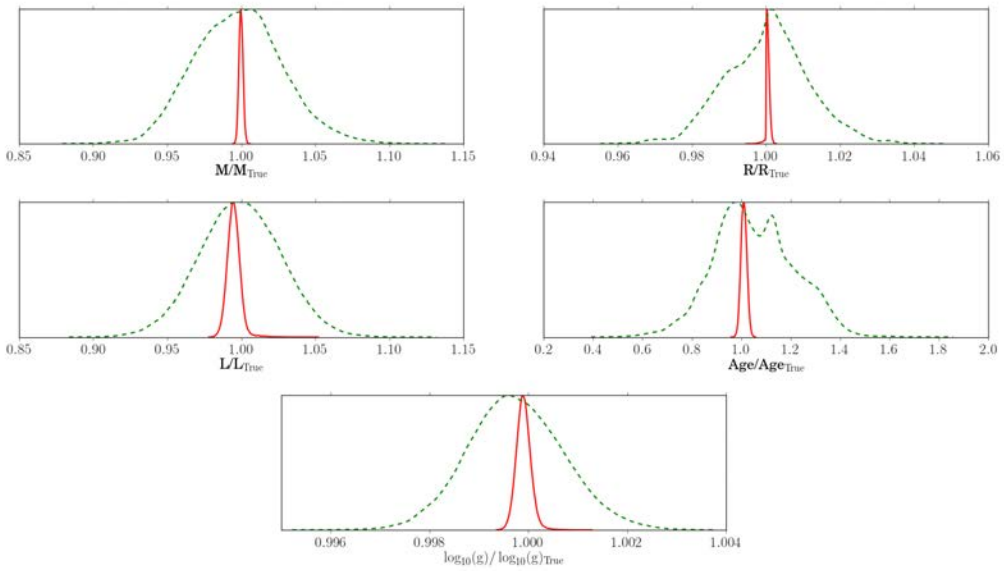

Figure 5.17: Comparison of the normalised posterior probability distributions for the MS model both with (red, solid) and without (green, dashed) the use of the individual mode frequencies.

individual frequencies were used and when only global asteroseismic constraints were applied. It should be stressed that the uncertainties displayed in Table 5.6 are purely statistical and do not account for any systematics within the code. Despite this, the effect of including the individual frequencies in the analysis is clear from Table 5.6. A reduction in uncertainty is seen for all parameters when using the individual frequencies, displaying the benefits of using this additional information. However, as discussed before, the direct use of individual frequencies as constraints can lead to underestimated uncertainties. This is particularly true for main-sequence stars, which often have very rich oscillation spectra. In that sense, being able to use frequency ratios in AIMS allows us to obtain a more realistic precision on stellar parameters and should generally be preferred.

The reduction between the RGB and MS uncertainties is not of the same order for case (vi) (section 5.6.2) for mass and age (case vi contains the initial artificial RGB test classical constraints and therefore is most appropriate to compare). The uncertainties in mass and age on the RGB decrease by factors of 18 and 4, while on the MS the reduction is by a factor of 20 and 15 respectively. The reduction in mass is quite similar for each evolutionary state, but the reduction in age is an order of magnitude greater for the MS. This is mainly due to the observed frequencies and the additional information they carry on the internal stellar structure. Indeed, the RGB fit used 9 frequencies while 21 frequencies were used on the MS. Besides the number differences, the MS fit used modes of $l = 0, 1$ and 2, containing a lot of information on the evolutionary stage on the MS, whereas the RGB fit only used radial modes. The $\ell = 1$ and $\ell = 2$ modes can of course be included within the RGB grid. However, their highly non-linear behaviour and the decreased sensitivity of the small separations to age in evolved stars (e.g. see Montalban et al. 2010), currently precludes their direct use in AIMS.

To further illustrate the impact of the inclusion of the $\ell = 1$ and $\ell = 2$ modes, an additional test on the MS using only the $\ell = 0$ modes from the previous tests (7

in total) was performed. The reduction in uncertainty in this instance was only a factor of ~ 5 in age, much more in line with the RGB results. This demonstrates the reliability with which stellar parameters can be derived and also points towards the potential improvement to make with RGB grids and data sets containing more than just the $\ell = 0$ mode frequencies.

5.7 Discussion and Conclusion

We have presented a new, open source, code for the determination of stellar parameters. It is unique as it is currently the sole code using a Bayesian and MCMC algorithm approach with grid interpolation to carry out asteroseismic inferences. The code's flexible, multidimensional approach to the analysis allows the user to analyse data as a function of 2 or more fixed grid parameters, affording more control over the analysis dimensions. We executed a comprehensive testing phase and presented the results. All aspects of the program were analysed, with the results proving satisfactory.

A test of the interpolation procedures revealed the accuracy to which the interpolation function within the program returns known values from within the grid. Primarily, the tests focused on the interpolation of the radial mode frequencies of the MS and RGB grids, showing that AIMS provides accurate interpolations well above the threshold values set from the literature. Additional inputs (e.g. mass, age, radius...) were then also tested and again found to be returned at a level matching or exceeding the desired threshold.

The parameter determination tests were very informative. Primary tests with artificial data shed light on some potential limitations of both the analysis code and underlying grid. We showed that the parameter uncertainties determined by AIMS are approximately an order of magnitude smaller than typically reported in the literature. Further investigations confirmed that the statistical analysis and propagation of observational uncertainties were robust. The uncertainties stated by

AIMS are thus statistical and do not account for biases in the input physics or model selection.

The artificial data tests were satisfactory, with parameters lying within a few σ of the true results. The input parameters of the model were not returned, but the results were sufficiently close to the input values for this not to be of great concern. Data for the Sun were analysed to test AIMS on real data with clearly defined parameters for comparison. As expected, the precision achieved when including individual oscillation modes leads to a comparable accuracy with the known values only if one has flawless models. As shown here, this objective is yet to be achieved. One can use the evidence from comparisons of a diffusive and non-diffusive grid to highlight the limitations of certain models and the need to improve upon model selection. As AIMS is strongly coupled to the input grid, its performance depends on the standard of the grid used and the final model selection and returned parameters are ultimately a reflection of this.

The AIMS code is highly flexible in terms of the parameter constraints one can use in the analysis. The code can be operated using individual mode frequencies, frequency ratios or large frequency separations as asteroseismic constraints. It is also possible to operate the code without these options, simply using classical constraints instead. Full posteriors are returned for determined parameters in each case, meaning any correlations are taken care of in the analysis process. The effect of altering the classical and asteroseismic constraints associated with the input observational file was explored, with the impact of including or excluding any asteroseismic constraints extremely clear. The inclusion of asteroseismic constraints improved the internal precision by a factor 2-20 for both the RGB and MS stars respectively for all of the tested parameters (M, R, ρ, age, Z/X, $\log_{10}$(g), $T_{\rm eff}$, L), underlining how important asteroseismology is to AIMS for accurate inferences and the improvement in measurements this technique allows for.

A comparison with an established stellar parameter code, PARAM, gave a valu-

able insight into the performance of AIMS. For red giant stars, a set of artificial data similar to those used in R17 was analysed using a variety of constraint combinations, including multiple global asteroseismic parameters. Some variation from the expected values for different combinations was observed, but upon comparison with the work in R17, the distributions and relative uncertainties show comparable trends. The similarity in results to an established code brings confidence to those being output by AIMS, showing that it performs to the standard expected by the field, even without the use of the individual mode frequencies it is designed to use.

The primary focus of constraint testing was on the precision to which the code can operate, but pushing it to the challenging limits of using the best constraints - i.e. individual oscillation frequencies with uncertainties of the order of $10^{-2}\mu$Hz. The robustness shown here by the results achieved gives confidence to explore more possibilities with the code.

Our tests show that, when using individual mode frequencies as constraints, one is in principle able to infer properties with exceedingly high precision. The latter, however, should not be taken as realistic expectations concerning accuracy. Individual mode frequencies are affected by systematic effects that will dominate the uncertainties on the inferred properties. We do not explore such effects in this work, except from the enlightening case of the Sun, where fitting individual mode frequencies results in very high precision estimates of its global properties, which are, however, highly inaccurate if one uses inaccurate models (see Sec. 5.5.2). This strong model-dependence is attenuated when one uses frequency ratios, as shown in the literature, at the cost of a reduced precision. Explorations of the systematic uncertainties in the models and the inclusion of additional free parameters (e.g. $Y_{\rm init}$, mixing length, surface effects) provide additional challenges to progress the code and maintain a high quality analysis tool for the community, and will be presented in a forthcoming work (e.g. see Nsamba et al. 2018). On a positive note, and as demonstrated by the tests using Solar data, AIMS can be used for the comparison of

competing models which can be selected using Bayesian inference, as derived from the full posterior distributions of various estimated properties. These tests will be instrumental to promote the development of next generation stellar models, and will improve our ability to determine stellar ages and chemical yields, with wide impact e.g. on the characterisation and ensemble studies of exoplanets, on evolutionary population synthesis, integrated colours and thus ages of galaxies.

The overall outcome of this work has proven Asteroseismic Inference on a Massive Scale to be a flexible, high precision stellar parameter determination program, fit for use to bring tighter constraints to the determinations of stellar parameters through robust asteroseismic analysis and grid modelling for both dwarf and giant stars. Its flexibility and open-source nature makes AIMS a suitable starting point for the development of the pipelines of future missions such as PLATO (Rauer et al. 2014). Moreover, its output can also be used for additional seismic investigations with for example non-linear inversion techniques as developed by Roxburgh (2002) or linear inversions of structural indicators (Reese et al., 2012; Buldgen et al., 2015, 2018b).

Chapter 6

Eclipsing Binary Stars and Open Clusters with AIMS

This chapter is an extension of the work of Buldgen et al. (2018), of which I was second author. The properties of the eclipsing binary stars are taken from this work, of which I contributed to the analysis with AIMS*. Individual mode frequencies for all of the stars in this chapter were provided by Guy Davies. The description of these data in chapter 6.2 is taken from Buldgen et al. (2018). All of the grids of models and analysis presented in this chapter are my own work. The description of the grid input parameters in chapter 6.3 follows largely the description in section 3 of Rendle et al. (2019), and chapter 5.3 of this work.*

6.1 Introduction

The previous chapter examined the use of AIMS as a research tool with asteroseismology. Despite showing excellent results and analysis capabilities, the test sample was limited to artificial data and an initial analysis of the Sun. Though ample to demonstrate how the code operates and what levels of precision one can expect to achieve, further testing with real observational data is necessary to truly demonstrate the capability of AIMS. Works by (Buldgen et al., 2018b; Nsamba et al., 2018) have started to explore the influence of systematics induced from parameters

such as the mixing length and surface-effects corrections on the final precision and accuracy of the results. In this chapter, we take the test of AIMS one step further. The properties of RGB stars inferred by AIMS are tested against independent constraints to determine the reliability of AIMS for the analysis of evolved stars. In addition, we examine the influence of the surface-effect correction used in the final parameter fits and how well the code is able to reproduce the observed frequencies.

In Rendle et al. (2019), the Sun was nominally chosen as an observational test case because of its comprehensively constrained and defined physical parameters from helioseismology and independent constraints on the solar radius, mass and age. There are no other stars for which we have such a comprehensive understanding, but this does not mean we do not have reliable measurements to which comparisons can be made. Stellar systems with parameters measured by methods other than asteroseismology, and those subject to multiple previous studies, will allow for an independent verification of the results returned by AIMS. Comparisons to such values achieved with both asteroseismology and independent methods will allow for greater understanding of any systematics between methods, and even possibly between the use of the asteroseismic scaling relations and the individual mode frequencies.

The *Kepler* field is an excellent source of well characterised RGB stars with asteroseismic oscillation detections. With a baseline of $\sim$ 4 years, it is possible to extract frequencies with uncertainties of order 10^{-2} μHz. Here, we focus on two different sets of stars: eclipsing binaries and open cluster members. The challenge is to test the asteroseismic mass and radius determinations down to a few percent, though. The only systems where this is possible for both mass and radius of individual stars are eclipsing binary (EB) systems. Stars in open clusters also provide adequate opportunity to do this. Clusters consist of stars with supposedly the same age, meaning approximately the same mass on the RGB, providing a statistical advantage over single star analysis. A final uncertainty on the mean mass of RGB stars will be $\sqrt{N}$ smaller than for a single star, allowing for high precision measurements

for comparison.

Making high precision determinations has limitations, particularly when performing analyses with grid modelling. Our understanding of how to correctly model the internal physics of star is at present incomplete. This means that often corrections or assumptions must be applied to the models in order for them to be representative of the observations. One of the challenges encountered when modelling oscillation frequencies is the known offset between the the modelled and observed frequencies. This was first discovered in the Sun due to offsets between the modelled and independently verified mass and radius (e.g. Christensen-Dalsgaard et al. 1988; Dziembowski et al. 1988; Christensen-Dalsgaard & Thompson 1997). The offset arises from improper modelling of the near-surface layers of the stellar atmosphere. Typically, mixing length theory is used to model convection. This leads to an inaccurate description of convection close to the surface. In addition, effects such as the interaction between the oscillations and magnetic fields, non-adiabatic effects and effects due to turbulent pressure, are often neglected due to the complexity of the modelling required. The influence of these additional components leads to an effect that is not properly accounted for within the models, and requires a correction if the model frequencies are to be compared to observed frequencies. There are multiple prescriptions available to use to correct for the surface-effect. Within AIMS, the corrections provided by Kjeldsen et al. (2008), Ball & Gizon (2014) and Sonoi et al. (2015) are available to use. In some cases, there are multiple options to use for each surface-effect correction, all of which are detailed below and the equations for which can be found in Table 6.1:

Kjeldsen et al. (2008) (K08): A solar-calibrated power law is used to describe the offset in frequencies. An exponent, b, is hard coded in AIMS to be 4.9 as determined in their work. This value of b has been widely adopted (see e.g. Metcalfe et al. 2010; Van Eylen et al. 2012; Gruberbauer et al. 2013), but the value of the exponent can vary depending upon the input physics used (e.g. Deheuvels et al. 2014; Ball &

Gizon 2017). Two options are used to determine the K08 surface correction here. The first, K08a, uses the hard coded exponent 4.9 as recommended by K08. The second, K08b, uses a scaling relation based on Sonoi et al. (2015) to determine the exponent.

Sonoi et al. (2015) (S15): The surface correction determined by S15 is an extension to the power law determined by K08. S15 found the K08 correction inadequate for fitting to frequencies in the high-frequency range. This was found to be due to the frequency difference, $\delta\nu$, profile, which becomes shallower as the frequencies increase above $\nu_{\rm max}$. The authors propose an alternative Lorentzian function, which was found to be a superior fit to K08 across the entire frequency range. It should be noted that the function proposed by S15 reduces to the relation proposed by K08 when $\nu \ll 1$, and is also a parametric expression inspired by the Sun. Three instances of the S15 relation are used in this work. S15a and S15b follow K08a and K08b, with a predetermined exponent, b, and one determined from the S15 scaling relation (albeit with different coefficients). The third correction, S15c, leaves the exponent as a free parameter to be determined.

Ball & Gizon (2014) (BG14): The BG14 corrections are based on the findings of Gough (1990) and Goldreich et al. (1991), who argue that perturbations caused by a magnetic field would cause changes in the frequencies proportional to ν^3/I, where I is the mode inertia. They also argue that a change in the description of convection is expected to lead to an alteration proportional to ν^{-1}/I. BG14 put forward two corrections, one containing only the cubic term (BG14a) and another that is a linear combination of the two terms (BG14b).

Table 6.1: Surface-effect correction equations and exponents as used in AIMS.

Surf. Corr.	Function	b_{AIMS}
BG14a	$a\nu^3/I$	-
BG14b	$\left(a\nu^{-1} + b\nu^3\right)/I$	-
K08	$a\nu^b$	4.9
S15	$a\left(1 - \left(1 + \nu^b\right)^{-1}\right)$	4.0

Recent works by Ball & Gizon (2017); Basu & Kinnane (2018); Compton et al. (2018); Li et al. (2018) have all looked at the relative performance of the surface corrections. The focus of these studies have predominantly been on artificial models, MS or sub-giant stars. Hence, it is important to understand the effects the corrections may have on the overall fitting of the stellar parameters for RGB stars. Consequently, we look at the effect of each correction (including not applying one) on the masses, radii and mean densities of a sample of eclipsing binary stars prior to examining the influence of the surface correction on the parameter fits for cluster members in NGC6791 and NGC6819.

6.2 Targets

A total of 51 stars were selected for the analysis (5 eclipsing binaries, 46 cluster members). All of the stars are situated on the red-giant branch and have been the subject of previous asteroseismic studies. Information regarding the targets is presented in the sections that follow. The asteroseismic information obtained for use in AIMS was extracted using a single methodology for all stars. The mode frequencies were estimated by performing bespoke mode fitting to each of the stars. Using the full set of available *Kepler* photometric data, we computed the estimate of the frequency power spectrum following García et al. (2011). We located the modes of oscillation using visual inspection and determined the mode identification (i.e., selected the radial and quadrupole modes). We also checked the consistency of the

detection with existing red giant measurements following Davies & Miglio (2016). In order to determine the frequencies for the radial modes, we fitted each pair of radial and quadrupole modes with a sum of Lorentzians. For full details of the mode fitting method, we refer to Davies et al. (2016). For the binary targets, due to their nature we have not applied a frequency correction to the mode frequencies normally applied to remove the Doppler shift as a result of the line-of-sight velocity (Davies et al., 2014b). In the case of the cluster members, the frequency correction has been applied and was found to be of order $5 - 20$ nHz as a linear trend of ν. Between $4 - 10$ modes were available for the stars.

6.2.1 Eclipsing Binary Stars

The sample of binary stars used is that of Buldgen et al. (2018b) (hereafter B18). The sample consists of 5 double-line spectroscopic binaries: KIC5786154, KIC7037405, KIC8410637, KIC8430105 and KIC9970396. The binary stars of B18 were all previously studied by Gaulme et al. (2016) (G16), with 2 of the sample also studied by Brogaard et al. (2018) (Br18). Both G16 and Br18 calculated the stellar properties from the radial-velocity (RV) and astrometric studies of the systems. Both G16 and Br18 compared their derived physical parameters to those determined from corrected asteroseismic scaling relations (e.g. Mosser et al. 2013; Sharma et al. 2016; Brogaard et al. 2018). G16 found the masses and radii to be overestimated by (15.4 $\pm$ 10.9)% and (5.1 $\pm$ 3.0)% respectively. Br18 tested against the dynamical masses and radii using corrections to the $\Delta\nu$ scaling relation as theoretically predicted by Rodrigues et al. (2017). In contrast to G16, they found agreement between the dynamical and corrected asteroseismic scaling relation masses and radii. Importantly, the masses and radii determined from the eclipse and RV data for the two stars common to both works are also consistent to within 2σ. B18 further developed the analysis of the binary systems, using AIMS to determine models for use in mean density inversions (see e.g. Roxburgh 2002; Reese et al. 2012; Buldgen et al. 2015,

Table 6.2: EB stellar properties. Where EBs have been observed by both G16 and Br18, the rows relating to these analyses are denoted by (G) and (B) respectively. Where possible, the G16 APOGEE values of [Fe/H] were used.

KIC	Mass [$M_\odot$]	[Fe/H]	Radius [$R_\odot$]	$T_{\rm eff}$ [K]
KIC5786154	1.06 ± 0.06	-0.06 ± 0.06	11.4 ± 0.2	4747 ± 100
KIC7037405 (G)	1.25 ± 0.03	-0.13 ± 0.06	14.1 ± 0.2	4516 ± 36
KIC7037405 (B)	1.17 ± 0.02	-0.27 ± 0.10	14.00 ± 0.09	4500 ± 80
KIC8410637	1.56 ± 0.03	0.16 ± 0.03	10.7 ± 0.1	4800 ± 100
KIC8430105	1.31 ± 0.02	-0.43 ± 0.08	7.65 ± 0.05	5042 ± 68
KIC9970396 (G)	1.14 ± 0.02	-0.18 ± 0.07	8.0 ± 0.2	4916 ± 68
KIC9970396 (B)	1.18 ± 0.02	-0.35 ± 0.10	8.04 ± 0.07	4860 ± 80

KIC	$\nu_{\rm max}$ [μHz]	$\Delta\nu$ [μHz]	Density [$10^{-3}\rho_\odot$]
KIC5786154	29.75 ± 0.16	3.52 ± 0.01	0.71 ± 0.02
KIC7037405 (G)	21.75 ± 0.14	2.79 ± 0.01	0.45 ± 0.01
KIC7037405 (B)	21.75 ± 0.14	2.79 ± 0.01	0.43 ± 0.01
KIC8410637	46.00 ± 0.19	4.64 ± 0.02	1.26 ± 0.06
KIC8430105	76.70 ± 0.57	7.14 ± 0.01	2.93 ± 0.03
KIC9970396 (G)	63.70 ± 0.16	6.32 ± 0.01	2.2 ± 0.1
KIC9970396 (B)	63.70 ± 0.16	6.32 ± 0.01	2.3 ± 0.7

2018b). The output masses and radii were only briefly discussed, with the accuracy of the inversion the main focus of the paper. Here, we look to develop this further, looking more closely at final parameters output from AIMS and comparing to the outputs of G16, Br18 and B18 respectively.

Table 6.2 shows the parameters obtained by G16 and Br18 for the masses, radii and mean densities of each star. The values of $\nu_{\rm max}$ and $\Delta\nu$ presented in G16 are included. These values were obtained using the DIAMONDS (Corsaro & De Ridder, 2014a,b) code to analyse the power spectra. The asteroseismic parameters of G16 were also adopted by Br18 in their analysis. Comparing the values returned by G16 and Br18 for the same stars, is apparent that there is some considerable variation in mass and [Fe/H] for KIC7037405 and KIC9970396. The difference demonstrates that no only should we be seeking to improve the asteroseismic determinations, but continued improvements in the accuracy of the spectroscopic and dynamical measurements are required.

6.2.2 Clusters

Two of the open clusters from the *Kepler* field were studied: NGC6791, NGC6819. Both clusters have been subjected to multiple asteroseismic studies (e.g. Stello et al. 2010; Basu et al. 2011; Hekker et al. 2011; Stello et al. 2011; Wu et al. 2014; Miglio et al. 2015; Corsaro et al. 2017; Handberg et al. 2017; McKeever et al. 2019) and have broadly different properties to each other. Table 6.3 shows the mean properties of the two clusters. It is clear from the table that the global parameters of the clusters vary greatly with respect to the expected mean mass of the RGB stars ($\langle M_{RGB} \rangle$) and metallicity ([Fe/H]) ranges. NGC6791 is a low $\langle M_{RGB} \rangle$, relatively old, super-solar metallicity cluster, whereas NGC6819 is more massive $\langle M_{RGB} \rangle$, of solar metallicity and young. The broad spread in parameter space that the clusters cover in mass, metallicity and age provides an excellent test of AIMS to analyse a variety of models.

Table 6.3: Mean parameters for the open clusters. Mean RGB mass and apparent distance moduli taken from studies of EBs by Brogaard et al. (2012) for NGC6791 and by Jeffries et al. (2013) and Sandquist et al. (2013) for NGC6819.

Cluster	$\langle M_{RGB} \rangle$ [$M_\odot$]	[Fe/H]	$(m - M)_V$	Age [Gyr]
NGC6791	1.15 ± 0.02	0.29 ± 0.1	13.51 ± 0.06	~ 8
NGC6819	1.55 ± 0.06	0.09 ± 0.1	12.42 ± 0.07	~ 2

The full sample of stars for each cluster are not tested here. We select stars for NGC6791 from Basu et al. (2011) and for NGC6819 from Handberg et al. (2017). Stars that appear over-massive, are not cluster members or lay outside the constraints of the grid (see below) were rejected from the samples. Sample sizes of 34 and 12 were used for NGC6791 and NGC6819 respectively.

Table 6.4: Properties of cluster members used in this work for NGC6819. Uncertainties on T_{eff} and [Fe/H] are 100K and 0.1 dex respectively. Values taken from Handberg et al. (2017).

KIC	Radius [$R_\odot$]	Mass [$M_\odot$]	T_{eff} [K]	[Fe/H]
5111940	10.21 ± 0.16	1.62 ± 0.06	4718.0	0.11
5112744	11.33 ± 0.21	1.63 ± 0.07	4643.0	-0.11
5024312	7.55 ± 0.10	1.60 ± 0.05	4795.0	-0.02
5113041	11.86 ± 0.23	1.54 ± 0.07	4587.0	0.03
5024143	6.60 ± 0.09	1.55 ± 0.06	4876.0	-0.09
5024583	12.43 ± 0.16	1.68 ± 0.06	4609.0	0.13
5113441	5.85 ± 0.06	1.58 ± 0.05	4837.0	0.20
5111718	6.31 ± 0.07	1.60 ± 0.05	4914.0	0.03
5112948	11.86 ± 0.18	1.75 ± 0.07	4643.0	0.02
5112072	6.47 ± 0.07	1.57 ± 0.05	4901.0	0.03
5024512	8.51 ± 0.13	1.57 ± 0.06	4740.0	-0.01
5024405	7.13 ± 0.09	1.43 ± 0.05	4714.0	-0.13

Table 6.5: Properties of cluster members used in this work for NGC6791. Uncertainty on T_{eff} is 100K. Values taken from Basu et al. (2011).

KIC	Radius [$R_\odot$]	Mass [$M_\odot$]	T_{eff} [K]
2435987	10.60 ± 0.50	1.21 ± 0.13	4355
2436097	10.50 ± 0.47	1.36 ± 0.13	4365
2436209	9.30 ± 0.25	1.45 ± 0.09	4493
2436332	12.49 ± 0.50	1.24 ± 0.10	4304
2436458	10.47 ± 0.36	1.05 ± 0.08	4340
2436540	8.81 ± 0.28	1.27 ± 0.11	4448
2436688	7.64 ± 0.27	1.31 ± 0.13	4530
2436814	12.55 ± 0.51	1.08 ± 0.10	4289
2436818	6.43 ± 0.51	1.22 ± 0.15	4545
2436824	10.98 ± 0.40	1.06 ± 0.09	4324
2436900	10.87 ± 0.55	1.19 ± 0.18	4402
2437240	9.83 ± 0.35	1.26 ± 0.11	4440
2437270	8.56 ± 0.19	1.47 ± 0.07	4499
2437325	6.69 ± 0.18	1.20 ± 0.11	4557
2437340	23.40 ± 2.90	1.26 ± 0.55	4007
2437402	9.76 ± 0.39	1.23 ± 0.10	4414
2437444	15.32 ± 1.01	1.26 ± 0.16	4186
2437488	8.38 ± 0.29	1.30 ± 0.12	4452
2437507	15.60 ± 0.75	1.40 ± 0.16	4246
2437653	7.79 ± 0.24	1.30 ± 0.10	4482
2437781	7.05 ± 0.26	1.21 ± 0.10	4456
2437816	15.88 ± 1.23	1.28 ± 0.22	4215
2437933	6.44 ± 0.47	1.34 ± 0.16	4610
2437957	6.56 ± 0.29	1.13 ± 0.16	4602
2437972	7.05 ± 0.28	1.21 ± 0.12	4543
2437976	6.94 ± 0.15	1.23 ± 0.06	4525
2438038	8.06 ± 0.21	1.08 ± 0.09	4450
2438140	7.56 ± 0.47	1.15 ± 0.21	4543
2438333	8.64 ± 0.33	1.30 ± 0.15	4501

6.3 Grids

The CLÉS and LOSC stellar evolution and oscillation codes were used to generate a new set of grids. Again, we use the Grevesse & Noels (1993) abundances, nuclear reaction rates of Adelberger et al. (2011), opacities of Iglesias & Rogers (1996), the FreeEOS equation of state (Irwin, 2012) and model atmospheres of Vernazza et al. (1981). The mixing-length parameter was kept to a solar calibrated value of 1.67 and a convective overshoot of 0.05 times the local pressure scale height was used, assuming instantaneous chemical mixing and the radiative temperature gradient in the overshooting region. Despite the improvements observed when modelling the Sun, microscopic diffusion was not included in the grid. The border of the convective zones was calculated following the guidelines of Gabriel et al. (2014) to avoid spurious solutions for the evolution of convective cores. As per Rendle et al. (2019), only the radial mode frequencies ($l = 0$) were computed for each model, with modes of radial order $n = 0 - 30$.

Seven grids are used in this work - one per binary system and cluster. Considering the broad parameter mass and metallicity scales of the targets, it was judged that the creation of a series of smaller grids would prove faster to compile and test than generating a large, single grid which incorporates all of the target stars. Each grid was parameterised by mass (steps of 0.01 $M_{\odot}$) and [Fe/H] (steps of 0.1 dex). The [Fe/H] range of the grid was determined by the [Fe/H] of the star/cluster, and extending the parameter range in either direction by $\pm 2\sigma$. This is extended to 3σ for the cluster grids to account for variability between cluster members.

After models were generated, the oscillations were only computed for stars with a core-Helium mass of greater than 0.05 $M_{\odot}$. This was enforced to ensure that only RGB models were saved out to the final grid and to reduce frequency computation time. The default timestep parameters was used to save out models with CLÉS. The default setting uses a variable timestep.

Table 6.6: The values of mass and [Fe/H] attributed to the grid of models. Number of tracks in the grid (N_{tracks}) is also shown.

Grid	Mass [$M_\odot$]	[Fe/H]	N_{tracks}
KIC5786154	1.0−1.50	-0.25−0.15	255
KIC7037405	1.10−1.45	-0.45−-0.05	180
KIC8410637	1.40−1.90	0.05−0.45	255
KIC8430105	1.20−1.65	-0.7−-0.3	230
KIC9970396	1.00−1.40	-0.55−-0.15	205
NGC6791	1.05−1.35	0.2−0.5	217
NGC6819	1.40−1.75	-0.3−0.3	252

6.4 Analysis

6.4.1 Eclipsing Binaries

A total of ten analysis runs were performed on the binary stars. For consistency with B18, only the effective temperature and [Fe/H] values for the stars were included as classical constraints for all tests. Below are the details of the surface-effects corrections used for each run and information regarding any additional constraints included in the input file:

(i) B14a
(ii) B14b
(iii) K08a
(iv) K08b
(v) S15a
(vi) S15b
(vii) S15c
(viii) None
(ix) B14b + L_{Gaia}, $\nu_{\rm max}$
(x) B14b + $\nu_{\rm max}$

The B14b correction was used in the solar analysis in the previous chapter, hence, for consistency, it is used in cases (ix) and (x) where the effect of different classical constraints is being explored, rather than the impact of the choice of surface-effect correction.

6.4.1.1 Frequency Determination

The main aspect of the analysis influenced by the surface-effects corrections is the mapping of the model frequencies to the original observed frequencies. It is expected that as the frequencies increase, the divergence between the model and observed fre-

quency also increases. The difference is typically non-linear and shows as a power law (hence the functional form of the corrections). Figure 6.1 illustrates the frequency differences for each of the corrections. It is evident how the magnitude, and sign, of the percentage correction is dependent upon the correction used, and subsequently the model on which the analysis is based. Figure 6.1 shows that despite the variance in magnitude of the correction, each variation appears to map the frequencies closely back to the observed. Some fluctuations and trends with frequency (BG14a, S15a/b in particular) are observed, but overall the corrections return frequencies apparently consistent with observations.

At ν_{max}, one can usually expect a deviation of order $< -1\%$ ($\nu_{obs.} - \nu_{theo.}$) for a model well suited to the observational data. Offsets greater than this, or that are positive (model frequencies are usually over-predicted) are indicative of poor model selection, forcing the surface correction to dominate the fit in order to be representative of the observation. Table 6.7 displays the percentage difference between the observed and uncorrected model frequencies at ν_{max}. The difference between the frequencies fluctuates from star-to-star, as well as varying between corrections. Though the frequencies used in the comparison have not been corrected, the type of correction used will influence the selection of models from the grid, giving rise to the variance between corrections. Both the BG14 and K08 corrections lead to the selection of model frequencies that typically lay within the expected percentage deviation. The fits assuming S15 corrections do not perform as well, with differences in excess of -1.5%. In particular, the S15b correction shows large deviations, of which the values are almost all positive. This indicates that the correction is consistently selecting poor models that underestimate the observed frequencies.

Though only KIC5786154 is shown here, the same figures were generated for the other binary stars. The K08a and K08b corrections show increased variance on a star-by-star basis, but the remainder show similar characteristics to the trends shown in Fig. 6.1. To determine which correction was the most consistent for the

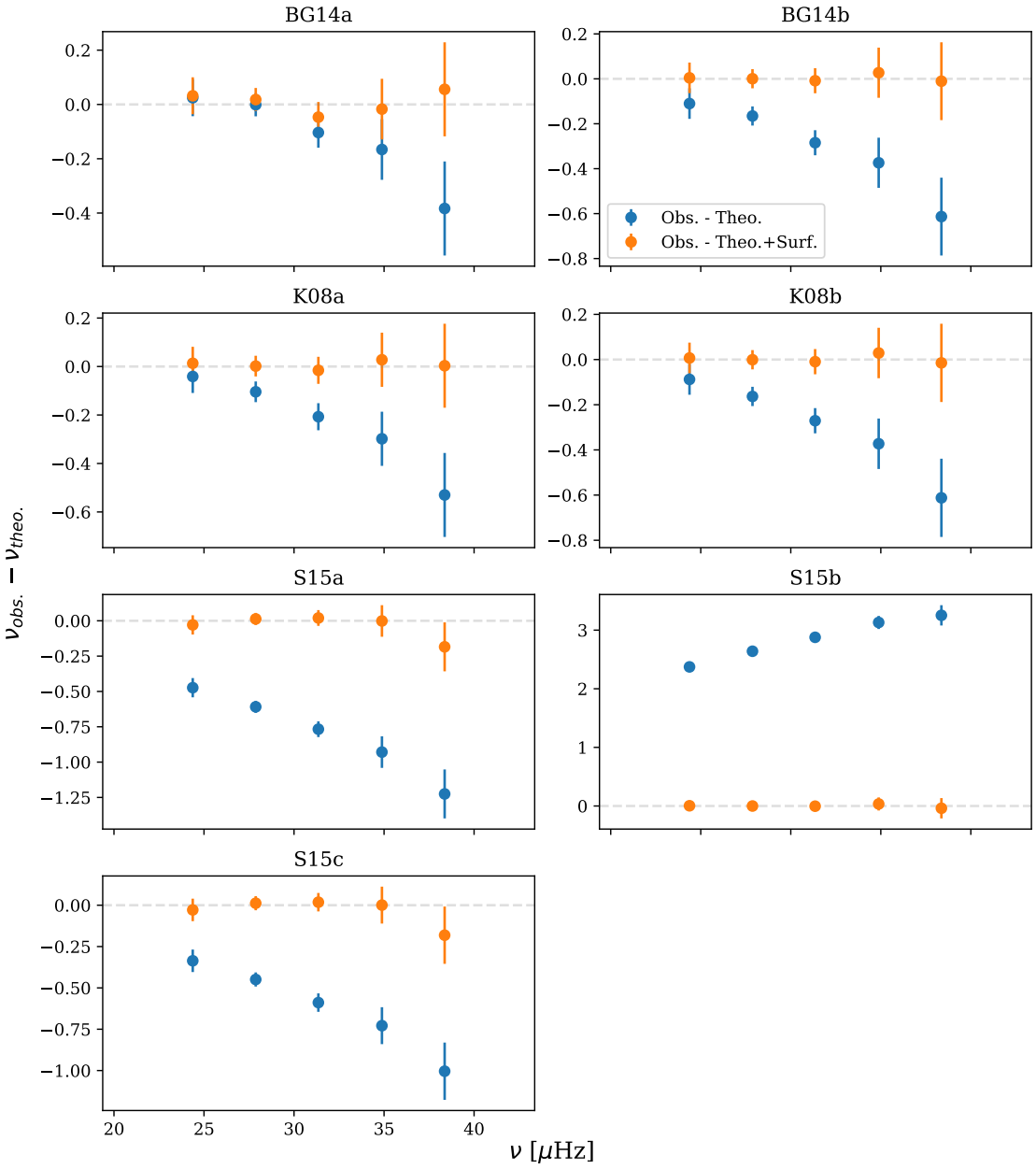

Figure 6.1: Difference between the observed frequencies ($\nu_{obs.}$) and model frequencies ($\nu_{theo.}$) returned by the best MCMC model for each surface-effect correction. Blue denotes the difference between the observed and non-corrected model frequencies. Orange shows the difference between the observed and surface-effect corrected frequencies. Observational uncertainties shown, and inflated by a factor of 5.

sample, the reduced χ^2 ($\chi^2_{\rm red.}$) value for the fit of the corrected model frequencies to the observed frequencies was determined as per Eq. 6.1,

$$\chi^2_{\rm red.} = \frac{1}{\rm N_{obs}} \sum_{i}^{\rm N_{obs}} \left(\frac{\nu_{obs,i} - \nu_{corr.,i}}{\sigma_{obs,i}} \right)^2 \tag{6.1}$$

for each star and corrections. The results are shown in Table 6.8. The smallest χ^2 is consistently returned for the BG14b correction. Though the S15b correction also returns consistently small $\chi^2_{\rm red.}$ values, the scale over which the correction typically occurs is much larger than for BG14b ($\sim$ 4% and $\sim$ 1% shifts at $\nu_{\rm max}$). Considering the relative stability of the correction across the binaries of different mass and metallicity, we adopted the BG14b correction for the analysis of the cluster stars.

Table 6.7: Percentage difference at $\nu_{\rm max}$ between the observed and surface-effect corrected frequencies.

Surf. Corr.	KIC5786154	KIC7037405	KIC8410637	KIC8430105	KIC9970396
BG14a	-0.45	-0.44	-0.20	0.16	-0.27
BG14b	-1.21	-1.30	-0.89	-0.60	-0.88
K08a	-0.81	-0.75	-0.45	0.09	-0.52
K08b	-1.02	-1.02	-0.55	-0.32	-0.74
S15a	-2.57	-2.12	-1.31	-1.13	-1.50
S15b	10.00	3.62	2.09	-0.36	4.94
S15c	-1.97	-1.99	-0.99	-1.09	-1.28

Table 6.8: $\chi^2_{\text{red.}}$ values for all EBs in the sample for each surface-effect correction used.

Surf. Corr.	KIC5786154	KIC7037405	KIC8410637	KIC8430105	KIC9970396
BG14a	0.25	1.85	2.77	14.31	4.17
BG14b	0.06	0.01	0.13	0.43	0.10
K08a	0.25	0.56	2.94	25.46	2.18
K08b	0.04	0.14	2.49	23.09	0.93
S15a	3.59	0.08	0.56	3.30	2.93
S15b	0.03	0.08	0.22	1.38	0.0014
S15c	3.57	0.11	0.09	3.58	2.57

6.4.1.2 Parameter Comparisons

Figure 6.2 presents the fractional difference between the dynamical parameters of G16 and Br18, and the asteroseismic parameters determined with AIMS. The difference is shown for all surface correction options. It obvious from a first glance that there is variability between the final parameters depending upon the correction used. In the majority of cases, these options are clustered together and consistent, but some outliers are present. The option where no surface-effect correction is selected has also been included (purple). Across each of the parameters shown in Fig. 6.2, this option consistently returns the largest fractional difference between the AIMS and dynamical value, and is therefore not considered in the analysis. The application of BG14a (dark blue) is typically the furthest from the dynamical values for KIC8410637 and KIC8430105. The K08a correction is also inconsistent with G16 for KIC8430105. The mass and radii of KIC9970396 determined using the S15b correction in comparison to the Br18 values is another example of a weaker comparative fit. As is the S15c fit for ν_{max} for KIC578654 and both comparisons of KIC9970396.

Reassuringly, the largest offsets are consistent with the $\chi^2_{\text{red.}}$ values for each star. The BG14a, K08a, S15b and S15c corrections return $\chi^2_{\text{red.}}$ values greater than 2 in

most cases where an outlier is found. Interestingly though, the $\nu_{\rm max}$ outliers occur with S15c and not S15b, which consistently shows the greatest percentage difference at $\nu_{\rm max}$ between the observed and theoretical frequencies. This highlights the importance of the final, corrected value of the frequencies to determine the model used in the analysis. In contrast to the outliers, there is no clear 'best' correction based on the parameter determination. The BG14b correction again shows consistency though. The application of the BG14b correction (green) consistently returns parameter values near the centre of the correction distributions, appearing more robust to star-by-star variation.

Considering the apparent stability of the BG14b correction, two more runs were performed using this correction. Additional constraints were applied to the observation file. A first run including $\nu_{\rm max}$ among the constraints was performed, and a second including $\nu_{\rm max}$ and the luminosity of the star. These are coloured light blue and pink respectively. The ambition was to observe if any improvement in the parameters with relation to the dynamical values could be achieved. The evidence presented by Fig. 6.2 shows negligible, if any, improvement through the addition of these constraints. The results show some variation within 1σ of the nominal BG14b test, but no significant improvement in value or uncertainty.

Comparisons to the mean density determinations of G16 and Br18 are shown in panel (D) of Fig. 6.2. Included in this panel are the values of B18 (black circles), determined by seismic inversion techniques. Overall, good agreement is shown between the dynamical and asteroseismic measurements of the stellar density. Apart from KIC7037405 (Br18), all determinations are within $\sim 1.2\sigma$ of the dynamical value. In addition, the asteroseismic determinations are all within 1σ of the B18 results. This result in particular is important as it shows consistency in the values returned by AIMS, even when different grids and techniques are used. An additional comparison is made between the mean density inferred from the large frequency separation, $\Delta\nu$ ($\Delta\nu_{\odot} = 135.1$ μHz), scaling relation and the dynamical mean densi-

ties. The fractional differences are denoted by grey, open triangles. Systematically, the values are offset lower by $\sim 5\%$ compared the values of B18 and those derived from the AIMS masses and radii. The consistency of the offset demonstrates the necessity to include a correction to the $\Delta\nu$ scaling relation. The determination of such a factor is complex as parameters such as $\nu_{\rm max}$ and $T_{\rm eff}$ have a strong influence on the correction factor (Brogaard et al., 2018).

Figure 6.2, panel (C) shows the comparisons to $\nu_{\rm max}$. The dynamical $\nu_{\rm max}$ values were determined with the $\nu_{\rm max}$ scaling relation, using the dynamical masses and radii and $T_{\rm eff}$ from spectroscopy. The solar $\nu_{\rm max}$ reference value of 3090 μHz was used. The $\nu_{\rm max}$ values from AIMS are also computed from the scaling relation, with the masses, radii and $T_{\rm eff}$ coming from the AIMS outputs. The agreement in $\nu_{\rm max}$ is not as tight as the mean density for each EB. Up to an $\sim 7\%$ offset is seen in some cases between the scaled dynamical and asteroseismic $\nu_{\rm max}$ values. However, the magnitude of the uncertainties on these values are likely slightly overestimated. As such, the largest offsets remain within $\sim 2\sigma$, showing a degree of consistency between the dynamical and asteroseismic values. The $\nu_{\rm max}$ values determined with DIAMONDS are also consistent with this trend, providing reassurance that the asteroseismic and dynamical values are consistent. Brogaard et al. (2018) show that offsets exist between the model and observed temperatures of order 100K (models typically cooler than observations), which is potential reason behind the significant offsets. Arentoft et al. (2017) also discuss the temperature offsets, with differences of 200K found to be common place. We find differences between 100-300 K for the EBs, with the models systematically cooler than the observations. It is known that the $T_{\rm eff}$ value for KIC8430105 presented in G16 is overestimated (K. Brogaard, priv.comms.), and such systematics will also influence the models selected. The largest differences in $T_{\rm eff}$ were found for KIC5786154 and KIC8410637. KIC5786154 shows the largest offset between the asteroseismic and dynamical values. Increasing the model dependent temperature derived from AIMS by 300K reduces the offset

from 7% to 2.5%. This shows the importance of being able to either correctly model stellar atmospheric properties, or understand the limitations of the methodology being used.

With the exception of the previously discussed models, the agreement between the dynamical and asteroseismic masses (panel A) is good. The majority of asteroseismic determinations are within either 5% or 1σ of the dynamical masses of both G16 and Br18. The results also show good agreement with the grid modelling results of Br18, where they made comparisons with asteroseismic masses determined by PARAM and the systematics shown by G16 were no longer present. The same trend is also observed for the radii measurements (panel B), with the asteroseismic radii typically within 2.5% of the dynamical values.

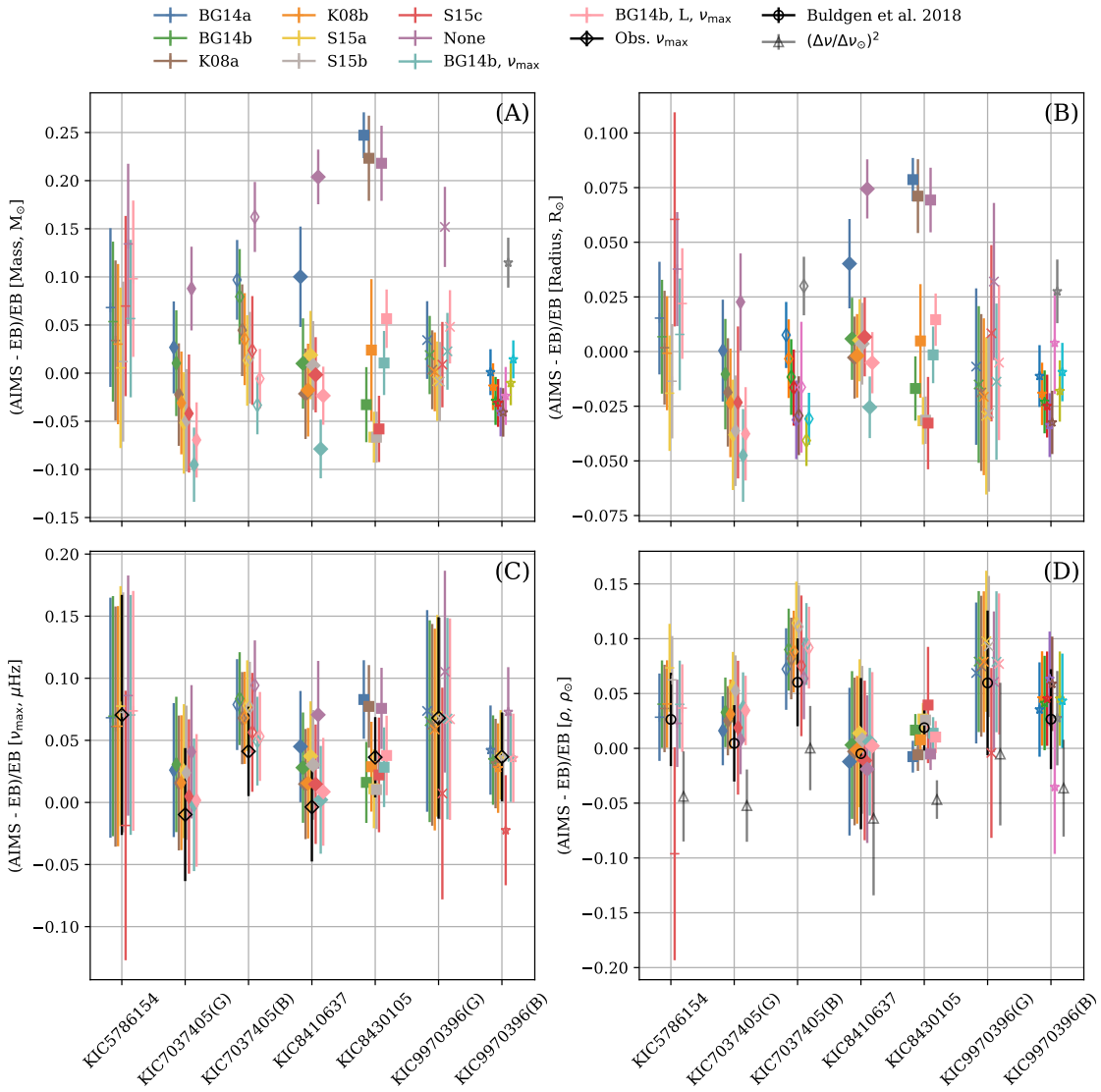

Figure 6.2: Fractional differences between the measurements of Gaulme and Brogaard for each binary. Differences in mass (A), radius (B), ν_{rmmax} (C) and mean density (D) are shown. Buldgen et al. sample included in density as main objective of their work. Literature $\nu_{\rm max}$ included in (C) for guidance (black diamonds). Where stars feature in both G16 and Br18, the comparative measurement is denoted by (G) and (B) in the KIC ID respectively.

Figure 6.3 further demonstrates how the surface correction can affect the model selection within AIMS. Though points are generally consistent within errorbars of other corrections, either a significant spread in mass or radius is observed. The trends are not consistent between stars and nor is the position of the points for each correction relative to the others. Whilst indicating that reasonable consistency can be expected between different corrections, it demonstrates that caution should

be taken when presenting final results as the surface-effect corrections can lead to parameter changes of order a few percent.

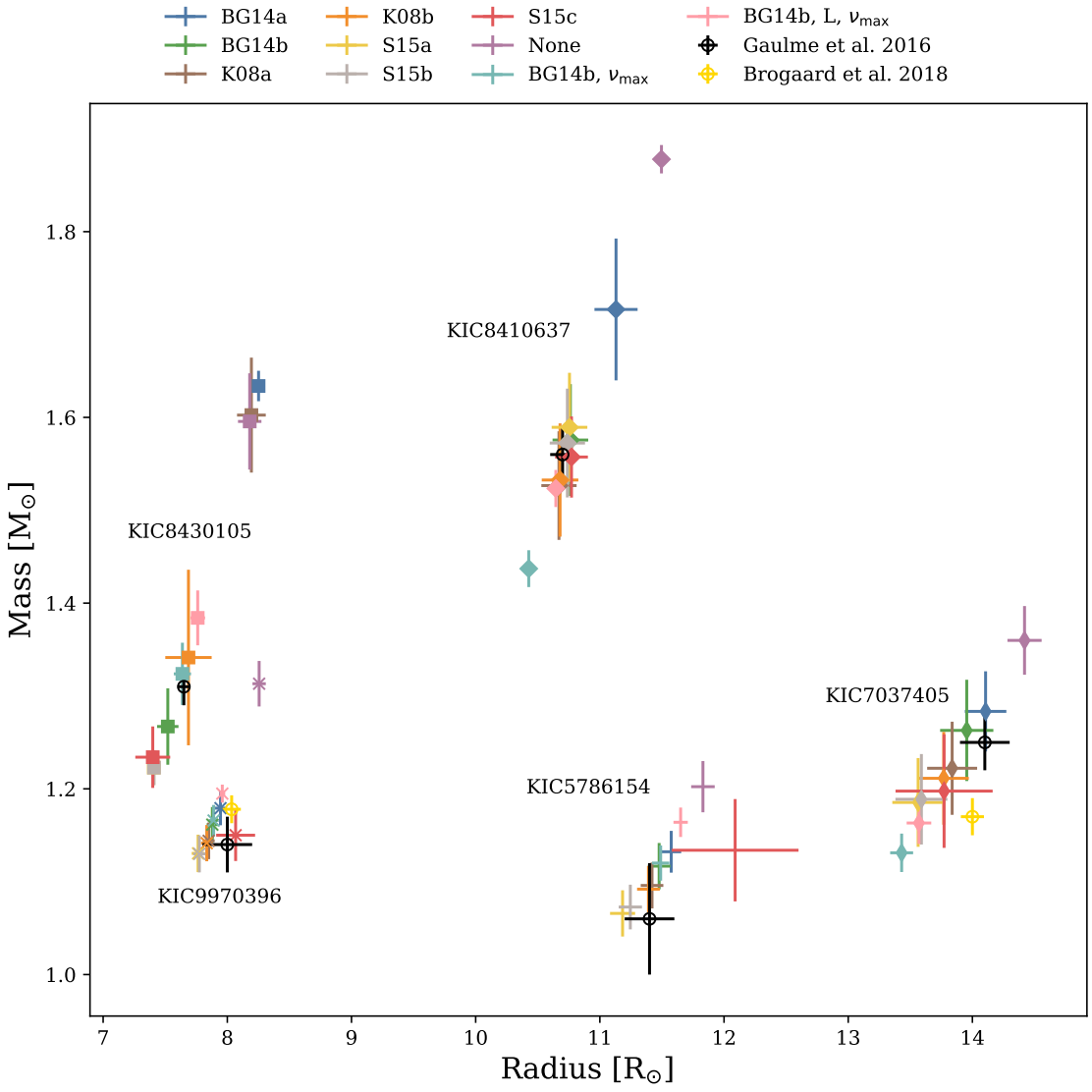

Figure 6.3: Radius vs Mass distribution of the EB stars observed. Each Eb is denoted by its identifier number and symbol. The points are coloured by the surface-effect correction used. The G16 (black stars) and Br18 (gold stars) mass and radius values are included where appropriate.

6.4.2 NGC6791 & NGC6819

The analysis performed with AIMS was much simpler for the cluster members. The BG14b surface-effect correction was applied for all stars, with $T_{\rm eff}$, [Fe/H] and $\nu_{\rm max}$ included as the classical constraints. Prior to analysing the ensemble properties

of the two clusters, based on the previous analysis in section 6.4.1.1, we explored the magnitude of the surface correction shift for each of the stars. All but 1 star in NGC6791 returned a percentage difference of approximately -0.5 to -1. In this instance, a positive value was returned. 25% of the stars in NGC6819 returned differences of $\sim -5\%$. The smallest difference returned for each cluster was of order -0.5%.

As discussed, the magnitude and sign of the difference are, in most cases, -0.5% to -1.0%. Considering the wide range of differences discovered for the stars in NGC6819, we look closer at the parameter fits to determine the quality of the model selection for these stars. The selected stars are KIC5113041 and KIC5024405. The stars returned percentage differences at $\nu_{\rm max}$ of -5.36% and -0.6% respectively. Two inspections were carried out to understand the model fitting. First, the echelle diagrams for each star were examined for any distinct or unusual trends. Second, the parameter sample distribution from the MCMC run was checked to see how well the parameter space had been explored.

Figure 6.4 and figure 6.5 show the echelle diagrams for KIC5113041 and KIC5024405 respectively. The diagrams display the frequencies of the best model selected after the MCMC process has completed (dark blue), the frequencies after the surface correction has been applied (cyan) and the original observed frequencies (red). The difference between the fitting of the two stars is clear. For KIC5113041 (Fig. 6.4), the selected model frequencies are clearly a poor fit to the observed frequencies. The difference between frequencies increases as the frequencies become larger, and the surface corrected values provide an inconsistent fit to the the observed values. In contrast, there Fig. 6.5 shows that for KIC5024405, the offset in freqency between the observed and model frequencies is smaller and the barely visible surface corrected points indicate that the model has been well fitted to the observations.

As further evidence of the contrasting model fitting, the corner plots produced by AIMS for each star are shown in Fig. 6.6 (KIC5113041) and Fig. 6.7 (KIC5024405).

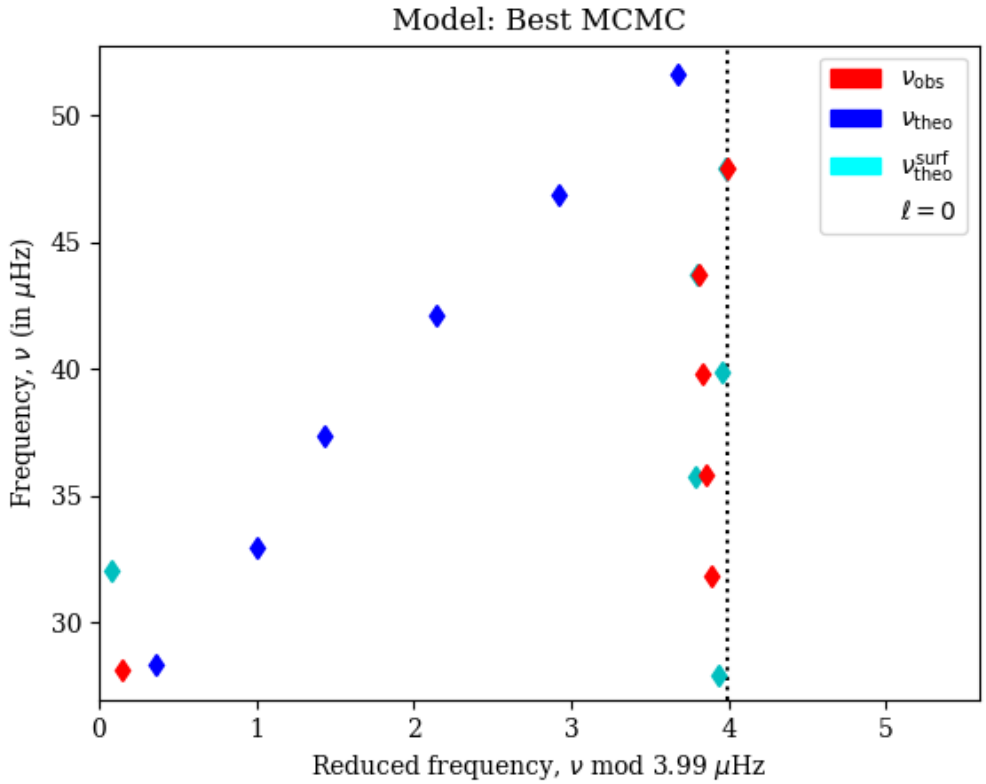

Figure 6.4: Echelle diagram for KIC5113041. The observed (red), model (blue) and surface-effect corrected model (cyan) frequencies are shown. Vertical dashed line indicates the value of $\Delta\nu$ of the star.

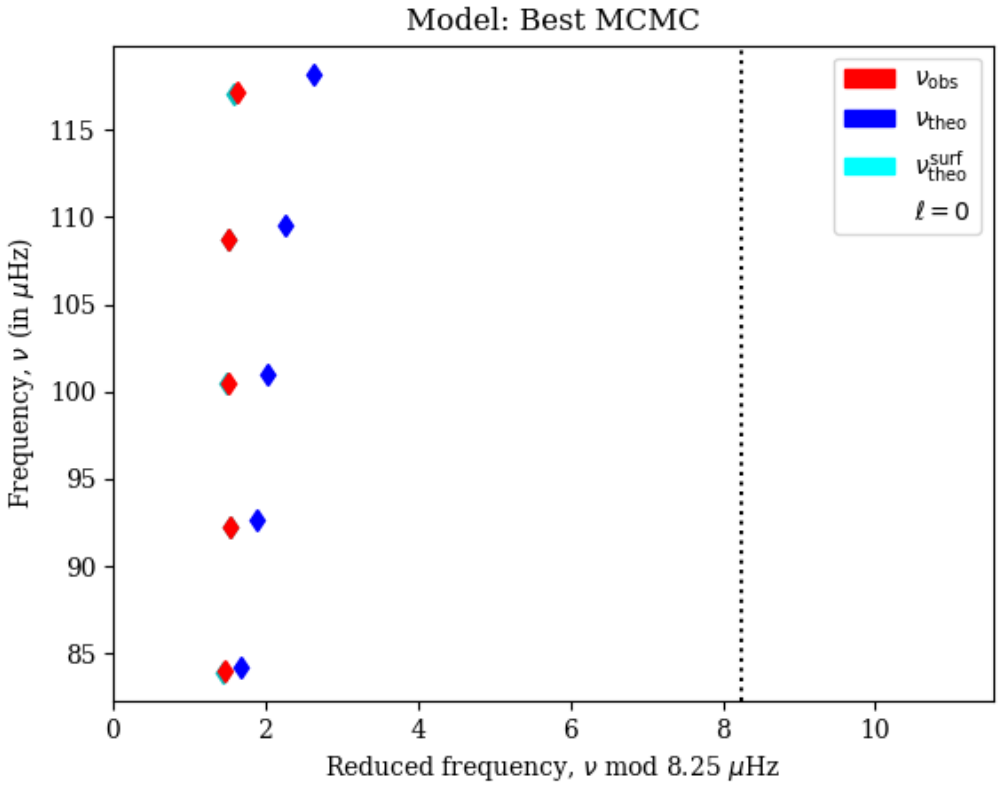

Figure 6.5: As Fig. 6.4, but for KIC5024405.

The corner plots show the density distribution of the samples taken during the MCMC run. Circularised distributions are typical indicators of well fit parameters, unless there is a correlation expected between the parameters being compared. The corner plots here show the fitting of the mass, metallicity in $\log(Z_0)$, the Helium-core mass (evolutionary tracer used) and the surface term parameters. Two surface term parameters are returned as the BG14b relation has been used.

As with the echelle diagrams, the distinction between the quality of the model fitting to the observations is clear. Though both sets of distributions show evidence of exploring the grid boundaries (in particular the lower mass bound of the grid), the sampling of the parameter space appears more uniform for KIC5024405 than KIC5113041. In particular, the mass metallicity and mass Helium-core mass distributions show a strong contrast, with the KIC5113041 distribution confined to small area of parameter space, preventing the more uniform sampling observed with KIC5024405. The model selection is key to this, with the likelihood determined for each model key to the parameter space that is explored. The surface-effect correction parameters are not predetermined and the priors on the constants are determined on the fly by the code. Consequently, the correction can influence the model determination and likelihood.

The echelle diagrams and corner plots were examined by eye for all of the stars analysed in the clusters. It was clearly evident that the quality of fit in the echelle diagram was closely related to how well the parameter space had been sampled. The stars with frequency differences of greater than $\sim |1.5|\%$ at $\nu_{\rm max}$ all showed disrupted sample distributions and poor fitting of the echelle diagram. These tests serve to show that one must always be wary of the quality of grid model fitting, even when using high quality input data. Inconsistencies between the model physics and the observations, parameters outside of the grid range and insufficient run time for the MCMC process may all be causes of the discrepancies, and should be strongly considered when using AIMS.

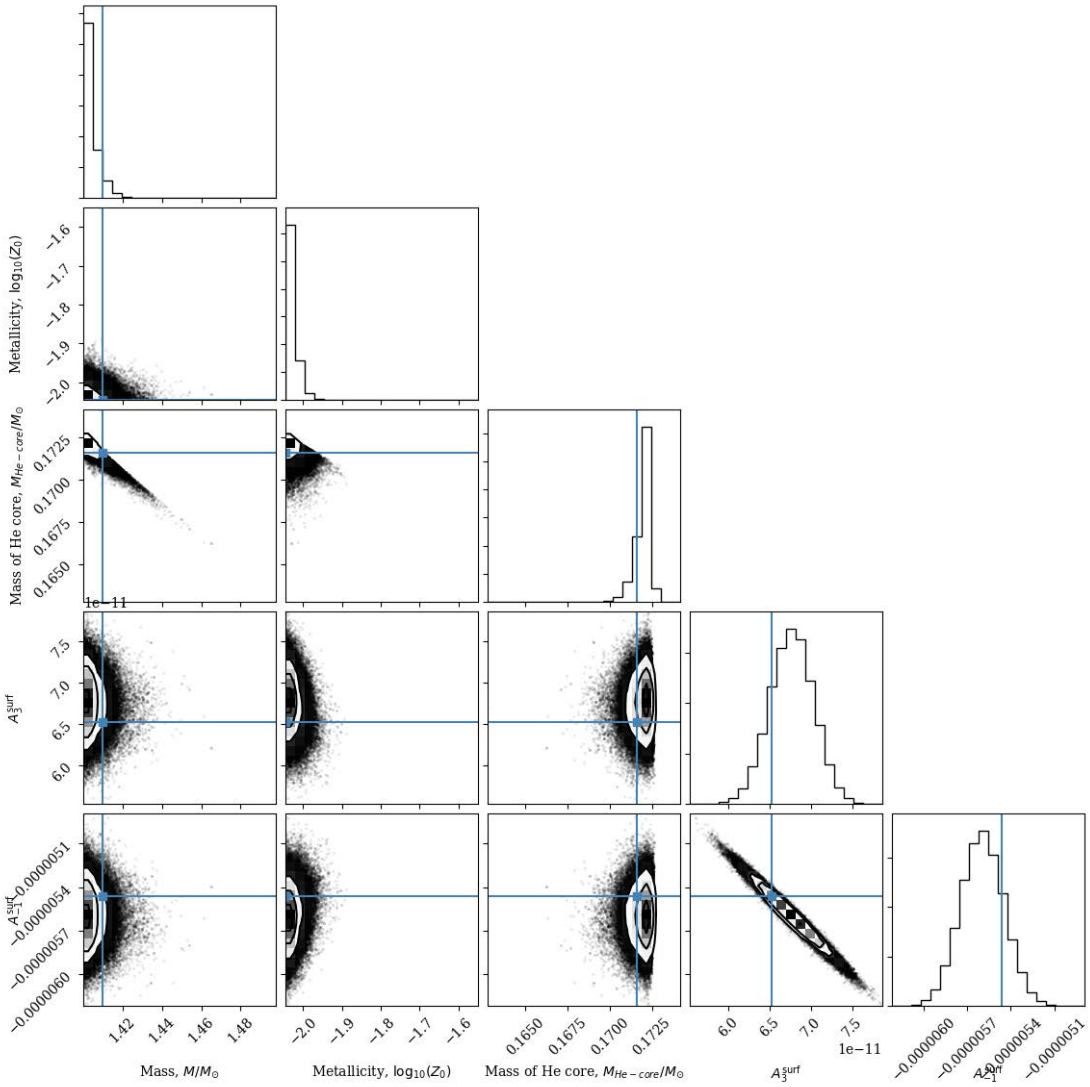

Figure 6.6: Corner plot for KIC5113041.

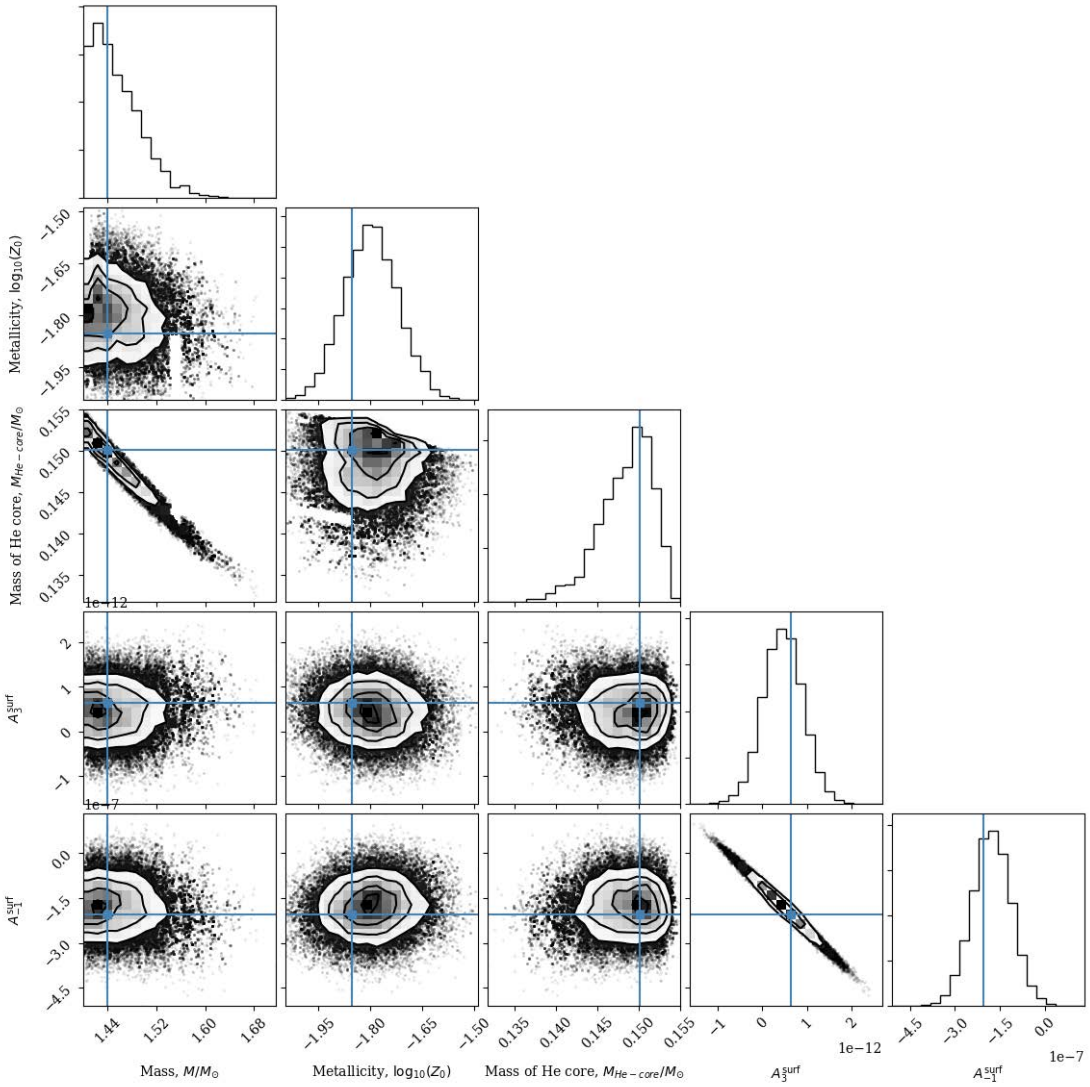

Figure 6.7: Corner plot for KIC5204405.

6.4.2.1 Cluster RGB Star Masses

The mean mass of the RGB stars for each cluster was determined using a Bayesian hierarchical model. It was assumed that the stellar masses could be drawn from a common, Gaussian distribution that describes the population[1] ($\mathcal{N}\left(\overline{M}, \sigma_M\right)$), including priors on the mean RGB mass and standard deviation from EBs. Through this method, one can obtain estimates for both $\overline{M}$ and σ_M. Using such a modelling method effectively pushes the individual mass estimates towards the population mean, reducing the scatter within the data. This provides a robust estimation of the underlying, mean population parameters.

Prior to applying the model, any stars situated on the grid boundary or differed by greater than 0.15 $M_\odot$ from expectation were removed from the data set as outliers. In the case of NGC6819, this led to the removal of 3 stars from the sample. All three stars underestimated the stellar masses (points on bottom left of Fig. 6.9; shown for completeness). The corresponding échelle diagrams showed large differences between the model and observed frequencies, and the corner diagrams indicated that the model search was restricted to the low mass grid boundary. The distributions were similar to those of KIC5113041 and therefore the fits were determined to be unrepresentative of the observations.

We found the mean RGB masses to be (1.14 ± 0.01) $M_\odot$ for NGC6791 and (1.56 ± 0.02) $M_\odot$ for NGC6819. Both of these values are consistent within in 1σ of the mean RGB masses from EBs, with similar uncertainties. In a direct comparison of mean RGB masses in the works of Handberg et al. (2017) (H17) and Basu et al. (2011) (B11), they appear lower. B11 returns a mean RGB mass of (1.20 ± 0.01) $M_\odot$ for NGC6791 and H17 (1.61 ± 0.02) $M_\odot$ for NGC6819. The B11 mean RGB mass in particular is high and in disagreement with the EBs, which is partly due to the use of scaling relations to determine the masses. This value has recently been updated in the paper of McKeever et al. (2019) as a result of their study into the

[1] Code based on example at https://github.com/grd349/PyStanExamples/blob/master/clusterfit.ipynb.

cluster Helium abundance. The RGB mass saw the B11 value revised down to (1.15 $\pm$ 0.008) $M_{\odot}$, inline with expectations from the EBs and our results. For NGC6819, only a small subsample of stars from the cluster was used, which may not truly reflect the global properties of the cluster. With this in mind, the average mass of the RGB stars in our sample was calculated using the masses derived in H17. Using only these stars and taking a simple weighted mean, the mean RGB mass was found to be (1.58 $\pm$ 0.02) $M_{\odot}$ - consistent with our results.

6.4.2.2 Distance Modulus

The distance moduli for both clusters have previously been determined using the EBs within the clusters. In Brogaard et al. (2015), the cluster distance moduli originally determined by Brogaard et al. (2012); Jeffries et al. (2013) and Sandquist et al. (2013) were recalculated using the bolometric corrections of Casagrande & VandenBerg (2014b). The mean values for each cluster are presented in Table 6.3. Using the results from AIMS, the distance modulus for each star in the sample was determined and compared to expectations of previous work. Where required, the distance modulus was calculated as per equation 6.2 (based on Eq. 10 from Torres 2010b for consistency with H17)

$$(m - M)_V = m + 2.5\log\left(L/L_{\odot}\right) - V_{\odot} - 31.572 + (BC_V - BC_{V,\odot}) \tag{6.2}$$

where m is the apparent magnitude, L the luminosity calculated from the radius and $T_{\rm eff}$, $V_{\odot}$ the V-band magnitude of the Sun (-26.76 $\pm$ 0.03), BC_V is the bolometric correction as calculated by Casagrande & VandenBerg (2014b) and $BC_{V,\odot}$ the solar bolometric correction (-0.06). The numerical constant is the solar distance modulus at 1 AU. For NGC6819, the distances were compared directly to those derived in H17. B11 does not present individual distance moduli for the candidate stars in NGC6791. Therefore, the distances were calculated using the original paper parameters. For

the AIMS distance moduli, the input parameters were the AIMS outputs for each star.

Figures 6.8 and Fig. 6.9 show the distance moduli as a function of mass for each cluster. The mean RGB mass and 1σ region for the cluster determined from the EBs is denoted, in addition to the EB cluster distance modulus. For each cluster there are two trends apparent: the distribution of masses from AIMS is more closely centred to the EB cluster mean RGB mass; the distance moduli are underestimated when using bolometric corrections determined with the log(g), [Fe/H] and $T_{\rm eff}$ from AIMS. The lower mass estimations from AIMS compared to the literature is expected considering the discussion in the previous section, where using individual mode frequencies was shown to provide better agreement with the EB mean RGB mass than using scaling relations as in B11. The distance modulus shift isn't a simple consequence of the lower mass determinations, as it can be seen that stars with higher masses predicted by AIMS than the literature still have underestimated values (see connected points on Fig. 6.8 and Fig. 6.9).

In section 6.4.1.2, a discussion of the model temperatures showed them to be cooler than expected from observations. Comparisons of the given and determined cluster temperatures found an offset of 50-150K between the observations and models. The models were again found to be on average cooler. The distance moduli using the AIMS determined parameters were then recomputed with the literature $T_{\rm eff}$ values, and again using the literature $T_{\rm eff}$ with an additional increase of 50 K (minimum offset) applied. Figure 6.10 shows the results for NGC6791. In contrast to Fig. 6.8, the distance moduli now resemble the range of values expected for the determined mass range. Applying a systematic increase in $T_{\rm eff}$ has a more significant effect than just using literature values, as it shifts the distribution of distance moduli to be centred closer to the expectation from EBs. The same impact is had on NGC6819, but the results are not shown here.

The effective temperature directly affects the luminosity ($L \propto R^2 T_{\rm eff}^4$) and Bolometric Correction (BC) calculations. Hence, it is an important quantity to determine

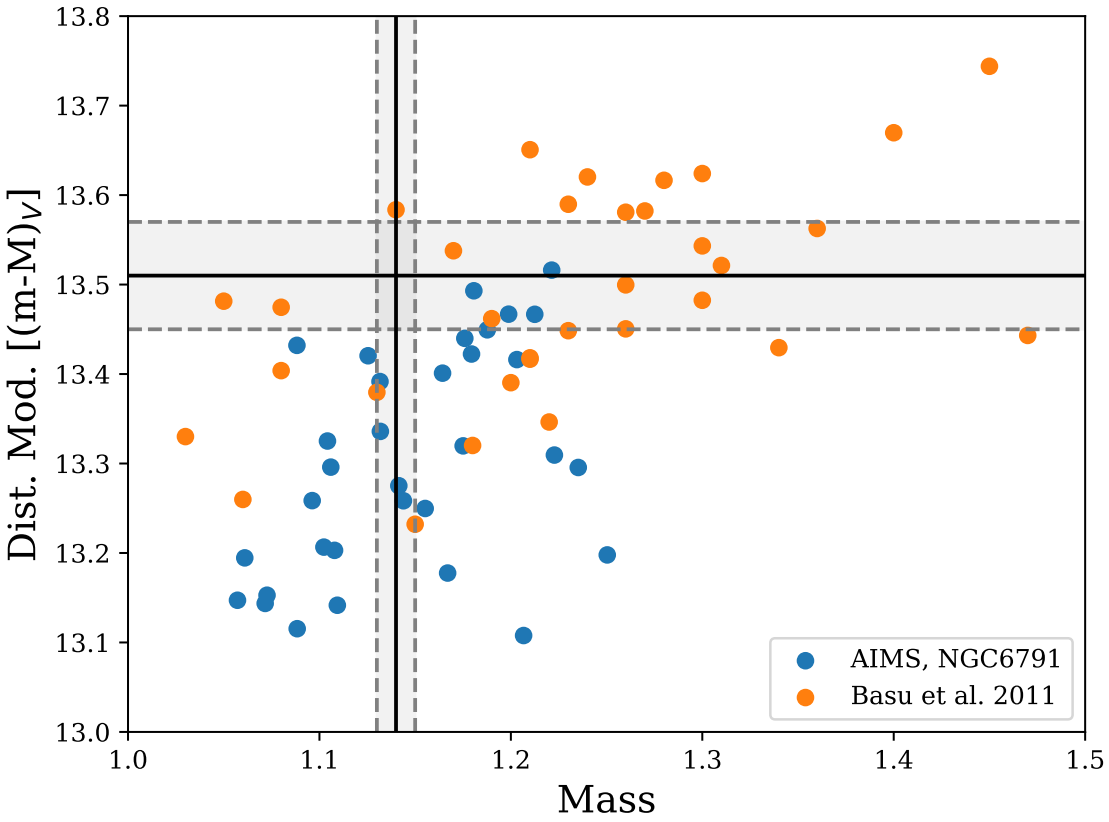

Figure 6.8: NGC6791 mass vs. distance modulus. The mean RGB mass and distance modulus determined from eclipsing binaries are denoted by the solid black lines. 1σ bounds are shown by the dashed black lines and shaded region. Dot-dashed lines connect the same star from each dataset.

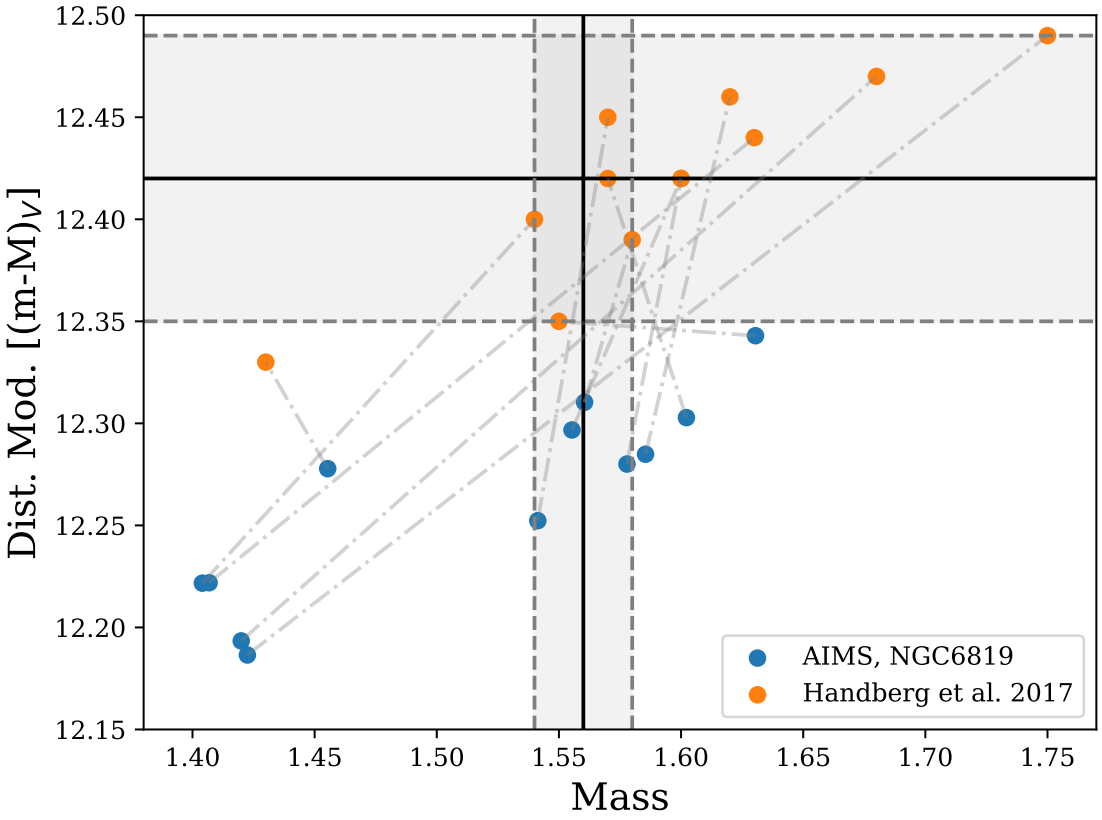

Figure 6.9: As Fig. 6.8, but for NGC6819.

accurately. For a 1.1 $M_\odot$ star with $T_{\rm eff}$ of 4355 K, an increase of 50 K results in a 4% decrease in luminosity and a 7% decrease in the BC. This translates as an approximately 1% increase in the distance modulus. This is about double the uncertainty on the mean EB value (0.44%), making it a non-insignificant shift in parameter space. It should again be stressed that improving the consistency between model and observational values of $T_{\rm eff}$ is highly important for reliable comparisons between methods to be made.

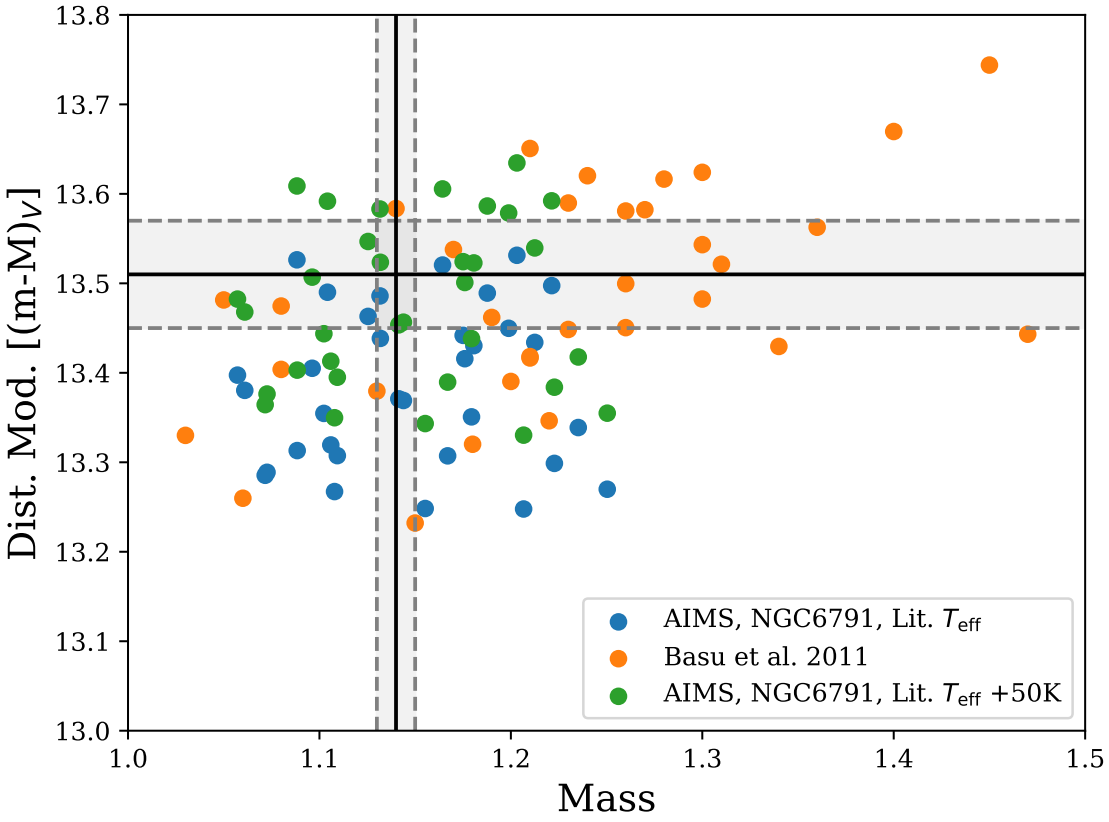

Figure 6.10: As Fig. 6.8, but with the inclusion of shifts in $T_{\rm eff}$. $T_{\rm eff}$ values from B11 (blue) and a systematic increase of 50K to the values returned by AIMS (green) have been used to calculate the distance moduli. The B11 values are shown in orange as before.

6.5 Conclusion

The analysis of a sample of 5 eclipsing binary stars focused on the repeatability of results from alternative methods. For each binary, the masses, radii and densities had all previously been inferred from radial velocity measurements. Using grid

modelling and the individual mode frequencies with AIMS, we found the masses and radii of each binary to be more agreeable with the dynamical values, as in Brogaard et al. (2018). Consistency between the $\nu_{\rm max}$ values computed using scaling relations from the dynamical and asteroseismic masses, radii and $T_{\rm eff}$ determinations was shown to be $\lesssim 2\sigma$. This is primarily due to uncertainties of order 5% in the scaled values, but offsets of 7% between the scaled values was concerning. The independently determined values of $\nu_{\rm max}$ from Gaulme et al. (2016) were also offset by this amount. As in Brogaard et al. (2018), cooler model temperatures compared to observations were found. An increase of the model dependent AIMS temperatures by 200K reduced the offsets from 7% to 2.5%.

Another systematic trend was observed for the mean density calculations from $\Delta\nu$. Though good agreement between the asteroseismic, dynamical and Buldgen et al. (2018b) values was observed, the determinations using the $\Delta\nu$ were systematically lower by 5%. Brogaard et al. (2018) extensively discusses the determination of the appropriate correction to apply to the $\Delta\nu$ scaling relation, and recognises that $T_{\rm eff}$ is a significant contributor to this.

Seven different surface-effect correction options are available to users of AIMS. Hence, for the eclipsing binary stars an analysis run was performed with each surface-effect correction. Overall, the returned values were found to be consistent with one another, and to the radial velocity measurements within 2σ. However, there was evidence that the result is influenced by the correction applied. Parameter value fluctuations show that different models are preferred for each correction. One must bare this in mind when selecting which correction to use. Further analyses were performed to understand how well the corrections fitted a selected model to the observed frequencies. The Ball & Gizon 2014 combined correction was found to demonstrate the greatest consistency with the expected difference between the theoretical and observed frequencies at $\nu_{\rm max}$ of $\sim -1\%$. It also returned the lowest $\chi^2_{red.}$ for most of the binary stars ($< 0.5\%$).

With a high proportion of $> 5\%$ offsets between frequencies at $\nu_{\rm max}$, NGC6819 was used to examine the effects of model selection on the final parameters. Rodrigues et al. (2017) also studied this cluster and they too had difficultly modelling the cluster parameters with larger than expected scatter in mass in particular, making it a good test case to understand any shortcomings in the models. A star with a difference of -5.36% was compared to a star with a difference of only -0.6%. The echelle diagrams and sample distributions after the MCMC runs were examined. The star with a large difference at $\nu_{\rm max}$ showed a large divergence between the model and observed frequencies and a very localised exploration of the parameter space compared to the star with a small percentage difference. With a large offset in frequencies, the surface-effect correction becomes significant. Examining all stars in the sample, it was apparent that those with the worst fits returned the largest corrections due to the surface-effect. There are multiple possible reasons for this (e.g. incorrect input physics, poor choice of correction), but further research is required is to get a true handle on the influence of the correction on the final model selection.

Members of the open clusters NGC6791 and NGC6819 were analysed to infer their mean RGB masses and distance moduli. A Bayesian, hierarchical model was used to determine the mean RGB masses from the final parameters determined by AIMS. The mean RGB masses were found to be (1.14 ± 0.01) $M_{\odot}$ for NGC6791 and (1.56 ± 0.02) $M_{\odot}$ for NGC6819. These values are consistent with the values determined using eclipsing binary stars within the systems. The mean RGB mass of NGC6791 was found to be consistent with a recent work by McKeever et al. (2019), as was the mean RGB mass of NGC6819 when the same sample of stars were considered from Handberg et al. (2017). Initially, the distance moduli calculated with parameters from AIMS were found to under-predict the expected literature values from eclipsing binary stars. The temperature offset between the models and observations was again found to be 50-150K. A 50K increase in $T_{\rm eff}$ led to a $\sim 1\%$ increase

in the distance modulus. This is of order the offset in distance modulus between the literature and AIMS values. As a non-insignificant shift, the importance of accurate determining model temperatures or understanding the systematics between models and observations cannot be underestimated.

Examining the Vertical Structure of the Milky Way with K2

Chapter 7

The K2 Galactic Caps Project

This chapter is a reformatted version of Rendle et al. (in prep.), of which I am to be first author. The paper is soon to be submitted to MNRAS. The asteroseismic parameters for the stars were provided by Benoit Mosser, Yvonne Elsworth and Savita Mathur. Photometric parameters from the SkyMapper survey were provided by Luca Casagrande. Clare Worley and Paula Jofre provided spectroscopic parameters from the Gaia-ESO survey, and Marica Valentini provided the same information for the RAVE and APOGEE samples. Gaia parallaxes were provided by Saniya Khan. I performed all cross-survey comparisons and completed all of the grid modelling analysis, using the PARAM *code with a provided grid of models. References in paragraph 2 sourced primarily from Miglio et al. 2017, of which I am a co-author, contributing analysis with* AIMS.

7.1 Introduction

Understanding and classifying the fundamental properties and formation mechanisms of galaxies is a cornerstone of characterising the evolutionary processes of large scale, extra-galactic structures. Galactic archaeology is a rapidly expanding field, using fossil remnants within the Milky Way to understand its formation history. The objective of the field is to understand the mechanisms of formation and structure of the galaxy through the study of the collective properties of stellar pop-

ulations. Accessing and correctly interpreting this information is key when wanting to understand Galactic evolution, especially during its earliest phases. High redshift disc galaxies appear to undergo the most significant formation changes between 12 and 8 Gyr ago at z $\sim$ 2 (e.g. Madau & Dickinson 2014). The expected bulge, halo and disc structures are typically formed during this time, with only thin disc formation steadily continuing to the present. This has been predicted by multiple theoretical models (e.g. Abadi et al. 2003a; Bird et al. 2013; Bournaud et al. 2009; Brook et al. 2004; Gibson et al. 2009; Guedes et al. 2013; Jones & Wyse 1983; Kawata & Chiappini 2016; Noguchi 1998; Sommer-Larsen et al. 2003; Steinmetz & Mueller 1994) and also appears to be true for the Milky Way (Chiappini et al., 1997; Chiappini, 2009; Kubryk et al., 2015; Minchev et al., 2013, 2014; Snaith et al., 2015). Current studies imply that thick disc formation started at z $\sim$ 3.5 (12 Gyr), whilst thin disc formation began at z $\sim$ 1.5 (8 Gyr) (e.g. Bensby et al. 2014; Bergemann et al. 2014; Fuhrmann 2011; Haywood et al. 2013; Robin et al. 2014; Helmi et al. 2018).

There are many unanswered questions in the formation of the Milky Way (e.g. see Miglio et al. 2017; Minchev 2016 for a review). One of the most fundamental questions is the characterisation of its vertical structure. It is commonly agreed that the Galaxy consists of a central bar/bulge, disc and halo components (e.g. Bland-Hawthorn & Gerhard 2016; Barbuy et al. 2018). The specific nature of each component has been subject to scrutiny, with the nature of the disc most fervently debated (see e.g. Kawata & Chiappini 2016). Since the results showing evidence for a multiple disc-like structure (Gilmore & Reid, 1983), astronomers have striven to fully classify these components and distinguish them chemically, dynamically and geometrically (see e.g. Freeman & Bland-Hawthorn 2002; Bovy et al. 2012a,c; Haywood et al. 2013; Rix & Bovy 2013; Bensby 2014; Anders et al. 2014; Recio-Blanco et al. 2014; Hayden et al. 2015; Minchev et al. 2015; Bovy et al. 2016b; Hayden et al. 2017). Typical constraints from the literature define the discs as

such: Thin Disc - scale height $\sim$ 300 pc, age $\lesssim$ 9 Gyr, solar-[Fe/H], solar-[α/Fe]; Thick Disc - scale height $\sim$ 900 pc, age $\gtrsim$ 10 Gyr, [Fe/H] ~ -0.7, enhanced [α/Fe] (> 0.2). Large scale spectroscopic and kinematic surveys have allowed the dissection of mono-age and mono-abundance populations (e.g. Bovy et al. 2012b; Martig et al. 2016b; Bovy et al. 2016b; Mackereth et al. 2017b; Mackereth et al. 2019), giving snapshots into different epochs of the Milky Way's past. Most studies concur on the existence of multiple stellar populations within the Galactic disc, but stress the importance of which metric is used to define the so-called thin and thick disc components respectively (Bovy et al., 2012a,c; Minchev et al., 2015), if the disc is to be classified as such.

Any inferences to be made about Galactic structure and evolution rely heavily upon having accurate measurements of the stellar population parameters (e.g. ages, metallicities...). The relevance of asteroseismology in stellar populations studies was recognised early on when the first data from CoRoT and *Kepler* became available (see, e.g. Miglio et al., 2009; Chaplin et al., 2011a). Subsequently, tests of the precision and accuracy of the asteroseismically inferred parameters enabled quantitative studies that made use of distributions of stellar masses and wide age bins (Miglio et al., 2013b; Casagrande et al., 2014; Anders et al., 2017).

This field has continued to mature alongside data-analysis and modelling procedures. It is now recognised that asteroseismic constraints coupled with high resolution spectroscopy enable inferences on stellar masses, radii and ages with uncertainties of $\sim$3-10%, $\sim$1-5% and $\sim$20-40% respectively (see Davies & Miglio 2016, Mosser et al. 2019, where seismic yields from different observations are discussed). These uncertainties (in particular in age; see Soderblom 2010 for a comprehensive review of determination methods) are not yet regularly achievable with spectroscopy alone, thus presenting asteroseismology as an attractive prospect for making precise parameter determinations on a large scale.

The upper limits of the parameter uncertainty are typically achievable using

the so-called asteroseismic scaling relations (Kjeldsen & Bedding, 1995). A 30-35% uncertainty in age is sufficient to pull out basic features of a distribution, but is not enough to conclusively interpret the true nature of the underlying population distribution. Crucially, further accuracy can be achieved when one goes beyond the scaling relations, using asteroseismic grid modelling (inclusion of global asteroseismic parameters in modelling process e.g. PARAM, da Silva et al. 2006; Rodrigues et al. 2014, 2017; BASTA, Silva Aguirre et al. 2015) or where possible, the individual acoustic modes themselves (see e.g. Rendle et al. 2019 and references therein). When these techniques are implemented, it is possible to achieve the lower bounds of precision quoted. This precision greatly reduces any ambiguity surrounding the mass, radius and age distributions, allowing confidence to be given to statements regarding the state of the Milky Way at given epochs.

Though powerful in its capabilities, asteroseismology has been relatively limited to observations of the Galactic mid-plane. CoRoT (Baglin et al., 2006; Anders et al., 2017) observed regions in the Galactic inner and outer disk and *Kepler* (Borucki et al., 2010b) provided exquisite data for a single field extending out of the Galactic plane. Neither mission, however, sampled sufficient fields for mapping radially and vertically the Milky Way. K2 (Howell et al., 2014) has revolutionised this, with 70 day observations in the ecliptic plane sampling a broad range of Galactic fields to depths of several kilo-parsecs (kpc). The depth of observations and ability to detect asteroseismic signatures of extensive populations has transformed K2 into an exciting prospect for the provision of improved constraints on Galactic evolution and structure (Stello et al., 2015).

The capability of asteroseismology to determine vertical stellar population trends out to and beyond $\sim$ 1.5 kpc has already been illustrated with the exquisite data from the CoRoT (Miglio et al., 2013b) and *Kepler* (Casagrande et al., 2016; Mathur et al., 2016; Silva Aguirre et al., 2018) missions. Repurposed as K2, asteroseismic observations towards the Galactic poles extend substantively beyond 1.5 kpc,

facilitating the first detailed examination of the vertical Galactic structure with asteroseismology. Though degraded in comparison to *Kepler*, the K2 data remains of high enough quality to make precise asteroseismic inferences (see Chaplin et al. 2015; Stello et al. 2015; Miglio et al. 2016). Hence, using K2 campaigns 3 and 6, we present an asteroseismic analysis of the vertical disc structure of the Milky Way with the K2 Galactic Caps Project (K2 GCP). We demonstrate the increased capability of these campaign fields compared to *Kepler* in determining vertical population trends and show the benefits of improved precision in age.

The paper is laid out as follows: Section 7.2 describes the input data and effects of the selection function used. Section 7.3 briefly details the analysis methods. Sections 7.4, 7.5 and 7.6 display the key results of the work, based on the analysis of the distributions in radius, mass, and age, of the red giants observed in the two fields C3 and C6 observed by K2. Finally, section 7.7 summarises our findings and discusses the potential of future work.

7.2 Data

The K2 mission provided photometric data for a range of fields located both in and out of the Galactic plane for a total of 4 years, observing 20 campaign fields (C0-19). A dedicated program for Galactic archaeology has been implemented, with observations of asteroseismic candidates in Galactic regions never previously explored with this technique on this scale. Stello et al. (2015) presents the asteroseismic results for K2 campaign 1, highlighting the potential of the mission and its capabilities. Of the 20 campaign fields, nine focus on the northern and southern Galactic caps. Asteroseismic analysis of these campaign fields will improve the characterisation of the stellar populations in these directions, which in turn will assist in improving our understanding of the vertical structure.

The K2 Galactic Archaeology Project (K2 GAP, Stello et al. 2017) focuses on the observations of thousands of red giants in each K2 campaign field for the purpose

Table 7.1: Population samples used throughout this work. Name and descriptions of the populations are provided.

Sample	Description
K2	K2 sample containing parameters from the K2 EPIC catalogue.
K2 Spec.	K2 cross-matched with spectroscopic surveys. Survey [Fe/H], [α/Fe] (where applicable) and $T_{\rm eff}$ values used.
K2 SM	K2 sample cross-matched with the SkyMapper survey. SkyMapper [Fe/H] and $T_{\rm eff}$ values used.
APOKASC/*Kepler*	PARAM results for the APOKASC-2 population from Miglio et al. (in prep.) .
APOKASC α-rich	α-rich APOKASC-2 sample from Miglio et al. (in prep.).
K2 α-rich	K2 Spec. sample with [α/Fe] > 0.1.
$\rm K2_{Gaia}$	As K2 SM sample, but with radii calculated from *Gaia* parallaxes.
$\rm K2_{HQ}$	K2 SM sample; all stars with $\sigma_{\rm age} < 35\%$.
$\rm K2\ Spec._{HQ}$	K2 Spec. sample; all stars with $\sigma_{\rm age} < 35\%$.

of performing Galactic archaeology with potential asteroseismic targets. Red giant stars are preferentially selected over dwarfs for the K2 GAP as they are intrinsically more luminous, accommodating observations to greater distances and more detail about the Galactic structure to be probed. They also show greater oscillation amplitudes than dwarfs with frequencies well suited to the main long-cadence mode of K2. This allows for asteroseismic detections to be made for a greater sample of the observed population and consequently a more robust analysis of the population parameters.

K2 campaign fields 3 (centred at: $l = 51.1^o, b = -52.5^o$) and 6 (centred at: $l = 321.3^o, b = +49.9^o$) were selected for this work. Campaign field 3 is a south Galactic pole pointing field, whereas campaign 6 points towards the north Galactic pole. The fields sample Galactic radii in the range 6-8 kpc, pointing towards the Galactic centre and observe stars up to 4kpc above and below the plane. The depth and range of these observations make these two campaign fields ideal for studies of the vertical properties of the Milky Way as both the so-called thin and thick disc populations are expected to be sufficiently sampled.

The observations of the Galactic poles are not limited to two campaign fields. Campaigns 1, 10, 14 and 17 observed the northern, and campaigns 8, 12 and 19 have observed the southern, Galactic cap. Though data is available for these fields, they are not included in this work. We limit ourselves to C3 and C6 to explore the potential of K2 to distinguish trends in the vertical Galactic structure prior to a comprehensive, multi-campaign analysis.

For comparative purposes, stars from the nominal *Kepler* mission are included in this work. The stars were selected from the APOKASC catalogue (Pinsonneault et al., 2014, 2017, 2018). Figure 7.1 shows the spatial distribution of the APOKASC sample compared to the respective K2 campaign fields used here. The values of Z (vertical distance above the galactic plane) and $R_{\rm Gal}$ (galactocentric radius) were determined using asteroseismic distances inferred using the Bayesian inference code

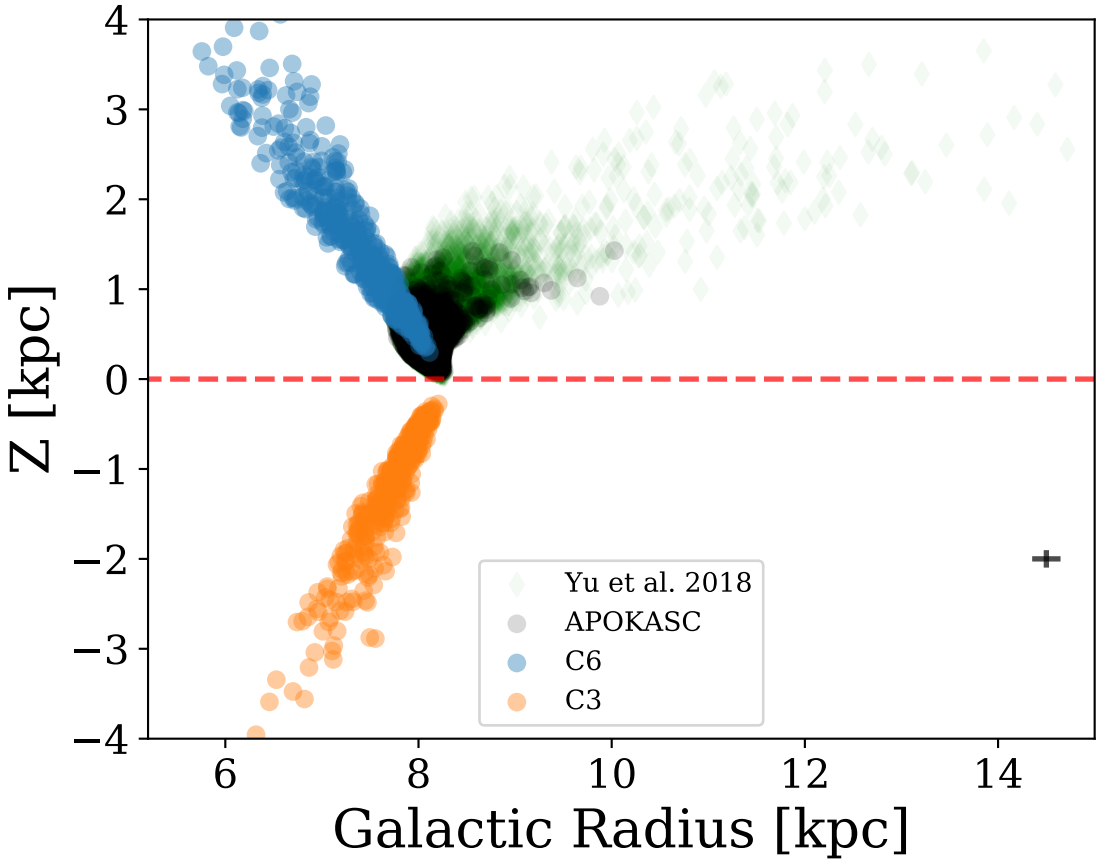

Figure 7.1: The distribution of stars in the APOKASC (black) and K2 campaigns 3 (orange) and 6 (blue). All Z and $R_{\rm Gal}$ values were calculated using asteroseismic distances. The black cross shows the typical uncertainties in Z and $R_{\rm Gal}$ of the combined K2 sample. The sample of 16000 red giants from the *Kepler* survey (green diamonds, Yu et al. 2018) shows the full range of the *Kepler* field compared to the APOKASC sample.

PARAM (Rodrigues et al., 2017), with an uncertainty typically below 6 per cent. *Gaia* DR2 (Gaia Collaboration et al., 2018b) distances are available for these stars, but the precision of asteroseismic distances has been shown to be approximately a factor of 2 better than *Gaia* distances for the *Kepler* and K2 C3 and C6 fields (Khan et al. *submitted*), therefore we adopt the asteroseismic measurements here. However, a robust treatment of *Gaia* parallaxes is used for the determination of initial stellar radii in this work (see section 7.2.2).

The extent to which the K2 fields probe vertically compared to *Kepler* illustrates why this sample is suited for studies of the Galactic structure. It is expected that thick disc members dominate the stellar population beyond $|Z| \sim$1.5kpc, a region poorly sampled by *Kepler* but with significant coverage by K2 across both fields. Increased coverage of stars beyond this distance is crucial for ensuring that a significant thick disc population is sampled and characterised for definitive conclusions on underlying population trends.

It is also notable from Fig. 7.1 that the two K2 campaign fields also explore regions in the inner disc, compared to the *Kepler* APOKASC population which is largely restricted to solar Galactocentric radii. Though our study focuses on the vertical properties of the field, the different pointings may be a cause of variability due to differing radial distributions. We take steps to account for this in section 7.6.

Multiple populations are used in this work and for clarity they are named in Table 7.1. The population name and a brief description of the sample are given for reference.

7.2.1 Asteroseismology

Three independent asteroseismic analysis pipelines - BHM (Elsworth et al. in preparation), A2Z (Mathur et al., 2010b), COR (Mosser & Appourchaux, 2009a) - have been used to analyse the light curves for each K2 campaign (K2P^2, Lund et al. 2015). The same sample of stars was analysed by each pipeline to extract the global

asteroseismic parameters: the large frequency separation ($\Delta\nu$) and the frequency of maximum power ($\nu_{\rm max}$) for each light curve. All of the pipelines utilise a different method to extract these global parameters. In many cases, multiple pipelines return a positive detection for the same star. There are also cases where a single pipeline has registered a detection where the others have not.

Having a detection from multiple pipelines provides an excellent opportunity to explore the consistency of different methodologies and verification of the results. Figure 7.2 displays comparisons of $\nu_{\rm max}$ and $\Delta\nu$ values between each of the asteroseismic pipelines for C3. The distribution of differences between values for crossover stars as a function of the combined uncertainty ($\sigma_{\rm comb.}$, mean uncertainty from cross-matches of all pipelines summed in quadrature) is shown. The mean (μ) and standard deviation (σ) of each distribution is also included. It is evident that there is greater consistency in $\nu_{\rm max}$ determinations compared to $\Delta\nu$.

The largest disagreements (beyond 2 $\sigma_{\rm comb.}$) typically occur at $\nu_{\rm max}$ around the position of the clump ($20 - 30$ μHz), highlighting an area of inconsistency between the different methodologies. Increased discrepancies are expected in this regime though, as the frequency spectra of core helium burning stars show more complex, low amplitude mode patterns and therefore parameter determinations are more dependent on the analysis techniques used.

The $\Delta\nu$ distributions show a larger degree of scatter, as evidenced by their greater standard deviations. The scatter appears consistent across the range of values for each pipeline, with the majority of values within twice the combined uncertainty of each other.

Comparing the distributions to an N(0,1) distribution, it is clear that the $\nu_{\rm max}$ standard deviations are all significantly lower than unity. This indicates that the methods show strong agreement, but with a large correlation. The $\Delta\nu$ standard deviations are much closer to unity, showing good agreement, but a reduced correlation between pipelines. These results indicate that there is little disparity in

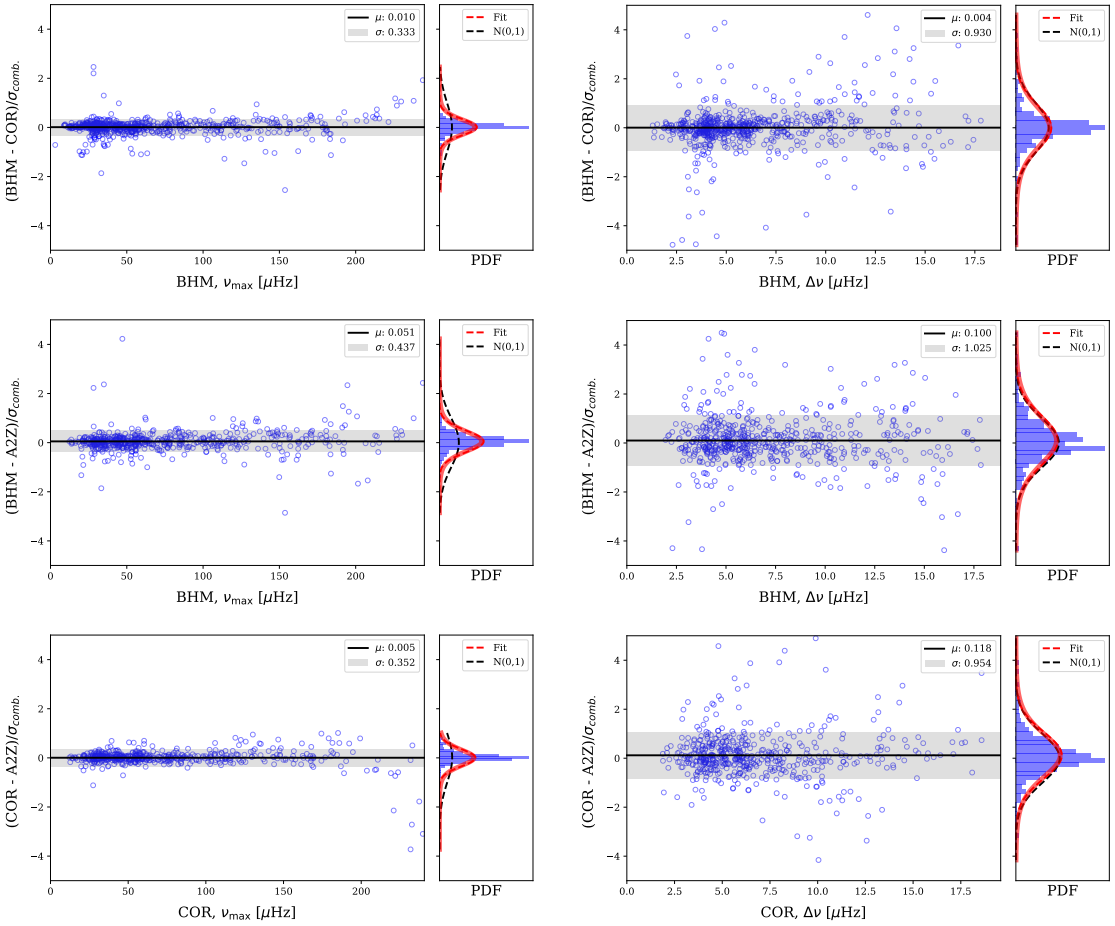

Figure 7.2: C3 asteroseismic pipeline comparisons. *Left:* $\nu_{\rm max}$ comparisons. *Right:* $\Delta\nu$ comparisons. *Top:* BHM vs COR. *Middle:* BHM vs A2Z. *Bottom:* COR vs A2Z. Black lines show the mean (μ) and the grey regions the 1σ region of the scatter about the mean. Values are shown in the legend. The Histograms show the distribution of points as a function of $\rm N_{\sigma_{comb}}$. Red lines show a Gaussian fit to the data using the values of μ and σ indicated in the legend of the main panel. Black dashed lines show a N(0,1) distribution for comparison.

the way $\nu_{\rm max}$ is calculated for these data, but that the pipelines differ more in how they determine $\Delta\nu$. To accommodate this, and ensure maximum confidence in the asteroseismic parameters used, we incorporated a difference limit into the selection function (see below).

7.2.2 Selection Function

The selection function used in this work was adapted from the K2 GAP proposals[1] for C3 and C6 (Sharma et al. *in prep.*). The K2 GAP selection function was designed to be much simpler to implement than that for the *Kepler* field (Farmer et al., 2013) and to ensure only red giants were observed. Its simplicity affords greater understanding of selection biases, and therefore trends, in the data. Cuts in colour and magnitude (JHK_s from the Two Micron All Sky Survey, Skrutskie et al. 2006; V calculated from J and K_s as per C6 K2 GAP observing proposal[2]) are implemented within the K2 GAP for campaigns 3 and 6 as follows:

$$\text{C3}: \begin{cases} 9.3 < \text{V} < 14.5 \\ \text{J} - \text{K}_\text{s} > 0.5 \end{cases} \qquad \text{C6}: \begin{cases} 9 < \text{V} < 15 \\ \text{J} - \text{K}_\text{s} > 0.5 \end{cases} \tag{7.1}$$

The V-band magnitude cuts differ between fields as the nominal cut for C3 was performed in the H-band ($7 < \text{H} < 12$). Further, the asteroseismic detection probability of each star was calculated according to the method described in Schofield et al. (2019) and Chaplin et al. (2011b). In brief, the detection probability test takes an estimate of the seismic properties, $\Delta\nu$ and $\nu_{\rm max}$, the granulation background and a theoretical Gaussian mode envelope for the star centred on the predicted $\nu_{\rm max}$. The signal-to-noise ratio of the estimated total mode power-to-background noise power within the envelope is used to determine the probability of an asteroseismic detection.

[1] All available at http://www.physics.usyd.edu.au/k2gap/.
[2] See http://www.physics.usyd.edu.au/k2gap/K2/C6 for proposal.

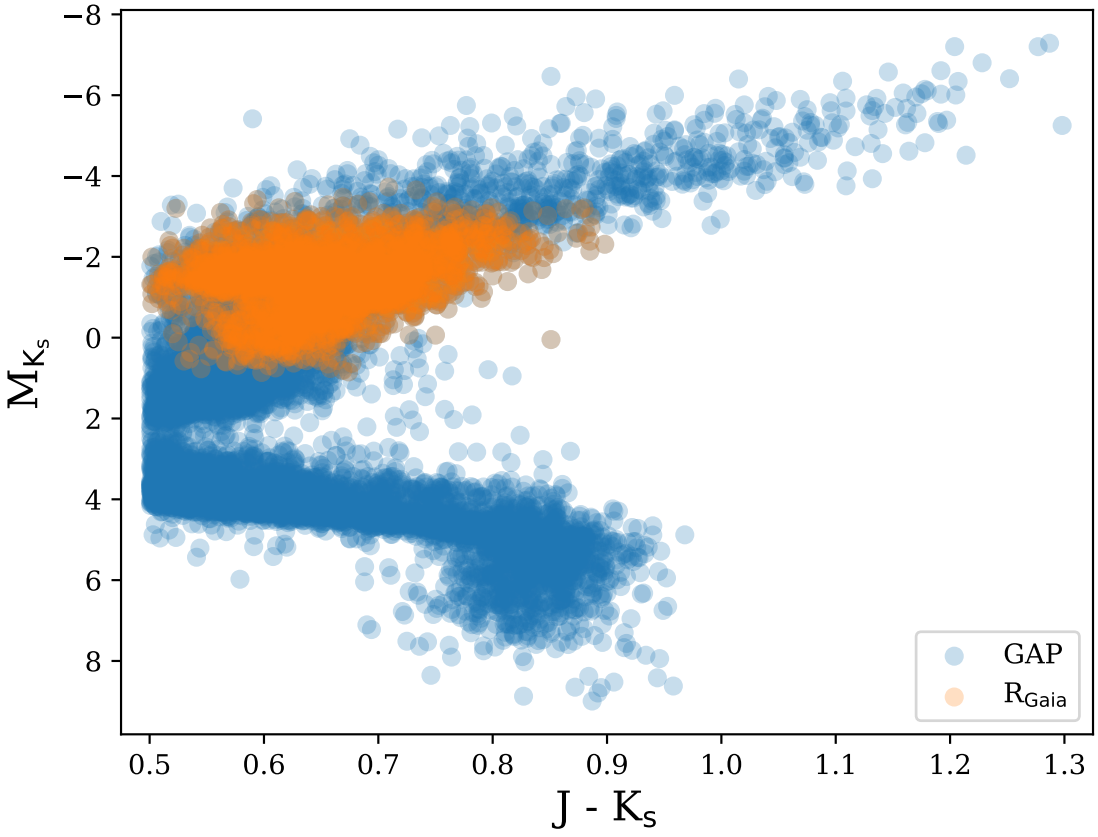

Figure 7.3: Colour-Magnitude Diagram for the C3 and C6 combined K2 GAP target lists. The blue markers indicate the full, original K2 GAP sample. Orange indicates the stars passing the detection probability test using radii derived from *Gaia* parallaxes ('Predicted' in Table 7.2).

The seismic properties mentioned above are estimated using stellar radii and luminosities which were derived using a combination of astrometric and photospheric constraints. Luminosities were inferred from Ks magnitudes, bolometric correction from Casagrande & VandenBerg (2014a, 2018a,b,d), extinction calculated using the `mwdust` package (Bovy et al., 2016a) with Green et al. (2015) dust maps (extinctions are typically $A_K < 0.05$ mag) and distances are based on Gaia DR2 data and the Astraatmadja & Bailer-Jones (2016) method. The input parallaxes were corrected for the zero-point offset based on their field location: $(-15\pm4)\mu$as for C3; $(-2\pm2)\mu$as for C6 (for calculation, see Khan et al. *submitted*). The values of $T_{\rm eff}$ used were from the EPIC catalogue (Huber et al., 2016).

The colour-magnitude diagram (CMD) in Fig. 7.3 shows the distribution of all

targets in the C3 and C6 fields registered in the K2 GAP target lists (blue). Overlaid is the population of stars passing the detection probability test using radii calculated from the *Gaia* parallaxes (orange; 'Predicted' in Table 7.2). All stars with calculated radii are grouped closely around the beginning of the red giant branch (RGB), the RGB bump (RGBb) and the red clump (RC). This is inline with the expectation of the selection function to deselect all MS stars.

Table 7.2 shows the number of stars from the K2 GAP predicted to pass the detection probability tests for each campaign field and the number of stars with actual detections within the predicted sample. There is $25-28\%$ reduction between the predicted and actual counts. The reductions predominantly affect faint magnitude (H $>$ 10, V $>$ 12) and $R < 10\,\mathrm{R}_{\odot}$ stars when comparing the predictions to observations. In C3, the initial star count with detections from the asteroseismic pipelines is 885. The star count is already significantly less than the number remaining in the C3 K2 GAP sample after the colour and magnitude cuts ($\sim$ 1300). This inherently means that one would typically observe a greater disparity in star counts when further cuts are made.

The noise model applied in the detection probability test follows that first proposed for *Kepler* in Chaplin et al. (2011b), modified for the noise performance of K2 by Lund et al. (2016). The procedure predicts the expected global signal-to-noise level in the detected oscillations against background from intrinsic stellar noise (granulation) and shot/instrumental noise. This approach assumes that the population model is a good model of observations. Though the predictions work well for the majority of stars, in reality some show higher noise than expected (i.e. the tendency is for the distribution of real stars to show a high-noise tail), which could be a potential contributor to the lower actual numbers of detections returned by the pipelines.

An additional factor is the consideration of stars only with values of both ν_{max} and $\Delta\nu$. Preliminary results from the BHM pipeline returned detections of ν_{max} only

Table 7.2: Number of K2 GAP stars predicted to have detections for campaign fields 3 and 6 using radii calculated from *Gaia* parallaxes ($R_{\rm Gaia}$). The number of stars from predictions that have true detections (Actual) is also shown. The 'Actual' counts are for stars with both $\nu_{\rm max}$ and $\Delta\nu$ values.

Field	$R_{\rm Gaia}$	
	Predicted	Actual
C3	1073	762
C6	1822	1374

for $\sim 10\%$ of the field. If just the stars with observational values for $\nu_{\rm max}$ and $\Delta\nu$ are considered, 818 remain after the detection probability cut is made. Comparing this to the 'Actual' $R_{\rm Gaia}$ value for C3 (see Tab. 7.2), only 7% reduction in star counts is observed compared to expectations. Under-predictions of the *Gaia* radii compared to asteroseismology (see section 7.4, Fig. 7.8) could be a cause of this. The mode amplitude scales as the radius squared (e.g. see Chaplin & Miglio 2013 and references therein), hence, an under-predicted radius value decreases the estimated mode amplitude, reducing the probability of seeing a detection.

A final cut was implemented based on observational detections. Any star with no detection or a detection from only a single analysis pipeline was removed from the final sample. Multiple detections were sought to improve the reliability of the measurement by cross-referencing. The values of $\nu_{\rm max}$ and $\Delta\nu$ were deemed consistent and the star accepted if the values for one pipeline lay within 2σ of another. Stars with values separated by greater than 2σ were rejected. The final asteroseismic inputs were selected from the COR and BHM pipelines due to greater yield of detections and less conservative uncertainties compared to A2Z. Though not explicitly used, the A2Z determinations are consistent with the final asteroseismic inputs.

Table 7.3 states the final number of stars remaining from each survey after the selection cuts. The values associated with K2 are the final sample sizes after they have been cross matched with improved photometric metallicities and effective temperatures (see Section 7.2.3.3).

Table 7.3: Number of stars in final samples for each K2 campaign field and supplementary surveys used in this work.

Survey	C3	C6
K2	483	929
K2 SM	377	646
RAVE	85	83
Gaia-ESO	38	-
APOGEE	101	25
K2 Spec.	128	102

7.2.3 Photospheric Constraints

7.2.3.1 Spectroscopy

Spectroscopic data were collected to complement those from asteroseismology, improving upon the values of parameters such as $T_{\rm eff}$ and [Fe/H] that can be obtained from photometry. Data from the RAVE (C3/C6, Kunder et al. 2017), APOGEE (C3/C6, Eisenstein et al. 2011a; Majewski et al. 2017; we make use of data to be released as a part of the Sloan Digital Sky Survey IV, Gunn et al. 2006; Holtzman et al. 2015; Nidever et al. 2015; García Pérez et al. 2016; Blanton et al. 2017; Zasowski et al. 2017) and Gaia-ESO (C3, Worley et al. *in prep.*; Gilmore et al. 2012) surveys have been used. After the selection cuts had been applied, these data were cross matched with the asteroseismic data. The final number of stars with spectroscopic information is low compared to the total sample, but still remains significant enough to draw sensible conclusions from the data and verify the wider trends observed with the larger photometric sample. Spectroscopic parameters from RAVE and Gaia-ESO were calibrated by adopting and iterating with asteroseismic log(g) values (Valentini et al. 2017; Worley et al. *in prep.*). Also, the log(g) values for the APOGEE sample are from asteroseismology, although the metallicities and $T_{\rm eff}$ are derived using the APOGEE spectroscopic log(g).

The use of multiple sources of spectroscopic data is excellent for maximising the yield of targets, but comes with its own complexities. There is little consistency

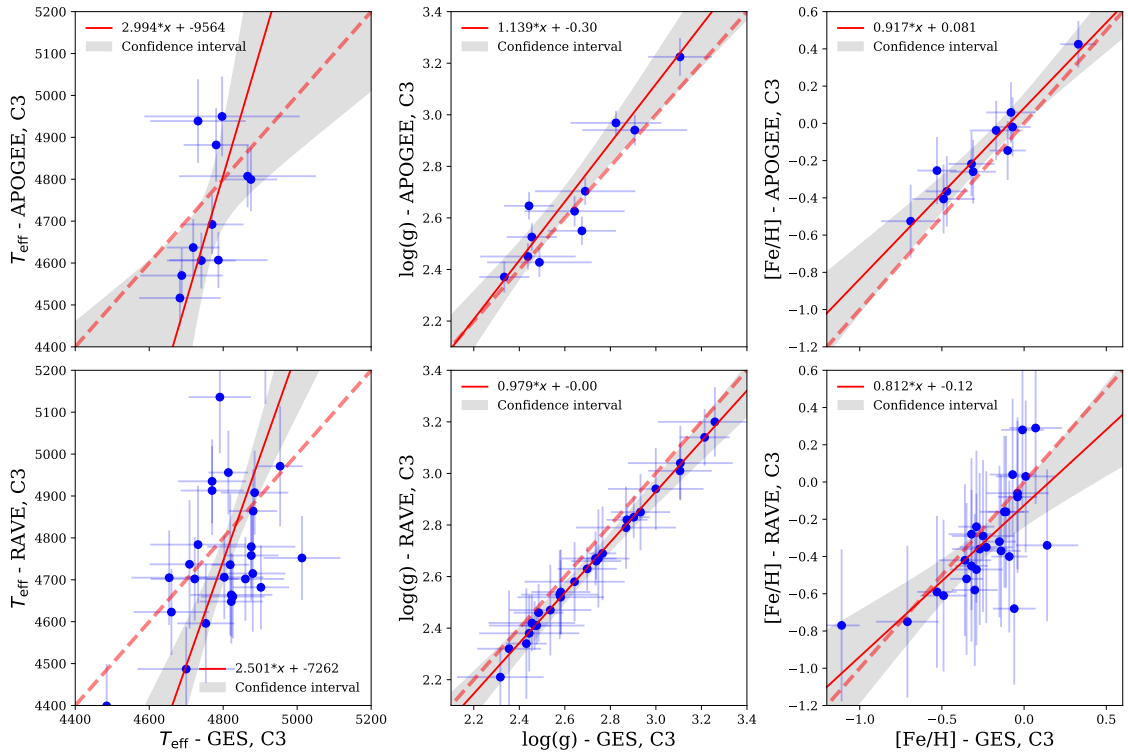

Figure 7.4: A comparison between the C3 spectroscopic data sources for $T_{\rm eff}$ (left panels), log(g) (middle) and [Fe/H] (right). Comparisons for APOGEE and Gaia-ESO (top row) and RAVE and Gaia-ESO (bottom row) are displayed. Blue points represent the data, with associated uncertainties. The red, dashed lines are the 1-to-1 relation to guide the eye. Red solid line is the best fit to the data (equations given in legends) and the grey regions denote the confidence intervals of the fits.

between survey observations, with observations of different spectral domains and resolutions common (Valentini et al., 2016; Jofré et al., 2018). In addition, each survey has a set of unique selection biases that need to be considered, which can manifest in systematic parameter trends (e.g. see Anguiano et al. 2018; Jönsson et al. 2018). Cross-calibrating surveys thus proves difficult. Even where overlaps exist, it is not easy to directly compare the values (Jofré et al., 2017).

Comparisons and attempts to calibrate surveys to one another were made for this work in order to have a consistent spectroscopic sample. Figure 7.4 shows the comparison between the surveys used in C3, where an overlap of greater than 10 stars was available (APOGEE to Gaia-ESO; RAVE to Gaia-ESO). The relations between $T_{\rm eff}$, log(g) and [Fe/H] are described by linear, orthogonal distance regressions (`odrpack, scipy`, Jones et al. 2001), with the resultant fits displayed on the

relevant subplots. It is evident that,though the generous uncertainties maintain consistency between values in each case, each gradient departs significantly from unity or is offset (except RAVE/Gaia-ESO log(g)) and the fitting parameters vary quite broadly. This is particularly strong in temperature and [Fe/H], revealing inconsistencies between the surveys. Consistent methodology to calibrate the log(g) values means reduced scatter, but a departure from unity is still observed.

We briefly explored the possibility of using the trend lines to calibrate the APOGEE and RAVE survey results to the Gaia-ESO values. The calibrations had little effect on the final parameter distributions as they appeared almost identical to the uncalibrated results. We therefore chose to proceed with the original survey values, but acknowledge the possibility of systematic trends in the data. We preferentially select the most represented surveys in each field for spectroscopic parameters to ensure as much consistency as possible.

7.2.3.2 Chemical Composition

Chemical space is often a key area used in the literature to distinguish between stars belonging to a thin or thick disc population. Typically, the thin disc is expected to be [Fe/H] rich and solar-[α/Fe]; the thick disc [Fe/H] poor and [α/Fe] enriched (e.g. see Fuhrmann 1998; Bensby et al. 2005, 2007; Reddy & Lambert 2008; Ruchti et al. 2011; Kordopatis et al. 2015). This trend is a consequence of the expected epochs of formation of these structures. The thick disc is considered to be older (10-12 Gyr) and has therefore formed rapidly in conditions with less metal enrichment and greater α-enhancement from core-collapse supernovae. The thin disc is thought to have started forming later (7-9 Gyr ago) and, as a consequence, is more metal-rich due to enrichment of the interstellar medium by type-Ia supernovae (see e.g. Matteucci 2001 and references therein).

The metallicity distributions observed with *Kepler* and the K2 fields studied here further demonstrate the suitability of the K2 fields for this study and are shown in Figure 7.5. The *Kepler* distribution peaks at [Fe/H] of -0.1 dex with a

standard deviation of ±0.5 dex. This distribution is highly indicative of a thin disc dominated population, with only a small tail in the metal poor regime. A peak for the thick disc would be expected at around -0.5 dex (see Minchev et al. 2013, 2014 and references therein).

The K2 Spec. distribution follows closely that of the APOKASC sample, though it peaks at a lower metallicity (-0.25 dex). The whole sample is clearly shifted towards lower metallicity and has an extended metal-poor tail. Given the greater vertical extension of K2 C3 and C6, the sample is likely to have a dominant contribution from the thick disc, explaining the shift compared to APOKASC. The K2 SM sample alludes to a much greater metal poor tail than K2 Spec. shows. This is potentially true, but the photometric distribution has greater scatter compared to the RAVE and APOGEE survey metallicities (see Casagrande et al. 2019). This is demonstrated by the extension to unlikely metallicities of > 0.5 dex for K2 SM.

The [Fe/H] vs. [α/Fe] distribution for the K2 APOGEE and APOKASC samples is shown in Fig. 7.6. The same spectroscopic survey has been used here for a direct comparison to negate the effect of any biases due to the survey selection function. The typically expected low- (solar) and high- α sequences associated with the evolution of the thin and thick discs are evident for these populations. Classifying the α-rich population as in Table 7.1 ([α/Fe] > 0.1), $\sim 60\%$ of the K2 C3/C6 sample consists of α-rich stars compared to only $\sim 15\%$ of the APOKASC sample. It is thus necessary to include comparisons of the K2 samples to the α-rich component of APOKASC and not only the full sample. Though the proportion of stars in this regime is smaller than in the K2 populations, the sample size is still significant enough (748 stars) for comparisons and conclusions to be drawn.

7.2.3.3 Photometry

Spectroscopic temperatures and metallicities were not available for all of the stars in the initial sample. To supplement this information, photometric values of $T_{\rm eff}$ and [Fe/H] determined from observations by the SkyMapper survey (Keller et al., 2007;

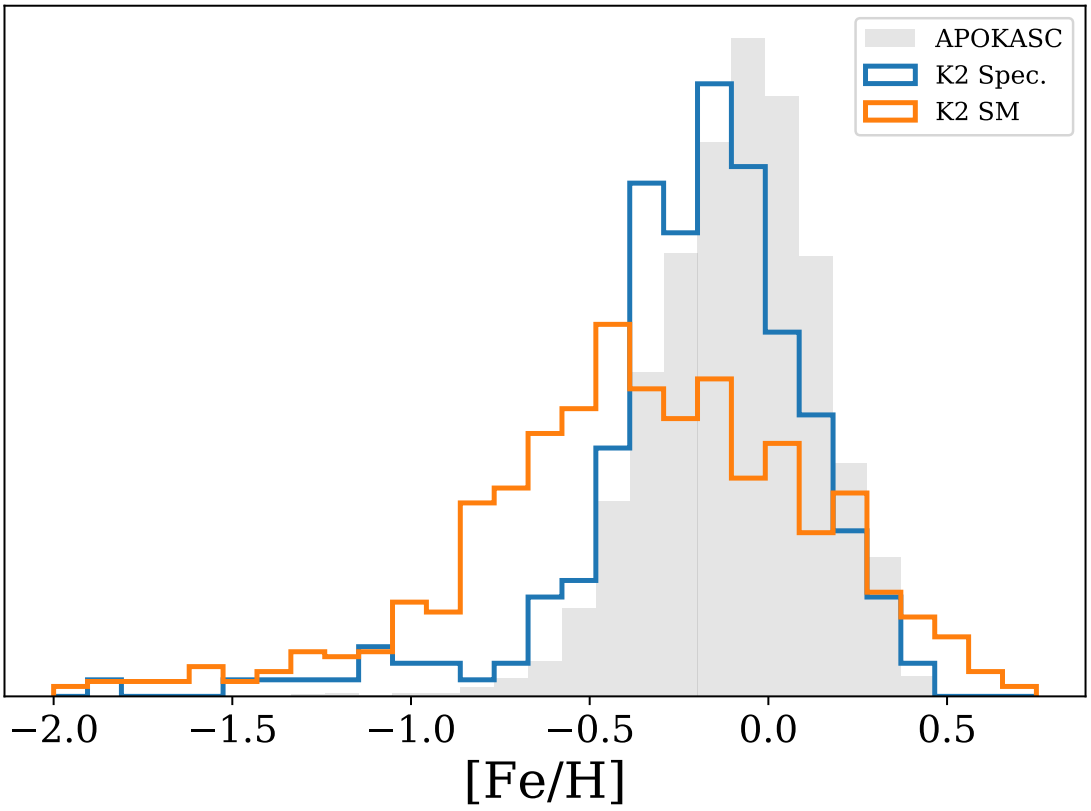

Figure 7.5: Normalised [Fe/H] distributions for the APOKASC (grey), K2 stars with spectroscopic values (blue) and SkyMapper values (orange).

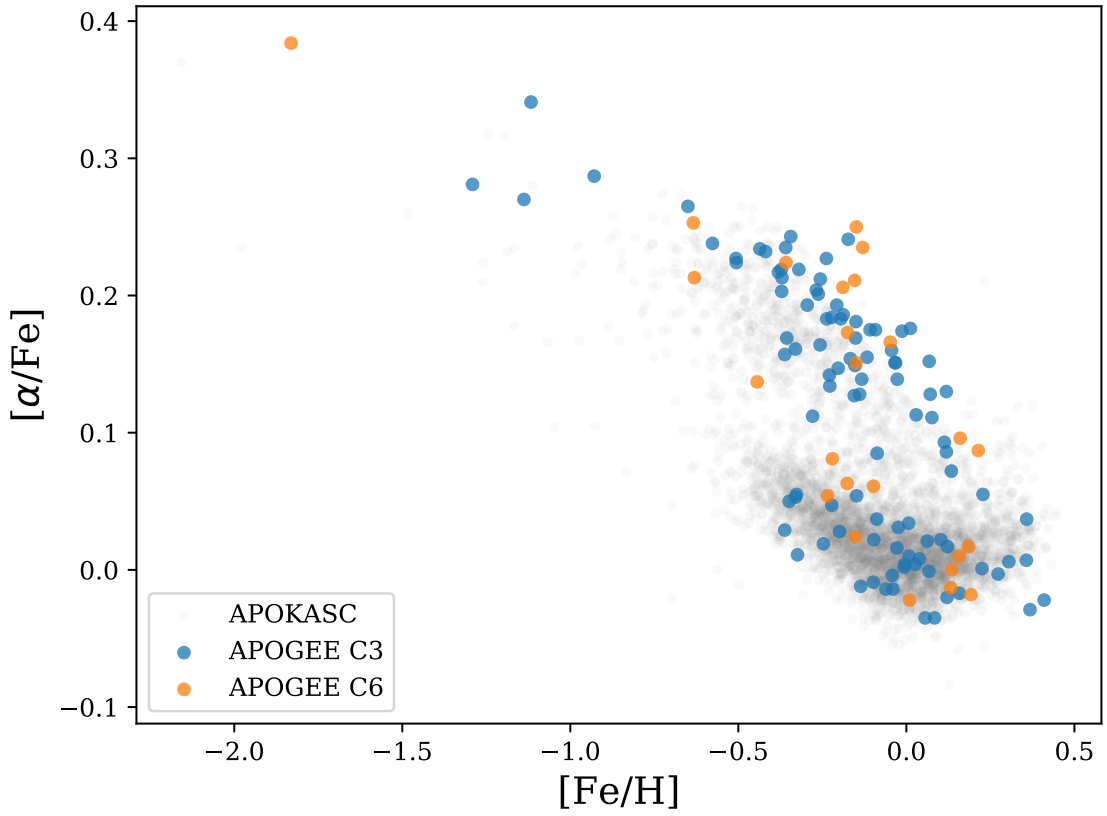

Figure 7.6: [Fe/H] vs. [α/Fe] distribution for the APOGEE survey in the K2 C3/C6 samples. The APOKASC distribution is shown in grey.

Wolf et al., 2018) have been used. SkyMapper is designed to take *uvgriz* photometry, from which stellar parameters can be derived (Casagrande et al., 2019). The reported survey parameters have been calibrated using GALAH (Buder et al., 2018) spectroscopic metallicities and $T_{\rm eff}$ from the InfraRed Flux Method, and validated against APOGEE DR14 (Abolfathi et al., 2018) and RAVE DR5 to ensure reliable parameter determinations.

The SkyMapper survey has covered most of the southern sky, subsequently observing stars across both C3 and C6. This provides a coherent photometry source for the fields and parameter determinations. Parameters were not available for all of the stars in the two campaigns, but the total number of stars remains significant for understanding population trends (377 - C3; 646 - C6). As they number fewer, the stars with spectroscopic values are considered a sub-sample of the total photometric population in this work. The spectroscopic values should provide tighter constraints on the final parameter distributions and better information regarding the chemistry of the stars than the photometry considering the higher-resolution observations. These are therefore viewed as a benchmark to which the larger photometric sample can be compared and underlying trends identified/ratified.

7.3 Method

We use grid based stellar modelling to extract the fundamental parameters of the stellar ensembles. A grid of models generated using MESA (Modules for Experiments in Stellar Astrophysics; Paxton et al. 2015) in conjunction with the Bayesian inference tool PARAM (da Silva et al., 2006; Rodrigues et al., 2014, 2017) were used. The PARAM code incorporates priors based on global asteroseismic properties to assist with a grid based, probabilistic parameter determination process. In addition to the luminosity, magnitudes and classical stellar parameters (e.g. log(g), $T_{\rm eff}$, [Fe/H]), the inclusion of $\nu_{\rm max}$ and $\Delta\nu$ as constraints is possible. An upper age prior can also be set, which we set as 20 Gyr. Though greater than the accepted age of the

Universe, 13.8 Gyr, current uncertainties on stellar ages are typically greater than 30%. Ages up to 20 Gyr are consistent with being drawn from a normal distribution centred on the Hubble age with $\sigma = 30\%$.

Unlike in previous chapters, the analysis code PARAM has been used here instead of AIMS. The projects to test AIMS and study the K2 Galactic Caps were run simultaneously. Hence, to ensure a timely production of results for K2, PARAM was chosen to perform the analysis. In addition, only the global asteroseismic parameters were available to use for the K2 stars. As PARAM had been shown to perform robustly with just this information (e.g. see Rodrigues et al. 2017), it was selected for use here over the (at the time) untested AIMS code.

The PARAM pipeline is compatible with multiple stellar evolution codes. Similarly to AIMS, it only requires a pre-determined grid of models in order to function. Nominally, the code was run using PARSEC grids of models, but it is also compatible with CLÉS and MESA models. The MESA models were selected for use in this instance as they display an improved performance in asteroseismic modelling compared to PARSEC and is able to model core-Helium burning stars, which is beyond the current capabilities of CLÉS.

Parameter values are determined statistically from the output probability density functions (PDF) produced by PARAM (Rodrigues et al., 2017). A choice of using the median or mode statistic is available to the user. The 68th and 95th percentiles are returned for all parameters in each case. Typical examples of the output distributions can be seen in Fig. 7.7. In each instance, the PDF, cumulative probability, mode (plus 68th percentile range) and median are displayed. Consistency between the modal and median values is indicative of a good parameter determination.

We adopt the modal values as the preferred choice of final parameter. The modal value is most representative of the distribution peak, particularly when approaching the limits of the underlying grid boundaries and priors. Post process, stars caught on the prior boundaries of the grid in age (20 Gyr) are removed from the sample.

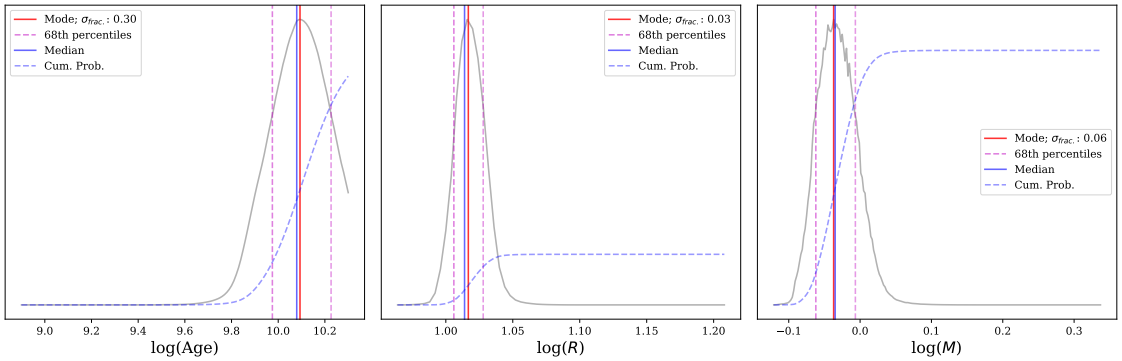

Figure 7.7: The normalised output PDF distributions for age (left), radius (middle) and mass (right) from PARAM for star EPIC 205909135 (C3). The PDF (grey), mode (red) and 68th percentiles (purple, dashed), median (blue) and cumulative probability curve (blue, dashed) are shown. The fractional uncertainty on the mode for each case is given.

These stars are forced to specific ages, potentially distorting the final parameters returned. The final sample sizes of C3 and C6 are 377 and 646 respectively (10% and 6% reduction).

7.4 Radii

An examination of the distribution of radii within the K2 sample provides a good indicator if a typical population of red giant stars is observed. Though the distribution will vary between observed populations, key features such as the red clump should be obvious from a pronounced peak at $\sim 10 - 11$ $R_{\odot}$. Figure 7.8 displays this characteristic, indicating the clump sample within the data. The figure shows a comparison of PARAM (i.e. asteroseismic) radii for K2 SM and APOKASC (panel A) and PARAM to *Gaia* K2 SM (panel B; $\sigma_{\varpi}/\varpi < 10\%$ cut applied) radii. Comparing K2 to APOKASC provides context for the results, but comparing the radii derived using PARAM and those computed using *Gaia* parallaxes provides insight into which values are most appropriate to use in future analyses. The *Gaia* distribution at the red clump peaks at a lower radius than that from PARAM for the same stars. As discussed in section 7.2.2, this shows evidence of an under-estimation of the stellar radii compared to asteroseismology.

An unexpected secondary peak at $\sim 7-8$ $R_{\odot}$ is present in both the spectroscopic

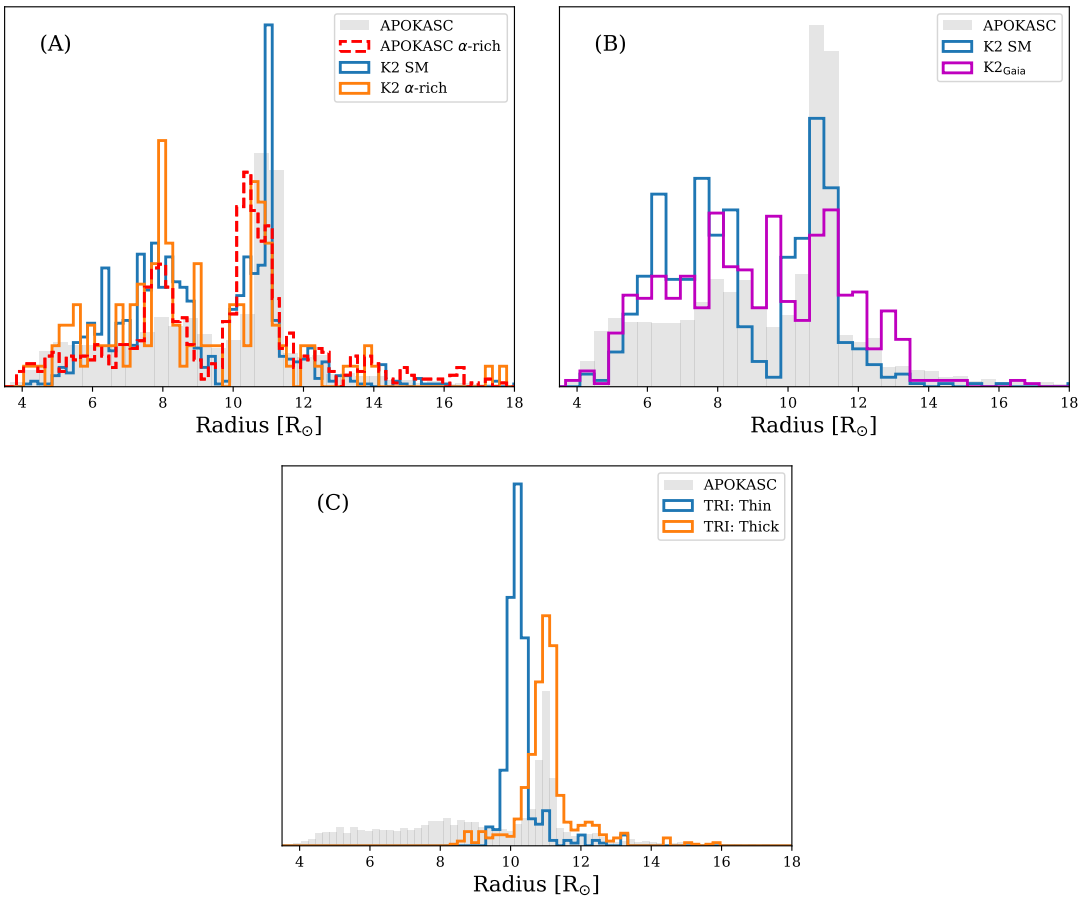

Figure 7.8: *(A):* Radius distributions from PARAM for the APOKASC (grey), APOKASC α-rich (red, dashed), K2 SM (blue) and the K2 α-rich (orange) samples. *(B):* Comparison of *Gaia* (magenta) and seismic (blue, PARAM) radii distributions for the same stars in K2 SM. Only stars with $\sigma_{\varpi}/\varpi < 10\%$ are shown. *(C):* TRILEGAL simulation of the K2 C3 field. The thin (blue) and thick (orange) disc populations within the simulation are shown. All distributions are normalised.

and photometric K2 data. The secondary peak is also a feature of a sample analysed in Miglio et al. (in prep.; red dashed, panel A). The sample is a population of α-rich ($[\alpha/\mathrm{Fe}] > 0.1$) stars from the APOKASC catalogue. This α-rich sample shows comparable features to those observed with the K2 stars, indicating that the feature is typically common to an older population, a trait synonymous with α-enhanced stars. A detailed examination of a Kiel diagram (Fig. 7.9) of the populations shows an overdensity of stars located at the RGB-bump, which is synonymous with the over density in radius observed.

The red giant branch bump (RGB-bump) is a notable feature of a stars ascent of the red giant branch. It is associated with the direct effect of the increase in the hydrogen abundance in the hydrogen-burning shell as it crosses the composition discontinuity left by the receding convective envelope, after the first dredge-up. In this scenario, the star reacts to the sudden increase in available fuel by lowering its surface luminosity and slowing down the evolutionary timescale. Refsdal & Weigert (1970) (see also Kippenhahn et al. 2012) noted a steep increase in the luminosity with the mean molecular weight, μ, and pointed out that the increase in the hydrogen abundance outside of the composition gradient caused a decrease in μ, and hence in luminosity. After the shell has moved past the discontinuity, the surface luminosity starts to increase again (see, e.g., King et al. 1985; Salaris et al. 2002; Riello et al. 2003).

The RGB-bump typically sits at a similar T_{eff} range, but a lower luminosity than the red clump (this varies in models with the position of the bump often predicted to be brighter than observations). As a consequence, the RGB-bump is predicted to peak at a lower radii range than that of the red clump, as evidenced by Fig. 7.8, panel (A) (RGB-bump at 8 $\mathrm{R}_{\odot}$; red clump: $\sim$ 11 $\mathrm{R}_{\odot}$). The mass and metallicity of the star has a greater effect on the luminosity of the RGB-bump than the red clump, hence there is a greater spread of radii values for the bump compared to the clump.

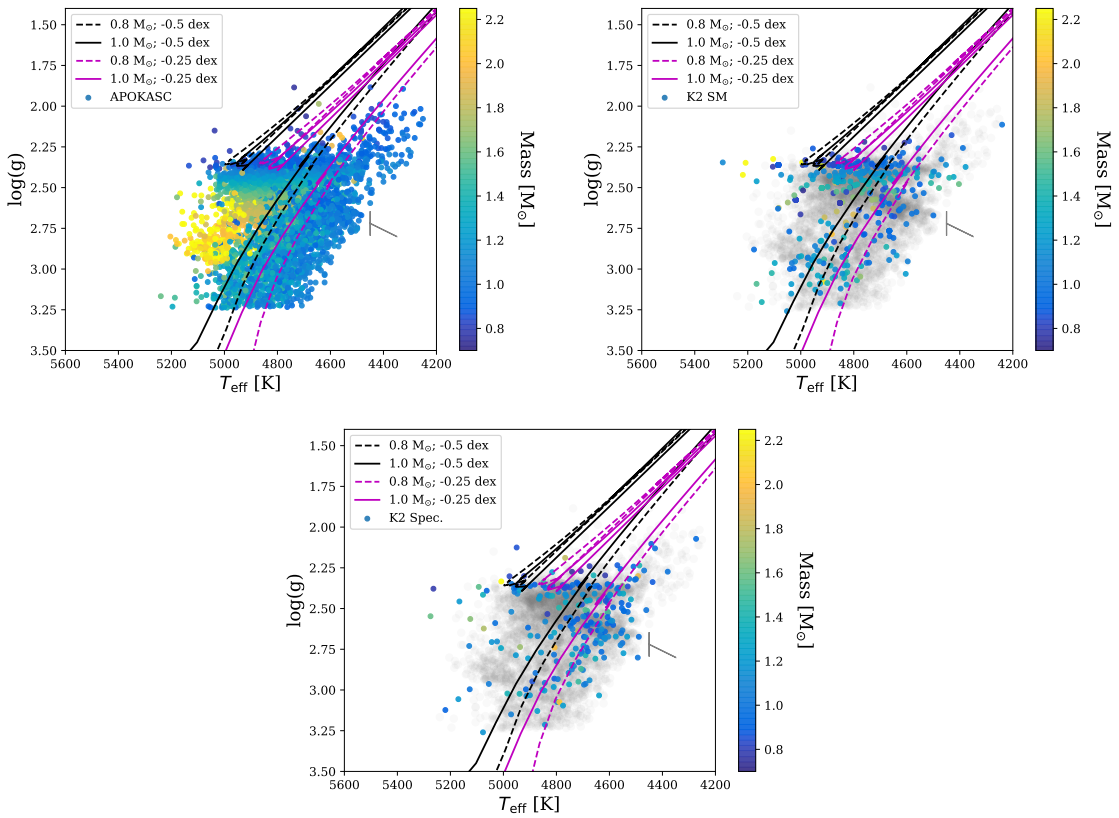

Figure 7.9: Kiel diagram with mass colour bar for the APOKASC (top left), photometric (top right) and spectroscopic (bottom) K2 samples. Tracks of different mass (0.8 $M_{\odot}$ - dashed; 1.0 $_{\odot}$ - solid) and metallicity (-0.5 dex - black; -0.25 dex - magenta) are overlaid as a guide. The α-rich APOKASC population is included in grey. Grey lines denote the location of the RGB-bump (RGBb).

Interestingly, there is a slight difference in the peak of the clump distributions of the full and α-rich samples for both APOKASC and K2. The clump distribution for the α-rich APOKASC sample peaks 0.5 $R_{\odot}$ lower than the full population. More metal poor stars were found to have lower radii. This difference is less significant ($\sim$0.1 $R_{\odot}$) in K2. Simulations from TRILEGAL (a TRIdimensional modeL of thE GALaxy, Girardi et al. 2012) predict that this is also related to the expected Galactic component that a star is a member of. The clump of the thick disc peaks at the observed α-rich radii and the thin disc at the full APOKASC radii as one may expect (see Fig. 7.8, panel C). The trend is a function of $T_{\rm eff}$, driven by mass and metallicity. Evidence of this can be seen in Fig. 7.10. Here, a Hertzsprung-Russell diagram, coloured by metallicity, of a K2 C3 TRILEGAL simulation is shown. It is evident that there is a division in the red clump population, whereby more metal poor stars are situated at hotter temperatures, hence, a lower radii than more metal rich stars, given that the luminosity is very similar. This is highlighted further by the inset of the Fig. 7.10, which shows a zoom in of the red clump population. The points circled in black are those identified as thick disc, with the remaining points belonging to the thin disc. The overlaid evolutionary tracks (as in Fig. 7.9) show this as a function of mass too. The hot clump sample ($>$ 4900 K) lies close to the low mass and metallicity track (0.8 $M_{\odot}$; -0.5 dex), whereas the cooler clump sample ($<$ 4900 K) is positioned closest to the high mass and metallicity track (1 $M_{\odot}$; -0.25 dex).

A separation in the populations in radius is apparent (though some contamination from first ascent RGB stars is present), further confirming the trends observed in Fig. 7.8 and Fig. 7.10. This is not conclusive evidence that the positioning of the peak clump radius can be used as a tracer for Galactic components/evolution, but opens up possibilities to explore this further (see Girardi 2016 and references therein).

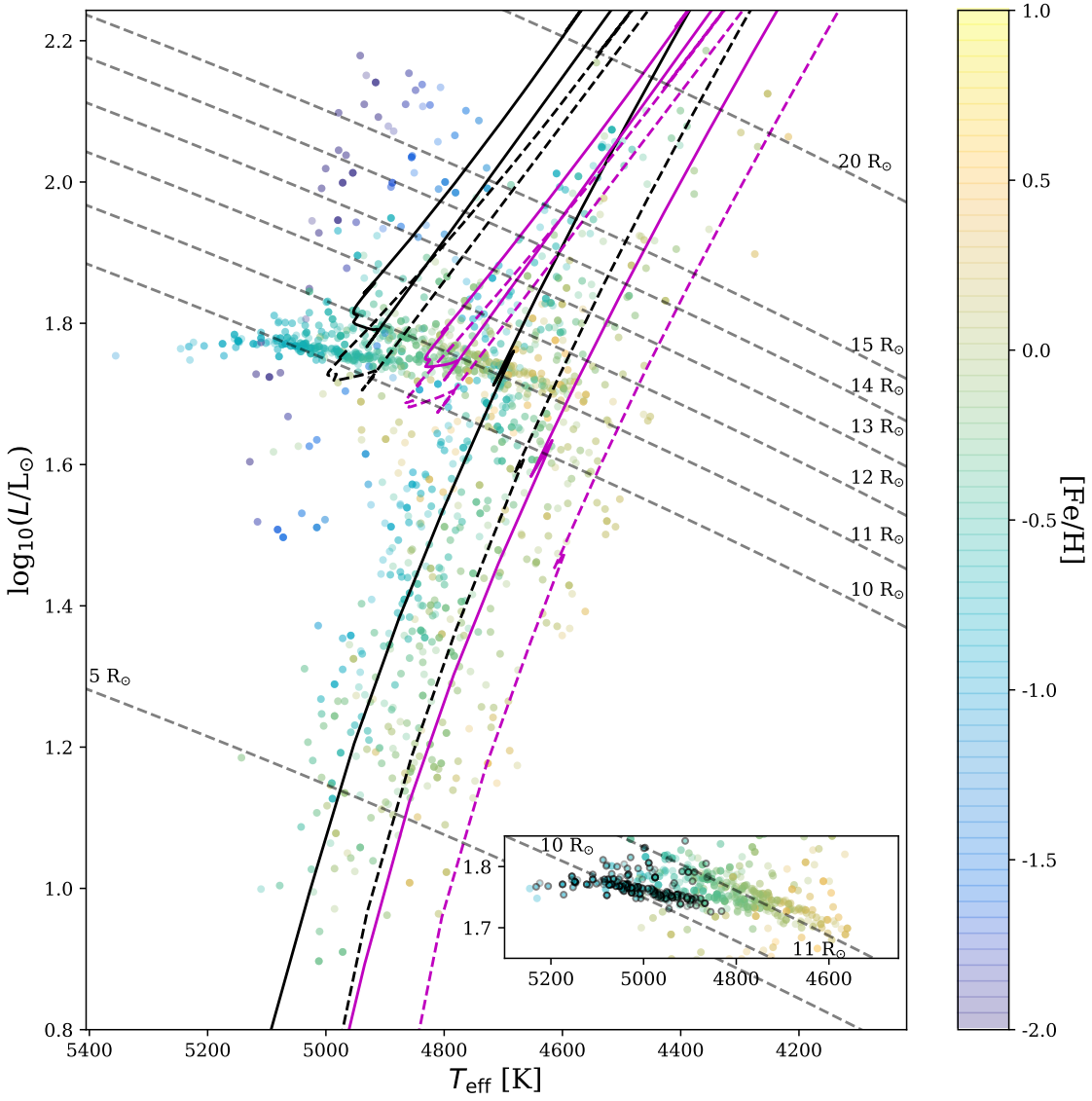

Figure 7.10: HRD of a K2 C3 TRILEGAL simulation. An [Fe/H] colour bar has been used, with lines of constant radius included (grey dashed line; values marked on plot). Tracks of different mass (0.8 $M_{\odot}$ - dashed; 1.0 $_{\odot}$ -solid) and metallicity (-0.5 dex - black; -0.25 dex - magenta) are overlaid as a guide. *Inset:* An enlargement of the red clump population, with stars classified as thick disc in the simulation denoted by black circles. Only red clump stars are shown here, using the classifier in TRILEGAL.

7.5 Masses

Given the tight age-mass relation expected for red giant stars (Kippenhahn et al., 2012), stellar masses inferred by asteroseismology provide an excellent proxy for age (e.g., see Miglio, 2012; Davies & Miglio, 2016). Understanding the mass distribution of a population therefore allows early inferences about the expected age distribution to be made. Panel A of Fig. 7.11 shows the mass distribution of the K2 SM, K2 Spec. and APOKASC samples as a function of vertical height, Z, from the Galactic plane. It can be seen that all samples show a trend of increasing vertical extent with decreasing mass. There is evidence of a metallicity gradient, with decreasing metallicity observed as one moves out of the plane and towards lower masses. These trends are comparative with those expected of a thin/thick disc structure, in particular with the low masses extending to greater vertical extent being reflective of the expectation of observing older stars further from the plane (see section 7.6; Miglio et al. 2013b; Casagrande et al. 2016).

The remaining panels of Fig. 7.11 show the resultant populations after additional cuts/re-analyses of the K2 SM and K2 Spec. data were made (same alterations applied to the background APOKASC samples). The effects due to using masses from scaling relations (Kjeldsen & Bedding, 1995) (B), removing the red clump by radius (C) and using a grid including microscopic diffusion (D) were explored to test for any property dependencies within the populations. Except additional scatter at low masses when the scaling relations are used (a likely over-estimation of the masses; see Viani et al. 2017 and references therein) and varying sample sizes, the initial trends seen in panel A are invariant to the changes implemented. The high mass scatter and shape of the mass/Z relations remain consistent throughout, as does the perceived metallicity gradient. The robustness of these trends gives confidence to the derived stellar properties in the K2 SM and K2 Spec. samples being a true reflection of the population and its features.

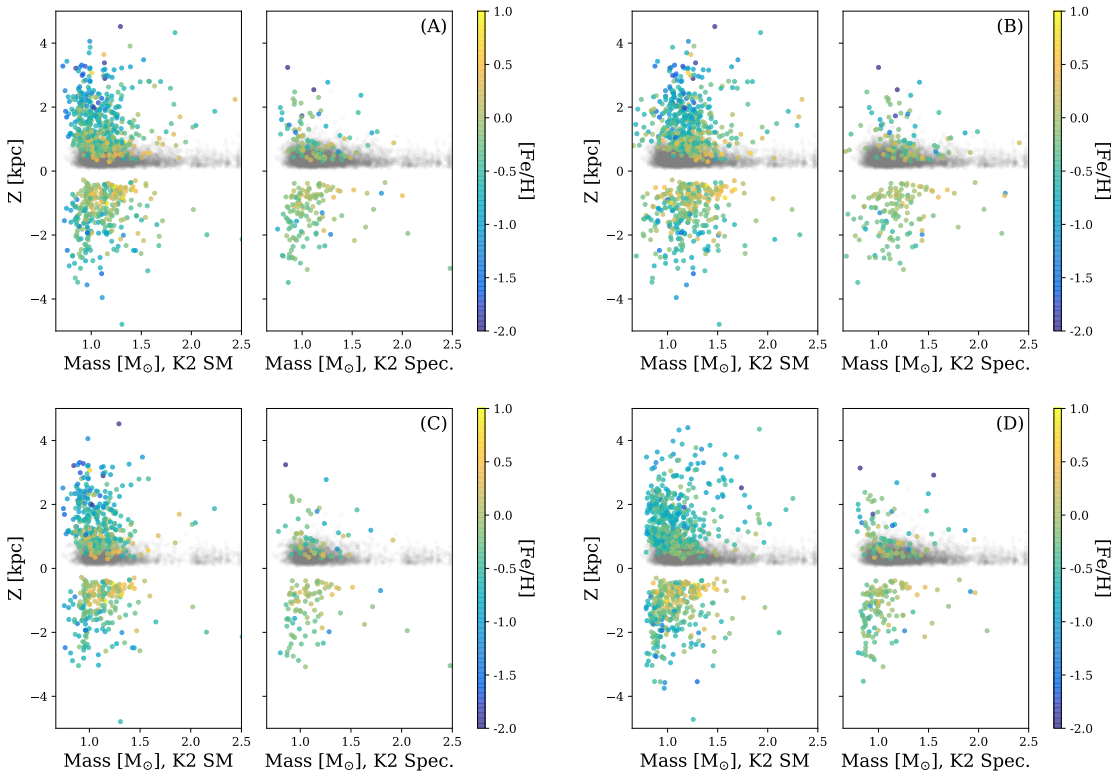

Figure 7.11: Mass against vertical height above and below the Galactic plane (Z) for the K2 SM (left) and K2 Spec. (right) samples in each panel. An [Fe/H] colour bar is shown. The metallicity scale is the same for each subplot. The APOKASC sample is shown in grey. *(A):* Original K2 SM and K2 Spec. samples. *(B):* Masses calculated from scaling relations. *(C):* Red clump population has been removed. *(D):* Populations re-analysed with a grid including diffusion.

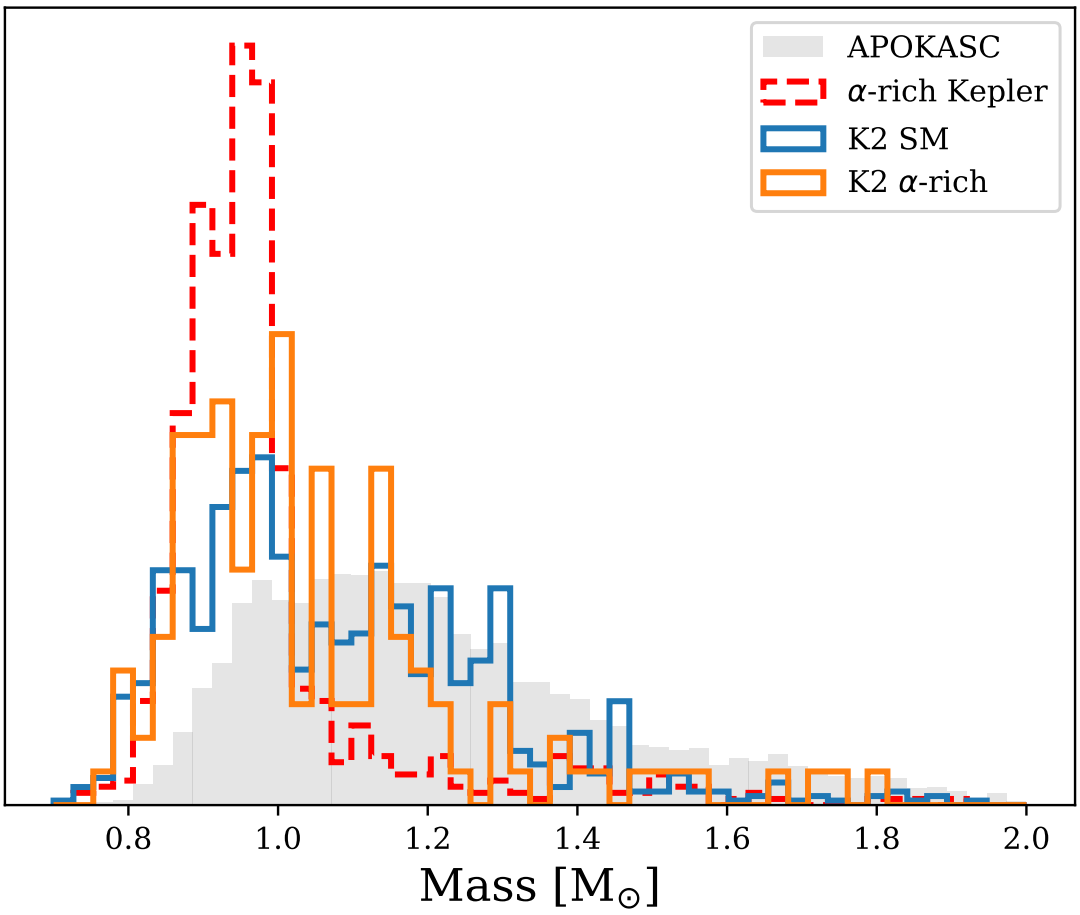

Figure 7.12: Normalised mass distributions from PARAM for the APOKASC (grey), APOKASC α-rich (red, dashed), K2 SM (blue) and the K2 α-rich (orange) samples.

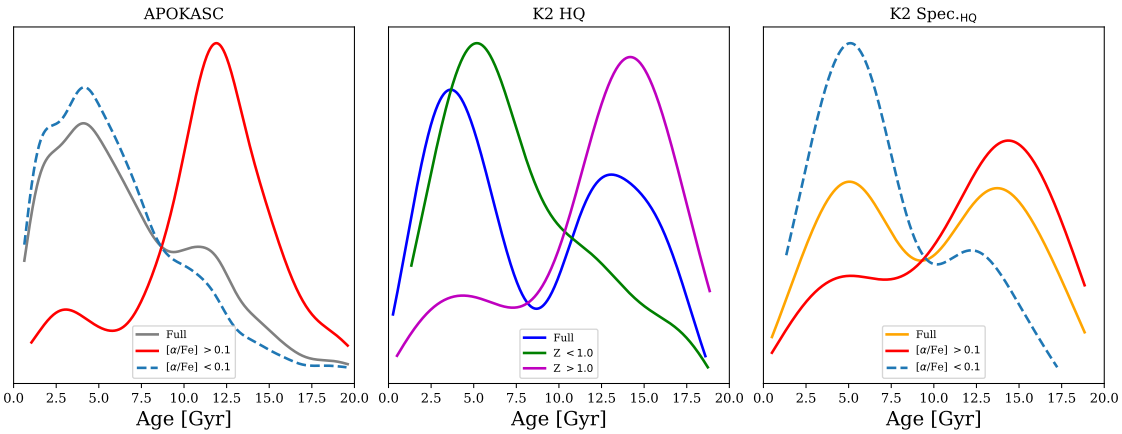

Figure 7.13: Normalised age distributions for the APOKASC and K2 populations. *Left:* Nominal (grey), α-rich (red) and α-poor ([α/Fe]$<$ 0.1; blue dashed) APOKASC sample age distributions. *Middle:* $\mathrm{K2_{HQ}}$ complete (blue), $|Z| < 1.0$ kpc (green) and $|Z| > 1.0$ kpc (purple) distributions. *Right:* K2 $\mathrm{Spec._{HQ}}$ (orange) and K2-APOGEE α-rich (red) and α-poor ([α/Fe]$<$ 0.1; blue dashed) distributions.

Figure 7.12 shows the mass distributions of both the full and α-rich APOKASC and K2 populations. The distributions show that the K2 SM sample contains a larger proportion of low mass stars than in APOKASC, suggesting that the population of these K2 fields is potentially older than that of APOKASC and is discussed further in section 7.6. It is also shown that the number of α-rich stars in these populations is enhanced for lower masses, suggesting the older a red giant star is, the more α-enhanced it is likely to be.

7.6 Ages

Many arguments surrounding the definition of the thin and thick discs, in particular their formation, centre largely on the age distribution of the populations and indications of enhanced star formation. Conclusively proving a distinction in age between the populations defined geometrically and/or chemically is difficult due to typical age uncertainties of $>$ 40%. The samples used in this work have median uncertainties of $<$ 35% ($\mathrm{X_{HQ}}$ samples), allowing general trends to be extracted.

Figure 7.13 shows a comparison of the age distributions[3] of the APOKASC

[3]Kernel Density Estimates were generated using the `python` module `PyQt-Fit`, `1DKDE`. Default smoothing applied.

(grey, left panel, Miglio and Davies et al., *in prep.*), $K2_{HQ}$ (blue, centre panel) and K2 Spec.$_{HQ}$ (orange, right) samples for stars with age uncertainties $< 35\%$. Each set of stars was analysed with an extended age prior of 20 Gyr, hence the un-physically extended age ranges. As previously stated, the magnitude of the uncertainties are such that these values remain consistent with the age of the Universe within 1-2 σ. It is the features of the distributions that are of most interest though. The APOKASC population follows closely the age distribution for giants shown by Casagrande et al. (2016) with a large peak at 5 Gyr and a smaller peak at 11 Gyr. In addition, the α-rich population (red) maps closely the distribution presented in Silva Aguirre et al. (2018). The distribution peaks broadly at $\sim$ 12 Gyr, with a small overdensity at 3 Gyr due to a population of young α-rich stars (e.g. see Fuhrmann 2011; Chiappini et al. 2015; Martig et al. 2015; Johnson & APOKASC Collaboration 2016; Jofré et al. 2016). The dominance of the 12 Gyr peak in the α-rich population indicates that this influences the appearance of the secondary peak in the nominal APOKASC sample. A reduced prominence at 12 Gyr for the α-poor ([α/Fe]< 0.1) APOKASC sample confirms this, reaffirming the expectations that older stellar populations have enhanced α-element abundances. The consistency of our results with these studies gives confidence to make clear comparisons with results from K2.

Considering the APOKASC and K2 populations extend vertically beyond 1 kpc, it is expected that some mixing will occur between disc populations as the thin disc transitions up into the thick disc. Hence, both samples should contain a prominence related to each component. The broadness of the peaks is not of concern here as it is known that the K2 data is not as high quality as the *Kepler* data and therefore greater uncertainties are expected. Figure 7.14 shows the impact of different age uncertainties on the shape of a simulated distribution. Large uncertainties mask the original features, emphasising the importance of obtaining high-precision age determinations.

The $K2_{HQ}$ photometric (blue) and K2 Spec.$_{HQ}$ (orange) distributions are shown

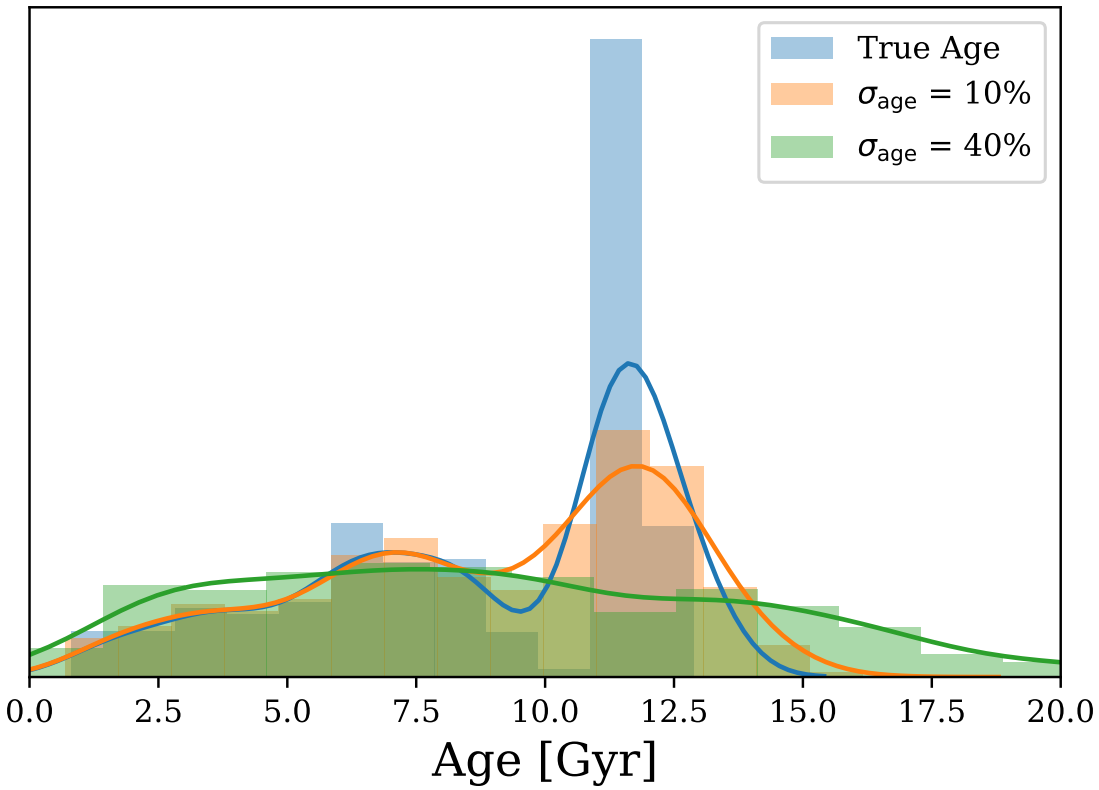

Figure 7.14: The normalised age distribution for a synthetic MW population (TRILEGAL; uniform thin disc star formation from 9 Gyr; short burst for thick disc formation at 11 Gyr) is shown (blue). This population is perturbed by age uncertainties of 10% (orange) and 40% (green) to demonstrate the necessity for high precision age determinations. It is clear that even at 10% some structural details of the population are blurred, with all structure lost when the uncertainty is 40%.

in the centre and right hand panels of Fig. 7.13. The $K2_{HQ}$ distribution peaks predominantly at 5 Gyr in concordance with APOKASC. The distribution then passes through a minimum at $\sim$ 9 Gyr before gradually increasing again towards older ages. This differs slightly to the spectroscopic sample, which shows an earlier minimum at 8 Gyr (as with APOKASC) and a clearly defined secondary peak at 14 Gyr. Given the current uncertainties on age, the fact that the two samples differ both in magnitude range and in photospheric parameters (e.g. for the stars in common the spectroscopic temperatures are on average $\sim$ 50 K lower than SkyMapper's) these small apparent age differences are likely due to be dominated by target selection biases and systematic effects. K2 Spec._{HQ} also shows a more even weighting between the young and old peaks, suggesting a split population. As previously discussed, the K2 age uncertainties are larger compared to APOKASC, which contributes to the overall washing out and extension of features in the distributions. The greater defined features of the spectroscopic sample compared to the photometric is symptomatic of the quality of the input parameters used in the analysis, with the spectroscopic surveys providing improved input parameters and, hence, final uncertainties. Similarly to with APOKASC, the α-rich and α-poor spectroscopic components from APOGEE were plotted. It is clearly shown that the young and old peaks are dominated by the α-poor and α-rich sub-samples respectively. This further confirms the expected chemical dichotomy of stars from different generations.

There is minimal difference between the age distributions in the K2 fields when diffusion is included within the grid models. The young population peak is shifted closer to 5-6 Gyr and the old population peak is again positioned at $\sim$13-14 Gyr. Considering the uncertainties, these shifts in the peaks of the age distribution are not significant deviations from those determined without the inclusion of diffusion. As the effect is minimal on the age distribution, we do not pursue the results including diffusion further.

The higher age peak, and larger proportion of stars at older ages when using

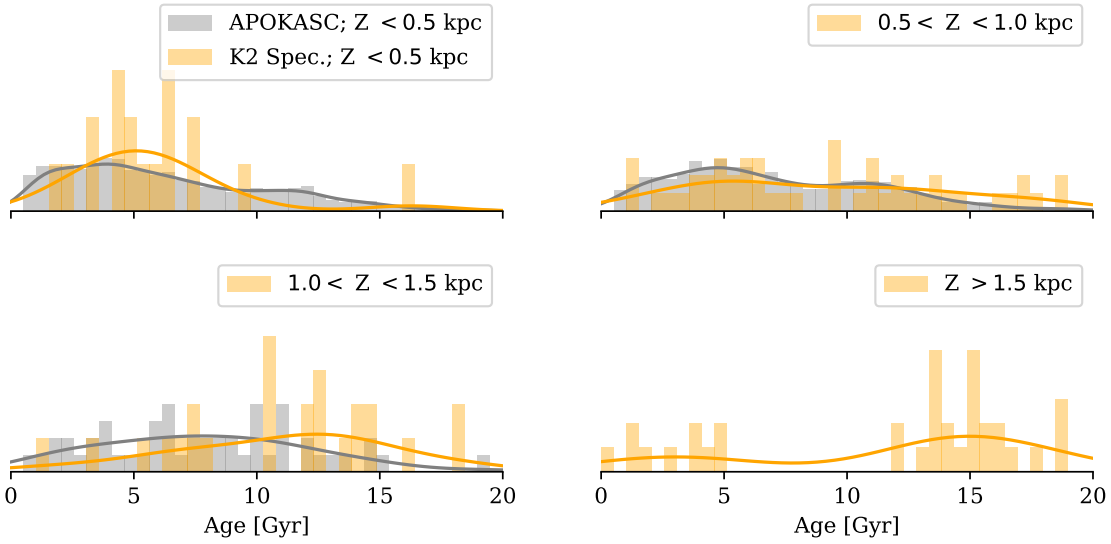

Figure 7.15: K2 Spec.$_{\rm HQ}$ sample age distribution as a function of Z (0.5 kpc bins). A comparison to the APOKASC sample is performed up to 1.5 kpc as beyond this the numbers are insufficient for a meaningful comparison. Samples of stars with $\sigma_{\rm age} < 35\%$ shown.

spectroscopic inputs, indicates that the K2 fields contain an older population than the *Kepler* sample; but is this just a radial selection effect or due to sampling a greater vertical extent? Considering the majority of the APOKASC sample extends out to 1 kpc, the population trends for the K2$_{\rm HQ}$ stars above (purple) and below (green) $\pm$1 kpc are also shown on the centre panel of Fig. 7.13. The sample below 1 kpc follows closely that of the APOKASC sample, with a very clearly defined young population at 5 Gyr, but has few stars beyond 10 Gyr, with the distribution dropping off significantly and flattening beyond 9 Gyr. In contrast, the population beyond 1 kpc shows a minimal peak at $\sim$5 Gyr and dominant old population peak at 15 Gyr. The difference in the shape of the age distributions above and below 1 kpc is stark enough to show that the stellar population changes with increasing Z.

For further confirmation that the age distribution changes primarily with Z and not with Galactic radius, Fig. 7.15 shows the age distribution of the K2$_{\rm HQ}$ field and APOKASC samples in vertical bins of 0.5 kpc. The C3 field was chosen as this field samples significantly beyond 1.5 kpc after all cuts are applied, whereas

C6 contains too few stars beyond 1.5 kpc for sensible conclusions. For the same reasoning, the APOKASC sample is only shown out to 1.5 kpc. The first two bins of Fig. 7.15 (0 - 1 kpc) show that the APOKASC and K2 populations follow each other closely. A two sample Kolmogorov-Smirnoff test confirms this consistency with p-values greater than 0.05 for each bin ($p_{Z<0.5} = 0.28, p_{0.5<Z<0.5} = 0.09$), rejecting the hypothesis that the APOKASC and K2 C3 population age distributions are significantly different in these ranges. This is a good indication that, up to 1 kpc, the age distribution of similarly selected stars is expected to be the same at these different Galactic radii. Consequently, any further inferences can be concluded to be due to the vertical rather than radial properties of the fields.

Reflecting the trend observed in Fig. 7.13, the bins beyond 1 kpc show an increasingly divergent population, with consistent young and old populations. This was not expected due to the typical belief that the thick disc is composed of older stars. An explanation of this is the presence of the aforementioned young (< 7 Gyr), α-rich stars. Considering the K2 Spec., $\sigma_{\rm age} < 35\%$ sample, $\sim 8\%$ of the stars (accounting for increased intrinsic uncertainties on age compared to *Kepler*) fall into this category, compared to $\sim 2\%$ in APOKASC (same $\sigma_{\rm age}$ cut). Of these stars, 20% can be found beyond 1 kpc from the Galactic mid-plane. This indicates an expectation to see non-insignificant numbers of these stars at high $|Z|$. Fig. 7.16 illustrates this trend. The figure is a replication of Fig. 7.1, but only for the K2 Spec.$_{\rm HQ}$ sample and is coloured by age. It is readily apparent that the older population stars (> 10 Gyr) dominate at high-$|Z|$ ($> |1.5|$ kpc), but contamination by young stars is clearly visible. This population also begins to demonstrate the bimodality in [α/Fe] between the discs, with some members of the young thick disc showing similar chemical properties to the older population. Only a small number of these stars have been observed, though. The significance of the population will only be known once a larger sample has been studied. The implications of the findings may be significant for understanding some of the mechanisms of Galactic evolution.

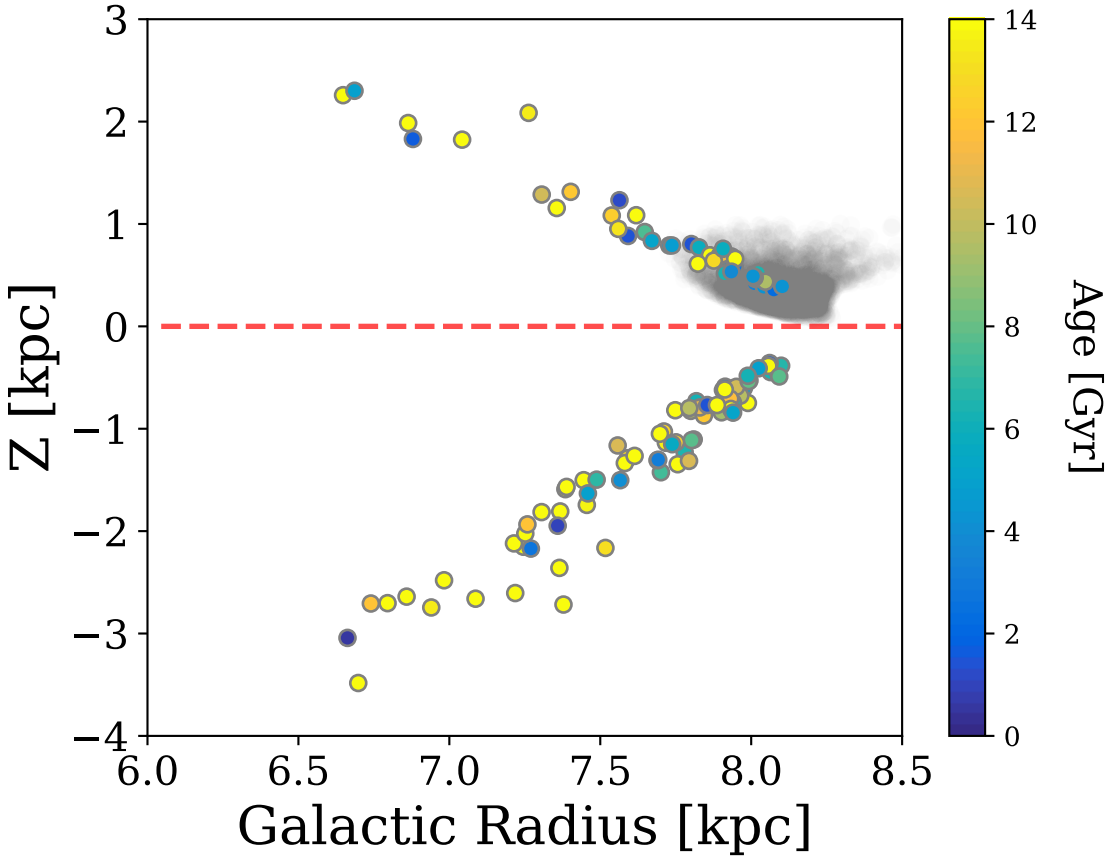

Figure 7.16: As Fig. 7.1, but showing the age distribution of the K2 Spec.$_{\rm HQ}$ sample.

The young, α-rich stars are not the only young stars at high $|Z|$ (e.g. Jofré et al. 2016; Hayes et al. 2018). There are many questions surrounding the young populations far from the Galactic mid-plane. These include whether these stars have formed in situ; they migrated and have been captured as they pass through this region of the Milky Way; or are they products of stellar binary evolution and mergers (Izzard et al., 2018)? Each scenario has implications on the evolution of the Galactic structure. A thorough treatment of the kinematics is required to further disentangle the origins of these stars. Though not a pressing concern for this work, future exploration with *Gaia* data to examine the kinematics and orbits of these stars will be undertaken to determine if they indeed belong to this population or are migrators.

The shape of the age distributions are a reflection of the star formation history of the Galaxy. A feature in common for all of the age distributions shown in Fig. 7.13 is a minimum. The presence of this feature is indicative of a quenching period, in which the star formation rate drops and reduction in stars of certain ages is observed. With well defined peaks in both the K2 SM and APOKASC distributions, there is evidence to support two epochs of star formation. Tighter age constraints are required before the lengths of any epochs of suppressed/enhanced star formation can be confirmed, but the results are concurrent with predictions of a cessation in star formation at $\sim$ 9 Gyr (e.g. Haywood et al. 2016) and the predictions of the two-infall model (Chiappini et al., 1997, 2001; Chiappini, 2009) of distinct formation epochs for the thin ($|Z| \leq 1.0$ kpc, $[\alpha/\mathrm{Fe}] \leq 0.1$, age ≤ 9 Gyr) and thick ($|Z| > 1.0$ kpc, $[\alpha/\mathrm{Fe}] > 0.1$, age > 10 Gyr) discs.

7.7 Conclusion

K2 campaign fields 3 and 6 have been used to demonstrate further the capacity of K2 as a Galactic archaeology mission. The existence of observations towards the Galactic poles in addition to the *Kepler* field highlight the importance of these

observations to contributing towards some of the key questions surrounding the existence of the Galactic thin and thick discs.

Initial investigations of the K2 campaigns C3 and C6, and *Kepler* populations provided evidence of the K2 fields presented containing a larger proportion of metal poor stars than found with *Kepler*. Further differences were found in the sample parameter distributions:

- *Radii* - Both populations exhibited the expected prominence due to the red clump, but the K2 distribution showed an additional, more pronounced compared to *Kepler*, peak at $\sim 8\,R_{\odot}$. The feature was also found to be significant in a sample of *Kepler* α-rich stars. It relates to the RGB-bump, and its prominence in 3 fields of different pointing means it could be used as a potential indicator of α-rich stellar populations in future.

  A shift in the position of the red clump peak was observed between the *Kepler* full (APOKASC) and α-rich (APOKASC α-rich) samples. The α-rich sample showed a peak $0.5\,R_{\odot}$ lower for the clump compared to the full sample. Using a TRILEGAL simulation of the *Kepler* field, a divergence in the clump location was evidenced when using the simulation's Galactic component identifier. The α-rich peak aligned with TRILEGAL expectations of the thick disc population as it is expected to be older and metal poor. The full sample aligned with the thin disc peak. The position of the peak of the red clump could therefore be considered as an indicator of the type of population being observed, but additional research beyond the scope of this paper would be required to establish this.

- *Mass* - We demonstrate the robustness of our results to population variance and underlying physical prescriptions when considering the mass against Z distribution of the K2 fields. A trend of decreasing mass with increasing $|Z|$ is observed, with some scatter at high mass. We also find evidence of a

decreasing metallicity gradient with decreasing mass and increasing $|Z|$. These trends remain consistent when different mass sources are used, the red clump is removed from the population and a different underlying grid is used for the analysis. The robust nature of these global trends lends confidence to our inferences of global population properties being representative of the sample.

- *Ages* - As an excellent example of one of the most metal-poor asteroseismic populations observed, the resultant K2 age distributions reveal possible epochs of enhanced star formation. The observed sample also shows the evolution of the age distribution as a function of height above the Galactic mid-plane, matching the *Kepler* sample closely out to ~ 1 kpc in concordance with the works by Casagrande et al. (2016) and Silva Aguirre et al. (2018), but differing significantly beyond this distance. Further investigation clearly indicated that as Z increases, the population becomes dominated by older stars. The changing distributions not only lend support to the theories indicating the thick disc is older than the thin disc, but reaffirm the desire for precise ages to allow for the confirmation of any possible epoch of quiescence in star formation and age bimodality associated with chemistry. It must be noted that some young stars (< 4 Gyr; possible binary products or migrators) remain at high Z and require further investigation as to their origin and nature.

  A strong bimodality was also observed in the age distribution for both *Kepler* and the K2 fields (Fig. 7.13), with distinct young and old population peaks at 5 and 14 Gyr. Clear associations with $|Z|$ and [α/Fe] were attributed to each peak: 5 Gyr - low-α, $|Z| \leq 1.0$ kpc (thin disc); 14 Gyr - high-α, $|Z| > 1.0$ kpc (thick disc). The chemical age dichotomy was also confirmed with the *Kepler* sample, where the peak at 12 Gyr is due to the α-rich population. Each sample presented contains a minimum, suggestive of a time delay between the formation of these populations. Given the geometric and chemical characteristics of the old and young populations, the argument can be made that this

is representative of a time difference in the formation histories of the thin and thick discs.

Further work remains prior to making definitive conclusions on the true age profile of the Galactic disc. The $K2_{HQ}$ sample shows a glimpse of what is achievable with improved precision in age determination, as does the K2 Spec. sample. However, an increase in the sample size is necessary to lend further weight to our conclusions regarding the population properties. The asteroseismic yield of stars towards the Galactic poles is continuing to increase with all sky observations from the NASA TESS mission (Ricker et al., 2015) currently in progress. Short observation periods of 30 days provides challenges to extract high-quality asteroseismic information though (e.g. see Miglio et al. 2017; Mosser et al. 2019), reducing the potential effectiveness of this data set at providing the high quality parameter determinations desired. Observation baselines in excess of 150 days are ideally necessary in order to achieve a precision in age below 20% (Miglio et al., 2017). An increase in spectroscopic coverage of the K2 campaign fields would yield improvements in parameter determination though, with the known high quality of the asteroseismic inferences linked closely to the quality of input spectroscopic parameters. With more wide field spectroscopic surveys coming online in the near future (e.g. WEAVE, 4MOST), in addition to increased asteroseismic information from additional K2 campaign fields with observations of the Galactic poles, the field is well positioned to continue to exploit the opportunities afforded by the K2 mission to understand the true nature of the vertical structures of the Milky Way.

Chapter 8

Conclusion and Future Prospects

In this thesis, we worked towards the objective of improving the precision and accuracy of stellar parameters in the context of trying to characterise the vertical structure of the Milky Way. In particular, the study of solar-like oscillations in red giant stars has been conducted. This class of star is believed to be an excellent tracer of Galactic structure due to the great distances at which high-precision parameters can be determined compared to main sequence and sub-giant stars. A focus on the improvements in age determinations using asteroseismology of these solar-like oscillators was the main driving force of this work, with attention given to the improvements achievable when using the individual mode frequencies themselves.

A new stellar parameter determination code, AIMS, was introduced in Chapter 5. The objective of this new tool is to be able to use the information available from the individual modes of oscillation to improve the current performance of asteroseismic grid modelling. We take a unique approach, combining a Markov-Chain Monte-Carlo algorithm with model interpolation for an accurate and efficient approach. Various tests are presented, designed to determine the performance levels of all aspects of the program. Comparisons to synthetic observations are performed for both main sequence and red giant branch stars, with consistency of $< 2\sigma$ with the expected value returned. Similar results were achieved when testing data from the Sun. In some cases, the disparities appeared significantly higher, but this can be

attributed to the high precision determination of the parameters when using the individual mode frequencies. Importantly, the age was determined to the same level of precision as the literature, showing its potential to provide precise determinations. One must be cautious when fitting with the individual mode frequencies though, as the uncertainties can be underestimated as they tend to be reflective of the statistical precision that can be achieved, and less informative regarding any systematics.

In addition to testing with artificial models and the Sun, a comparison to an existing asteroseismic analysis code, PARAM, was performed. PARAM utilises the global asteroseismic parameters the large frequency separation, $\Delta\nu$, and frequency of maximum amplitude, $\nu_{\rm max}$, as constraints for grid modelling. It is possible to run AIMS in a similar way to PARAM, hence a comparison between the codes modelling similar red giant branch stars was performed. Without the explicit use of the individual frequencies as a constraint in any form, AIMS showed comparable performance to PARAM in mass and age uncertainty for all combinations of classical constraints used. An order of magnitude improvement in the precision of the mass and age determinations (0.2% in mass; 3% in age) were observed when testing the same star, but including the individual frequencies as a constraint. This leap in precision clearly highlights the importance of exploiting the individual modes.

During testing, it was observed that the surface effect correction designed to correct for the systematic offset between model frequencies and observed frequencies may be influencing the model selection and affecting the final parameters. In Chapter 6, a series of tests were performed using five eclipsing binary stars and members from open clusters observed by the *Kepler* telescope. The variability of the model selection dependent upon the surface correction selected and the influence of the model selection on the goodness of fit to the data were tested. Applying various prescriptions for surface effect corrections to the binary stars, it was shown that, though generally consistent, the choice of surface correction clearly influenced the final model selection. Shifts of up to a few percent were found in mass and radius,

despite all other parameters remaining the same. The Ball & Gizon (2014) combined term was found to be the most stable of the corrections, with an offset between the theoretical and observed frequencies of order 1% at $\nu_{\rm max}$ and an average $\chi^2_{\rm red.}$ value of 0.15 for all of the binaries. Comparisons to the parameters determined through RV measurements by Gaulme et al. (2016) and Brogaard et al. (2018) were also performed. It was shown that the mass and radii determinations were improved in relation to the radial velocity determination compared to corrected scaling relations, again highlighting the potential of AIMS for excellent parameter determination.

Using the preferred surface correction from the binary stars, members of the open clusters NGC6791 and NGC6819 were analysed. The mean mass of the RGB stars were found to be consistent with expectations from eclipsing binaries observed in the clusters, though the distance moduli determined through parameters from AIMS were lower than anticipated in each instance. The quality of the model fitting was also examined for NGC6819. Examples of echelle diagrams and posterior sample distributions were shown for star with a small (0.6%) and large (5.4%) percentage difference between the observed and theoretical frequencies at $\nu_{\rm max}$. Systematic trends in frequency, poor fitting of the surface corrected frequencies and limited parameter space sampling were observed for the star with a large percentage difference. This was consistent with other stars with large offsets not presented here. The large offsets in frequency mean the surface correction parameter begins to dominate the fit as a large value is required to recover the observations. As with any grid modelling, one should be vigilant and check the returned fits and distributions to ensure that a reasonable model has been selected for analysis. Improvements in the grid selection and inputs as well as the choice of correction may improve results.

In Chapter 7 we explored how the application of asteroseismology to red giant stars can be utilised in the context of Galactic Archaeology. As K2 data was used, it was not possible to obtain individual mode frequencies for the stars in the sample. Therefore, using high-resolution spectroscopic data in combination with the global

asteroseismic information for stars in the K2 campaign fields 3 and 6, a study of the stellar populations extending towards the Galactic caps was performed. The populations analysed were found to probe further out of the Galactic plane than the nominal *Kepler* mission, making them excellent fields to study the disc-like component of the Milky Way. The K2 populations were shown to be more metal poor than the *Kepler* too, making this one of the most metal poor populations studied with asteroseismology to date. A strong metallicity trend in radius was observed. The position of the radius of the red clump was found to shift to a lower value for an [α/Fe] enhanced (> 0.1) population. Comparisons with a synthetic population showed this to be consistent with the expected red clump radii peaks of the the thin and thick discs, whereby the thick disc is positioned at a lower radius than the thin disc. The key result though is the presence of a bimodal age distribution, with peaks at 5 and 14 Gyr respectively. We show that the older peak primarily consists of the [α/Fe] enhanced population for both the K2 and *Kepler* fields. We also demonstrate the age distributions change as one moves further from the Galactic plane, with the younger population dominating below 1 kpc, and the older population more prominent beyond this. This result is indicative of the vertical disc structure of the Milky Way towards the Galactic centre, with an old [α/Fe] enhanced component observed at high $|Z|$ (thick disc), and a solar-[α/Fe], young population closer to the Galactic plane.

8.1 Future Prospects

The results presented in this thesis showcase the potential for the use of asteroseismology within Galactic Archaeology, even though the ensemble results were limited by the precision achievable on the ages. The key results from K2 were determined from a sub-sample with age uncertainties $< 35\%$, but this needs to be improved further for any serious definitions of populations by age can be inferred. Longer observational baselines of ~ 150 days are required in order to resolve the individ-

ual mode frequencies, double the duration of the K2 field observations. Fortunately, there is potential for the observational baselines to be increased. The ongoing NASA TESS and future ESA PLATO missions will perform all sky surveys, opening up the sky to asteroseismic detections. Overlapping observations between missions will extend the baseline observations for targets, allowing greater information to be extracted from the power spectra and eventually the individual modes themselves. For now, the *Kepler* mission remains the benchmark for asteroseismic observations, and needs to be exploited further to improve current analysis methods ready for subsequent improvements in data quality.

Clearly, one still needs to explore further the systematic effects on the ages, masses and radii of stars due to the input model physics. Improvements in data quality will only propagate into more accurate and precise stellar parameters if the systematics are understood. Here, we showed an example of the testing required with the surface-effects corrections and began to examine the temperature offsets between models and observations. These studies need to be taken further and applied to a greater range of parameters (e.g. mixing length parameter, convective overshooting, mass loss...) to add further clarity to and build upon the platform laid out here.

The field of Galactic Archaeology itself is wonderfully poised to continue growing and achieve its main objective of characterising the fossil record of the Milky Way. *Gaia* DR2 has already been transformative in our view of the Milky Way, and further data releases will only add clarity and greater detail to what has already been achieved. An increasing number of large scale spectroscopic surveys such as the WEAVE and 4MOST are being developed with specific Galactic Archaeology programs in mind. With the volume and breadth of data available to the field, the future success will be built on the precision and accuracy to which the stellar parameters can be determined. In particular, if the age precision can be reliably reduced, then the prospects of what can be achieved in the near future are incredibly exciting.

Chapter 9

Publications

A list of publications on which I have led or co-authored during the course of my Ph.D.:

i **B. M. Rendle**, G. Buldgen, A. Miglio, D. R. Reese, A. Noels, G. R. Davies, T. L. Campante, W. J. Chaplin, M. N. Lund, J. S. Kuszlewicz, L. A. J. Scott, R. Scuflaire, W. H. Ball, J. Smetana, and B. Nsamba, AIMS - A new tool for stellar parameter determinations using asteroseismic constraints, Monthly Notices of the Royal Astronomical Society, 484 (2019), pp 771-786

ii L. Bugnet, R. A. García, G. R. Davies, S. Mathur, E. Corsaro, O. J. Hall, and **B. M. Rendle**, FliPer: A global measure of power density to estimate surface gravities of main-sequence Solar-like stars and red giants, Astronomy & Astrophysics, (2018)

iii G. Buldgen, **B. M. Rendle**, T. Sonoi, G. R. Davies, A. Miglio, S. J. A. J. Salmon, D. R. Reese, D. Bossini, P. Eggenberger, A. Noels, and R. Scuflaire, Mean density inversions for red giants and red clump stars, Monthly Notices of the Royal Astronomical Society, 482 (2019), pp. 2305-2319

iv B. Nsamba, T. L. Campante, M. J. P. F. G. Monteiro, M. S. Cunha, **B. M. Rendle**, D. R. Reese, and K. Verma, Asteroseismic modelling of solar-type

stars: internal systematics from input physics and surface correction methods, Monthly Notices of the Royal Astronomical Society, 477 (2018), pp. 5052-5063

v A. Miglio, C. Chiappini, B. Mosser, G. R. Davies, K. Freeman, L. Girardi, P. Jofré, D. Kawata, **B. M. Rendle**, M. Valentini, L. Casagrande, W. J. Chaplin, G. Gilmore, K. Hawkins, B. Holl, T. Appourchaux, K. Belkacem, D. Bossini, K. Brogaard, M.-J. Goupil, J. Montalbán, A. Noels, F. Anders, T. Rodrigues, G. Piotto, D. Pollacco, H. Rauer, C. Allende Prieto, P. P. Avelino, C. Babusiaux, C. Barban, B. Barbuy, S. Basu, F. Baudin, O. Benomar, O. Bienaymé, J. Binney, J. Bland-Hawthorn, A. Bressan, C. Cacciari, T. L. Campante, S. Cassisi, J. Christensen-Dalsgaard, F. Combes, O. Creevey, M. S. Cunha, R. S. Jong, P. Laverny, S. Degl'Innocenti, S. Deheuvels, É. Depagne, J. Ridder, P. Di Matteo, M. P. Di Mauro, M.-A. Dupret, P. Eggenberger, Y. Elsworth, B. Famaey, S. Feltzing, R. A. García, O. Gerhard, B. K. Gibson, L. Gizon, M. Haywood, R. Handberg, U. Heiter, S. Hekker, D. Huber, R. Ibata, D. Katz, S. D. Kawaler, H. Kjeldsen, D. W. Kurtz, N. Lagarde, Y. Lebreton, M. N. Lund, S. R. Majewski, P. Marigo, M. Martig, S. Mathur, I. Minchev, T. Morel, S. Ortolani, M. H. Pinsonneault, B. Plez, P. G. Prada Moroni, D. Pricopi, A. Recio-Blanco, C. Reylé, A. Robin, I. W. Roxburgh, M. Salaris, B. X. Santiago, R. Schiavon, A. Serenelli, S. Sharma, V. Silva Aguirre, C. Soubiran, M. Steinmetz, D. Stello, K. G. Strassmeier, P. Ventura, R. Ventura, N. A. Walton, and C. C. Worley, PLATO as it is : A legacy mission for Galactic archaeology, Astronomische Nachrichten, 338 (2017), pp. 644-661

vi V. Silva Aguirre, M. N. Lund, H. M. Antia, W. H. Ball, S. Basu, J. Christensen-Dalsgaard, Y. Lebreton, D. R. Reese, K. Verma, L. Casagrande, A. B. Justesen, J. R. Mosumgaard, W. J. Chaplin, T. R. Bedding, G. R. Davies, R. Handberg, G. Houdek, D. Huber, H. Kjeldsen, D. W. Latham, T. R. White, H. R. Coelho, A. Miglio, and **B. M. Rendle**, Standing on the Shoulders of Dwarfs: the Kepler

Asteroseismic LEGACY Sample. II. Radii, Masses, and Ages, The Astrophysical Journal, 835 (2017), p. 173

vii G. R. Davies, M. N. Lund, A. Miglio, Y. Elsworth, J. S. Kuszlewicz, T. S. H. North, **B. M. Rendle**, W. J. Chaplin, T. S. Rodrigues, T. L. Campante, L. Girardi, S. J. Hale, O. Hall, C. D. Jones, S. D. Kawaler, I. Roxburgh, and M. Schofield, Using red clump stars to correct the Gaia DR1 parallaxes, Astronomy & Astrophysics, 598 (2017), p. L4

Bibliography

Abadi M. G., Navarro J. F., Steinmetz M., Eke V. R., 2003a, ApJ, 591, 499

Abadi M. G., Navarro J. F., Steinmetz M., Eke V. R., 2003b, ApJ, 597, 21

Abolfathi B., et al., 2018, ApJS, 235, 42

Adelberger E. G., et al., 2011, Reviews of Modern Physics, 83, 195

Aerts C., Christensen-Dalsgaard J., Kurtz D. W., 2010, Asteroseismology. Springer

Anders F., et al., 2014, A&A, 564, A115

Anders F., et al., 2017, A&A, 597, A30

Andersen M. F., et al., 2014, in Revista Mexicana de Astronomia y Astrofisica Conference Series. pp 83–86

Andrews B. H., Weinberg D. H., Schönrich R., Johnson J. A., 2017, ApJ, 835, 224

Anguiano B., et al., 2018, A&A, 620, A76

Arentoft T., Brogaard K., Jessen-Hansen J., Silva Aguirre V., Kjeldsen H., Mosumgaard J. R., Sand quist E. L., 2017, ApJ, 838, 115

Asplund M., Grevesse N., Sauval A. J., Scott P., 2009, ARA&A, 47, 481

Astraatmadja T. L., Bailer-Jones C. A. L., 2016, ApJ, 832, 137

Athanassoula E., 2005, MNRAS, 358, 1477

Baglin A., Auvergne M., Barge P., Deleuil M., Catala C., Michel E., Weiss W., COROT Team 2006, in Fridlund M., Baglin A., Lochard J., Conroy L., eds, ESA Special Publication Vol. 1306, The CoRoT Mission Pre-Launch Status - Stellar Seismology and Planet Finding. p. 33

Bahcall J. N., Pinsonneault M. H., Wasserburg G. J., 1995, Reviews of Modern Physics, 67, 781

Baker N., Kippenhahn R., 1962, Zeitschrift fur Astrophysik, 54, 114

Ball W. H., Gizon L., 2014, A&A, 568, A123

Ball W. H., Gizon L., 2017, A&A, 600, A128

Ballot J., Appourchaux T., Toutain T., Guittet M., 2008, A&A, 486, 867

Barber C. B., Dobkin D. P., Dobkin D. P., Huhdanpaa H., 1996, ACM Trans. Math. Softw., 22, 469

Barbuy B., Chiappini C., Gerhard O., 2018, ARA&A, 56, 223

Bash F. N., 1981, ApJ, 250, 551

Basu B., Chaplin W., 2017, Asteroseismic Data Analysis. Prineton University Press

Basu S., Kinnane A., 2018, ApJ, 869, 8

Basu S., et al., 2011, ApJ, 729, L10

Baudin F., et al., 2012, A&A, 538, A73

Bazot M., Bourguignon S., Christensen-Dalsgaard J., 2008, Mem. Soc. Astron. Italiana, 79, 660

Bedding T. R., 2014, Solar-like oscillations: An observational perspective. Cambridge University Press, Cambridge, UK, p. 60

Bedding T. R., Kjeldsen H., 2003, Publications of the Astronomical Society of Australia, 20, 203

Bedding T. R., et al., 2011, Nature, 471, 608

Belkacem K., Goupil M. J., Dupret M. A., Samadi R., Baudin F., Noels A., Mosser B., 2011, A&A, 530, A142

Belkacem K., Samadi R., Mosser B., Goupil M. J., Ludwig H. G., 2013, in Shibahashi H., Lynas-Gray A. E., eds, Astronomical Society of the Pacific Conference Series Vol. 479, Progress in Physics of the Sun and Stars: A New Era in Helio- and Asteroseismology. p. 61 (arXiv:1307.3132)

Bensby T., 2014, in Feltzing S., Zhao G., Walton N. A., Whitelock P., eds, IAU Symposium Vol. 298, Setting the scene for Gaia and LAMOST. pp 17–27 (arXiv:1308.5191), doi:10.1017/S1743921313006169

Bensby T., Feltzing S., Lundström I., 2003, A&A, 410, 527

Bensby T., Feltzing S., Lundström I., Ilyin I., 2005, A&A, 433, 185

Bensby T., Zenn A. R., Oey M. S., Feltzing S., 2007, ApJ, 663, L13

Bensby T., Alves-Brito A., Oey M. S., Yong D., Meléndez J., 2011, ApJ, 735, L46

Bensby T., Feltzing S., Oey M. S., 2014, A&A, 562, A71

Bergemann M., et al., 2014, A&A, 565, A89

Bird J. C., Kazantzidis S., Weinberg D. H., Guedes J., Callegari S., Mayer L., Madau P., 2013, ApJ, 773, 43

Bland-Hawthorn J., Gerhard O., 2016, ARA&A, 54, 529

Blanton M. R., et al., 2017, AJ, 154, 28

Borucki W. J., et al., 2010a, Science, 327, 977

Borucki W. J., et al., 2010b, Science, 327, 977

Bournaud F., Elmegreen B. G., Martig M., 2009, ApJ, 707, L1

Bovy J., Rix H.-W., Hogg D. W., 2012a, ApJ, 751, 131

Bovy J., Rix H.-W., Liu C., Hogg D. W., Beers T. C., Lee Y. S., 2012b, ApJ, 753, 148

Bovy J., Rix H.-W., Hogg D. W., Beers T. C., Lee Y. S., Zhang L., 2012c, ApJ, 755, 115

Bovy J., Rix H.-W., Green G. M., Schlafly E. F., Finkbeiner D. P., 2016a, ApJ, 818, 130

Bovy J., Rix H.-W., Schlafly E. F., Nidever D. L., Holtzman J. A., Shetrone M., Beers T. C., 2016b, ApJ, 823, 30

Brickhill A. J., 1991, MNRAS, 251, 673

Brogaard K., et al., 2012, A&A, 543, A106

Brogaard K., Sandquist E., Jessen-Hansen J., Grundahl F., Frandsen S., 2015, in Asteroseismology of Stellar Populations in the Milky Way. p. 51 (arXiv:1409.2271), doi:10.1007/978-3-319-10993-0˙6

Brogaard K., et al., 2018, MNRAS, 476, 3729

Brook C. B., Kawata D., Gibson B. K., Freeman K. C., 2004, ApJ, 612, 894

Brook C. B., et al., 2012, MNRAS, 426, 690

Broomhall A.-M., Chaplin W. J., Davies G. R., Elsworth Y., Fletcher S. T., Hale S. J., Miller B., New R., 2009, MNRAS, 396, L100

Brown T. M., Gilliland R. L., Noyes R. W., Ramsey L. W., 1991, ApJ, 368, 599

Bruntt H., et al., 2010, MNRAS, 405, 1907

Buder S., et al., 2018, MNRAS, 478, 4513

Buldgen G., Reese D. R., Dupret M. A., 2015, A&A, 583, A62

Buldgen G., et al., 2018a, MNRAS,

Buldgen G., Reese D. R., Dupret M. A., 2018b, A&A, 609, A95

Burstein D., 1979, in Evans D. S., ed., Photometry, Kinematics and Dynamics of Galaxies Vol. 79, Photometry, Kinematics and Dynamics of Galaxies. p. 81

Casagrande L., VandenBerg D. A., 2014a, MNRAS, 444, 392

Casagrande L., VandenBerg D. A., 2014b, MNRAS, 444, 392

Casagrande L., VandenBerg D. A., 2018a, BCcodes: Bolometric Corrections and Synthetic Stellar Photometry, Astrophysics Source Code Library (ascl:1805.022)

Casagrande L., VandenBerg D. A., 2018b, MNRAS, 475, 5023

Casagrande L., VandenBerg D. A., 2018c, MNRAS, 475, 5023

Casagrande L., VandenBerg D. A., 2018d, MNRAS, 479, L102

Casagrande L., et al., 2014, ApJ, 787, 110

Casagrande L., et al., 2016, MNRAS, 455, 987

Casagrande L., Wolf C., Mackey A. D., Nordlander T., Yong D., Bessell M., 2019, MNRAS, 482, 2770

Chaplin W. J., Miglio A., 2013, ARA&A, 51, 353

Chaplin W. J., et al., 2011a, Science, 332, 213

Chaplin W. J., et al., 2011b, ApJ, 732, 54

Chaplin W. J., Elsworth Y., Davies G. R., Campante T. L., Handberg R., Miglio A., Basu S., 2014, MNRAS, 445, 946

Chaplin W. J., et al., 2015, PASP, 127, 1038

Cheng J. Y., et al., 2012a, ApJ, 746, 149

Cheng J. Y., et al., 2012b, ApJ, 752, 51

Chiappini C., 2009, in Andersen J., Nordström B., Bland-Hawthorn J., eds, IAU Symposium Vol. 254, The Galaxy Disk in Cosmological Context. pp 191–196, doi:10.1017/S1743921308027580

Chiappini C., Matteucci F., Gratton R., 1997, ApJ, 477, 765

Chiappini C., Matteucci F., Romano D., 2001, ApJ, 554, 1044

Chiappini C., et al., 2015, A&A, 576, L12

Christensen-Dalsgaard J., 1986, in Gough D. O., ed., NATO Advanced Science Institutes (ASI) Series C Vol. 169, NATO Advanced Science Institutes (ASI) Series C. pp 23–53

Christensen-Dalsgaard J., 2002, Reviews of Modern Physics, 74, 1073

Christensen-Dalsgaard J., Thompson M. J., 1997, MNRAS, 284, 527

Christensen-Dalsgaard J., Dappen W., Lebreton Y., 1988, Nature, 336, 634

Christensen-Dalsgaard J., Proffitt C. R., Thompson M. J., 1993, ApJ, 403, L75

Cirasuolo M., et al., 2014, in Ground-based and Airborne Instrumentation for Astronomy V. p. 91470N, doi:10.1117/12.2056012

CoRot Team 2016, Foreword. EDP Sciences, doi:10.1051/978-2-7598-1876-1.c001

Coelho H. R., Chaplin W. J., Basu S., Serenelli A., Miglio A., Reese D. R., 2015, MNRAS, 451, 3011

Combes F., Sanders R. H., 1981, A&A, 96, 164

Compton D. L., Bedding T. R., Ball W. H., Stello D., Huber D., White T. R., Kjeldsen H., 2018, MNRAS, 479, 4416

Conroy C., van Dokkum P., 2012a, ApJ, 747, 69

Conroy C., van Dokkum P. G., 2012b, ApJ, 760, 71

Cooper A. P., et al., 2010, MNRAS, 406, 744

Corsaro E., De Ridder J., 2014a, DIAMONDS: high-DImensional And multi-MOdal NesteD Sampling (ascl:1410.001)

Corsaro E., De Ridder J., 2014b, A&A, 571, A71

Corsaro E., et al., 2017, in European Physical Journal Web of Conferences. p. 05002, doi:10.1051/epjconf/201716005002

DESI Collaboration et al., 2016, arXiv e-prints, p. arXiv:1611.00036

Dalcanton J. J., Bernstein R. A., 2002, AJ, 124, 1328

Dalton G., et al., 2014, in Ground-based and Airborne Instrumentation for Astronomy V. p. 91470L (arXiv:1412.0843), doi:10.1117/12.2055132

Davies G. R., Miglio A., 2016, Astronomische Nachrichten, 337, 774

Davies G. R., Broomhall A. M., Chaplin W. J., Elsworth Y., Hale S. J., 2014a, MNRAS, 439, 2025

Davies G. R., Handberg R., Miglio A., Campante T. L., Chaplin W. J., Elsworth Y., 2014b, MNRAS, 445, L94

Davies G. R., et al., 2015, MNRAS, 446, 2959

Davies G. R., et al., 2016, MNRAS, 456, 2183

De Silva G. M., Freeman K. C., Bland-Hawthorn J., 2009, PASA, 26, 11

Deheuvels S., et al., 2014, A&A, 564, A27

Dehnen W., 2000, AJ, 119, 800

Deng L.-C., et al., 2012, Research in Astronomy and Astrophysics, 12, 735

DePontieu B., et al., 2014, Solar Physics, 289, 2733

Dobbs C. L., Pringle J. E., 2010, MNRAS, 409, 396

Drimmel R., Spergel D. N., 2001, ApJ, 556, 181

Dwek E., et al., 1995, ApJ, 445, 716

Dziembowski W. A., Paterno L., Ventura R., 1988, A&A, 200, 213

Efremov Y. N., 2011, Astronomy Reports, 55, 108

Eggen O. J., Lynden-Bell D., Sandage A. R., 1962, ApJ, 136, 748

Eggenberger P., Montalbán J., Miglio A., 2012, A&A, 544, L4

Eisenstein D. J., et al., 2011a, AJ, 142, 72

Eisenstein D. J., et al., 2011b, AJ, 142, 72

Farmer R., Kolb U., Norton A. J., 2013, MNRAS, 433, 1133

Field D. A., 1991, Advances in Engineering Software and Workstations, 13, 263

Foreman-Mackey D., Hogg D. W., Lang D., Goodman J., 2013, PASP, 125, 306

Frankel N., Rix H.-W., Ting Y.-S., Ness M., Hogg D. W., 2018, ApJ, 865, 96

Freeman K., Bland-Hawthorn J., 2002, ARA&A, 40, 487

Fuhrmann K., 1998, A&A, 338, 161

Fuhrmann K., 2011, MNRAS, 414, 2893

Gabriel M., Noels A., Montalbán J., Miglio A., 2014, A&A, 569, A63

Gaia Collaboration et al., 2018b, A&A, 616, A1

Gaia Collaboration et al., 2018a, A&A, 616, A1

García Pérez A. E., et al., 2016, AJ, 151, 144

García R. A., et al., 2011, MNRAS, 414, L6

Gaulme P., et al., 2016, ApJ, 832, 121

Georgelin Y. M., Georgelin Y. P., 1976, A&A, 49, 57

Gibson B. K., Courty S., Sánchez-Blázquez P., Teyssier R., House E. L., Brook C. B., Kawata D., 2009, in Andersen J., Nordström B., Bland-Hawthorn J., eds, IAU Symposium Vol. 254, The Galaxy Disk in Cosmological Context. pp 445–452 (arXiv:0808.0576), doi:10.1017/S1743921308027956

Gilmore G., Reid N., 1983, MNRAS, 202, 1025

Gilmore G., et al., 2012, The Messenger, 147, 25

Girardi L., 2016, Annual Review of Astronomy and Astrophysics, 54, 95

Girardi L., et al., 2012, Astrophysics and Space Science Proceedings, 26, 165

Goldreich P., Murray N., Willette G., Kumar P., 1991, ApJ, 370, 752

Goodman J., Weare J., 2010, Communications in Applied Mathematics and Computational Science, 5, 65

Gough D. O., 1990, in Osaki Y., Shibahashi H., eds, Lecture Notes in Physics, Berlin Springer Verlag Vol. 367, Progress of Seismology of the Sun and Stars. p. 283, doi:10.1007/3-540-53091-6

Gough D. O., 2001, in von Hippel T., Simpson C., Manset N., eds, Astronomical Society of the Pacific Conference Series Vol. 245, Astrophysical Ages and Times Scales. p. 31

Green G. M., et al., 2015, ApJ, 810, 25

Grevesse N., Noels A., 1993, in Prantzos N., Vangioni-Flam E., Casse M., eds, Origin and Evolution of the Elements. pp 15–25

Gruberbauer M., Guenther D. B., Kallinger T., 2012, ApJ, 749, 109

Gruberbauer M., Guenther D. B., MacLeod K., Kallinger T., 2013, MNRAS, 435, 242

Grundahl F., et al., 2017, ApJ, 836, 142

Guedes J., Mayer L., Carollo M., Madau P., 2013, ApJ, 772, 36

Guenther D. B., Brown K. I. T., 2004, ApJ, 600, 419

Guggenberger E., Hekker S., Basu S., Bellinger E., 2016, MNRAS, 460, 4277

Gunn J. E., et al., 2006, AJ, 131, 2332

Guth A. H., 1981, Phys. Rev. D, 23, 347

Hale S. J., Howe R., Chaplin W. J., Davies G. R., Elsworth Y. P., 2016, Sol. Phys., 291, 1

Handberg R., Brogaard K., Miglio A., Bossini D., Elsworth Y., Slumstrup D., Davies G. R., Chaplin W. J., 2017, MNRAS, 472, 979

Handler G., 2009, MNRAS, 398, 1339

Handler G., 2013, Asteroseismology. Springer Science and Business Media Dordrecht, p. 207, doi:10.1007/978-94-007-5615-1˙4

Hart A. B., 1954, MNRAS, 114, 17

Hart A. B., 1956, MNRAS, 116, 38

Hawkins K., Jofré P., Masseron T., Gilmore G., 2015, MNRAS, 453, 758

Hayden M. R., et al., 2015, ApJ, 808, 132

Hayden M. R., Recio-Blanco A., de Laverny P., Mikolaitis S., Worley C. C., 2017, A&A, 608, L1

Hayes C. R., et al., 2018, ApJ, 852, 49

Haywood M., Di Matteo P., Lehnert M. D., Katz D., Gómez A., 2013, A&A, 560, A109

Haywood M., Lehnert M. D., Di Matteo P., Snaith O., Schultheis M., Katz D., Gómez A., 2016, A&A, 589, A66

Haywood M., Di Matteo P., Lehnert M. D., Snaith O., Khoperskov S., Gómez A., 2018, ApJ, 863, 113

Hekker S., Christensen-Dalsgaard J., 2017, A&A Rev., 25, 1

Hekker S., Mazumdar A., 2014, in Guzik J. A., Chaplin W. J., Handler G., Pigulski A., eds, IAU Symposium Vol. 301, Precision Asteroseismology. pp 325–331 (arXiv:1311.1914), doi:10.1017/S1743921313014531

Hekker S., et al., 2011, A&A, 530, A100

Helmi A., White S. D. M., Springel V., 2003, MNRAS, 339, 834

Helmi A., Babusiaux C., Koppelman H. H., Massari D., Veljanoski J., Brown A. G. A., 2018, Nature, 563, 85

Hogg D. W., et al., 2016, ApJ, 833, 262

Holtzman J. A., et al., 2015, AJ, 150, 148

Howell S. B., et al., 2014, PASP, 126, 398

Hubble E. P., 1936, Realm of the Nebulae. New Haven: Yale University Press, 1936. ISBN 9780300025002

Huber D., et al., 2011, ApJ, 743, 143

Huber D., et al., 2013, Science, 342, 331

Huber D., et al., 2016, ApJS, 224, 2

Hunt J. A. S., Hong J., Bovy J., Kawata D., Grand R. J. J., 2018, MNRAS, 481, 3794

Iglesias C. A., Rogers F. J., 1996, ApJ, 464, 943

Irwin A. W., 2012, FreeEOS: Equation of State for stellar interiors calculations, Astrophysics Source Code Library (ascl:1211.002)

Ivezić Ž., Beers T. C., Jurić M., 2012, ARA&A, 50, 251

Izzard R. G., Preece H., Jofre P., Halabi G. M., Masseron T., Tout C. A., 2018, MNRAS, 473, 2984

Jeffries Mark W. J., et al., 2013, AJ, 146, 58

Jofré P., et al., 2016, A&A, 595, A60

Jofré P., Heiter U., Buder S., 2017, in Astronomical Society of India Conference Series. pp 37–44 (arXiv:1709.09366)

Jofré P., Heiter U., Soubiran C., 2018, arXiv e-prints,

Johnson J. A., APOKASC Collaboration 2016, Astronomische Nachrichten, 337, 917

Jones B. J. T., Wyse R. F. G., 1983, A&A, 120, 165

Jones E., Oliphant T., Peterson P., et al., 2001, SciPy: Open source scientific tools for Python, http://www.scipy.org/

Jönsson H., et al., 2018, AJ, 156, 126

Jørgensen B. R., Lindegren L., 2005, A&A, 436, 127

Jurić M., et al., 2008, ApJ, 673, 864

Kawata D., Chiappini C., 2016, Astronomische Nachrichten, 337, 976

Kazantzidis S., Zentner A. R., Kravtsov A. V., Bullock J. S., Debattista V. P., 2009, ApJ, 700, 1896

Keller S. C., et al., 2007, PASA, 24, 1

King C. R., Da Costa G. S., Demarque P., 1985, ApJ, 299, 674

Kippenhahn R., Weigert A., Weiss A., 2012, Stellar Structure and Evolution. Astronomy and Astrophysics Library. ISBN 978-3-642-30255-8. Springer-Verlag Berlin Heidelberg, 2012, doi:10.1007/978-3-642-30304-3

Kjeldsen H., Bedding T. R., 1995, A&A, 293, 87

Kjeldsen H., Bedding T. R., 1997, in Bedding T. R., Booth A. J., Davis J., eds, IAU Symposium Vol. 189, IAU Symposium. pp 279–284 (arXiv:astro-ph/9704045)

Kjeldsen H., Bedding T. R., Christensen-Dalsgaard J., 2008, ApJ, 683, L175

Kordopatis G., et al., 2015, A&A, 582, A122

Kraft R. P., 1967, ApJ, 150, 551

Kubryk M., Prantzos N., Athanassoula E., 2015, A&A, 580, A126

Kunder A., et al., 2017, AJ, 153, 75

Lagarde N., et al., 2019, A&A, 621, A24

Lebreton Y., Goupil M. J., 2014, A&A, 569, A21

Leibacher J. W., Stein R. F., 1971, Astrophys. Lett., 7, 191

Leighton R. B., Noyes R. W., Simon G. W., 1962, ApJ, 135, 474

Li T., Bedding T. R., Huber D., Ball W. H., Stello D., Murphy S. J., Bland-Hawthorn J., 2018, MNRAS, 475, 981

Libbrecht K. G., 1992, ApJ, 387, 712

Lillo-Box J., et al., 2014, A&A, 562, A109

Lin C. C., Shu F. H., 1964, ApJ, 140, 646

Linde A., 2018, Foundations of Physics, 48, 1246

Lund M. N., Reese D. R., 2018, Asteroseismology and Exoplanets: Listening to the Stars and Searching for New Worlds, 49, 149

Lund M. N., Handberg R., Davies G. R., Chaplin W. J., Jones C. D., 2015, AJ, 806, 30

Lund M. N., et al., 2016, Publications of the Astronomical Society of the Pacific, 128, 124204

Lund M. N., et al., 2017, ApJ, 835, 172

Mackereth J. T., et al., 2017a, MNRAS, 471, 3057

Mackereth T. J., et al., 2017b, MNRAS, 471, 3057

Mackereth J. T., et al., 2019, arXiv e-prints,

Madau P., Dickinson M., 2014, Annual Review of Astronomy and Astrophysics, 52, 415

Majewski S. R., 1992, in Barbuy B., Renzini A., eds, IAU Symposium Vol. 149, The Stellar Populations of Galaxies. p. 61

Majewski S. R., et al., 2017, AJ, 154, 94

Marques J. P., et al., 2013, A&A, 549, A74

Martig M., Bournaud F., Teyssier R., 2009, in Andersen J., Nordströara m B., Bland - Hawthorn J., eds, IAU Symposium Vol. 254, The Galaxy Disk in Cosmological Context. pp 429–434 (arXiv:0807.1693), doi:10.1017/S1743921308027920

Martig M., Bournaud F., Croton D. J., Dekel A., Teyssier R., 2012, ApJ, 756, 26

Martig M., et al., 2015, MNRAS, 451, 2230

Martig M., et al., 2016a, MNRAS, 456, 3655

Martig M., Minchev I., Ness M., Fouesneau M., Rix H.-W., 2016b, ApJ, 831, 139

Masseron T., Gilmore G., 2015, MNRAS, 453, 1855

Mathur S., et al., 2010a, A&A, 511, A46

Mathur S., et al., 2010b, A&A, 511, A46

Mathur S., García R. A., Huber D., Regulo C., Stello D., Beck P. G., Houmani K., Salabert D., 2016, ApJ, 827, 50

Matteucci F., 2001, in Astrophysics and Space Science Library. , doi:10.1007/978-94-010-0967-6

McKeever J. M., Basu S., Corsaro E., 2019, ApJ, 874, 180

Metcalfe T. S., Creevey O. L., Christensen-Dalsgaard J., 2009, ApJ, 699, 373

Metcalfe T. S., et al., 2010, ApJ, 723, 1583

Miglio A., 2012, Astrophysics and Space Science Proceedings, 26, 11

Miglio A., Montalbán J., 2005, A&A, 441, 615

Miglio A., et al., 2009, A&A, 503, L21

Miglio A., et al., 2010, A&A, 520, L6

Miglio A., Montalbán J., Noels A., 2012, Astrophysics and Space Science Proceedings, 26

Miglio A., et al., 2013a, in European Physical Journal Web of Conferences. p. 03004 (arXiv:1301.1515), doi:10.1051/epjconf/20134303004

Miglio A., et al., 2013b, MNRAS, 429, 423

Miglio A., Brogaard K., Handberg R., 2015, in IAU General Assembly. p. 2251619

Miglio A., et al., 2016, MNRAS, 461, 760

Miglio A., et al., 2017, Astronomische Nachrichten, 338, 644

Minchev I., 2016, Astronomische Nachrichten, 337, 703

Minchev I., Chiappini C., Martig M., 2013, A&A, 558, A9

Minchev I., Chiappini C., Martig M., 2014, A&A, 572, A92

Minchev I., Martig M., Streich D., Scannapieco C., de Jong R. S., Steinmetz M., 2015, ApJ, 804, L9

Montalban J., Miglio A., Noels A., Scuflaire R., Ventura P., 2010, Astronomische Nachrichten, 331, 1010

Morrison H. L., Flynn C., Freeman K. C., 1990, AJ, 100, 1191

Morrison H. L., et al., 2009, ApJ, 694, 130

Mosser B., Appourchaux T., 2009a, A&A, 508, 877

Mosser B., Appourchaux T., 2009b, A&A, 508, 877

Mosser B., et al., 2010, A&A, 517, A22

Mosser B., et al., 2011, A&A, 532, A86

Mosser B., et al., 2012a, A&A, 537, A30

Mosser B., et al., 2012b, A&A, 540, A143

Mosser B., et al., 2013, A&A, 550, A126

Mosser B., et al., 2014, A&A, 572, L5

Mosser B., Michel E., Samadi R., Miglio A., Davies G. R., Girardi L., Goupil M. J., 2019, A&A, 622, A76

Navarro J. F., Abadi M. G., Venn K. A., Freeman K. C., Anguiano B., 2011, MNRAS, 412, 1203

Ness M., Hogg D. W., Rix H. W., Martig M., Pinsonneault M. H., Ho A. Y. Q., 2016, ApJ, 823, 114

Nidever D. L., et al., 2014, ApJ, 796, 38

Nidever D. L., et al., 2015, AJ, 150, 173

Noels A., Bragaglia A., 2015, in Asteroseismology of Stellar Populations in the Milky Way. p. 167 (arXiv:1409.2281), doi:10.1007/978-3-319-10993-0˙19

Noels A., Montalbán J., Chiappini C., 2016, Astronomische Nachrichten, 337, 982

Noguchi M., 1998, Nature, 392, 253

Nsamba B., Campante T. L., Monteiro M. J. P. F. G., Cunha M. S., Rendle B. M., Reese D. R., Verma K., 2018, MNRAS, 477, 5052

Otí Floranes H., Christensen-Dalsgaard J., Thompson M. J., 2005, MNRAS, 356, 671

Paxton B., et al., 2015, ApJS, 220, 15

Peebles P. J. E., 1971, Physical cosmology. Princeton Series in Physics, Princeton, N.J.: Princeton University Press, 1971

Pérez Hernández F., García R. A., Corsaro E., Triana S. A., De Ridder J., 2016, A&A, 591, A99

Pinna F., et al., 2019, A&A, 623, A19

Pinsonneault M. H., et al., 2014, ApJS, 215, 19

Pinsonneault M. H., Elsworth Y. P., APOKASC 2017, in American Astronomical Society Meeting Abstracts #229. p. 305.05

Pinsonneault M., et al., 2018, in American Astronomical Society Meeting Abstracts #231. p. 450.13

Plaskett H. H., 1916, ApJ, 43, 145

Pompéia L., et al., 2011, MNRAS, 415, 1138

Prada Moroni P. G., Valle G., Dell'Omodarme M., Degl'Innocenti S., 2016, Astronomische Nachrichten, 337, 819

Press W. H., Schechter P., 1974, ApJ, 187, 425

Ragan S. E., Moore T. J. T., Eden D. J., Hoare M. G., Urquhart J. S., Elia D., Molinari S., 2018, MNRAS, 479, 2361

Raha N., Sellwood J. A., James R. A., Kahn F. D., 1991, Nature, 352, 411

Rauer H., et al., 2014, Experimental Astronomy, 38, 249

Recio-Blanco A., et al., 2014, A&A, 567, A5

Reddy B. E., Lambert D. L., 2008, MNRAS, 391, 95

Reese D. R., 2016a, AIMS: Asteroseismic Inference on a Massive Scale, Astrophysics Source Code Library (ascl:1611.014)

Reese D. R., 2016b, Astrophysics Source Code Library, p. ascl:1611.014

Reese D. R., Marques J. P., Goupil M. J., Thompson M. J., Deheuvels S., 2012, A&A, 539, A63

Reese D. R., et al., 2016, A&A, 592, A14

Refsdal S., Weigert A., 1970, A&A, 6, 426

Rejkuba M., Mouhcine M., Ibata R., 2009, MNRAS, 396, 1231

Rendle B. M., et al., 2019, MNRAS, 484, 771

Ricker G. R., et al., 2015, Journal of Astronomical Telescopes, Instruments, and Systems, 1, 014003

Riello M., et al., 2003, A&A, 410, 553

Rix H.-W., Bovy J., 2013, A&A Rev., 21, 61

Robin A. C., Reylé C., Fliri J., Czekaj M., Robert C. P., Martins A. M. M., 2014, A&A, 569, A13

Rodrigues T. S., et al., 2014, MNRAS, 445, 2758

Rodrigues T. S., et al., 2017, MNRAS, 467, 1433

Rosseland S., Randers G., 1938, Astrophysica Norvegica, 3, 71

Roxburgh I. W., 2002, in Battrick B., Favata F., Roxburgh I. W., Galadi D., eds, ESA Special Publication Vol. 485, Stellar Structure and Habitable Planet Finding. pp 75–85

Roxburgh I. W., Vorontsov S. V., 2003, A&A, 411, 215

Ruchti G. R., et al., 2011, ApJ, 737, 9

Saito R. K., et al., 2012, A&A, 544, A147

Salaris M., 2016, Astronomische Nachrichten, 337, 805

Salaris M., Cassisi S., Weiss A., 2002, PASP, 114, 375

Salaris M., Pietrinferni A., Piersimoni A. M., Cassisi S., 2015, A&A, 583, A87

Sandage A., 1961, The Hubble Atlas of Galaxies. Washington: Carnegie Institution, 1961

Sandquist E. L., et al., 2013, ApJ, 762, 58

Schiavon R. P., 2007, The Astrophysical Journal Supplement Series, 171, 146

Schmidt M., 1959, ApJ, 129, 243

Schmidt M., 1963, ApJ, 137, 758

Schofield M., et al., 2019, arXiv e-prints, p. arXiv:1901.10148

Schönrich R., Binney J., 2009a, MNRAS, 396, 203

Schönrich R., Binney J., 2009b, MNRAS, 399, 1145

Scuflaire R., Théado S., Montalbán J., Miglio A., Bourge P.-O., Godart M., Thoul A., Noels A., 2008a, Ap&SS, 316, 83

Scuflaire R., Montalbán J., Théado S., Bourge P.-O., Miglio A., Godart M., Thoul A., Noels A., 2008b, Ap&SS, 316, 149

Sellwood J. A., Carlberg R. G., 1984, ApJ, 282, 61

Serenelli A., et al., 2017, ApJS, 233, 23

Sharma S., Stello D., Bland-Hawthorn J., Huber D., Bedding T. R., 2016, ApJ, 822, 15

Silva Aguirre V., et al., 2015, MNRAS, 452, 2127

Silva Aguirre V., et al., 2017, ApJ, 835, 173

Silva Aguirre V., et al., 2018, MNRAS, 475, 5487

Skrutskie M. F., et al., 2006, AJ, 131, 1163

Snaith O., Haywood M., Di Matteo P., Lehnert M. D., Combes F., Katz D., Gómez A., 2015, A&A, 578, A87

Soderblom D. R., 2010, ARA&A, 48, 581

Soderblom D., 2013, in Asteroseismology of Stellar Populations in the Milky Way. p. 2

Sommer-Larsen J., Götz M., Portinari L., 2003, ApJ, 596, 47

Sonoi T., Samadi R., Belkacem K., Ludwig H.-G., Caffau E., Mosser B., 2015, A&A, 583, A112

Soubiran C., Bienaymé O., Siebert A., 2003, A&A, 398, 141

Spitoni E., Silva Aguirre V., Matteucci F., Calura F., Grisoni V., 2019, A&A, 623, A60

Steinmetz M., Mueller E., 1994, A&A, 281, L97

Stello D., et al., 2007, MNRAS, 377, 584

Stello D., et al., 2009, ApJ, 700, 1589

Stello D., et al., 2010, ApJ, 713, L182

Stello D., et al., 2011, ApJ, 739, 13

Stello D., et al., 2015, ApJ, 809, L3

Stello D., et al., 2017, ApJ, 835, 83

Taylor R. J., 1993, Galaxies: structure and evolution. Cambridge University Press, University of Cambridge, The Pitt Building, Trumpington Street, Cambridge, CB2 1RP

Thoul A. A., Bahcall J. N., Loeb A., 1994, ApJ, 421, 828

Ting Y.-S., Hawkins K., Rix H.-W., 2018, ApJ, 858, L7

Tinsley B. M., 1980, Fundamentals of Cosmic Physics, 5, 287

Toomre A., 1981, in Fall S. M., Lynden-Bell D., eds, Structure and Evolution of Normal Galaxies. pp 111–136

Toonen S., 2017, arXiv e-prints, p. arXiv:1703.05415

Toonen S., Perets H. B., Hamers A. S., 2018, A&A, 610, A22

Torres G., 2010a, ApJ, 140, 1158

Torres G., 2010b, AJ, 140, 1158

Toutain T., Appourchaux T., 1994, A&A, 289, 649

Tsikoudi V., 1979, ApJ, 234, 842

Ulrich R. K., 1970, ApJ, 162, 993

Ulrich R. K., 1986, ApJ, 306, L37

Urquhart J. S., Figura C. C., Moore T. J. T., Hoare M. G., Lumsden S. L., Mottram J. C., Thompson M. A., Oudmaijer R. D., 2014, MNRAS, 437, 1791

Valentini M., et al., 2016, Astronomische Nachrichten, 337, 970

Valentini M., et al., 2017, A&A, 600, A66

Van Eylen V., Kjeldsen H., Christensen-Dalsgaard J., Aerts C., 2012, Astronomische Nachrichten, 333, 1088

Verma K., Raodeo K., Antia H. M., Mazumdar A., Basu S., Lund M. N., Silva Aguirre V., 2017, ApJ, 837, 47

Vernazza J. E., Avrett E. H., Loeser R., 1981, The Astrophysical Journal Supplement Series, 45, 635

Verner G. A., Roxburgh I. W., 2011, arXiv e-prints, p. arXiv:1104.0631

Viani L. S., Basu S., Chaplin W. J., Davies G. R., Elsworth Y., 2017, ApJ, 843, 11

Villalobos Á., Helmi A., 2008, MNRAS, 391, 1806

Vorontsov S. V., 1988, in Christensen-Dalsgaard J., Frandsen S., eds, IAU Symposium Vol. 123, Advances in Helio- and Asteroseismology. p. 151

Vrard M., Mosser B., Samadi R., 2016, A&A, 588, A87

Wang B., Han Z., 2012, New Astronomy Reviews, 56, 122

Wegg C., Gerhard O., Portail M., 2015, MNRAS, 450, 4050

Weinberg S., 1977, The first three minutes. A modern view of the origin of the universe. London: Andre Deutsch

Weiss A., Salaris M., Ferguson J. W., Alexand er D. R., 2006, arXiv e-prints, pp astro–ph/0605666

White S. D. M., Rees M. J., 1978, MNRAS, 183, 341

White T. R., Bedding T. R., Stello D., Christensen-Dalsgaard J., Huber D., Kjeldsen H., 2011, ApJ, 743, 161

Wolf C., et al., 2018, PASA, 35, e010

Wu T., Li Y., Hekker S., 2014, ApJ, 786, 10

Yanny B., et al., 2009, AJ, 137, 4377

Yıldız M., Çelik Orhan Z., Kayhan C., 2016, MNRAS, 462, 1577

Yoachim P., Dalcanton J. J., 2006, AJ, 131, 226

Yoachim P., Dalcanton J. J., 2008, ApJ, 682, 1004

Yoshii Y., 1982, Publications of the Astronomical Society of Japan, 34, 365

Yu J., Huber D., Bedding T. R., Stello D., Hon M., Murphy S. J., Khanna S., 2018, The Astrophysical Journal Supplement Series, 236, 42

Zasowski G., et al., 2017, AJ, 154, 198

Zhao G., Zhao Y.-H., Chu Y.-Q., Jing Y.-P., Deng L.-C., 2012, Research in Astronomy and Astrophysics, 12, 723

da Silva L., et al., 2006, A&A, 458, 609

de Jong R. S., et al., 2014, in Ground-based and Airborne Instrumentation for Astronomy V. p. 91470M, doi:10.1117/12.2055826

de Vaucouleurs G., 1959a, Handbuch der Physik, 53, 275

de Vaucouleurs G., 1959b, Handbuch der Physik, 53, 311

van Saders J. L., Pinsonneault M. H., 2013, ApJ, 776, 67